SAPIENZA
UNIVERSITÀ DI ROMA

Facoltà di Ingegneria dell'Informazione, Informatica e Statistica

Dipartimento di Ingegneria dell'Informazione, Elettronica e Telecomunicazioni

Wi-Fi sensing: fusion of non-cooperative and device-based RF sensors for short-range localization

PhD in Information and Communication Technologies

Cycle XXXII

PhD student: Ileana Milani

Advisor: Prof. Pierfrancesco Lombardo

This thesis was evaluated by the two following external referees:

Prof. Alessio Balleri, Cranfield University, Shrivenham, United Kingdom

Prof. Silvia Liberata Ullo, University of Sannio, Benevento, Italy

The time and effort of the external referees in evaluating this thesis,
as well as their valuable and constructive suggestions,
are very much appreciated and greatly acknowledged.

Abstract

Through the years, target localization has captured the attention of both academic and industrial worlds, thanks to the huge amount of applications which require the knowledge of the position information.

Several works can be found on this topic, where the target localization has been addressed in different ways, depending on the type of target, the specific application and the surrounding scenario.

The main goal of this thesis is the definition of innovative methodologies able to solve the problem of the localization of human targets and small objects in local area environments in any operating conditions. In addition to the achievement of important improvements in positioning accuracy, we are also interested in performing the localization for the entire observation time where the target stays in the area of interest.

To achieve this result, in this work we decided to propose the joint use of different positioning techniques, based on their fusion in a unified system. The advantage of this fusion lies in the possibility of compensating for the intrinsic limitations of each proposed methodology, especially when complementary techniques are employed.

Two different sensors are considered in this work. Both exploit the Wi-Fi transmissions, based on the IEEE 802.11 Standard, therefore also the same receiver can be employed to receive measurements and information about the target present in the area of interest from multiple sensors, without increasing the complexity of the receiving system. Specifically, the first candidate to be used is the Passive Bistatic Radar (PBR) that exploits the Access Point (AP) as illuminator of opportunity. Due to the possibility to obtain the human target position without the necessity for the target to carry a device, this technique can be inserted into the group of the "Device-free localization" methodologies. It makes the WiFi-based passive radar attractive for local area surveillance and monitoring applications, especially where the targets cannot be assumed to be cooperative, as in typical security applications. With reference to the second sensor, the Passive Source Location (PSL) is another possible strategy to estimate the target position. In contrast to the PBR, this is a device-based technique that uses the device transmissions to perform the localization of the specific target.

Considering the characteristics of the proposed strategies, it is evident that they present complementary aspects. We can take advantage from this complementarity in several ways. Firstly, due to the Time Division Multiple Access (TDMA) approach used in the Wi-Fi Standard, devices and AP cannot transmit simultaneously, so we can compensate for the lack of signals from one sensor with the measures estimated by the other one. Secondly, we can use the device-based strategy when the target is stationary, and the Passive Radar cannot estimate its position because of the cancellation stage performed during the processing. On the other hand, the Passive Radar is necessary when the target does not carry an active mobile device, or it does not want to be localized (surveillance and monitoring activities). Finally, we can discriminate even very closely spaced target (if both carry an active mobile device) thanks to the possibility to read the MAC Address written into the packets of their devices.

The first part of this thesis is dedicated to the characterization of the single sensors, based on the description of the measurement extraction and the evaluation of the related positioning techniques. With respect to the measurement extraction, the PBR provides the target position through the combination of different sets of measures as range/Doppler/Angle of Arrival (AoA). For the PSL, the Time Difference of Arrival (TDoA) and the AoA can be exploited for the same purpose. Since the properties of the PBR have been extensively defined by our research group in the past, in this work more attention has been dedicated to the PSL description. In particular, proper techniques for measurement estimation are reviewed and innovative techniques for TDoA estimation of the PSL sensor are proposed, which provide improved performance with respect to existing techniques. The accuracies achieved with different positioning techniques exploiting several combinations of the estimated measurements are then evaluated. The results show that in short range applications it is desirable to use only AoA measurements, if possible.

After the characterization of the sensors, the localization performance of the two techniques are analyzed and compared. This analysis has shown both the effectiveness of the two sensors in target localization and their inherent limitations. In particular, we have studied the relationship between data traffic conditions and performance, and we have seen that it is strictly linked to the number of data available for the estimation of the measures of interest. In addition, the complementarity of the two methodologies has been demonstrated through the evaluation on experimental data acquired in appropriate measurement campaigns, in different network traffic conditions. In this phase, a tracking stage has not been performed. In order to improve the localization performance and carry out the desired sensor fusion, the second part of the thesis has been dedicated to the definition of innovative techniques for target tracking which exploit the characteristics of the employed sensors. Specifically, a new Sensor Fusion tracking filter is proposed. It uses a modified version of the Interacting Multiple Model (IMM) approach, where a Modified Innovation (MI) is introduced, together with Data Fusion techniques. In particular, in this strategy the information related to the presence or absence of the PBR estimates is used to help the choice between the employed filters, in order to improve the localization performance of human targets in the typical “stop & go” motion scenario.

The performance of the proposed strategy has been evaluated on both simulated and experimental data. The performance has shown that the IMM-MI outperforms the other strategies, since it provides the best performance in terms of positioning accuracy, target motion recognition capability and percentage of acquisition time covered by this strategy.

Table of Contents

Chapter 1 Introduction 8
1.1 Background and State of the Art 8
1.2 Research challenges and selected approach 10
1.3 Outline of the Thesis 13
Chapter 2 Sensors description 15
2.1 IEEE 802.11 Standard and WiFi packets features 15
2.2 Passive Bistatic Radar (PBR) 16
2.2.1 Measurement extraction 17
2.2.2 Positioning techniques 19
2.2.3 Processing scheme 22
2.3 Passive Source Location (PSL) 23
2.3.1 Measurement extraction 24
2.3.1.1 Techniques for Time Difference of Arrival (TDoA) estimation 24
2.3.1.1.1 Cross-Correlation and Oversampling Method (CCF-OVS) 26
2.3.1.1.2 Cross-Correlation and Fast Parabolic Interpolation Method (CCF-FPI) 28
2.3.1.1.3 Average Square Difference Function and FPI Method (ASDF-FPI) 29
2.3.1.1.4 CCF + Slope-based Method 31
2.3.1.1.5 Iterative Slope-based Method 35
2.3.1.1.6 Comparison of TDoA estimation methods 40
2.3.1.2 Techniques for Angle of Arrival (AoA) estimation 42
2.3.2 Positioning techniques 44
2.3.2.1 Positioning techniques based on TDoA measurements 45
2.3.2.1.1 Measurement and positioning errors 48
2.3.2.1.2 Theoretical performance evaluation 50
2.3.2.1.3 Closed-form solution 53
2.3.2.2 Positioning techniques based on AoA measurements 54
2.3.2.2.1 Measurement and positioning errors 56
2.3.2.2.2 Theoretical performance evaluation 59
2.3.2.2.3 Solution for the minimum number of receiving nodes 61
2.3.2.3 Positioning techniques based on AoA/TDoA measurements 62
2.3.3 Processing scheme 65
Chapter 3 Comparative analysis of PBR and PSL 66
3.1 Experimental setup and equipment description 66
3.1.1 Acquisition site and geometry 66

3.1.2 Access Point ... 68
3.1.3 Receiving system ... 69
3.1.3.1 Wi-Fi antennas ... 69
3.1.3.1.1 D-LINK ANT24-1200 ... 69
3.1.3.1.2 TP-LINK TL-ANT2409A ... 71
3.1.3.2 Multi-channel receiver: NI USRP-2955 ... 73
3.1.4 Antenna configurations ... 76
3.2 Low data traffic for PSL sensor ... 78
3.2.1 Acquisition campaign description ... 78
3.2.2 Relationship between data traffic conditions and performance ... 79
3.2.2.1 Accuracy of device-based AoA measurements ... 81
3.2.2.2 Accuracy of passive radar AoA measurements ... 85
3.2.3 Performance comparison of the two techniques ... 91
3.2.3.1 Passive Source Location performance ... 91
3.2.3.2 Passive Bistatic Radar performance ... 93
3.2.3.3 Techniques comparison and complementarity ... 95
3.3 High data traffic for PSL sensor ... 97
3.3.1 Acquisition campaign description ... 97
3.3.2 Performance comparison of the two techniques ... 98
3.3.2.1 Passive Source Location performance ... 98
3.3.2.2 Passive Bistatic Radar performance ... 100
3.3.2.3 Techniques comparison and complementarity ... 102
3.4 Summary ... 103
Chapter 4 Tracking techniques ... 106
4.1 Kalman Filter (KF) ... 106
4.2 Interacting Multiple Model (IMM) ... 107
Chapter 5 Interacting Multiple Model - Modified Innovation (IMM-MI) ... 110
5.1 Motion and Observation Models ... 111
5.2 Augmentation and Reduction ... 114
5.3 Sensor Fusion ... 115
5.4 State interaction ... 116
5.5 Filtering ... 117
5.6 Innovation Modification and Probability Update ... 118
5.6.1 Absence of PBR detections ... 120
5.6.2 Presence of PBR detections ... 121
5.7 Combination ... 122

Chapter 6 Tests on simulated target 123
6.1 Measurements generation 123
6.2 Setting of the employed methodologies 125
6.2.1 KF-NCV (Single Sensor) 125
6.2.2 KF-NCV (Sensor Fusion) 128
6.2.3 IMM (Single Sensor) 128
6.2.4 IMM (Sensor Fusion) 130
6.2.5 IMM-MI (Sensor Fusion) 131
6.3 Case study: Simulated Move-Stop-Move Target with changes of direction 132
6.4 Evaluation of the RMSE as a function of simulation time 133
6.5 Evaluation of the RMSE as a function of the Detection Probability for the PBR sensor 136
Chapter 7 Tests on experimental data 142
7.1.1 KF-NCV (Single Sensor) 146
7.1.2 KF-NCV (Sensor Fusion) 147
7.1.3 IMM (Single Sensor) 148
7.1.4 IMM (Sensor Fusion) 149
7.1.5 IMM-MI (Sensor Fusion) 151
7.1.6 Comparison of the analyzed methodologies in terms of positioning error 152
Chapter 8 Conclusion 155
BIBLIOGRAPHY 157
LIST OF PUBLICATIONS 161

Chapter 1
Introduction

1.1 Background and State of the Art

In the recent years, great effort has been devoted to the localization of human targets and small objects in local area environments. The interest on this topic is motivated by the huge amount of possible applications that require the knowledge of the target position:

- for monitoring and surveillance applications in critical areas, such as ports or airports;
- as support in rescue missions inside buildings (for example in case of fire), where the capability of quickly and accurately coordinating the components of rescue teams is a key element for the success of the rescue operation, as discussed in [1];
- in medical applications focused on the improvement of quality of life for disabled people (for example, in [2] an application for blind persons is supposed, while in [3] an extensive review is performed on the use of Radio Frequency (RF) sensing for healthcare applications);
- in the offer of different kind of services (for museums, shops, hospital and universities).

In outdoor environments, this operation is obtained through the exploitation of satellite signals, using global navigation satellite systems as GPS, Glonass or Galileo. As well known, these signals have strong limitations indoor and require targets to cooperate in order for them to be detected and localized. For this reason, an alternative solution is to employ other RF signals already available, for localization aims. They have a wide coverage also in indoor areas and can be used to detect and localize non-cooperative targets. Depending on the requirements of the specific application, several waveforms can be exploited as, for example, FM [4]-[6], DVB-T [7]-[12] and Wi-Fi signals [13]-[20].

Different approaches can be considered to perform localization when exploiting these signals. In particular, these strategies can be discriminated based on whether an active device carried by the human target is required or not, and on the level of cooperation of the specific target. Obviously, all the classes of localization techniques have inherent advantages and drawbacks. A recent comprehensive review of such techniques is presented in [21], which compares the relative merits and issues, while a review of the only device-free localization strategies is reported in [22].

In particular, the expansion of the Wi-Fi networks in urban environments has led to the employment of Wi-Fi signals in several applications, thanks to the coverage that they offer in both indoor and outdoor environments. It is clear that this characteristic makes them especially suitable for short range localization and surveillance applications [16], as well as for extracting target characteristics as cross-range profiles, [23].

Based on the aforementioned classification of the localization techniques, a brief description of the main strategies for each class is now presented.

Cooperative localization

When the target voluntarily tries to be localized, we refer to cooperative localization. Several studies can be found in the technical literature, related to this case; one of the most used techniques is fingerprinting. It is of great interest the exploitation of Wi-Fi signals, when this strategy is used.

In many cases, the Received Signal Strength (RSS) is measured at different locations of the considered environment. The prints obtained in this way are stored into a dataset (offline measurements or 'calibration stage'), and are used as a benchmark to evaluate target position (online measurements or 'localization stage'). This stage is performed applying different strategies, e.g. K-Nearest Neighbor (K-NN), Support Vector Machine (SVM), etc. which are the preferred ones in this kind of studies.

Moreover, fingerprinting is not only defined based on signal strength, but also based on channel impulse response, [24]. This strategy leads to better performance, and it is particularly suitable to be applied when channel response can be easily inferred.

In other studies, use of Radio-Frequency Identification (RFID) technology has been proposed. This technology is often used in positioning systems where active cooperation from the user that needs to be localized can be exploited (as already mentioned in the example of rescue teams coordination, described in [1]). One of the main drawbacks of RFID technology is the need of a dedicated infrastructure, thus resulting in increased deployment costs.

All these strategies lead to good localization results (mainly with the application of advanced probabilistic methods), if particular conditions occur. Specifically, due to the need of active cooperation from the target, these strategies cannot be applied whether the object/person to be localized does not carry a mobile device or the Wi-Fi connection is disables. Moreover, obtainable accuracy strongly depends on actual operating conditions.

Partially cooperative localization

When the target provides involuntary contribution to positioning, we refer to partially cooperative localization. The target can be defined as system user, since it carries an active device and its transmissions are exploited. It is a non-cooperative localization, but the target, by carrying a device, provides a contribution to the definition of its position. We refer, in this case, to passive positioning: user does nothing to be voluntarily located, but localization occurs just as a consequence of carrying an emitting device. Even in this case Wi-Fi signals can be exploited, as the communications between Access Point (AP) and device when they are connected.

Specifically, detection of packets transmitted from the target (object/person) under exam is performed through multiple receiving antennas (typically 3 of 4, depending on the desired measurements and on the

capabilities provided by the receiving platform). Data collected by the antennas are processed by means of proper techniques to obtain an estimate of user position.

The techniques mainly used are Time of Arrival (ToA) estimation, Angle of Arrival (AoA) estimation and Time Difference of Arrival (TDoA) estimation.

These techniques allow the determination of the position of user carrying the mobile device; specifically, estimation is more reliable the more the target is stationary, since in this case an increased number of packets is available to perform the estimation. It would therefore be interesting evaluating the relationship between estimation reliability and number of available packets.

They are potentially characterized by low accuracy in position estimation, mainly in indoor scenarios, due to the difficulty in defining the propagation model for signals in complex environments (multipath, etc.). Nevertheless, different studies have been carried out aiming at removing this kind of problem, in most cases by jointly using AoA and ToA estimations, [25].

Main contributions in this area are related to scenarios with user voluntarily cooperating to be located, so great effort is requested with respect to the possibility to exploit only the communications occurring during usual Wi-Fi connection activities.

Non-cooperative localization

Finally, if there is no collaboration from the target, neither voluntary nor involuntary, and it is detected only due to its interaction with signals present in the environment, we refer to non-cooperative localization.

In this framework, interesting studies have been carried out by University of Utah, by exploiting Radio Tomographic Imaging (RTI) technique to localize a person not carrying a mobile device (this is the reason why this methodology is usually referred in technical literature as 'device-free localization'). As described in [26], RTI is based on the principles of two different systems for the realization of images: radar systems and computed tomography, used for medical applications.

Another method to perform non-cooperative localization foresees the use of passive radars exploiting Wi-Fi signals as waveforms of opportunity. This topic has been widely addressed by our research group in the DIET Department at Sapienza University of Rome. The developed WiFi-based passive radar demonstrator performs the localization and tracking of moving targets, there including vehicles and human targets. Some interesting studies in this field are described in [14]-[17],[23] and [27].

1.2 Research challenges and selected approach

The localization of human targets and small objects in local area environments is one of the most attractive issues of the last years. As explained before, each strategy is characterized by inherent advantages and drawbacks. In particular, in some cases the main problem is the impossibility for the single technique to detect and localize a target in particular conditions. To face this problem, we decided to propose the joint use of different positioning techniques.

In addition to the achievement of important improvements in positioning accuracy, we are also interested in performing the localization for the entire observation time where the target stays in the area of interest.

To do that, two different techniques based on Wi-Fi signals have been considered in this work: firstly, the Passive Bistatic Radar (PBR) that exploits the AP as illuminator of opportunity is an interesting solution, especially for surveillance applications in local area environments, because it provides the position of non-cooperative targets, which do not carry an active device (the so called "device-free localization"), [17]. Secondly, supposing that the target has the possibility to transmit Wi-Fi signals (use of mobile devices for a human target), the Passive Source Location (PSL) that in contrast uses the device transmissions to define the position of the target, is another possible strategy to reach the same goal, [21]. Their concept is depicted in Figure 1.1.

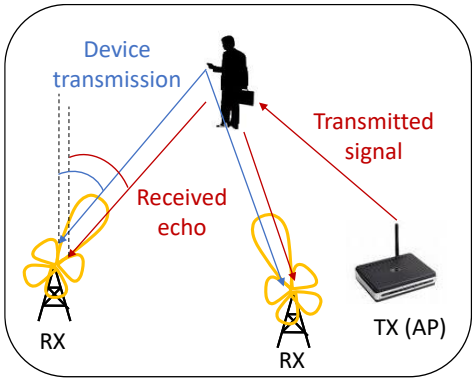

Figure 1.1. Sketch of WiFi-based PBR and PSL approaches.

As well known, the passive radar is very effective in detecting moving targets by using clutter cancellers. The extraction of stationary targets echoes is generally more complex and less effective, due to the background echoes cancellation stage performed during the processing. Moreover, due to the frequency bandwidth of the Wi-Fi waveforms, spanning from 11 to 20 MHz, the range resolution is not better than a few meters, which makes it difficult to discriminate closely spaced persons. In contrast, good Doppler frequency resolution is available, which provides good localization performance when the target is well separated in Doppler from the other targets and even allows to obtain cross-range profiles, [23].

As explained before, the use of Wi-Fi signals allows also exploiting the waveforms emitted directly by the device to localize them, [21].

The autonomous RF emissions of devices that attempt to connect to the Wi-Fi network allow us a different way to localize the human targets. As mentioned also in [21], to reach this purpose, many techniques have been investigated and applied. Largely used are position solutions based on the estimation of AoA, ToA and TDoA. As apparent, this only allows localizing human targets carrying an active Wi-Fi device. In addition, it could be potentially inaccurate for moving targets. On the other hand, it is an interesting solution for stationary targets localization and it allows the unambiguous association of the transmission to a specific target, based on the device MAC address, so that even very closely spaced persons can be discriminated.

Our purpose is to compare the relative performance of this two localization techniques based on the IEEE 802.11 Standard, [28], and to verify their complementarity, aiming at their joint exploitation in a unified system, which exploits at the best the features of both the employed sensors.

Through the years, great interest is also devoted to the target tracking. This topic has still several open issues. In particular, one of the most interesting problems is the tracking of move-stop-move targets. In fact, despite the low complexity of the single motions, its management is very hard in practical applications. First of all, the detection of stationary targets is still a problem when the passive radar is exploited. Secondly, the similarity between the two types of motion could generate important ambiguities when particular techniques are employed.

The aforementioned problems increase when the examined target frequently and rapidly changes its motion status. This is the case, for example, of the smallest targets which can be found in local area environments, as persons or drones. In this case, the Kalman Filter (KF) and the classical Interacting Multiple Model (IMM) are not effective to reach this purpose.

In order to find a solution to this problem, in this thesis two novelties in common tracking strategies have been introduced:

1) Data Fusion techniques are applied in order to exploit the advantages of the two employed sensors and extend the time in which the examined target is localized.
2) A modified version of the IMM, that we called *Interacting Multiple Model - Modified Innovation* (*IMM-MI*) is devised with the purpose of compensating for the limitation of the existing techniques. Even this time the knowledge of the characteristics of the single sensors is exploited, in order to help the decision on the motion model that has to be used.

The research approach followed in this thesis to obtain these results is represented in Figure 1.2.

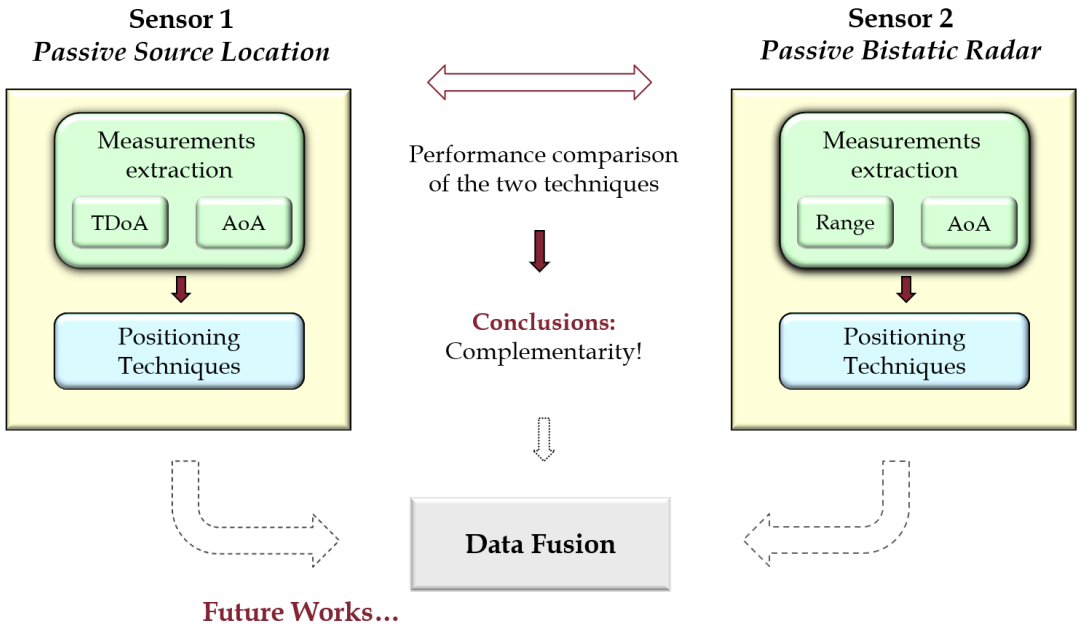

Figure 1.2. Research approach followed in this thesis

The first step is the characterization of the two sensors. In this phase, we focused on the analysis of the measurements that the specific sensor can exploit to estimate the target position and the derivation of the related positioning techniques. In particular, since the PBR has been extensively studied by our research group, greater attention was devoted to the characterization of the device-based sensor, for which innovative techniques for the estimation of the TDoA are also presented.

After the sensor descriptions, their performance is analyzed and compared. The inherent features of the two strategies and the results obtained from their comparison on experimental data have shown an interesting complementarity between them. This result opens the way to the development of appropriate sensor fusion techniques, which characterizes the final part of this thesis. The proposed strategy is then evaluated on both simulated and experimental data on a move-stop-move target, and its performance is compared with existing techniques (KF and IMM). Even the employment of sensor fusion techniques on classical tracker is tested. The results show that the use of more sensors provide better performance with respect to the use of single sensor versions. However, some problems still appear when the target changes its motion. The IMM-MI is a possible solution to these problems. In fact, it outperforms the other strategies, since it provides the best performance in terms of positioning accuracy, target motion recognition capability and percentage of acquisition time covered by this strategy.

1.3 Outline of the Thesis

With reference to the scheme presented in Figure 1.2 this thesis has been organized as follows.

Chapter 2. The two PBR and PSL sensors and the related localization strategies are described in detail. For each sensor, the analysis has been divided in three main parts. Firstly, different techniques for the measurement extraction have been studied. In particular, a deepened analysis has been carried out for the TDoA estimation, for which innovative techniques are also proposed. Secondly, based on the measures studied in the first part of this Chapter, the relative positioning strategies are derived and compared in terms of localization accuracies. Finally, the processing schemes of the two sensors are presented and the main blocks are described.

Since the PBR has been extensively analyzed by our research group in the past, in Chapter 2 the main features of the passive radar are briefly summarized, giving more importance to the enhancement with respect to the previous system, while larger space has been dedicated to the PSL description.

Chapter 3. As the deepened knowledge of the two sensors is now available, the performance of the PBR and PSL sensors in terms of localization accuracy is faced in this Chapter. In particular, the relationship between data traffic conditions and performance for the two strategies, and their performance comparison are evaluated on experimental data. Specifically, the comparison of the two localization strategies has been performed on two different data sets characterized by different network conditions.

Chapter 4. After the target localization, the tracking stage can be applied in order to improve the positioning performance. Therefore, the main existing tracking algorithms, namely the KF and the IMM, are briefly presented, and the relative advantages and limitations are recalled.

Chapter 5. A new methodology for target tracking is proposed, which exploits the inherent differences between the PSL and the PBR sensors, in order to develop a consistent and effective method for small target localization and tracking, especially for move-stop-move targets. The proposed strategy uses a modified version of the IMM approach together with Data Fusion techniques, that take into account the differences between the measurement's accuracies of the employed sensors. In the modified version of the IMM method, the information related to the presence or absence of the PBR estimates is used to help the choice between the employed filters, through the modification of the Innovation.

Chapter 6. The proposed strategy is then compared with the KF and the IMM methods over a simulated target. Specifically, the stop & go motion has been simulated, aiming at showing the capability of the proposed strategy to follow the target behavior, thanks to the possibility to exploit the knowledge of the characteristic of the employed sensors. In this analysis, for the KF and the IMM, both the single sensor and the sensor fusion versions are considered, in order to highlight the advantages of the joint use of two different sensors. Two analysis have been performed: 1) the evaluation of the Root Mean Square Error (RMSE) as a function of the simulation time, and 2) the evaluation of the RMSE as a function of the Detection Probability for the Passive Radar.

Chapter 7. The evaluation of the performance for the aforementioned techniques has finally been carried out on experimental data, through the design of appropriate acquisition campaigns.

Chapter 8. In the last Chapter the conclusions are drawn.

Chapter 2
Sensors description

Before starting with the detailed description of the two proposed sensors, it is convenient to briefly describe the main characteristics of the employed Wi-Fi signals.

2.1 IEEE 802.11 Standard and WiFi packets features

The IEEE 802.11 Standard, [28], defines the main characteristics of Wireless Local Area Networks (WLANs). It presents one Medium Access Control (MAC) and several Physical (PHY) layer specifications. In the last years, different versions of this standard have been developed. In particular, the IEEE 802.11a Standard uses the 5 GHz band, while 802.11b/g/n operate in the 2.4 GHz band. Different data rates can be used, thanks to the employment of different modulation and coding schemes.

In the 2.4 GHz band the spectrum is divided into 14 channels, spaced 5 MHz each other. Due to the Wi-Fi bandwidth, spanning from 11 to 20 MHz (or higher values in some cases), depending on the specific Standard version or modulation type, it is evident that the Wi-Fi channels are partially overlapped and so it is possible to have interference among transmissions occurred in consecutive channels. Moreover, multiple users can share the same channel, therefore they have to alternate the medium occupation (TDMA approach) in order to avoid contemporary transmissions. To reduce the risk of collisions, the Carrier Sense Multiple Access with Collision Avoidance (CDMA/CA) access mechanism is adopted.

As well known, the Wi-Fi communications use the packet switching approach to exchange information. The function of a specific packet is defined by the type/subtype field. There are three different packet types (management, control and data), and several subtypes for each of them, e.g. beacon, association request, authentication, etc.

To establish the connection between APs and devices, which is the primary operation before any communication activity, management packets are transmitted. There are two ways to perform the searching of stations in a given area: the passive and the active scanning techniques. In the first case, the AP periodically sends beacons in broadcast mode to announce its presence. The transmission rate and the operating channel are set previously. The latter foresee that a mobile station sends probe requests in broadcast mode on a single channel and waits for answers from the APs in proximity. If it does not receive any probe response, it switches to another channel and it repeats the same operation.

After that, the mobile station sends the authentication frame to the desired AP, after the reception of the AP answer, it transmits the association request and, when the association stage is completed, the data transfer

between AP and device can start. Even very short communications are therefore characterized by the exchange of many packets of different types, which have different features and frame formats. It is also important to notice that the packet length varies according to its subtype. This is related to the differences among the frame formats of different packets. In addition, it also depends on the dimension of the payload in data packets.

These considerations confirm that the exploitation of the huge amount of Wi-Fi signals exchanged during common connection or communication activities represents an attractive solution for localization applications.

2.2 Passive Bistatic Radar (PBR)

The Passive Radar is one of the most attractive solution for the localization of different types of target.

It works as a common radar, but its main feature is the bistatic form. In fact, the Passive Radar exploits the signals emitted by transmitters of opportunity, namely it does not use its own waveform, but pre-existent transmissions devised for other communication purposes. This means that receiver and transmitter are located in different places.

Among the advantages of this technique, we can mention the low costs of realization and maintenance (due to the lack of the transmitter), the possibility to avoid electromagnetic disturbances, the low impact on the environment, and so on. On the other hand, the impossibility to properly design and control the transmitted waveform makes the processing much more complicated (reference reconstruction, etc.) and the performance can decrease if proper techniques are not employed.

In particular, as explained in the Introduction, for short-range applications Wi-Fi signals are particularly suitable, thanks to the coverage that they have reached in recent years in local area environments. For this reason, in this thesis we focus on this typology of signals. The specific transmitter of opportunity is the Access Point, whose signals emitted for communication purposes in this case are used for the localization of human targets and small objects. As explained above, the Wi-Fi Standard established that the information is not transmitted with a continuous wave, but it is divided in packets. This means that a pulsed shape characterizes the transmissions exploited by the PBR. Following this consideration, in this work the terms *pulse* and *packet* are used as synonyms. In particular, the specific packets (*beacons*) that the AP periodically sends in broadcast mode to announce its presence in a specific area, represent an interesting choice for the design of the described passive radar: the possibility to exploit a constant Pulse Repetition Time (PRT), due to the definition of a constant Beacon Interval (BI), which is defined as the time spacing between consecutive beacons, encourages the use of these signals. Typical beacon transmissions are shown in Figure 2.1.

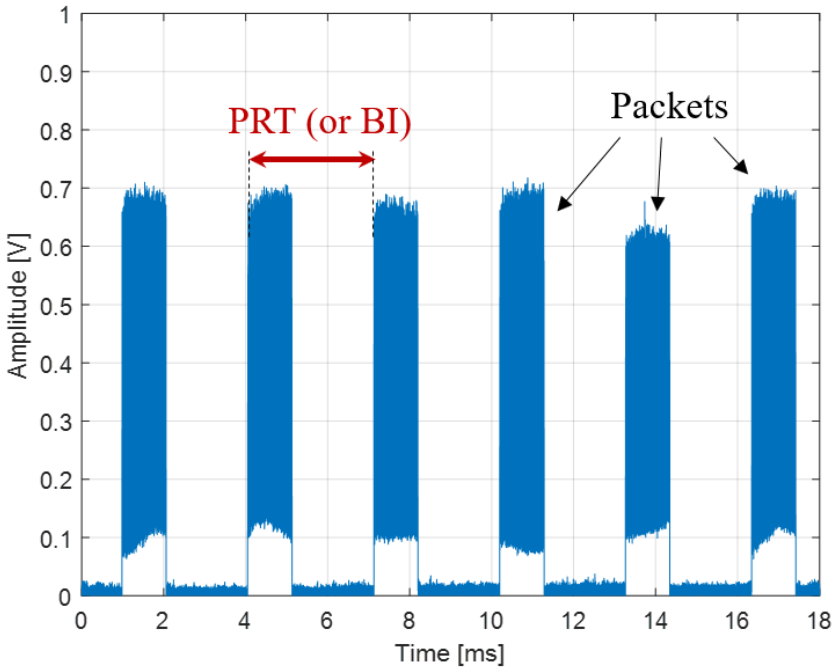

Figure 2.1. Example of a sequence of Wi-Fi packets.

In the next sections, the main parameters measurable by the Passive Radar are presented together with their combination to perform the positioning in the XY-plane.

2.2.1 Measurement extraction

The PBR sensor can provide different measurements. Each measure is estimated on the specific target detection, namely after the applications of all the operations summarized in the processing scheme that will be described in detail in Section 2.2.3.

A single surveillance antenna can estimate both the bistatic range and the bistatic Doppler frequency (which is directly connected to the bistatic velocity) of a target. With a couple of closely spaced antennas, it is possible to estimate even the Angle of Arrival (AoA) of the received target echo. A sketch of the considered geometry with the relevant parameters in shown in Figure 2.2, where the line defined by the AoA, and the ellipse defined by the bistatic range are displayed.

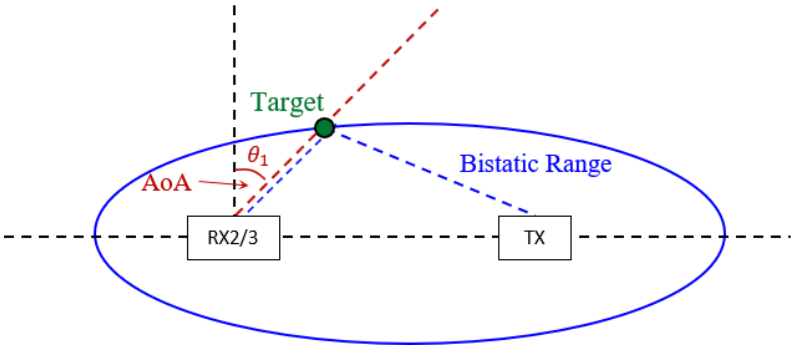

Figure 2.2. Sketch of the considered geometry with the relevant parameters.

Specifically, the bistatic velocity of the target is obtained from the Doppler frequency, f_D, measured on the received target echo. As it is well known, the relationship between Doppler frequency and velocity is the following

$$v_{bis} = f_D \cdot \lambda \tag{2.1}$$

where λ is the wavelength related to the Wi-Fi channel where the transmitter, in our case the Access Point, is transmitting.

The bistatic range is defined as the sum of two contributions: *i)* the distance between transmitter (AP) and target and *ii)* the distance between target and receiver

$$R_{bis} = R_{TX,target} + R_{target,RX} \tag{2.2}$$

where $R_{TX,target}$ and $R_{target,RX}$ are the two contributions described above.

Therefore, we obtain

$$R_{bis} = \sqrt{(\mathrm{x}_{TX} - \mathrm{x}_\mathrm{u})^2 + (\mathrm{y}_{TX} - \mathrm{y}_\mathrm{u})^2} + \sqrt{(\mathrm{x}_{RX} - \mathrm{x}_\mathrm{u})^2 + (\mathrm{y}_{RX} - \mathrm{y}_\mathrm{u})^2} \tag{2.3}$$

where (x_{TX}, y_{TX}) are the coordinates of the transmitter, (x_{RX}, y_{RX}) are the coordinates of the receiver, while (x_u, y_u) are the coordinates of the target, which have to be estimated.

In particular, the bistatic range is directly connected to time of arrival, τ, through the following relation

$$R_{bis} = c \cdot \tau \tag{2.4}$$

where c is the speed of light.

Combining the equations (2.3) and (2.4), we obtain

$$\sqrt{(\mathrm{x}_{TX} - \mathrm{x}_\mathrm{u})^2 + (\mathrm{y}_{TX} - \mathrm{y}_\mathrm{u})^2} + \sqrt{(\mathrm{x}_{RX} - \mathrm{x}_\mathrm{u})^2 + (\mathrm{y}_{RX} - \mathrm{y}_\mathrm{u})^2} = c \cdot \tau \tag{2.5}$$

As it is clear from (2.5), in this way we have only one equation in two unknowns (x_u and y_u).

For the localization in the XY-plane, it is therefore necessary to add a further equation that is provided by the employment of an additional receiver.

As mentioned above, if the second receiver is very close to the first one, it is possible to estimate also the AoA, $\hat{\theta}$. As shown in Figure 2.3, this angle is linked to the phase difference between the signals received by the two surveillance antennas, $\widehat{\Delta\varphi}$, through the relation

$$\widehat{\Delta\varphi} = \frac{2\pi d}{\lambda} \sin\hat{\theta} \tag{2.6}$$

where λ represents the wavelength related to the Wi-Fi channel on which the device is transmitting, while d is the distance between the antenna elements, as defined above.

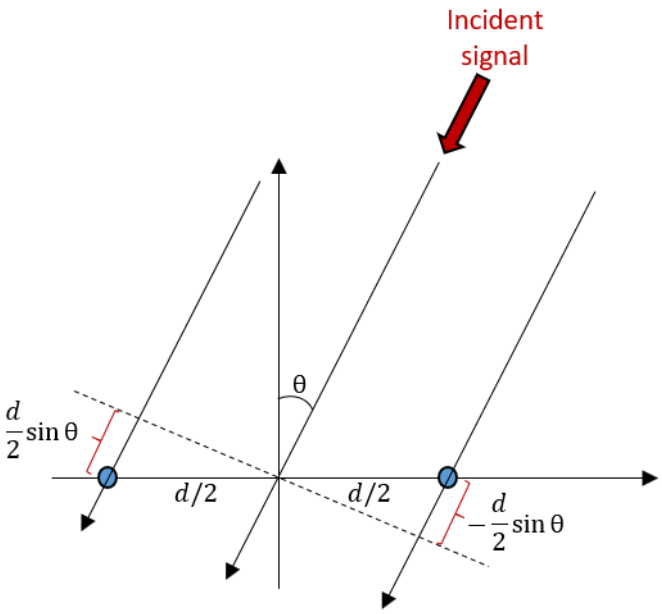

Figure 2.3. Direction of Arrival estimation.

From (2.6), it can be easily derived

$$\hat{\theta} = arcsin\left(\frac{\lambda \cdot \widehat{\Delta\varphi}}{2\pi d}\right) \tag{2.7}$$

All parameters in the equation (2.7) are known, except for the phase difference which, instead, has to be estimated from the received target echoes. In this case, the following expression applies

$$\widehat{\Delta\varphi} = \arg\left(\frac{x_2}{x_1}\right) \tag{2.8}$$

where x_1 and x_2 are the samples in the bi-dimensional Cross-Correlation Functions (2D-CCF) corresponding to the location of the specific target detection, for the two receivers exploited for the angle estimation.

2.2.2 Positioning techniques

After the definition of the measures that can be used for the PBR sensor, it is important to have an idea of the possible strategies to obtain the target localization in the XY plane.

The positioning can be performed in different ways, also depending on the number of receiving nodes available and the number of antennas contained in each node.

As explained in the previous section, for the Passive Bistatic Radar, the bistatic range and the angle of arrival can be exploited for the target localization.

The considered combinations of bistatic range and AoA for target localization are summarized in Table 1.

Table 1. Measurement combinations for target localization with the PBR sensor.

Number of nodes	PBR sensor
1 Receiving Node (2 Antennas)	1 Range + 1 AoA
2 Receiving Nodes (max 4 Antennas)	2 Ranges
	1 AoA + 2 Ranges

In this table, when two measures of angle are used, four surveillance antennas are employed to acquire the echoes scattered by the target.

The positioning techniques for the PBR sensor are extensively discussed in [17]. In particular, the treatment is divided into two blocks:

1) The target localization using the minimum number of measures.
2) The target localization using multiple measurements.

The following combinations were analyzed for the first case.

A) Two bistatic range measurements provided by two receiving nodes after the detection stage.
B) Two bistatic range measurements obtained from two receiving nodes after a range/Doppler tracking stage.
C) A range measurement and an AoA measurement provided by a single receiving node.

Instead, for the second case, two bistatic range measurements and one AoA measurement estimated by two nodes were exploited. Each of the three measurements defined a specific equation where the unknowns were the coordinates of the target in the XY-plane, i.e. (x_u, y_u). This means that the system was overdetermined, therefore the Least Square (LS) solution and the Maximum Likelihood (ML) solution were used for the 2D localization of the target.

In the following, we briefly summarize the main results reported in [17], where this study has been extensively discussed.

The system of equations when two measurements of range and one of AoA are exploited is the following

$$\begin{cases} \hat{R}_{bis_1} = \sqrt{(\mathrm{x}_{TX} - \mathrm{x_u})^2 + (\mathrm{y}_{TX} - \mathrm{y_u})^2} + \sqrt{\left(\mathrm{x}_{RX_1} - \mathrm{x_u}\right)^2 + \left(\mathrm{y}_{RX_1} - \mathrm{y_u}\right)^2} \\ \hat{R}_{bis_2} = \sqrt{(\mathrm{x}_{TX} - \mathrm{x_u})^2 + (\mathrm{y}_{TX} - \mathrm{y_u})^2} + \sqrt{\left(\mathrm{x}_{RX_2} - \mathrm{x_u}\right)^2 + \left(\mathrm{y}_{RX_2} - \mathrm{y_u}\right)^2} \\ \hat{\theta} = \tan^{-1}\left(\frac{\mathrm{x_u}}{\mathrm{y_u}}\right) \end{cases} \tag{2.9}$$

where (x_{TX}, y_{TX}) are the coordinates of the transmitter, (x_{RX}, y_{RX}) are the coordinates of the receiver, (x_u, y_u) are the coordinates of the target, which have to be estimated, $\hat{R}_{bis_1}$ and $\hat{R}_{bis_2}$ are the bistatic ranges measured

by the two nodes, while $\hat{\theta}$ is the angle of arrival estimated by the receiver containing two closely spaced antennas.

The LS solution of the system in (2.9) is

$$\mathbf{u} = \left(\mathbf{H}^{\mathrm{T}}\mathbf{H}\right)^{-1}\mathbf{H}^{\mathrm{T}}(\mathbf{m} - \mathbf{m}_0) + \mathbf{u}_0 \tag{2.10}$$

where $\mathbf{u}$ is the vector containing the target coordinates, $\mathbf{u}_0$ is the target tentative position used for the first-order Taylor series approximation, $\mathbf{H}$ is the matrix of the direction cosines, $\mathbf{m}$ is the representation with the matrix notation of the known terms $\hat{R}_{bis_1}$, $\hat{R}_{bis_2}$ and $\hat{\theta}$, namely

$$\mathbf{m} = \begin{bmatrix} \hat{R}_{bis_1} & \hat{R}_{bis_2} & \hat{\theta} \end{bmatrix}^T \tag{2.11}$$

and $\mathbf{m}_0$ is its expression calculated in $\mathbf{u}_0$.

The corresponding positioning error over the XY-plane is given by

$$\boldsymbol{\Sigma}_{\boldsymbol{u}}^{LS} = (\mathbf{H}^{\mathrm{T}}\mathbf{H})^{-1}\mathbf{H}^{\mathrm{T}}\boldsymbol{\Sigma}_{\mathbf{M}}\mathrm{H}(\mathrm{H}^{\mathrm{T}}\mathrm{H})^{-1} \tag{2.12}$$

where $\boldsymbol{\Sigma}_{\mathbf{M}}$ indicates the covariance matrix of the measurement errors defined as

$$\boldsymbol{\Sigma}_{\boldsymbol{M}} = \begin{bmatrix} \sigma_{R_1}^2 & 0 & 0 \\ 0 & \sigma_{R_2}^2 & 0 \\ 0 & 0 & \sigma_{\theta}^2 \end{bmatrix} \tag{2.13}$$

and $\sigma_{R_1}^2$, $\sigma_{R_2}^2$ and σ_{θ}^2 are the variances of the errors on R_{bis_1}, R_{bis_2} and θ, respectively.

For the ML solution, the target position can be expressed as

$$\mathbf{u} = \left(\mathbf{H}^{\mathrm{T}}\boldsymbol{\Sigma}_{\mathbf{M}}^{-1}\mathbf{H}\right)^{-1}\mathbf{H}^{\mathrm{T}}\boldsymbol{\Sigma}_{\mathbf{M}}^{-1}(\mathbf{m} - \mathbf{m}_0) + \mathbf{u}_0 \tag{2.14}$$

The results reported in [17] have shown that the ML produced better results with respect to LS approach, since the ML provides the possibility to weigh the measurements according to their accuracy, therefore it relies mainly on the angular information.

The comparison of all the methodologies has shown that the localization can be performed by using only range measurements, but before the localization a tracking stage in the bistatic range/Doppler plane has to be applied. In addition, it has been demonstrated that the use of the angular information provides an improvement in performance.

According to the aforementioned results, in the next analysis we will use one bistatic range measurement and one AoA measurement to perform the target localization in the XY-plane. This choice allows *i)* increasing the achievable positioning accuracy with respect to the use of only range measurements, thanks to the exploitation of an additional measurement of AoA, and *ii)* reducing the processing time avoiding the employment of iterative methods.

2.2.3 Processing scheme

The passive radar demonstrator developed at Sapienza University of Rome ([16]-[17]) has been applied. The generic processing scheme is sketched in Figure 2.4.

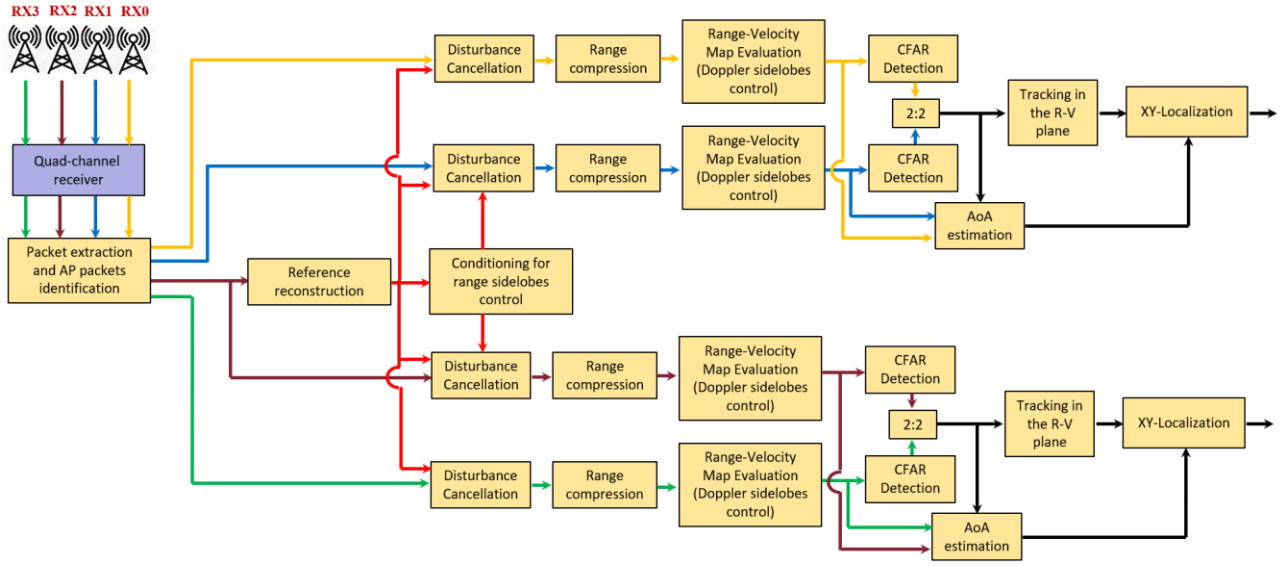

Figure 2.4. Processing scheme of the Passive Bistatic Radar exploiting four receiving channels and the reference reconstruction.

After the acquisition of the Wi-Fi signals through the available surveillance antennas, the first step is the packet extraction and their subsequent identification based on the source MAC address written in each packet. In this way the signals emitted by the AP can be discriminated and used as transmissions of opportunity for the Passive Radar.

The processing scheme presented in Figure 2.4 is the most generic representation when a quad-channels receiver is employed. However, a basic distinction can be made with respect to the number of channels actually dedicated to the acquisition of surveillance signals.

In particular, we are interested in considering two different situations, namely

1) The exploitation of the minimum number of receiving channels;
2) The exploitation of all the four receiving channels.

With reference to the first point, we can exploit three receiving channels for the acquisition of the signals of interest. In particular, two channels are occupied by the two surveillance antennas, while the third one can be dedicated to the acquisition of a clean copy of the reference signal, directly extracted by the Access Point. This choice provides the advantage to know exactly the signals emitted by the transmitter of opportunity, producing an improvement in performance. For this reason, the *Reference reconstruction* block in Figure 2.4 can be discarded and the subsequent operation can be performed exploiting the real reference signal.

For the second case, all the receiving channels are connected to the surveillance antennas. This provides on one hand the possibility to exploit more information, through the estimation of additional measurements (for example two AoA measurements) but, on the other hand, it disables the reference signal acquisition. This means

that such signal must be reconstructed with further post-processing operations, since this is necessary to perform the target localization with the passive radar system.

After these preliminary steps, the processing continues with the evaluation of the 2D-CCF, obtained by cross-correlating the surveillance signals with the reference signal (real or reconstructed) on a pulse by pulse basis. Thereafter, the obtained results are coherently integrated over a set of consecutive pulses. This requires to be repeated for all Doppler frequencies of interest, thus providing the 2D output as a function of both bistatic range and bistatic Doppler frequency.

As shown in [29], the Ambiguity Function (AF) of the Wi-Fi signals is characterized by high sidelobes in both range and Doppler dimensions. Therefore, proper techniques for the Range and Doppler sidelobes control are applied. In particular, the knowledge of the modulation of the beacons periodically transmitted by the AP (DSSS) allowed to devise suitable weighting networks. For the range sidelobes control, the two weighting networks proposed in [30] are used. The first one is called Barker Weighting Network (BWN) and is necessary to reduce the sidelobes within time delays of 1μs that are due to the 11-chip Barker code which characterized this signal. The second one is used to control the sidelobes due to the cyclical repetition of the Barker code. The doppler sidelobes reduction has been devised in [31] and uses well-known linear programming algorithms.

The processing scheme includes the clutter/multipath cancellation stage for the disturbance removal. In particular, the Sliding Extensive Cancellation Algorithm (ECA-S) is used, [32].

After that, the range/Doppler maps are evaluated and the CFAR threshold is applied; when the two-out-of-two criterion is exploited, target detection is declared only for the targets that exceed the threshold on both the receiving channels. Thereafter, the tracking of the detected targets is performed on the Range/Doppler plane. As demonstrated in [17], this tracking stage increases the positioning accuracy when the localization in the XY-plane is performed.

For the plots of the selected tracks, both the filtered bistatic range and the angle of arrival are estimated.

2.3 Passive Source Location (PSL)

The PSL sensor can estimate the target position through the combination of Time Difference of Arrival (TDoA) and AoA measurements. Specifically, the localization can be performed by exploiting only AoA measurements, only TDoA measurements or their combination. In Figure 2.5, a sketch of the above-mentioned measurements is shown with reference to a typical geometry with two receiving nodes. In the case shown in Figure 2.5(a), only three antennas are necessary to perform the target localization in the XY-plane, while when two measurements of AoA are considered, each node needs at least two antennas, as displayed in Figure 2.5(b).

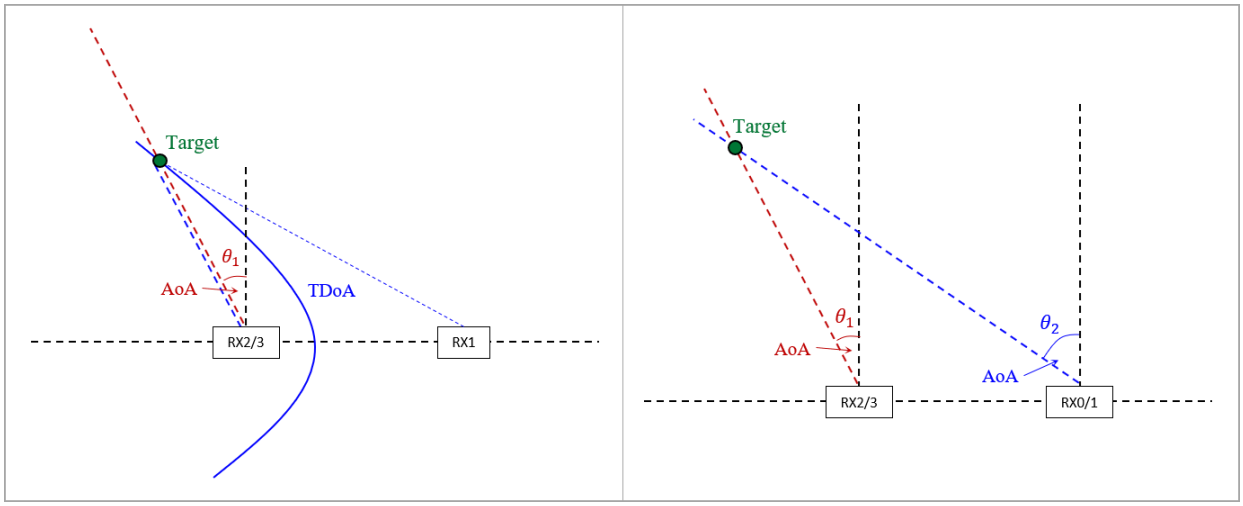

(a) (b)

Figure 2.5. Typical geometry with two receiving nodes: AoA + TDoA (a), AoA + AoA (b).

2.3.1 Measurement extraction

2.3.1.1 Techniques for Time Difference of Arrival (TDoA) estimation

The TDoA between two signals received by two different surveillance antennas provides a measurement related to the target position. In particular, it defines the hyperbola on which the target is located.

As mentioned above, to achieve a more accurate localization of a target, it is necessary to choose conveniently the technique for TDoA estimation that yields better performance in terms of positioning accuracy and processing time. To this purpose, different strategies have been investigated.

Before starting to describe the approach followed for this study and the proposed techniques, it is necessary to introduce the main strategies that can be applied when the TDoA measure has to be estimated. There are two ways to define the TDoA, through the exploitation of two separated antennas:

- By neglecting the typology of the signal;
- By exploiting the a priori knowledge of the signal available, namely its modulation format (we will use the Wi-Fi emissions of the target (mobile device or drone), that can be modulated in different ways defined into the IEEE 802.11 standard, [28]).

In the first case, we would use the data received by two antennas, made available to a “Master” sensor (e.g. ‘RX2/3’ node in Figure 2.5(a)) that will be able to realize the operations necessary for the TDoA estimation on the two received signals. As apparent, this implies the need to transfer data at the original data rate, from a sensor (e.g. ‘RX1’ node in Figure 2.5(a)) to the “Master” sensor, therefore a dedicated infrastructure must be realized.

In contrast, in the second case, the a priori knowledge of the modulation format of the received signal allows the exploitation of its known parts (usually the preamble) for the comparison of the signal received by the

antenna and a clean copy of this known portion of signal, pre-recorded in the receiving nodes. In this way, each receiving node estimates the delay of the signal in input with respect to the reference one (Time of Arrival) and then transmits only the estimated value, and the difference of these values (TDoA) can be defined later.

As mentioned above, both these strategies have inherent advantages and drawbacks. Firstly, the second approach is interesting because it provides the possibility to avoid the transfer of the entire signal to obtain the estimation of the measure of interest; in addition, the reduction of the used packets dimensions (limitation to a shorter portion of the signal containing the preamble) allows to reduce the elaboration time but, on the other hand, it could introduce a deterioration of the estimation accuracy, due to the exploitation of less samples. However, this strategy needs additional pre-processing operations, which provide the information about the typology of the received signal, in order to compare it with the correct preamble associated to that specific standard.

In this first part of the study, we decided to totally free ourselves from the necessity to know the characteristics of the received signals (if we exclude the information of the bandwidth and the carrier frequency), and so we examine in depth the first strategy, but it is important to highlight that the same techniques can be extended also to the other case.

In particular, the analysis has been performed on real data, namely signals actually transmitted by a Wi-Fi transmitter, but in favorable conditions, that is:

- The estimation is performed on the Reference signal, namely the packets directly acquired from the Access Point (AP), therefore the signal is clean (high Signal-to-Noise Ratio, SNR).
- A fixed length (1500 samples) is considered for the employed packets.
- We deliberately inject white Gaussian noise to the Reference signal to degrade the SNR, in order to emulate the signal received by the antennas.
- In order to simulate the signal received by the second surveillance antenna, the Reference signal is duplicated and additive noise is injected even to it; a delay of a fraction of sample is generated and applied to this Reference copy, so that a cleaner performance evaluation can be obtained.
- It is important to understand that the noise realizations applied to the two “surveillance” signals are independent one another and they are generated with respect to a specific noise power, defined by the desired SNR. In particular, we analyze 9 different values of SNR (from -5 dBs to 35 dBs, with steps of 5 dBs).

Different strategies have been proposed in literature, [33]-[40]. In the following Sections, the considered techniques for TDoA estimation are described. The basic idea is briefly explained and the principal formulas are derived. In addition, we present the evaluation of the performance in terms of accuracy. The whole discussion is faced taking also into account the possibility to reduce the elaboration time.

2.3.1.1.1 Cross-Correlation and Oversampling Method (CCF-OVS)

The first technique that we analyze exploits the simple cross-correlation between the signals of which we want to evaluate the time difference of arrival. Without further modifications, this strategy allows to estimate the TDoA with a resolution defined by the sampling time, and so fractional delay cannot be estimated. To do that, it is therefore necessary to oversample the curve obtained through the cross-correlation operation, by using an oversampling factor that allows to reach the desired resolution.

The main steps of this method are the following:

1) Calculation of the Cross-Correlation (over single packets) between the signals received by the two antennas, that is

$$R_{s_1 s_2}(\tau) = \frac{1}{N}\sum_{k=1}^{N} s_1(kT) \cdot s_2(kT + \tau) \tag{2.15}$$

where T represents the sampling time, whereas s_1 and s_2 are the signals received by the two antennas.

2) Coarse estimation of the Cross-Correlation peak, through the following expression

$$\widehat{\Delta\tau} = \underset{\Delta\tau}{\operatorname{argmax}} \{R_{s_1 s_2}\} \tag{2.16}$$

3) Oversampling of a small portion of this correlation (10 samples) around its peak.
4) Determination of the time difference of arrival after oversampling (fine estimation), applying again the equation (2.16) on the new curve.

In Figure 2.6, the performance of the Cross-Correlation and Oversampling (CCF-OVS) method in terms of accuracy has been shown. In particular, we reported the Root Mean Square Error (RMSE) on the distance resulting from the TDoA estimation with respect to the Signal-to-Noise Ratio (SNR), for different oversampling factors.

For each oversampling factor, we have considered two different relative delays between the signals received by the surveillance antennas: the best case (solid line in the figure), when the delay corresponds to the new sample after oversampling (in fact, in this case, there are not errors due to the available resolution), and the worst case (indicated with stars in the same plot), that is when the delay is exactly in the mid-point of two consecutive samples of the signals (in this second case, the CCF-OVS method estimates a value of TDoA that corresponds to one of the two adjacent samples, defining an error equal to half sample of the oversampled signal). This behavior is evident in Figure 2.6 (where Q represents the oversampling factor, whereas Delay indicates the actual delay in samples between the two signals) and specifically by observing the limit value reached in the cases [Q=1, Delay=1/2] and [Q=2, Delay=1/4], that is exactly the distance related to half sample and 1/4 of sample, respectively, regardless the SNR. On the other hand, for the best cases (solid lines) the errors decrease rapidly to zero, even with low values of SNR.

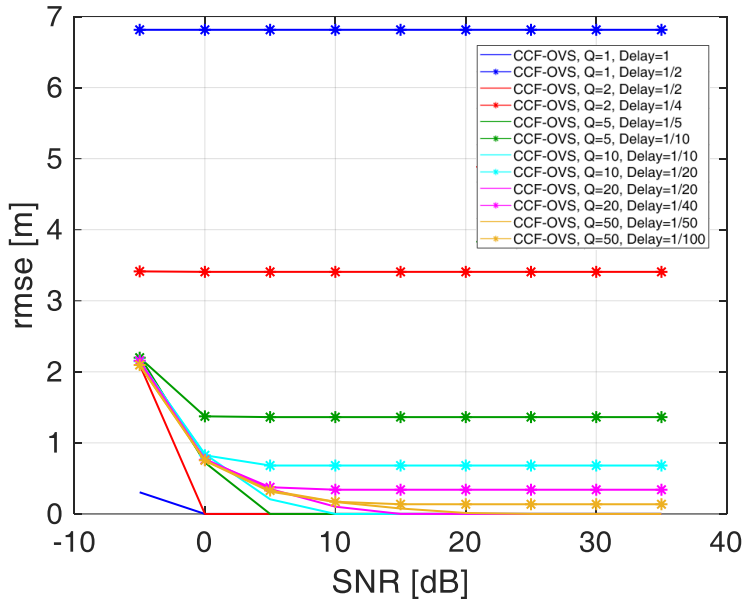

Figure 2.6. Performance of the CCF-OVS method for different oversampling factors and delays.

In addition, it is possible to notice that, as expected, the performance increases when the oversampling factor increases.

In order to see in detail the behavior of the curves, we have reported in Figure 2.7 the same results shown in Figure 2.6, but in semilogarithmic scale. In particular, in the figure on the right we have reported only the worst cases.

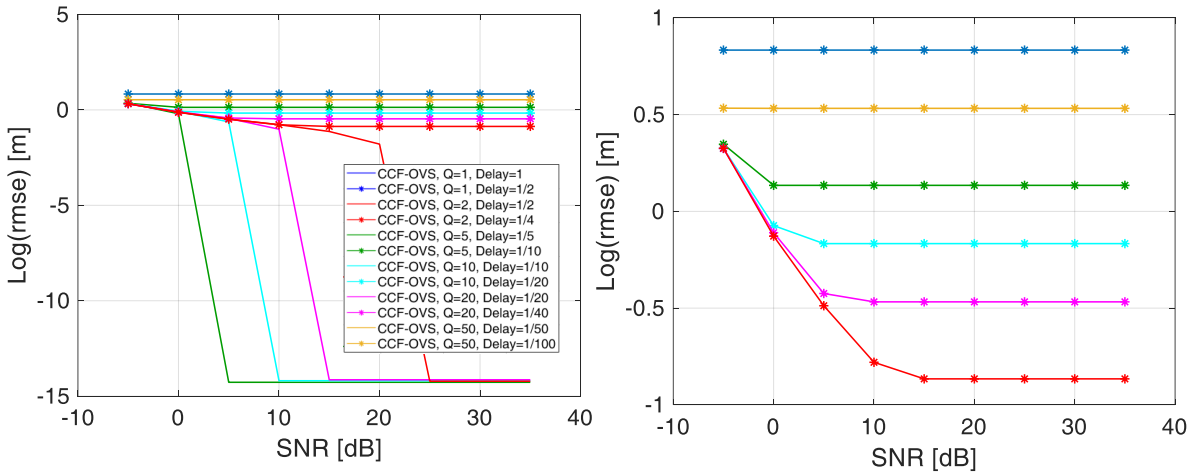

Figure 2.7. Performance of the CCF-OVS method for different oversampling factors and delays (semilog scale).

This technique leads to good results, especially when higher oversampling factors are used, because they allow to reach higher accuracy. Nevertheless, even the computational cost increases when the oversampling factor increases, therefore it is necessary to find a tradeoff between these two components.

Alternatively, it is possible to study other strategies characterized by a lower computational cost.

2.3.1.1.2 Cross-Correlation and Fast Parabolic Interpolation Method (CCF-FPI)

A possible solution that allows to reduce the computational cost is the implementation of the Fast Parabolic Interpolation (FPI), as described in [33].

This technique is based on the assumption that the main lobe of the cross-correlation, containing the peak, can be approximated with a parabola; therefore, the research of the peak corresponding to the TDoA can be easily and accurately performed by searching the apex of this parabola, avoiding in this way the increasing of the elaboration time due to the oversampling operation (especially if a high factor is used) of the previous strategy.

In particular, the following steps are used:

1) Calculation of the Cross-Correlation (over single packet) between the signals received by the two surveillance antennas, as in (2.15).

2) Search of the peak of the Cross-Correlation (coarse estimation) through the formula (2.16).

3) Extraction of three samples around the peak, namely the sample related to the peak, the sample before it, and the sample after the peak

$$x = R_{s_1 s_2}(\tau_P - \frac{T}{Q}), \quad y = R_{s_1 s_2}(\tau_P + \frac{T}{Q}), \quad z = R_{s_1 s_2}(\tau_P) \tag{2.17}$$

where τ_P is the instant related to the peak of the correlation, T is the sampling time and Q is the oversampling factor.

4) Definition of the parabola passing for the three points

$$g(\tau) = a\tau^2 + b\tau + c \tag{2.18}$$

finding the coefficients a, b, c through the resolution of the system of equations consisting of the three parabolas determined by the points defined in (2.17), from which we obtain:

$$a = \frac{x + y - 2z}{2} \cdot \frac{Q^2}{T^2} \tag{2.19}$$

$$b = -(x + y - 2z) \cdot \frac{Q^2}{T^2} \cdot \tau_P + \frac{(y - x)}{2} \cdot \frac{Q}{T} \tag{2.20}$$

$$c = z + \frac{x + y - 2z}{2} \cdot \frac{Q^2}{T^2} \cdot {\tau_P}^2 - \frac{(y - x)}{2} \cdot \frac{Q}{T} \cdot \tau_P \tag{2.21}$$

5) Calculation of the apex of the parabola (fine estimation) defined in (2.18), after having replaced the values in (2.19), (2.20) and (2.21), by using the known formula:

$$\widehat{\Delta\tau} = -\frac{b}{2a} \tag{2.22}$$

It is also possible, before point 3), to add an oversampling with a factor Q=2, that increase the estimation accuracy.

It is evident that the simple calculation of the numerical values necessary for the determination of the vertex of the parabola requires less elaboration efforts with respect to an oversampling characterized by a high Q.

In Figure 2.8, we have reported the results obtained with the CCF-FPI method. We perform the same analysis carried out for the CCF-OVS method, namely the observation of the effect on the best and the worst cases for the delay, when a low oversampling (Q=2) is used or not (Q=1).

In this case, it can be noticed a general improvement of the performance in terms of estimation accuracy, as well as processing times.

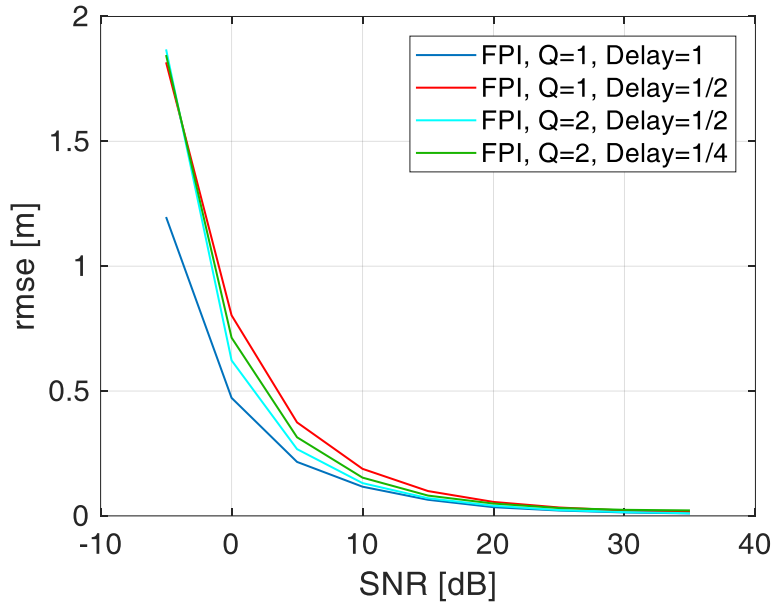

Figure 2.8. Performance of the CCF-FPI method for different oversampling factors and delays.

2.3.1.1.3 Average Square Difference Function and FPI Method (ASDF-FPI)

In spite of performance improvement, the main problem for the processing times is determined by the calculation of the cross-correlation function.

Therefore, in [33], another type of strategy has been defined, with the purpose of avoiding the evaluation of the cross-correlation. This methodology, instead of evaluating the product and sum which defines the cross-correlation, is based on the calculation of the sum of the differences of the values of the two signals. Therefore, replacing the product with the difference, even the computational cost should improve. This time it is the minimum of this function that has to be found, because it represents the point where the two signals are aligned, and so the TDoA to be found. After this operation, the FPI is applied also this time, in order to perform the "fine estimation" of the delay.

The main steps are the following:

1) Calculation of the Average Square Difference Function (ASDF), over single packet, between the signals received by the two surveillance antennas, that is

$$R_{s1s2}(\tau) = \frac{1}{N}\sum_{k=1}^{N} |s_1(kT) - s_2(kT+\tau)|^2 \tag{2.23}$$

2) Search of the minimum of the ASDF of the signals (coarse estimation), as

$$\widehat{\Delta\tau} = \underset{\Delta\tau}{\operatorname{argmin}} \{R_{s1s2}\} \tag{2.24}$$

At this point, we can apply the steps and the formulas for the FPI.

3) Extraction of three samples around the minimum, (2.17).

4) Definition of the parabola passing through the three points, by the formulas (2.18), (2.19), (2.20) and (2.21).

5) Calculation of the apex of the parabola, (2.22).

Even this time, before the point 3), it is possible to add an oversampling with Q=2, that improve the estimation accuracy.

In Figure 2.9, we show the results for the ASDF-FPI method, for the same cases analyzed with the CCF-FPI method.

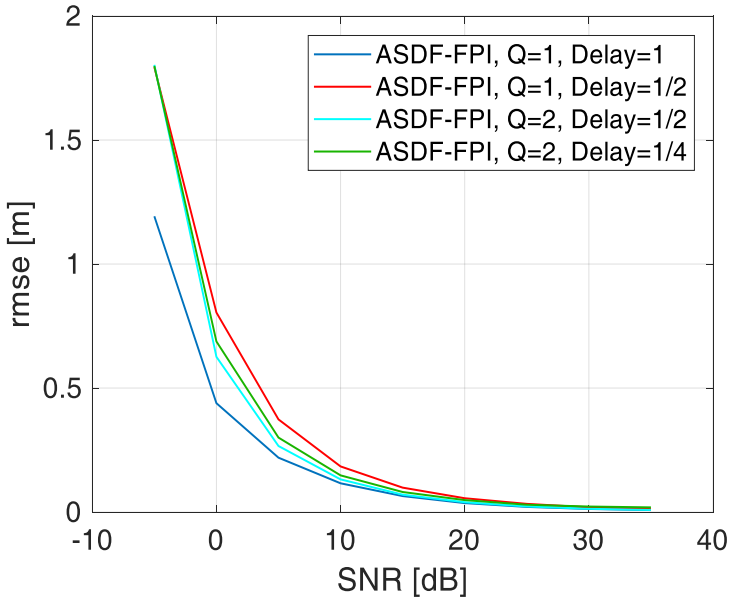

Figure 2.9. Performance of the ASDF-FPI method for different oversampling factors and delays.

It can be noticed that these results are comparable with those shown in Figure 2.8 for the CCF-FPI. In fact, the accuracy seams to depend principally on the way that is used to find the peak of the curve.

2.3.1.1.4 CCF + Slope-based Method

The slope-based method exploits the phase variation generated by a delay in the signal. In fact, a delay in time corresponds to a phase shift in frequency domain:

$$x(t-\tau) \overset{F}{\rightarrow} X(f) \cdot e^{-j2\pi f\tau} \tag{2.25}$$

As apparent, this phase shift is linear in frequency and the line that describes its trend has slope equal to $2\pi\tau$.

In particular, instead of estimating the ToA of each single signal through the comparison with a reference signal (as reported in literature, [34]-[35]), in this case it is directly estimated the Time Difference of Arrival (TDoA) between two surveillance signals. Moreover, in contrast to the strategies adopted in [34] and [35], in our approach the features of the OFDM signal were not directly exploited; in this way, these techniques can be applied over a generic signal, regardless the modulation format. In detail, the strategy to obtain this measurement is based on the estimation of the ratio of the spectra of the received signals (or equivalently, on the product of a spectrum and the complex conjugate of the other one), whose phase is represented by the difference of the phases of the two signals. As can be easily understood from (2.25), the slope of this new phase is linked to the relative delay between the two signals, namely $\Delta\tau$, which represents the TDoA we are looking for, thanks to the equation

$$\Delta\tau = -\frac{\Delta\Phi}{2\pi \cdot \Delta f} \tag{2.26}$$

where the "slope" is $\Delta\Phi/\Delta f$ (or $-2\pi\Delta\tau$, as explained before).

This method has been applied on both OFDM and DSSS signals. In the first case, simulated signals have been used. These signals have been generated by a generator of Wi-Fi "HT Format" signals, which uses OFDM modulation. In the second case, real data have been used. In particular, we have used the clean signal transmitted by the Access Point (AP).

In both cases, we applied additive noise and a delay (fraction of a sample) in order to emulate the signal received by a surveillance antenna. In order to make the performance analysis simpler, one signal has been delayed, while to the other one a null delay has been applied. In addition, before performing the ratio of the spectra, for both the typologies of signal, the frequency bands where the spectrum has too low values (lateral bands for DSSS and lateral + central bands for OFDM), have been eliminated.

In the following sections, we reported only the results obtained on DSSS signals, because it is more useful for the comparison with the other techniques that we have studied.

During the study, different issues related to the slope-based method arose. Some problems are already known and faced in literature, while other issues are due to the operating conditions where we worked, as for example, the additive noise level applied to the signals and the choice of the relative delay between the received signals.

In particular, two are the criticalities found during the analysis. The proposed solutions are then presented.

1) Non oversampled CCF before slope-based method (CCF-slope method)

First of all, we have to keep in mind that in the calculation of the phase of the ratio of the spectra, the use of the Matlab 'unwrap' function causes problems for low values of SNR: in fact, for values of SNR lower than about 20 dB, the phase has jumps of 2π, if calculated in this way. Nevertheless, this function is necessary if the relative delay between the two signals is greater than one sample.

This situation has also been highlighted in [34], where hypothetical solutions have also been described.

In our work, however, we have decided to address the problem in a different way.

In fact, to overcome this problem, a first step of cross-correlation between the two signals (CCF) was applied in the initial phase of the estimation. Since no oversampling has been carried out for the estimation of this time, this methodology allows to estimate integer samples of delay between the two signals, as discussed in Section 2.1. This will then be compensated in frequency in the relative signal. In this way, the residual delay to be estimated with the slope method will always be a fraction of the sample. Consequently, there will be no more problems in estimating the phase as the use of unwraps is no longer necessary.

2) Iterative Slope-based Method

At this point it is sufficient to analyze the performance of the slope-based method for delays less than a sample, leaving to the CCF method to compensate for delays that are multiple of a sample. The analyses were conducted on a limited number of samples of the starting signals; in this case 1500 samples were used.

In Figure 2.10, we reported the Root Mean Square Error (RMSE) as a function of the signal-to-noise ratio (SNR). This figure shows that the trend of the obtained curves seems to be dependent on the relative delay between the two signals.

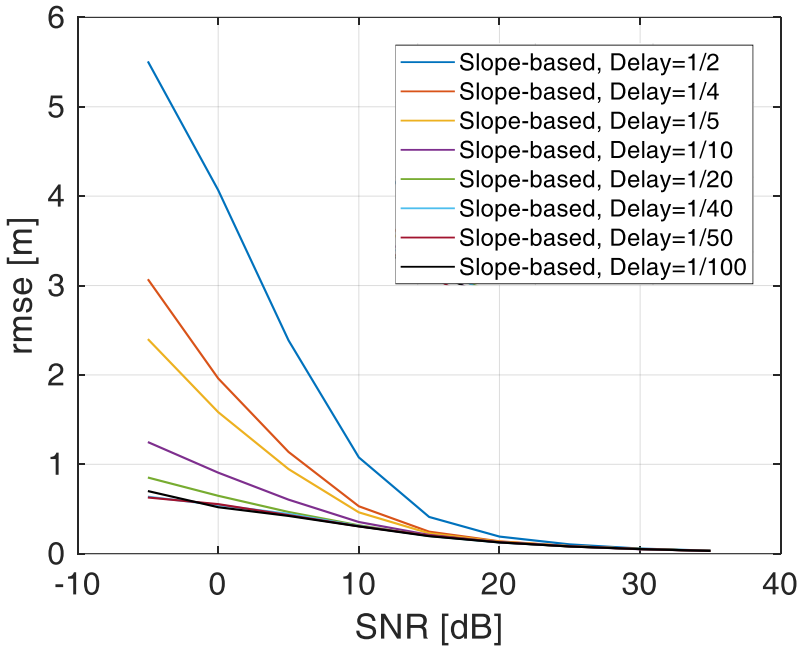

Figure 2.10. Rmse vs SNR of the slope-based method for different values of delay to be estimated.

This behavior is not acceptable for our purposes and it is also interesting and necessary to understand the reason for this phenomenon. To do this, the phase of the ratio of the spectra of the starting signals has been analyzed in detail, each time obtained for a different SNR and for a different delay. As a consequence, being for us useful only the information related to the average slope of the phase, the latter has been approximated with a straight line (linear fitting) defined by the relative slope (angular coefficient), and its evolution has been observed as the noise increases.

To simplify the analysis, the phases (in blue) and the straight lines defined by the relative slopes (in red) are reported here (Figure 2.11) for only two cases which could be interesting for our study, i.e. the extreme cases of relative delay equal to **half a sample** and **one fiftieth of a sample**.

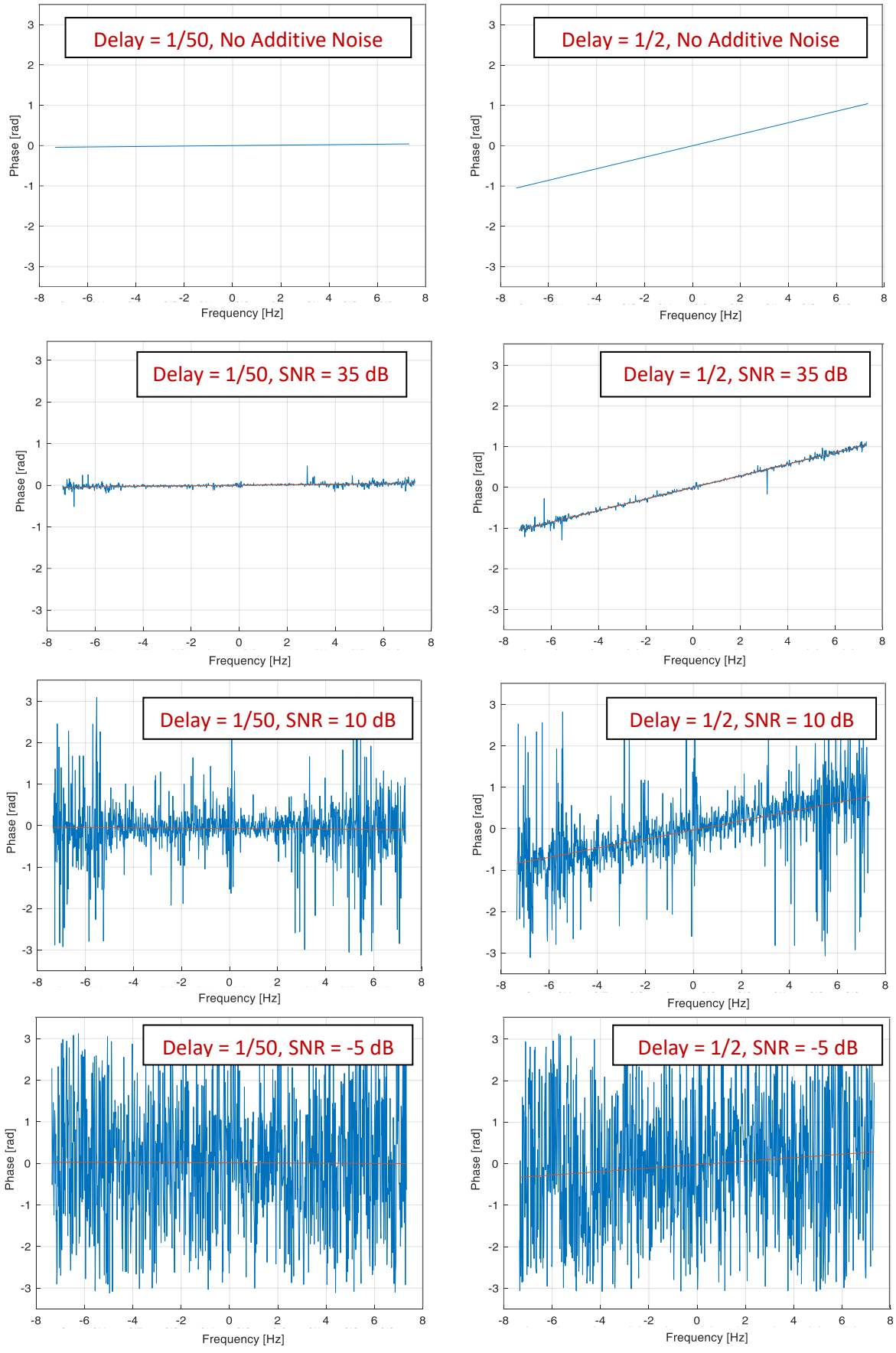

Figure 2.11. Phases and linear fitting for different SNR, for Delay = 1/2 and Delay = 1/50.

In fact, it can be noticed from these images reported in Figure 2.11 that as noise increases, and therefore as the SNR decreases, the phase becomes more disturbed, presenting peaks especially at the lateral frequencies, which, in some cases, cause phase wrappings, i.e. what exceeds the upper limit of π (remember that the phase is defined between - π and + π), is displayed at the opposite extreme (i.e., -2π far from this). Consequently, the trend of the line that approximates the phase will differ from the exact one. This event is more evident for higher values of the slope, since a lower noise value will be enough to raise the phase, at the lateral frequencies, above the value of π. Moreover, the wrapping of the phase, defining phase values in the opposite half-plane with respect to the correct one, will generate a drop of the slope, to a value close to zero in the case of very noisy environment. It is clear that in the definition of the RMSE, this phenomenon will affect performance more in those cases where the delay generates a slope very different from zero. This justifies the results reported in Figure 2.11.

Obviously, as mentioned above, this behavior is not acceptable for our purposes. Therefore, it is necessary to find a possible strategy that solves this problem, or at least limits its effects, especially for SNR of practical interest.

For this purpose, it was decided to implement the iterative version of the slope-based method.

2.3.1.1.5 Iterative Slope-based Method

The idea behind this methodology is to make a first rough estimate of the delay, then compensate it in the ratio of spectra and then apply again the method for estimating the slope in an iterative manner, until you reach a predetermined stopping criterion. This allows a more accurate estimation of the delay.

The iterative procedure is schematically presented in Figure 2.12.

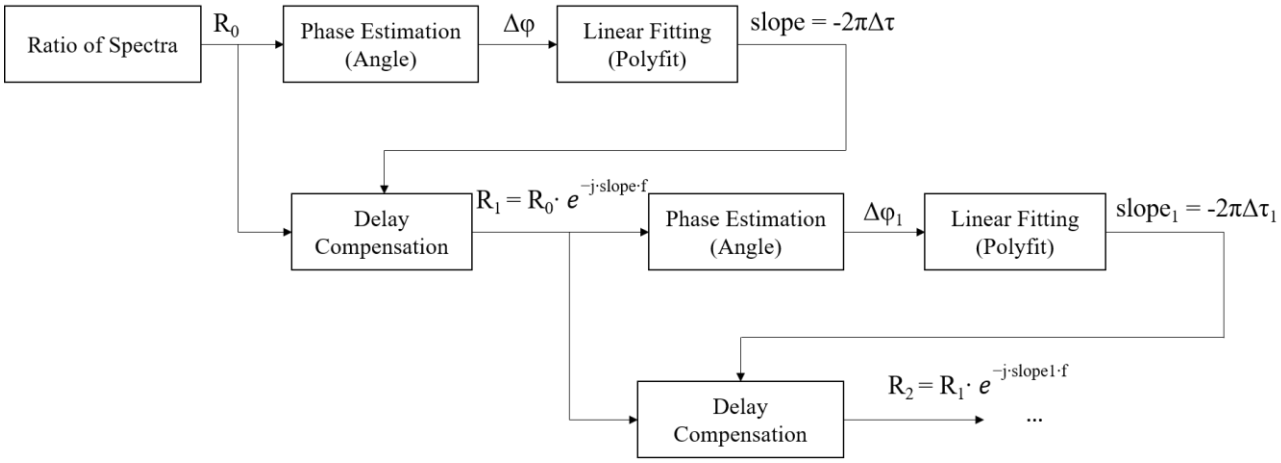

Figure 2.12. Block diagram of the iterative slope-based method.

- ***Estimation update:***

From the initial formulas ((2.25) and (2.26)) and from what is shown in the previous diagram in Figure 2.12, it is possible to describe the ratio of the spectra through the following expression:

$$R(f) \cdot e^{-j2\pi f \Delta\tau} \tag{2.27}$$

where $\Delta\tau$ represents the real value.

We indicate with $\widehat{\Delta\tau}$ the value estimated through the slope-based method, which will then be compensated before the next iteration, in the following way:

$$R(f) \cdot e^{-j2\pi f \Delta\tau} \cdot e^{j2\pi f \widehat{\Delta\tau}} = R(f) \cdot e^{-j2\pi f (\Delta\tau - \widehat{\Delta\tau})} \tag{2.28}$$

where $(\Delta\tau - \widehat{\Delta\tau})$ represents the residue due to the difference between the real delay and the estimated delay (difference caused by noise, among other things) which, after compensation, determines the new slope of the input signal at the next iteration. Obviously, without noise and other disturbances, the two values coincide and the slope of the line describing the phase difference is zero.

At the next iteration we have:

$$R(f) \cdot e^{-j2\pi f (\Delta\tau - \widehat{\Delta\tau})} \cdot e^{j2\pi f \widehat{\Delta\tau 2}} = R(f) \cdot e^{-j2\pi f (\Delta\tau - \widehat{\Delta\tau} - \widehat{\Delta\tau 2})} \tag{2.29}$$

As it is defined, $\widehat{\Delta\tau_2}$ is an estimate of $\Delta\tau - \widehat{\Delta\tau}$, therefore

$$\widehat{\Delta\tau_2} = \Delta\tau - \widehat{\Delta\tau} \tag{2.30}$$

And so

$$\Delta\tau = \widehat{\Delta\tau} + \widehat{\Delta\tau_2} \tag{2.31}$$

For the same reason, after the third iteration we will have

$$\Delta\tau = \widehat{\Delta\tau} + \widehat{\Delta\tau_2} + \widehat{\Delta\tau_3} \tag{2.32}$$

In general, the correction will be performed by adding the estimates of the delay obtained at each iteration and then the total delay will be estimated as

$$\Delta\tau = \sum_k \widehat{\Delta\tau_k} \tag{2.33}$$

- ***Stopping criterion:***

The stopping criterion has been established empirically, i.e. by noting that on the results reported in Figure 2.10, the curves are almost similar for delays of less than 1/40 of sample, while they start to deviate from the previous trend for delays of more than 1/20 of sample. Therefore, it may make sense to enter the procedure only if the estimated TDoA exceeds the time corresponding to the delay of 1/40 of sample. This choice later

proved appropriate, after examining the effects of iterations on small delays (see next section, where iterative procedure produces improvements for large delays but worsens performance for small delays).

In summary, a threshold must be found that meets the following condition:

$$\Delta\tau_{1/40} \leq Th \leq \Delta\tau_{1/20} \tag{2.34}$$

where Th represents the threshold, while $\Delta\tau_{1/40}$ and $\Delta\tau_{1/20}$ are the theoretical delays expressed in time, generated by the delay in samples corresponding, respectively, to 1/20 and 1/20 of sample, namely

$$\Delta\tau_{1/40} = \frac{1}{f_s} \cdot \frac{1}{40} = 1.13 \cdot 10^{-9} \; (for \; f_s = 22 \; MHz) \tag{2.35}$$

$$\Delta\tau_{1/20} = \frac{1}{f_s} \cdot \frac{1}{20} = 2.27 \cdot 10^{-9} \; (for \; f_s = 22 \; MHz) \tag{2.36}$$

where f_s is the sampling frequency and, as a consequence, $1/f_s$ is the time related to a sample.

Therefore, the stopping criterion will be defined as

$$\widehat{\Delta\tau}_k < Th \tag{2.37}$$

And the threshold can be set initially to $\mathbf{1.5 \cdot 10^{-9}}$, which meets with the condition (2.34). In particular, this choice is good also for $f_s = 20 \; MHz$.

It is interesting to compare at first the performance achievable with the two slope-based methods in order to understand the actual usefulness of an iterative approach, intrinsically more expensive in terms of computational cost than the non-iterative version.

Even in this case, we analyze the curves of the RMSE as a function of the SNR, for different delays. Estimates are made through Monte Carlo simulation on 20 different packets for 100 different noise realizations for each of them. Even this time, the evaluations were carried out on 1500 samples for each packet used.

The typical trend (small changes can occur for different noise realizations) of the RMSE when the non-iterative method is applied is the one already reported in Figure 2.10. In Figure 2.13, instead, the results obtained with the iterative method are reported.

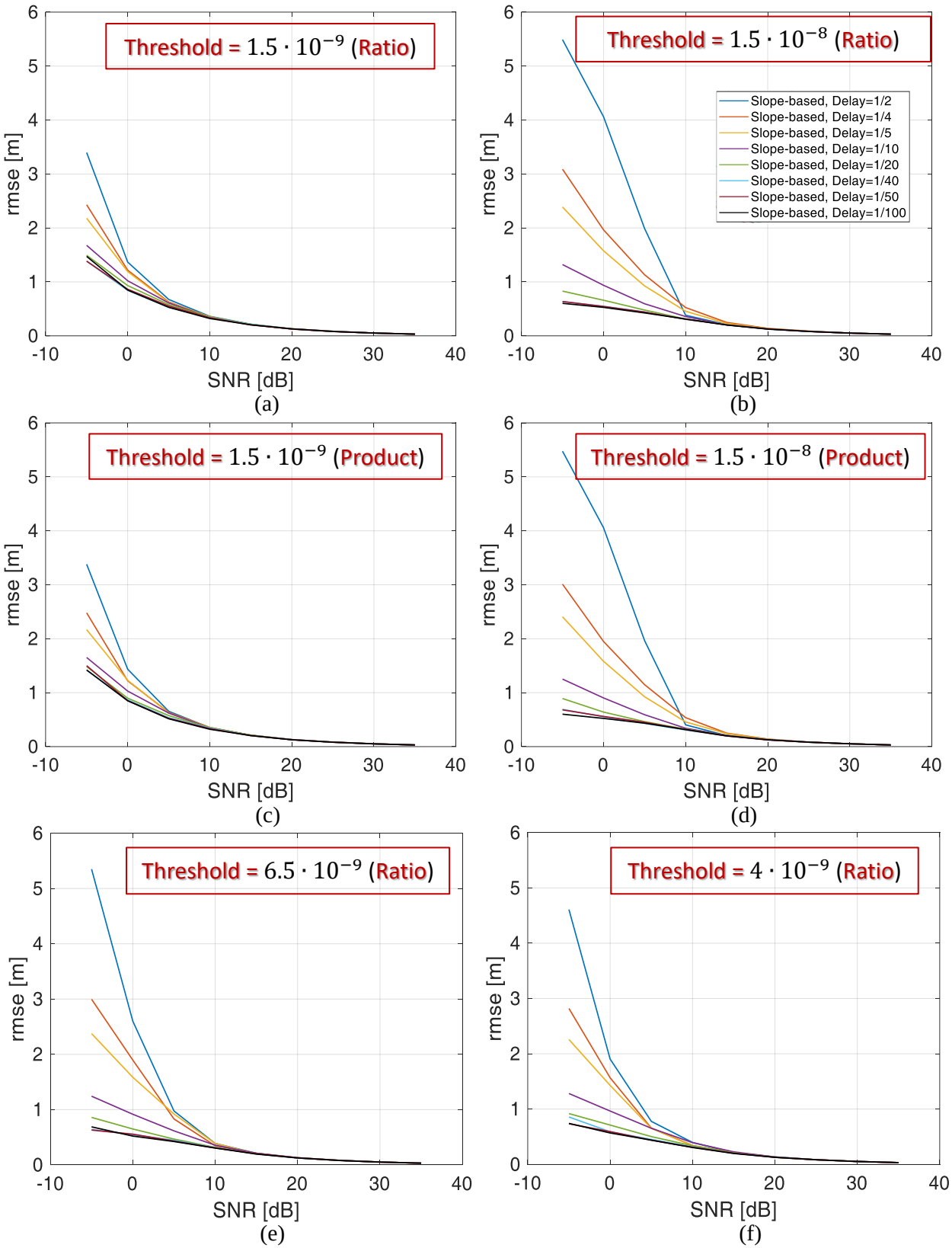

Figure 2.13. RMSE vs SNR for the iterative slope-based method.

As can be easily guessed, the iterative method is strongly linked to the choice of the threshold that determines the stopping criterion (and, at the same time, the input criterion to the iterative procedure). In fact, a higher threshold reduces the probability of entry into the iterative part, thus producing results identical to the basic

case; on the other hand, a lower threshold favors the use of the iterative procedure, introducing a greater difference between the two results.

For this reason, in Figure 2.13 we reported the results for two (potentially) limit cases, i.e. a threshold of $1.5 \cdot 10^{-9}$ and $1.5 \cdot 10^{-8}$. In addition, after an initial analysis of the curves obtained, two intermediate situations were also included (thresholds equal to $6.5 \cdot 10^{-9}$ and $4 \cdot 10^{-9}$, respectively), to better understand the impact of using the iterative process. Moreover, to remove any doubt on the correct implementation of the entire method, both the slopes obtained from the ratio of the spectra and those obtained from the product of one spectrum for the conjugate of the other have been observed.

From these results it can be seen that:

- as we would have expected, there is no difference between determining the difference of phases of the two spectra through the ratio or the product of these (compare Figure 2.13(a)-(b), with Figure 2.13(c)-(d)).
- Observing the first two images in Figure 2.13, it is clear that:
  a. a higher threshold ($\mathbf{1.5 \cdot 10^{-8}}$, Figure 2.13(b)) allows the entry into the iterative procedure only in those cases in which the relative delay between the two signals is quite high (half sample, in the specific case of the threshold just analyzed) while, with the same threshold, for other delays the curves are comparable with those of Figure 2.10 (this result is linked to the definition of the stop criterion and not only to the threshold chosen for it). In particular, with this threshold, for the delay of half a sample, we can observe how the iterative procedure improves the performance for higher SNR: very good results are obtained for SNR greater than 10 dBs, but slight improvements are also observed for SNR equal to 5 dBs.
  b. a lower threshold ($\mathbf{1.5 \cdot 10^{-9}}$, Figure 2.13(a)) allows: *i)* the execution of at least one iteration, for any delay, and *ii)* the repetition of a higher number of iterations, especially for large delays. It is evident that in this case the results obtained are very different from those obtained with a non-iterative procedure (see Figure 2.10). Furthermore, the curves are more compact, i.e. there is less dependence of the curves on the relative delay between the signals. It is possible to notice that also in this case two different zones can be distinguished: for SNR $\geq$ 10 dB very good results are obtained regardless of the delay, while for SNR $\leq$ 5 dB the curves show a substantial improvement in performance for high delays (greater than 1/5 or 1/10 of sample) and a worsening for lower delays.
- looking at the last two images in Figure 2.13, where the curves resulting from the application of two intermediate thresholds have been reported, it can be noted that also the performances are intermediate with respect to the two previously described. In particular, for a threshold equal to $\mathbf{6.5 \cdot 10^{-9}}$ (Figure 2.13(e)), the iterative procedure involves only the first two or three delays under examination, generating for these delays an improvement in performance. For the other threshold ($\mathbf{4 \cdot 10^{-9}}$, Figure

2.13(f)), however, the entry seems guaranteed for all delays, with the related consequences described in point b, namely for lower threshold, although with less evident effects.

In order to conclude this first analysis, a possible choice of threshold according to the SNR could also be considered.

2.3.1.1.6 Comparison of TDoA estimation methods

The various techniques for estimating TDoA have been presented. It is now interesting to make a final comparison of the relative performance. Since we have a fairly large number of curves, only two signal delays will be examined, and the curves obtained for them compared in two separate graphs to simplify the visualization of the results.

In Figure 2.14, we show the comparisons for delay of one fiftieth of sample (left column) and delay of half sample (right column). Zooms were also displayed for low SNR and high SNR.

As expected, for high values of SNR the best performance in terms of accuracy (low error) is obtained by using a high oversampling factor in the CCF-OVS method. However, this results in a higher computational cost. In contrast, for lower values of SNR, this technique may have some problems in estimating small delays due to higher sensitivity to noise.

Very good performance is obtained also with the methods that use the parabolic interpolation, namely the CCF-FPI and the ASDF-FPI, which, besides showing excellent results, are characterized by a remarkable reduction of the computational cost.

Finally, the slope-based method is characterized by an excellent computational cost and provides good results when compared with some of the techniques proposed, although there is still a need for some improvements. Moreover, in the comparison between slope-based and iterative slope-based the considerations made in the previous section are evident also in this case.

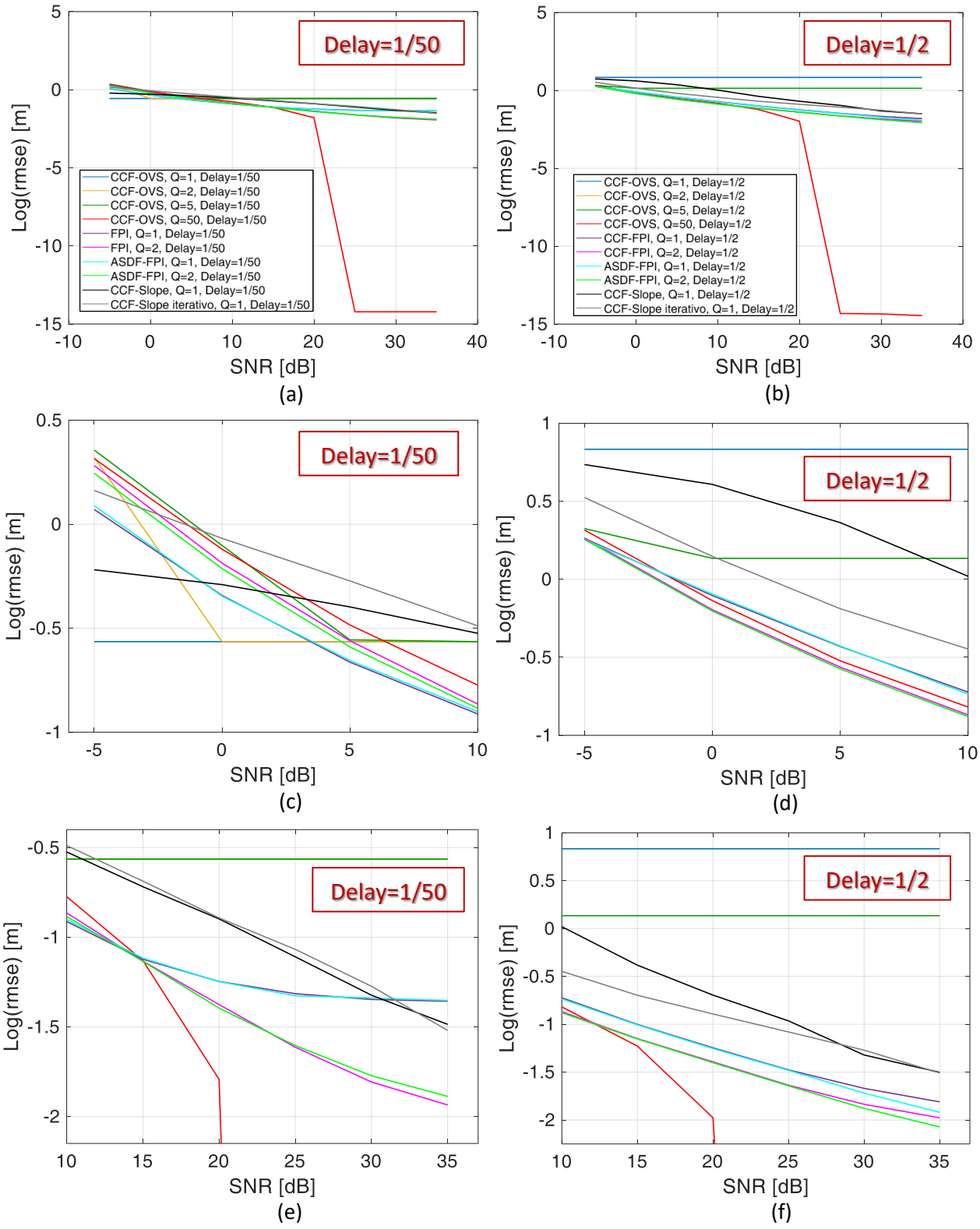

Figure 2.14. Comparison of the method for the TDoA estimation for: (a) Delay=1/50, (b) Delay=1/2, (c) Delay=1/50, zoom for low SNR, (d) Delay=1/2, zoom for low SNR, (e) Delay=1/50, zoom for high SNR, (f) Delay=1/2, zoom for high SNR.

2.3.1.2 Techniques for Angle of Arrival (AoA) estimation

The Angle of Arrival (AoA) estimated over the signals emitted by a device which exploits Wi-Fi transmissions (drones, smartphones, tablet, and so on), provides an information on the position of the target that transmits them. In particular, the geometric place of points that the angle defines is a line. Specifically, the AoA represents the slope of this line.

In contrast with the TDoA estimation (see Section 2.3.1.1), for which it is necessary to have a higher distance between the antennas involved in the measurement operation, for the AoA estimation the distance between the receiving antennas has to be lower, aiming at reducing angle ambiguities.

Therefore, in order to estimate the angle of arrival, each receiving node must be composed by at least two antennas. This means that in this case one node is sufficient to estimate the AoA.

As it is obvious, it is necessary to choose conveniently both the number of elements of the antenna and their configuration within the node.

We have focused on two different solutions:

1) Circular systems with a limited number of elements;
2) Systems with a minimum number of antennas, i.e. two.

The first case allows us to perform a theoretical treatment independent of the pointing of the employed antennas.

In the second case, instead, this configuration allowed to study simple practical cases of greater interest. In fact, for the experimental tests we have employed arrays with only two antennas, properly configured.

With reference to the specific techniques for the AoA estimation, one of the most accredited and suitable solutions for our purpose is the use of the interferometric approach, which determines the angle of arrival by estimating the phase difference between the signals received from the antennas present in the receiving node. Depending on the typology of receiving node, different considerations about the characteristics of the generic antenna system should be further discussed, so a detailed description will be reported when necessary.

Suppose to have N_{Rx} receiving nodes, each containing at least two antenna elements.

The detailed description of the system with the minimum number of elements is proposed here, since its mathematical characterization is also useful for the next experimental analysis, where this system has been actually used. On the other hand, the extensive characterization of the circular system is not important for the purposes of this thesis, therefore the related description is not presented.

As well known, the difference in the paths that the incident signal must cover in order to reach the different antenna elements results in a relative phase shift between the received signals. In Figure 2.15 is reminded the case of linear array with the minimum number of elements (two) for the estimation of the direction of arrival.

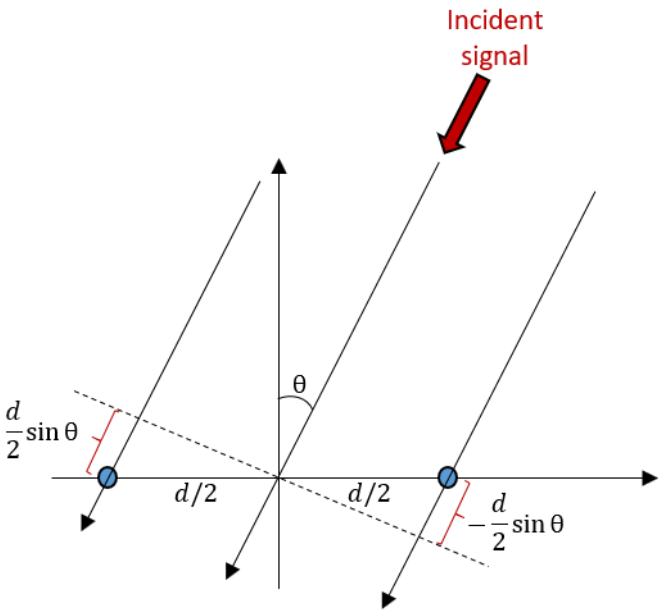

Figure 2.15. Direction of Arrival estimation.

In this figure, θ indicates the incidence angle with respect to the line perpendicular to the axis of the array, while d represents the distance between the two elements.

The phase difference between the signals received by the two antennas is determined by the following expression:

$$\widehat{\Delta\varphi} = \frac{2\pi d}{\lambda}\sin\hat{\theta} \tag{2.38}$$

Therefore, it can be easily derived

$$\hat{\theta} = arcsin\left(\frac{\lambda \cdot \widehat{\Delta\varphi}}{2\pi d}\right) \tag{2.39}$$

where λ represents the wavelength related to the Wi-Fi channel on which the device is transmitting, while d is the distance between the elements, as defined above. This last quantity must be chosen in such a way as to reduce as much as possible the area in which the angle is ambiguous, so as to avoid any positioning errors.

These considerations can be easily extended, with the appropriate modifications, even for the case where a different number of antennas is employed.

All parameters in the equation (2.39) are known, except for the phase difference which, instead, has to be estimated from the received signals. In order to obtain a reliable evaluation of this parameter, $\widehat{\Delta\varphi}$, a Maximum Likelihood (ML) estimation has been performed which leads to the following expression:

$$\widehat{\Delta\varphi} = \angle \boldsymbol{s}_1^H \boldsymbol{s}_2 \tag{2.40}$$

where $\boldsymbol{s}_1$ and $\boldsymbol{s}_2$ are the signals received by the two antennas contained in the receiving node.

By construction, this estimation is made directly by the single receiving node, since co-located antennas are used. Therefore, it is clear that in this case, unlike what happens for the estimate of TDoA, it is not necessary to create a dedicated infrastructure for the transfer of the entire data flow from one sensor to another. At the

same time, it is not even necessary to have a prior knowledge of the waveform transmitted by the mobile device, namely the modulation format of the Wi-Fi signal, as no known part of the signal is used.

From this point of view, the positioning based on only angle measurements appears to be more advantageous than when using TDoA measurements. Actually, the performance of both are also dependent on the geometry of the system and especially on the actual position of the target with respect to the different receiving nodes, as will be seen in the next sections.

2.3.2 Positioning techniques

After the definition of the measures that can be used for the PSL sensor, and the characterization of the techniques for the measurement extraction, it is interesting to analyze the possible strategies to obtain the target localization in the XY plane.

The positioning can be performed in different ways, also depending on the number of receiving nodes available and the number of antennas contained in each node.

Considering the measures described in Section 2.3.1, namely TDoA and AoA, their possible combination for target localization are summarized in Table 2.

Table 2. Measurement combinations for target localization with the PSL sensor.

	PSL sensor
2 Receiving Nodes (3 or 4 Antennas)	1 AoA + 1 TDoA
	2 AoA
	2 AoA + 1 TDoA
3 Receiving Nodes (max 6 Antennas)	3 AoA
	2 TDoA
	3 AoA + 2 TDoA
	3 AoA + 1 TDoA
	2 AoA + 2 TDoA
	1 AoA + 2 TDoA

In this table, we made a distinction between the case where two receiving nodes are available and the case where three nodes can be used. Obviously, the number of combinations increases if a higher number of antennas can be exploited. Moreover, it is possible to notice that there are three main possibility for the localization:

1) Exploitation of only TDoA measures.
2) Exploitation of only AoA measures.
3) Hybrid solution with both AoA and TDoA measures.

In the next sub-sections, we reported only the detailed description of the combination of measures that could be interesting for the purposes of this thesis.

In particular, the analysis of the cases where only one type of measure is exploited is useful to compare the accuracy achievable with the different measures. In order to perform an effective comparison, three receiving nodes are considered for this first study, since this is the condition to obtain the target localization with only TDoA measures.

In a second phase of this preliminary evaluation, we focused on the combinations provided by two nodes, which is the situation that we find in our experimental tests. Therefore, the use of hybrid solutions is evaluated only in this part of the study. A further explanation of this choice is also mentioned after the discussion on the first results.

2.3.2.1 Positioning techniques based on TDoA measurements

As affirmed in the previous sections, it is possible to estimate the position of the target through the Time Difference of Arrival (TDoA) measurements obtained from the signals transmitted by its mobile device. We have to remind that the measurement can be obtained *i)* through the direct estimation of TDoA between the two signals received from two distinct surveillance antennas, or *ii)* through the separate estimation of the times of arrival of the signals to the single receivers and the subsequent difference of these between pairs of receivers. In this section we analyze the second situation, therefore the measurement errors will be attributed separately to the measurements obtained by the individual receivers. This choice is guided by two main reasons.

Firstly, this situation is more representative of real cases, where noise is independent between the two receiving antennas. Secondly, this is a sort of "Worst Case", as the combination of the two errors in principle produces a higher error than the other case. This does not cause a problem with previous analyses because, as already discussed in Section 2.3.1.1, the studied techniques for TDoA estimation can be easily applied also to this situation.

After this first consideration, we can proceed with the treatment considering that to each TDoA corresponds (except for a scale factor equal to the speed of propagation of the signal) a difference between distances that defines a geometric place of points corresponding to a hyperbola. Thus, we obtain N-1 hyperboles, at the intersection of which the target is located.

Suppose to have N_{Rx} receiving nodes located in the generic point $\mathbf{p}_i = (x_i, y_i)$ of a local Cartesian system. From the previous considerations, we need to have at least three receiving nodes to localize a target by using only TDoA measures.

Let $\mathbf{u}$ be the vector containing the target coordinates defined over the same Cartesian reference system of the receiving nodes.

The distance between the target and the i-th receiver Rx_i can be calculated as

$$R_i = |\mathbf{p}_i - \mathbf{u}| \tag{2.41}$$

From this value it is possible to measure the time of arrival t_i of the signal transmitted by the target at the i-th receiver.

Since the target transmits a signal at an unknown time t_{Tx}, we can use one of the receiving nodes as a reference (for instance Rx_0) and calculate $N_{Rx} - 1$ time differences of arrival.

$$\Delta t_i = t_i - t_0, \qquad \forall\, i = 1, \dots, N_{Rx} - 1 \tag{2.42}$$

where t_0 is the reception time of the reference node.

Therefore, it is possible to write

$$R_i - R_0 = c\Delta t_i \tag{2.43}$$

where c is the speed of light and $R_i - R_0$ can be defined as

$$R_i - R_0 = \sqrt{(x_i - x_u)^2 + (y_i - y_u)^2} - \sqrt{(x_0 - x_u)^2 + (y_0 - y_u)^2} \tag{2.44}$$

For a certain $c\Delta t_i$, the relation (2.43) identify the geometric place of points such that the difference between the distance of the generic point and the i-th receiver is constant ad equal to $c\Delta t_i$. This place of points is a hyperbola, whose foci are the generic receiver R_i and the reference receiver R_0.

In this way, it is obtained a system of $N_{Rx} - 1$ different equations, which identify the same number of hyperboles in the two unknows (x_u, y_u). By solving this system, we obtain the intersection of these hyperboles, which provides the target position

$$\begin{cases} R_1 - R_0 = c\Delta t_1 \\ R_2 - R_0 = c\Delta t_2 \\ \quad \cdots \\ R_{N_{Rx}-1} - R_0 = c\Delta t_{N_{Rx}-1} \end{cases} \tag{2.45}$$

It can be observed that this system is non-linear, therefore it is necessary a linearization procedure to solve it.

Let $\hat{\mathbf{u}} = (\hat{x}_u, \hat{y}_u)$ be the estimated coordinates of the target. A first order Taylor series expansion around $\hat{\mathbf{u}}$ can be operated over each single equation.

$$(R_i - R_0)|_{u=\hat{u}} + \left[\left.\frac{\partial(R_i - R_0)}{\partial x_u}\right|_{u=\hat{u}} \quad \left.\frac{\partial(R_i - R_0)}{\partial y_u}\right|_{u=\hat{u}} \right] \cdot \begin{bmatrix} \Delta x_u \\ \Delta y_u \end{bmatrix} = c\Delta t_i \tag{2.46}$$

Then, we define

$$(R_i - R_0)|_{u=\hat{u}} = \hat{R}_i - \hat{R}_0 \tag{2.47}$$

$$\Delta\mathbf{u} = \begin{bmatrix} \Delta x_u \\ \Delta y_u \end{bmatrix} \tag{2.48}$$

$$\frac{\partial R_i}{\partial y_u} = -\frac{y_i - y_u}{\|\mathbf{p}_i - \mathbf{p}_{\hat{u}}\|} = -\alpha_{yi}, \qquad \forall i = 0, \dots, N_{Rx} \tag{2.49}$$

where α_{xi}, α_{yi} are the i-th direction cosines along x-axis and y-axis, respectively.

Therefore, it is obtained

$$[-\alpha_{xi} + \alpha_{x0} \quad -\alpha_{yi} + \alpha_{y0}] \cdot \Delta u = -(\widehat{R}_i - \widehat{R}_0 - c\Delta t_i) \tag{2.50}$$

which leads to

$$[\alpha_{xi} - \alpha_{x0} \quad \alpha_{yi} - \alpha_{y0}] \cdot \Delta u = \Delta R_i \tag{2.51}$$

where $\Delta R_i = \widehat{R}_i - \widehat{R}_0 - c\Delta t_i$.

After the application of these procedure over all the equation of the system in (2.45) and defining

$$\mathbf{H} = \begin{bmatrix} \alpha_{x1} - \alpha_{x0} & \alpha_{y1} - \alpha_{y0} \\ \alpha_{x2} - \alpha_{x0} & \alpha_{y2} - \alpha_{y0} \\ \vdots & \vdots \\ \alpha_{xN_{Rx}-1} - \alpha_{x0} & \alpha_{yN_{Rx}-1} - \alpha_{y0} \end{bmatrix} \tag{2.52}$$

The following general relation can be derived

$$\mathbf{H}\Delta\mathbf{u} = \Delta\mathbf{R} \tag{2.53}$$

where **H** is the matrix of the system and $\Delta\mathbf{R}$ is defined as follows

$$\Delta\mathbf{R} = \begin{bmatrix} \Delta R_1 \\ \Delta R_2 \\ \vdots \\ \Delta R_{N_{Rx}-1} \end{bmatrix} \tag{2.54}$$

$\Delta\mathbf{u}$ is obtained by inverting the system in (2.53). It represents the correction to be applied to $\hat{\mathbf{u}}$ to refine the estimate:

$$\hat{\mathbf{u}}(k) = \hat{\mathbf{u}}(k-1) + \Delta\mathbf{u}(k) \tag{2.55}$$

where k is the index of the current iteration, $\hat{\mathbf{u}}(k-1)$ is the target position estimated at the previous iteration, while $\hat{\mathbf{u}}(k)$ is the new position estimate.

More accurate target positions can be obtained by iterating this procedure. Two types of stopping criterion can be defined: 1) when the absolute value of the correction $\Delta\mathbf{u}$ reaches an established value, and/or 2) when the maximum number of iterations has be reached.

As apparent, the same procedure can be applied also in the 3D case, where the z-axis has to be considered in the definition of the equations.

2.3.2.1.1 Measurement and positioning errors

In the ideal case where $\Delta\mathbf{R}$ is not affected by errors, the only contribution of error will be the linearization error, which can be reduced making an appropriate number of iterations.

In the case where an error in the distance measure is present, it is necessary to evaluate its influence on the positioning error, described by the covariance matrix $\boldsymbol{\Sigma_u}$.

The evaluation of this error is made by the following steps:

1) Evaluation of the covariance matrix $\boldsymbol{\Sigma_R}$ of the distance measure.
2) Application of techniques for system solution (Least Square or Maximum Likelihood).
3) Calculation of the covariance matrix $\boldsymbol{\Sigma_u}$ as a function of $\boldsymbol{\Sigma_R}$ and of the geometry (described by $\boldsymbol{H}$).

These steps are valid for both the 2D and 3D cases.

Evaluation of the covariance matrix $\boldsymbol{\Sigma_R}$

With measure errors, the distance R_i between the *i-th* receiving node and the target is

$$R_i \rightarrow R_i + \partial R_i \tag{2.56}$$

where ∂R_i is a Gaussian random variable with zero mean and variance $c^2\sigma_i^2$, and where σ_i^2 is the variance of the error referred to the *i-th* TDoA.

Therefore, the difference between the distance to the generic receiving node R_i and the distance to the reference node R_0 can be written as follows.

$$\Delta R_{i0} = R_i - R_0 \rightarrow (R_i + \partial R_i) - (R_0 - \partial R_0) = (R_i - R_0) + (\partial R_i - \partial R_0) = \Delta R_{i0} + \partial \Delta R_{i0} \tag{2.57}$$

The covariance matrix $\boldsymbol{\Sigma_R}$ of the distance measurement error, $\Delta\mathbf{R}$, can be calculated through the following generic relation.

$$\Sigma_{hk}^{R} = E\{(\partial R_h - \partial R_0)\cdot(\partial R_k - \partial R_0)\} = c^2 E\{(\partial t_h - \partial t_0)\cdot(\partial t_k - \partial t_0)\} \tag{2.58}$$

where Σ_{hk}^{R} is the generic element of the covariance matrix.

For the two-dimensional case, with the minimum number of receiver (i.e. three), we obtain

$$\begin{aligned}
\Sigma_{11}^{R} &= c^2 E\{(\partial t_1 - \partial t_0)\cdot(\partial t_1 - \partial t_0)\} = c^2(\sigma_0^2 + \sigma_1^2) \\
\Sigma_{22}^{R} &= c^2 E\{(\partial t_2 - \partial t_0)\cdot(\partial t_2 - \partial t_0)\} = c^2(\sigma_0^2 + \sigma_2^2) \\
\Sigma_{12}^{R} &= \Sigma_{21}^{R} = c^2 E\{(\partial t_1 - \partial t_0)\cdot(\partial t_2 - \partial t_0)\} = c^2\sigma_0^2
\end{aligned} \tag{2.59}$$

where ∂t_i represents the time of arrival error related to the specific receiving node, whereas $\sigma_0^2, \sigma_1^2, \sigma_2^2$ are the variances of the time measures of the three receiving nodes.

Therefore,

$$\Sigma_R = c^2 \begin{bmatrix} \sigma_0^2 + \sigma_1^2 & \sigma_0^2 \\ \sigma_0^2 & \sigma_0^2 + \sigma_2^2 \end{bmatrix} \tag{2.60}$$

Techniques for system solution

As explained before, when measurement errors are present, the system is characterized by the following error

$$\boldsymbol{\epsilon} = \Delta\mathbf{R} - \mathbf{H}\Delta\mathbf{u} \tag{2.61}$$

This means that, in order to solve the problem, the following objective function has to be minimized

$$f: E\{\boldsymbol{\epsilon}^T\mathbf{K}\boldsymbol{\epsilon}\} = E\{(\Delta\mathbf{R} - \mathbf{H}\cdot\Delta\mathbf{u})^T\mathbf{K}(\Delta\mathbf{R} - \mathbf{H}\cdot\Delta\mathbf{u})\} \tag{2.62}$$

where **K** is a suitable matrix which is used to limit the contribution of the equations with the higher variance.

1) Least Square (LS) solution

For the Least Square solution (LS), we have $\mathbf{K} = \mathbf{I}$, where **I** is the identity matrix.
The objective function becomes

$$f: E\{\boldsymbol{\epsilon}^T\boldsymbol{\epsilon}\} = E\{(\Delta\mathbf{R} - \mathbf{H}\cdot\Delta\mathbf{u})^T(\Delta\mathbf{R} - \mathbf{H}\cdot\Delta\mathbf{u})\} \tag{2.63}$$

The minimization of the (2.63) produces the following result

$$\Delta\mathbf{u} = (\mathbf{H}^T\mathbf{H})^{-1}\mathbf{H}^T\Delta\mathbf{R} \tag{2.64}$$

where the pseudoinverse $(\mathbf{H}^T\mathbf{H})^{-1}\mathbf{H}^T$ is used to invert the system in (2.53).

2) Maximum Likelihood (ML) solution

For the Maximum Likelihood solution (ML), we have $\mathbf{K} = \boldsymbol{\Sigma}_\mathbf{R}^{-1}$, where $\boldsymbol{\Sigma}_\mathbf{R}^{-1}$ is the inverse of the covariance matrix of the measurement errors.

The objective function becomes

$$f: E\{\boldsymbol{\epsilon}^T\boldsymbol{\Sigma}_\mathbf{R}^{-1}\boldsymbol{\epsilon}\} = E\{(\Delta\mathbf{R} - \mathbf{H}\cdot\Delta\mathbf{u})^T\boldsymbol{\Sigma}_\mathbf{R}^{-1}(\Delta\mathbf{R} - \mathbf{H}\cdot\Delta\mathbf{u})\} \tag{2.65}$$

The minimization of the (2.63) produces the following result

$$\Delta\mathbf{u} = (\mathbf{H}^T\boldsymbol{\Sigma}_\mathbf{R}^{-1}\mathbf{H})^{-1}\mathbf{H}^T\boldsymbol{\Sigma}_\mathbf{R}^{-1}\Delta\mathbf{R} \tag{2.66}$$

where the system in (2.53) is solved through the use of the weighted pseudoinverse $(\mathbf{H}^T\boldsymbol{\Sigma}_\mathbf{R}^{-1}\mathbf{H})^{-1}\mathbf{H}^T\boldsymbol{\Sigma}_\mathbf{R}^{-1}$.

Evaluation of the covariance matrix $\boldsymbol{\Sigma_u}$

The parameter that we use for the evaluation of the accuracy is the variance σ_{u}^2. Therefore, defining $\partial\mathbf{u}$ as the positioning error of the target position estimate $\mathbf{u}$ and considering the generic relation

$$\Delta\mathbf{u} = (\mathbf{H}^{\mathrm{T}}\mathbf{K}\mathbf{H})^{-1}\mathbf{H}^{\mathrm{T}}\mathbf{K}\Delta\mathbf{R} \tag{2.67}$$

It is possible to write

$$\partial\mathbf{u} = (\mathbf{H}^{\mathrm{T}}\mathbf{K}\mathbf{H})^{-1}\mathbf{H}^{\mathrm{T}}\mathbf{K}\,\partial\mathbf{R} \tag{2.68}$$

The covariance matrix of the positioning errors is defined as follows

$$\boldsymbol{\Sigma}_u = \mathrm{E}\{\partial\mathbf{u}^{\boldsymbol{T}}\,\partial\mathbf{u}\} \tag{2.69}$$

Through the equations (2.68)-(2.69) the generic form of the covariance matrix can be defined as

$$\boldsymbol{\Sigma_u} = (\mathbf{H}^{\boldsymbol{T}}\mathbf{K}^{\boldsymbol{T}}\mathbf{H})^{-\mathbf{1}}\mathbf{H}^{\boldsymbol{T}}\mathbf{K}^{\boldsymbol{T}}\boldsymbol{\Sigma_R}\mathrm{KH}(\mathrm{H}^{\mathrm{T}}\mathrm{KH})^{-1} \tag{2.70}$$

For the LS solution ($\mathbf{K} = \mathbf{I}$), the specific expression becomes

$$\boldsymbol{\Sigma}_{\boldsymbol{u}}^{\boldsymbol{LS}} = (\mathbf{H}^{\mathrm{T}}\mathbf{H})^{-1}\mathbf{H}^{\mathrm{T}}\boldsymbol{\Sigma}_{\mathbf{R}}\mathrm{H}(\mathrm{H}^{\mathrm{T}}\mathrm{H})^{-1} \tag{2.71}$$

For the ML solution ($\mathbf{K} = \boldsymbol{\Sigma}_{\mathbf{R}}^{-1}$), the specific expression becomes

$$\boldsymbol{\Sigma}_{\boldsymbol{u}}^{\boldsymbol{ML}} = (\mathbf{H}^{\mathrm{T}}\Sigma_{\mathrm{R}}^{-1}\mathbf{H})^{-1}\mathbf{H}^{\mathrm{T}}\Sigma_{\mathrm{R}}^{-1}\mathrm{H}(\mathrm{H}^{\mathrm{T}}\Sigma_{\mathrm{R}}^{-1}\mathrm{H})^{-1} \tag{2.72}$$

Therefore, for the standard deviation of the positioning errors we have

$$\sigma_{\boldsymbol{u}}^{\boldsymbol{LS}} = \sqrt{Tr\{\boldsymbol{\Sigma}_{\boldsymbol{u}}^{\boldsymbol{LS}}\}} \tag{2.73}$$

$$\sigma_{\boldsymbol{u}}^{\boldsymbol{ML}} = \sqrt{Tr\{\boldsymbol{\Sigma}_{\boldsymbol{u}}^{\boldsymbol{ML}}\}} \tag{2.74}$$

Finally, when the measurement errors are non-homogeneous, the following relationship applies

$$\sigma_{\boldsymbol{u}}^{\boldsymbol{LS}} > \sigma_{\boldsymbol{u}}^{\boldsymbol{ML}} \tag{2.75}$$

2.3.2.1.2 Theoretical performance evaluation

For the theoretical evaluation, we suppose to have three receiving nodes. According to the analytical study reported in the previous sections, one of these nodes will be used as reference. Therefore, two measures of TDoA will be available, both obtained by the estimation of the time differences of the remaining two receiver with respect to the reference one.

In this phase of the study, we use the same value of the variance for each point of the area of interest. In other words, we do not take into account the dependence of the measurement accuracy by the SNR, and consequently to the distance between target and receiver.

The following analysis have been performed for the two-dimensional case.

The specific geometry consists in three receivers positioned along a circumference with a radius of 500 meters and an angle of 120° between them.

Therefore, the positions of the three receiving nodes are:

- $\mathbf{p_1} = (500, 0)$
- $\mathbf{p_2} = \big(500\cos(120), 500\sin(120)\big)$
- $\mathbf{p_3} = (500\cos(240), 500\sin(240))$

Two different situations have been considered:

1) All the standard deviations have the same value (uniform): $c\sigma_0 = c\sigma_1 = c\sigma_2 = 1.5\ [m]$
2) All the standard deviations have different values: $c\sigma_0 = 1.5\ [m],\ c\sigma_1 = 2.5\ [m],\ c\sigma_2 = 3.5\ [m]$

For this analysis, a square area with the side length of 1200 m has been considered. The matrix H has been calculated for each point of this area, then σ_u^{LS} and σ_u^{ML} can be derived from (2.71)-(2.73) and (2.72)-(2.74), respectively, since the matrix $\boldsymbol{\Sigma_R}$ is known.

<u>Case 1</u>: $\boldsymbol{c\sigma_0 = c\sigma_1 = c\sigma_2 = 1.5\ [m]}$

The standard deviation of 1.5 m represents the case where the measurements of time/distance are rather noisy. In fact, this is on average what happens for low values of SNR for the techniques analyzed in Section 2.3.1.1. Obviously, as shown during the evaluation of the presented techniques, when the SNR is low, there are situations (related to the specific technique, to the oversampling factor and/or to the relative delay between the signals) for which the errors can be lower or higher than this quantity. We will study these situations when different values of variance are used.

The performance related to the Case 1 are reported in Figure 2.16, where each point of the positioning accuracy map identifies a x and y coordinate of the hypothetical target position.

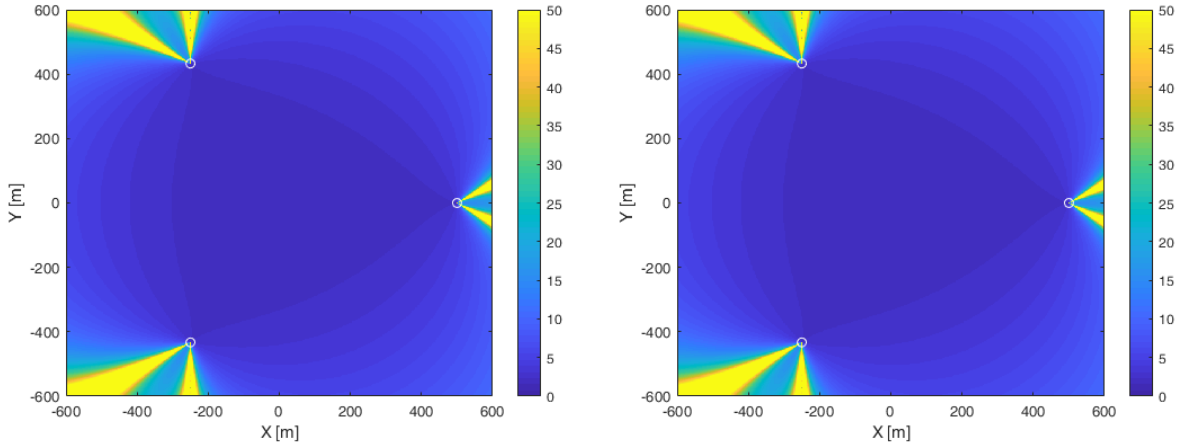

(a) (b)

Figure 2.16. Standard deviation of the theoretical positioning errors for uniform standard deviations of the distance errors equal to 1.5 m for: (a) **LS** method and (b) **ML** method, for 2 TDoA.

It is possible to notice that in this case the two methods lead to the same performance. In fact, the LS solution corresponds to the ML solution when the standard deviations of the measures are identical for all the receivers.

In addition, it is evident that the positioning error is lower within the triangle drawn by the three nodes, where it is below 5-10 m.

<u>Case 2</u>: $\boldsymbol{c\sigma_0 = 1.5\ [m],\ c\sigma_1 = 2.5\ [m],\ c\sigma_2 = 3.5\ [m]}$

In this case, the standard deviations are different for the times/distances measured by the three receivers. This situation is more representative of real cases as the three employed receivers are inherently different from each other. Moreover, also in relation to the chosen technique, in all those cases in which the performances are somehow linked to the delay of the signals and so to the relative time difference of arrival, this choice is particularly illustrative, as the signals will arrive to the different receivers with a different delay, which is a function of the position of the target with respect to them.

The use of higher standard deviations (2.5 m and 3.5 m) represents both the situation described above and the possible deterioration in performance when applying these techniques to real data.

The results are shown in Figure 2.17, where it is possible to observe that the position error is greater than that shown in Figure 2.16, even in the area enclosed by the three receivers, where it remains below 10-15 m. This is obviously due to the fact that the chosen standard deviations have higher values than in the previous case.

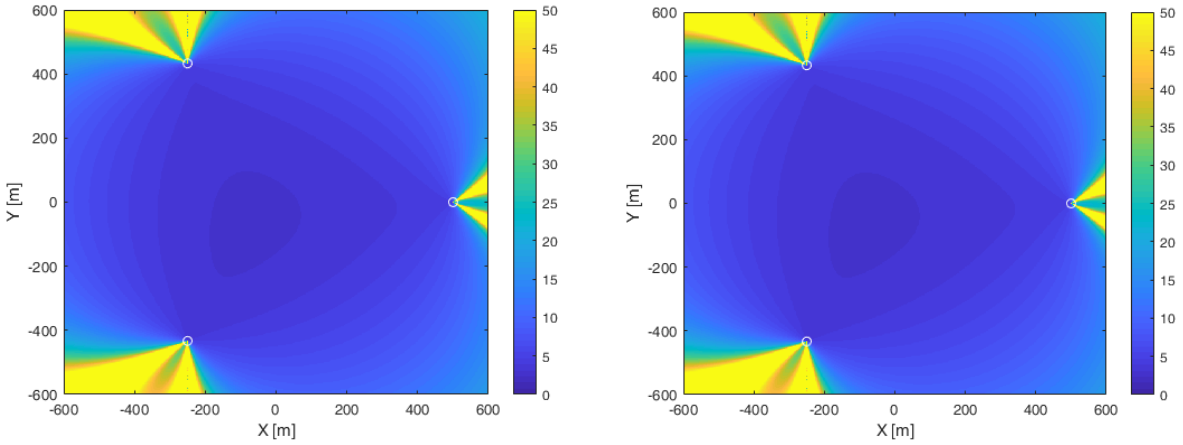

(a) (b)

Figure 2.17. Standard deviation of the theoretical positioning errors for non-uniform standard deviations of the distance errors equal to 1.5 m, 2.5 m and 3.5 m for: (a) **LS** method and (b) **ML** method, for 2 TDoA.

Even this time, the two solutions provide the same results because the minimum number of receivers has been used.

Moreover, since the standard deviations of the TDoA errors are different for each receiver, the positioning error increases in a non-uniform way along the lines passing through the origin of the Cartesian reference system and the three nodes. This is in contrast with the results shown in Figure 2.16.

A further consideration can also be drawn from the above figures. If we draw three lines passing through the various pairs of receivers, so as to form the triangle mentioned above, along the six straight lines outside this triangle, whit origin in the respective receivers, it is possible to notice that the error increases considerably.

This can be explained mathematically. In fact, we can write the equation of the straight line passing through any pair of receivers. Considering that the target is in a point of this line and replacing the obtained result within the matrix **H**, we achieve the following expression for matrix **H**.

$$\boldsymbol{H} = \begin{bmatrix} \alpha_{x1} - \alpha_{x0} & \alpha_{y1} - \alpha_{y0} \\ 0 & 0 \end{bmatrix} \tag{2.76}$$

where it is evident that in these points the matrix **H** becomes singular. In fact, since it has a row whose elements are all zeros, it will not be possible to inverts the initial system, resulting in the generation of very high errors. Consequently, the correction term $\Delta\boldsymbol{u}$ will tend to infinity and the system will not converge to the desired solution.

2.3.2.1.3 Closed-form solution

In the 2D case, with three receivers, it is possible to solve the system in (2.53) avoiding the use of the iterative method described above. In fact, we can write the system containing the equations of the two hyperboles, which define the TDoA measures, as a function of the unknowns x_u and y_u:

$$\begin{cases}\sqrt{(x_1 - x_u)^2 + (y_1 - y_u)^2} - \sqrt{(x_0 - x_u)^2 + (y_0 - y_u)^2} = c\Delta t_1 \\ \sqrt{(x_2 - x_u)^2 + (y_2 - y_u)^2} - \sqrt{(x_0 - x_u)^2 + (y_0 - y_u)^2} = c\Delta t_2\end{cases} \quad (2.77)$$

where (x_i, y_i) represents the coordinates of the i-th receiving nodes.

This type of solution is convenient because it significantly reduces the calculation time since the process is direct and not iterative. Furthermore, it leads directly to the exact solution (no convergence problems). On the other hand, however, the closed-form solution introduces ambiguous solutions, which in most cases can be eliminated by following small expedients.

2.3.2.2 Positioning techniques based on AoA measurements

Once the angle of arrival has been estimated, it will be possible to proceed with the determination of the line defined by it.

Since the intersection of two lines uniquely defines a single point on the plane, at least two angle measurements are required to unambiguously estimate the position of the target on the XY plane. This means that if we only want to use AoA measurements to determine the target position, at least two receiving nodes are necessary, each one consisting of at least two antenna elements (for the reasons described in the previous section); in other words, you need to have at least 4 antennas in total.

Obviously, more information could provide an improvement in system performance in terms of positioning accuracy. Firstly, the employment of more antennas, for example, would produce two main advantages: 1) the possibility of using more measurements to refine the position estimate; 2) the possibility of making the system more robust in case of faults. Secondly, the increase in information can also be represented by the hybrid solution AoA/TDoA, which will be discussed in Section 2.3.2.2.3.

As defined in Section 2.3.2.1, assume to have N_{Rx} receiving nodes located in the generic point $\mathbf{p}_i = (x_i, y_i)$ of a local Cartesian system. Each node must contain at least two elements of antenna, in order to estimate the angle θ_i related to the specific signal transmitted by the target and received by the i-th receiver. With $\mathbf{u} = (x_u, y_u)$ it is indicated the vector containing the target coordinates defined over the same Cartesian reference system of the receiving nodes.

The angle estimated by the *i-th* receiver can be calculated as

$$\theta_i = \tan^{-1}\frac{(x_u - x_i)}{(y_u - y_i)} \quad (2.78)$$

where (x_u, y_u) are the target coordinates, while (x_i, y_i) are the coordinates of the *i-th* receiver.

As already mentioned above, the geometric place of points defined by θ_i is a line passing through $\mathbf{u}$ and $\mathbf{p}_i$.

In this way, it is obtained a system of N_{Rx} different equations, which identify the same number of lines in the two unknows $(x_u,\ y_u)$. By solving this system, we obtain the intersection of these lines, which provides the target position

$$\begin{cases} \theta_1 = \tan^{-1}\dfrac{(x_u - x_1)}{(y_u - y_1)} \\ \theta_2 = \tan^{-1}\dfrac{(x_u - x_2)}{(y_u - y_2)} \\ \quad \dots \\ \theta_{N_{Rx}} = \tan^{-1}\dfrac{(x_u - x_{N_{Rx}})}{(y_u - y_{N_{Rx}})} \end{cases} \tag{2.79}$$

The first step is the linearization of this system.

With this purpose, it is defined $\hat{\mathbf{u}} = (\hat{x}_u, \hat{y}_u)$ as the estimated target position. A first order Taylor series expansion around $\hat{\mathbf{u}}$ can be operated over each single equation.

$$(\theta_i)|_{u=\hat{u}} + \left[\left.\frac{\partial(\theta_i)}{\partial x_u}\right|_{u=\hat{u}} \quad \left.\frac{\partial(\theta_i)}{\partial y_u}\right|_{u=\hat{u}}\right] \cdot \begin{bmatrix}\Delta x_u \\ \Delta y_u\end{bmatrix} = \theta_i \tag{2.80}$$

Then, we define

$$\frac{\partial\theta_i}{\partial x_u} = \frac{1}{1 + (\frac{x_u - x_i}{y_u - y_i})^2} * \frac{(y_u - y_i)}{(y_u - y_i)^2} = \alpha_{xi} \quad , \qquad \forall i = 1, \dots, N_{Rx} \tag{2.81}$$

$$\frac{\partial\theta_i}{\partial y_u} = \frac{1}{1 + (\frac{x_u - x_i}{y_u - y_i})^2} * -\frac{(x_u - x_i)}{(y_u - y_i)^2} = -\alpha_{yi} \quad , \qquad \forall i = 1, \dots, N_{Rx} \tag{2.82}$$

$$\Delta\mathbf{u} = \begin{bmatrix}\Delta x_u \\ \Delta y_u\end{bmatrix} \tag{2.83}$$

where α_{xi}, α_{yi} are the i-th direction cosines along x-axis and y-axis, respectively.

Therefore, it is obtained

$$\theta_i - \hat{\theta}_i = [\alpha_{xi} \quad -\alpha_{yi}] \cdot \Delta\mathbf{u} \tag{2.84}$$

where we have indicated $(\theta_i)|_{u=\hat{u}} = \hat{\theta}$.

The equation (2.84) leads to

$$[\alpha_{xi} \quad -\alpha_{yi}] \cdot \Delta\mathbf{u} = \Delta\theta_i \tag{2.85}$$

where $\Delta\theta_i = \theta_i - \hat{\theta}_i$.

After the application of these procedure over all the equation of the system in (2.79), the following general relation can be derived

$$\mathbf{H} \cdot \Delta\mathbf{u} = \Delta\boldsymbol{\theta} \tag{2.86}$$

where $\mathbf{H}$ is the matrix containing the direction cosines

$$\mathbf{H} = \begin{bmatrix} \alpha_{x1} & \alpha_{y1} \\ \alpha_{x2} & \alpha_{y2} \\ \vdots & \vdots \\ \alpha_{x,N_{Rx}} & \alpha_{y,N_{Rx}} \end{bmatrix} \tag{2.87}$$

and $\Delta\boldsymbol{\theta}$ is defined as follows

$$\Delta\boldsymbol{\theta} = \begin{bmatrix} \Delta\theta_1 \\ \Delta\theta_2 \\ \vdots \\ \Delta\theta_{N_{Rx}} \end{bmatrix} \tag{2.88}$$

$\Delta\mathbf{u}$ is obtained by inverting the system in (2.86). It represents the correction to be applied to $\hat{\mathbf{u}}$ to refine the estimate:

$$\hat{\mathbf{u}}(k) = \hat{\mathbf{u}}(k-1) + \Delta\mathbf{u}(k) \tag{2.89}$$

where k is the index of the current iteration, $\hat{\mathbf{u}}(k-1)$ is the target position estimated at the previous iteration, while $\hat{\mathbf{u}}(k)$ is the new position estimate.

More accurate target positions can be obtained by iterating this procedure. The two types of stopping criterion presented in Section 2.3.2.1 can be applied also in this case.

2.3.2.2.1 Measurement and positioning errors

Suppose to have a number of receiver higher than two, that is the minimum number required to perform the localization by using only AoA measures.

In this case, we have a system of $N_{Rx} > 2$ nonlinear equations in two unknowns: the system is therefore overdetermined. In order to obtain a solution, the two methods described above can be applied even in this case, namely the Least Square (LS) method and the Maximum Likelihood (ML) method, but not the closed-form solution, unless we decide to discard some measures.

In the case where an error in the angle measure is present, it is necessary to evaluate its influence on the positioning error, described by the covariance matrix $\boldsymbol{\Sigma_u}$.

The evaluation of this error is made by the following steps:

1) Evaluation of the covariance matrix $\boldsymbol{\Sigma_\theta}$ of the angle measure errors.
2) Application of techniques for system solution (Least Square or Maximum Likelihood).
3) Calculation of the covariance matrix $\boldsymbol{\Sigma_u}$ as a function of $\boldsymbol{\Sigma_\theta}$ and of the geometry (described by $\boldsymbol{H}$).

Evaluation of the covariance matrix $\boldsymbol{\Sigma_\theta}$

Consider the case where angle measure errors are present:

$$\theta_i \rightarrow \theta_i + \partial\theta_i \tag{2.90}$$

where $\partial\theta_i$ is a Gaussian random variable with zero mean and variance $\sigma^2_{\theta_i}$.

The covariance matrix $\boldsymbol{\Sigma}_\theta$ of the angle measurement error, $\boldsymbol{\Delta\theta}$, can be calculated through the following generic relation, where the generic element of the covariance matrix can be written as

$$\Sigma^{\theta}_{ij} = E\{\partial\theta_i \cdot \partial\theta_j\} \tag{2.91}$$

With three receivers, we obtain

$$\Sigma_\theta = \begin{bmatrix} \sigma^2_{\theta_1} & 0 & 0 \\ 0 & \sigma^2_{\theta_2} & 0 \\ 0 & 0 & \sigma^2_{\theta_3} \end{bmatrix} \tag{2.92}$$

where $\sigma^2_{\theta_1}, \sigma^2_{\theta_2}, \sigma^2_{\theta_3}$ are the variances of the angle measures of the three receiving nodes.

As apparent, this is a diagonal matrix, as the measures of angle are independent among the different receivers.

Techniques for system solution

As explained before, when measurement errors occur, the system is characterized by the following error

$$\boldsymbol{\epsilon} = \boldsymbol{\Delta\theta} - \mathbf{H} \cdot \boldsymbol{\Delta u} \tag{2.93}$$

This means that, in order to solve the problem, the following objective function has to be minimized

$$f: E\{\boldsymbol{\epsilon}^T \mathbf{K} \boldsymbol{\epsilon}\} = E\{(\boldsymbol{\Delta\theta} - \mathbf{H} \cdot \boldsymbol{\Delta u})^T \mathbf{K} (\boldsymbol{\Delta\theta} - \mathbf{H} \cdot \boldsymbol{\Delta u})\} \tag{2.94}$$

where **K** is a suitable matrix which is used to limit the contribution of the equations with the higher variance.

1) Least Square (LS) solution

For the Least Square solution (LS), we have $\mathbf{K} = \mathbf{I}$, where **I** is the identity matrix.

The objective function becomes

$$f: E\{\boldsymbol{\epsilon}^{\mathrm{T}} \boldsymbol{\epsilon}\} = E\{(\boldsymbol{\Delta\theta} - \mathbf{H} \cdot \boldsymbol{\Delta u})^{\mathrm{T}} (\boldsymbol{\Delta\theta} - \mathbf{H} \cdot \boldsymbol{\Delta u})\} \tag{2.95}$$

The minimization of the (2.95) produces the following result

$$\boldsymbol{\Delta u} = (\mathbf{H}^{\mathrm{T}} \mathbf{H})^{-1} \mathbf{H}^{\mathrm{T}} \boldsymbol{\Delta\theta} \tag{2.96}$$

where the pseudoinverse $(\mathbf{H}^{\mathrm{T}} \mathbf{H})^{-1} \mathbf{H}^{\mathrm{T}}$ is used to invert the system in (2.86).

2) Maximum Likelihood (ML) solution

For the Maximum Likelihood solution (ML), we have $\mathbf{K} = \mathbf{\Sigma_\theta^{-1}}$, where $\mathbf{\Sigma_\theta^{-1}}$ is the inverse of the covariance matrix of the measurement errors.

The objective function becomes

$$f: E\{\boldsymbol{\epsilon}^{\mathrm{T}}\mathbf{\Sigma_\theta^{-1}}\boldsymbol{\epsilon}\} = E\{(\Delta\boldsymbol{\theta} - \mathbf{H}\cdot\Delta\mathbf{u})^{\mathrm{T}}\mathbf{\Sigma_\theta^{-1}}(\Delta\boldsymbol{\theta} - \mathbf{H}\cdot\Delta\mathbf{u})\} \tag{2.97}$$

The minimization of the (2.97) produces the following result

$$\Delta\mathbf{u} = (\mathbf{H}^{\mathrm{T}}\mathbf{\Sigma_\theta^{-1}}\mathbf{H})^{-1}\mathbf{H}^{\mathrm{T}}\mathbf{\Sigma_\theta^{-1}}\Delta\boldsymbol{\theta} \tag{2.98}$$

where the system in (2.86) is solved through the use of the weighted pseudoinverse $(\mathbf{H}^{\mathrm{T}}\mathbf{\Sigma_\theta^{-1}}\mathbf{H})^{-1}\mathbf{H}^{\mathrm{T}}\mathbf{\Sigma_\theta^{-1}}$.

Evaluation of the covariance matrix $\boldsymbol{\Sigma_u}$

The parameter that we use for the evaluation of the accuracy is the variance σ_{u}^2. Therefore, defining $\partial\mathbf{u}$ as the positioning error of the target position estimate $\mathbf{u}$ and considering the generic relation

$$\Delta\mathbf{u} = (\mathbf{H}^{\mathrm{T}}\mathbf{K}\mathbf{H})^{-1}\mathbf{H}^{\mathrm{T}}\mathbf{K}\Delta\boldsymbol{\theta} \tag{2.99}$$

It is possible to write

$$\partial\mathbf{u} = (\mathbf{H}^{\mathrm{T}}\mathbf{K}\mathbf{H})^{-1}\mathbf{H}^{\mathrm{T}}\mathbf{K}\,\partial\boldsymbol{\theta} \tag{2.100}$$

The covariance matrix of the positioning errors is defined as follows

$$\mathbf{\Sigma}_u = \mathrm{E}\{\partial\mathbf{u}^{\boldsymbol{T}}\,\partial\mathbf{u}\} \tag{2.101}$$

Through the equations (2.100)-(2.101) the generic form of the covariance matrix can be defined as

$$\mathbf{\Sigma_u} = (\mathbf{H}^{\boldsymbol{T}}\mathbf{K}^{\boldsymbol{T}}\mathbf{H})^{-1}\mathbf{H}^{\boldsymbol{T}}\mathbf{K}^{\boldsymbol{T}}\mathbf{\Sigma_\theta}\mathrm{K}\mathrm{H}(\mathrm{H}^{\mathrm{T}}\mathrm{K}\mathrm{H})^{-1} \tag{2.102}$$

For the LS solution ($\mathbf{K} = \mathbf{I}$), the specific expression becomes

$$\mathbf{\Sigma_u^{LS}} = (\mathbf{H}^{\mathrm{T}}\mathbf{H})^{-1}\mathbf{H}^{\mathrm{T}}\mathbf{\Sigma_\theta}\mathrm{H}(\mathrm{H}^{\mathrm{T}}\mathrm{H})^{-1} \tag{2.103}$$

For the ML solution ($\mathbf{K} = \mathbf{\Sigma_\theta^{-1}}$), the specific expression becomes

$$\mathbf{\Sigma_u^{ML}} = \left(\mathbf{H}^{\mathrm{T}}\Sigma_{\boldsymbol{\theta}}^{-1}\mathbf{H}\right)^{-1}\mathbf{H}^{\mathrm{T}}\Sigma_{\boldsymbol{\theta}}^{-1}\mathrm{H}\left(\mathrm{H}^{\mathrm{T}}\Sigma_{\boldsymbol{\theta}}^{-1}\mathrm{H}\right)^{-1} \tag{2.104}$$

Therefore, for the standard deviation of the positioning errors we have

$$\sigma_{\boldsymbol{u}}^{LS} = \sqrt{Tr\{\mathbf{\Sigma_u^{LS}}\}} \tag{2.105}$$

$$\sigma_{\boldsymbol{u}}^{ML} = \sqrt{Tr\{\mathbf{\Sigma_u^{ML}}\}} \tag{2.106}$$

Finally, when the measurement errors are non-homogeneous, the following relationship applies

$$\sigma_{\boldsymbol{u}}^{LS} > \sigma_{\boldsymbol{u}}^{ML} \tag{2.107}$$

2.3.2.2.2 Theoretical performance evaluation

For the theoretical evaluation, we suppose to have three receiving nodes.

As described in Section 2.3.1.2, se employed receiving systems with a circular symmetry, with at least two antenna elements. Therefore, in the next discussion any condition on their pointing has been considered.

The specific geometry is the same presented in Section 2.3.2.1.2.

Even this time, two different situations have been considered:

1) All the standard deviations have the same value (uniform): $\sigma_{\theta_1} = \sigma_{\theta_2} = \sigma_{\theta_3} = 0.3\ [deg]$

2) All the standard deviations have different values: $\sigma_{\theta_1} = 5\ [deg],\ \sigma_{\theta_2} = 0.3\ [deg],\ \sigma_{\theta_3} = 1\ [deg]$

For this analysis, a square area with the side length of 1200 m has been considered. The matrix H has been calculated for each point of this area, then σ_u^{LS} and σ_u^{ML} can be derived from (2.103)-(2.105) and (2.104)-(2.106), respectively, since the matrix $\boldsymbol{\Sigma_R}$ is known.

<u>Case 1</u>: $\boldsymbol{\sigma_{\theta_1} = \sigma_{\theta_2} = \sigma_{\theta_3} = 0.3\ [deg]}$

For brevity, we indicate $\sigma_\theta = \sigma_{\theta_1} = \sigma_{\theta_2} = \sigma_{\theta_3}$, since in this case the value of the standard deviation is identical for all the receivers.

The performance related to the Case 1 are reported in Figure 2.18, where each point of the positioning accuracy map identifies a x and y coordinate of the hypothetical target position.

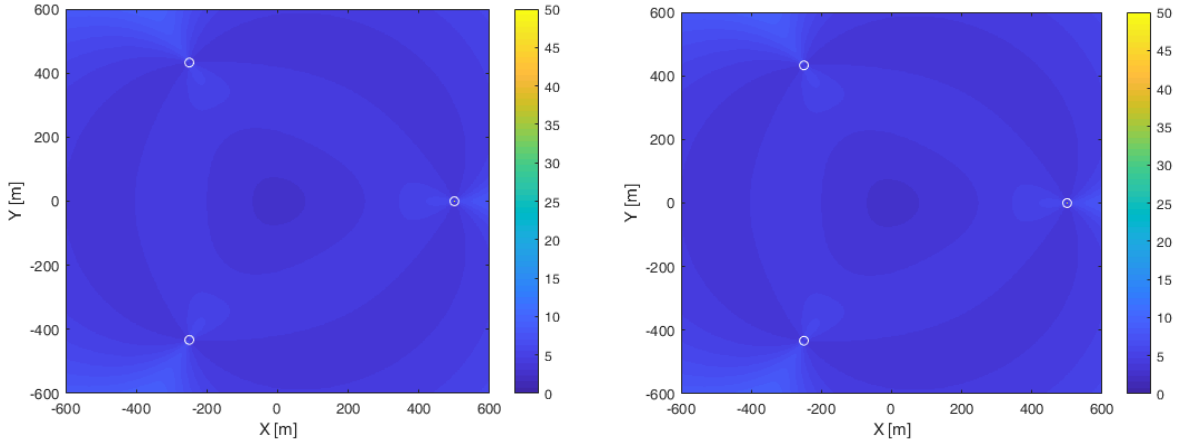

Figure 2.18. Standard deviation of the theoretical positioning errors for uniform standard deviations of the angle errors equal to 0.3° for: (a) **LS** method and (b) **ML** method, for 2 AoA.

As expected, in this case the two methods lead to the same performance. This is due to the fact that the LS solution corresponds to the ML solution when the standard deviations of the measures are identical for all the receivers.

In addition, it is evident that the positioning error is lower than 5 m for the entire examined area. Comparing these results with the images in Figure 2.16, we can notice that the employment of only AoA measurements avoids the increase of the error when the target lies on the six lines outside the area covered by the nodes, mentioned in Section 2.3.2.1.2. This provides the possibility to estimate fairly accurate positions regardless the specific target positions. However, there is a slight decrease of the accuracy when the target is on the straight lines connecting the receivers. This is due to the parallelism of two out of three lines defined by the angles. In fact, without a third receiver it is impossible to determine the target position when it lies on the mentioned lines.

Case 2: $\boldsymbol{\sigma_{\theta_1} = 5\ [deg],\ \sigma_{\theta_2} = 0.3\ [deg],\ \sigma_{\theta_3} = 1\ [deg]}$

In this case, the standard deviations are different for the angles measured by the three receivers. This situation is more representative of real cases as the three employed receivers are inherently different from each other.

The use of higher standard deviations (1° and 5°) represents the possible deterioration in performance when applying these techniques to real data.

The results are shown in Figure 2.19, where it is possible to observe that the position error is greater than that shown in Figure 2.18, therefore we also increased the scale to provide an easier visualization. This is obviously due to the fact that the chosen standard deviations have higher values than in the previous case.

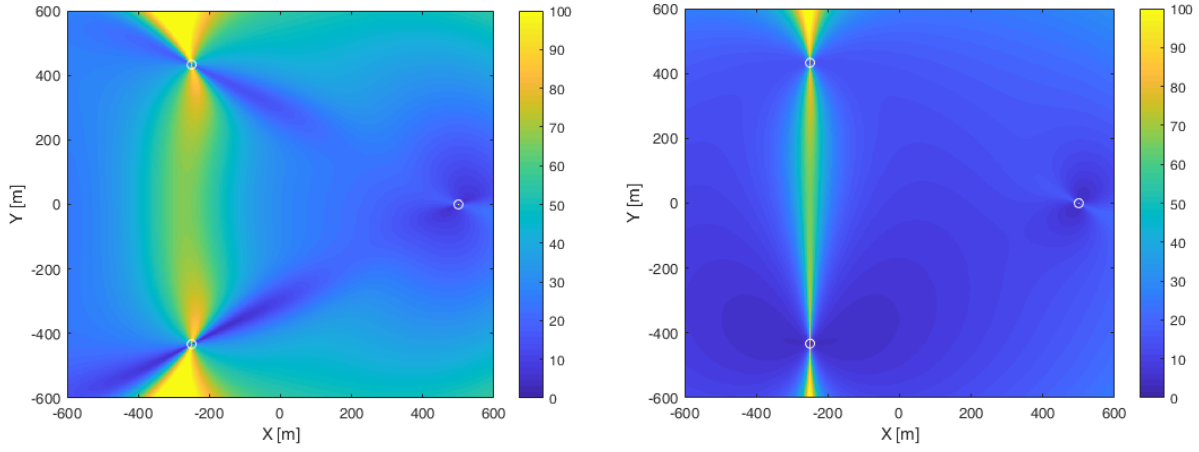

(a) (b)

Figure 2.19. Standard deviation of the theoretical positioning errors for non-uniform standard deviations of the angle errors equal to 5°, 0.3° and 1° for: (a) **LS** method and (b) **ML** method, for 2 AoA.

In contrast with the results shown in Figure 2.18, in this case, since the standard deviations of the AoA errors are different for each receiver, the positioning error increases in a non-uniform way.

Moreover, as already explained, if the target lies on the line which connects two receivers, it is practically impossible to determine its position, without the help of a third receiver.

Observing Figure 2.19(a), we can see that, as expected, σ_u^{LS} near the line that connects the two receivers on the left side of the image is much larger than the remaining two lines; this happens because, in these points, the determination of the target position depends mainly on the third receiver (on the right) which is the receiver with the higher value of σ_{θ_i}.

This time, the two solutions (LS and ML) provide different results. In detail, the ML solution is characterized by the lowest errors, since it chooses and then 'weights' the estimated position according to the measurements it considers most reliable. In general, therefore, even in cases where we have non-homogeneous measurements (hybrid techniques AoA/TDoA) it is preferable to use the ML method.

2.3.2.2.3 Solution for the minimum number of receiving nodes

As explained before, the minimum number of nodes for the position estimation based on only AoA measurements is two. In fact, each receiving node estimates an angle, which in turn defines a particular line in the plane. In total, there are two lines, at the intersection of which the target can be found. Mathematically, the intersection point is determined by solving the following linear system of two equations (the two lines) in two unknowns (the coordinates of the target):

$$\begin{cases} y_u = m_1 x_u + q_1 \\ y_u = m_2 x_u + q_2 \end{cases} \tag{2.108}$$

where (x_u, y_u) are the coordinates of the target in the chosen Cartesian reference system, m_1 and m_2 are the angular coefficients related to the lines passing through the target position and the receivers RX1 and RX2, respectively, while q_1 and q_2 represent the values of the intercept of the same lines.

This system admits a closed-form solution, without the use of iterative algorithm (sub-optimal methods).

If this analysis produces satisfactory results, it represents a good alternative to the aforementioned methods, especially if we desire to reduce the costs (economical and computational).

Suppose to have only two receivers with the same values for the standard deviations. In Figure 2.20, we reported the performance for $\sigma_{\theta_1} = \sigma_{\theta_2} = 0.3°$.

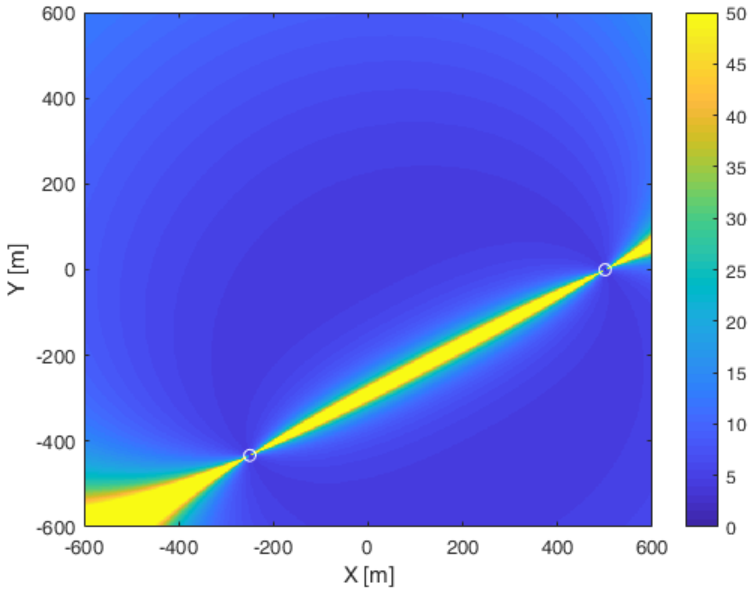

Figure 2.20. Standard deviation of the theoretical positioning errors for uniform standard deviations of the angle errors equal to 0.3°, for 2 AoA.

It can be noticed that the considerations expressed for the LS and ML cases apply even this time. In fact, the error is much higher in the points adjacent to the line that connects the two receivers. This is due to the fact that on these points the two lines are almost parallel, therefore it is very difficult to determine the position of the target univocally.

Moreover, comparing with the results reported in Figure 2.18(a), the position error that occurs on this line is greater in this case, since in the case previously analyzed, the third receiver allows in any case to eliminate the ambiguity in the positioning, contributing to a significant reduction of the error.

2.3.2.3 Positioning techniques based on AoA/TDoA measurements

As introduced in Section 2.3.2, we analyze the hybrid solutions only when two receiving nodes are employed.

Therefore, considering the combinations reported in Table 2, we focus on the following two cases:

1) 1 AoA + 1 TDoA
2) 2 AoA + 1 TDoA

as the case where 2 AoA are exploited has been already discussed in Section 2.3.2.2.3.

Case 1: 1 AoA + 1 TDoA

For the first case, three antennas are enough for the localization in the XY plane, namely one receiving node can also be composed by only one antenna.

As we have already said, the AoA defines a geometric place of points corresponding to a line passing through the receiver and the target, while the TDoA corresponds (less than a scale factor equal to the speed of

propagation of the signal) to a difference between distances that defines a geometric place of points corresponding to a hyperbola.

In this case, it is possible to find the closed-form solution by solving the following system, which represents the intersection of a line (AoA) and a hyperbola (TDoA).

$$\begin{cases} \sqrt{(x_1 - x_u)^2 + (y_1 - y_u)^2} - \sqrt{(x_0 - x_u)^2 + (y_0 - y_u)^2} = \widehat{\Delta\tau} \cdot c \\ y_u = m_2 x_u + q_2 \end{cases} \tag{2.109}$$

where $(\widehat{x_u}, \widehat{y_u})$ are the estimated coordinates of the target in the chosen Cartesian reference system, (x_1, y_1) are the coordinates of the receiving node containing only one antenna in the same reference system, , (x_0, y_0) are the coordinates of the receiving node considered as reference, c is the speed of light, $\widehat{\Delta\tau}$ is the estimated TDoA, $\hat{m}$ is the slope of the line defined by the AoA, while q_2 represents the value of the intercept of the same line.

In Figure 2.21, we reported the performance for $\sigma_\theta = 0.3°$ and $\sigma_R = 1.5$ m.

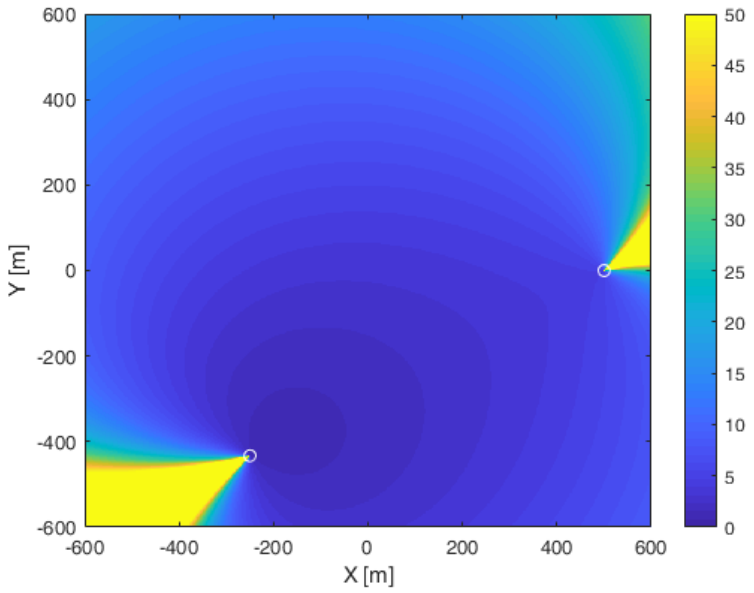

Figure 2.21. Standard deviation of the theoretical positioning errors for $\sigma_\theta = 0.3°$ and $\sigma_R = 1.5$ m, for 1 AoA + 1 TDoA.

When only one AoA and one TDoA are used, the error increases more rapidly with respect to the cases analyzed previously, as the distance between the target and the receiving nodes increases. This is due to i) the elimination of one receiver, which provides the reduction of the information available for the target position estimation, and ii) compared with the results obtained with 2 AoA, the replacement of the AoA with the TDoA measure, which is characterized by lower accuracies.

Case 2: 2 AoA + 1 TDoA

If two receivers, each one with at least two elements, are available, it is theoretically possible to carry out three different measurements: two of AoA and one of TDoA.

Even this time, the system is overdetermined, and it is not possible to solve directly the system. Therefore, we must rely on the sub-optimal solution described before. The basic steps are the same seen for the previous cases, the only thing that changes is the definition of the matrix **H**.

We can indicate with $\mathbf{H}_{\mathrm{AoA}}$ the matrix containing the direction cosines related to the AoA measures as defined in the equation (2.87), and with $\mathbf{H}_{\mathrm{TDoA}}$ the matrix containing the direction cosines related to the TDoA measures as defined in the equation (2.52).

Therefore, the matrices $\mathbf{H}_{\mathrm{AoA}}$ and $\mathbf{H}_{\mathrm{TDoA}}$ have a number of row equal to two, because we operate in the XY-plane, and a number of columns equal to $\mathrm{N}_{\mathrm{AoA}}$ and $\mathrm{N}_{\mathrm{TDoA}}$, respectively, namely to the number of receivers that are able to measure an angle and to the number of pairs of receiver that can discriminate a time difference of arrival.

The generic form of the matrix **H** is therefore defined as follows

$$\mathbf{H} = [\mathbf{H}_{AoA} \quad \mathbf{H}_{TDoA}]^T \tag{2.110}$$

of dimensions (N_{AoA} + N_{TDoA}) x 2, that in this case is 3 x 2.

As asserted before, when we have non-homogeneous measurements (hybrid techniques AoA/TDoA) it is preferable to use the ML method, therefore we analyzed the results only for this solution.

In Figure 2.22, we reported the performance for $\sigma_{\theta_1} = \sigma_{\theta_2} = 0.3°$ and $\sigma_{\theta} = 1.5$ m.

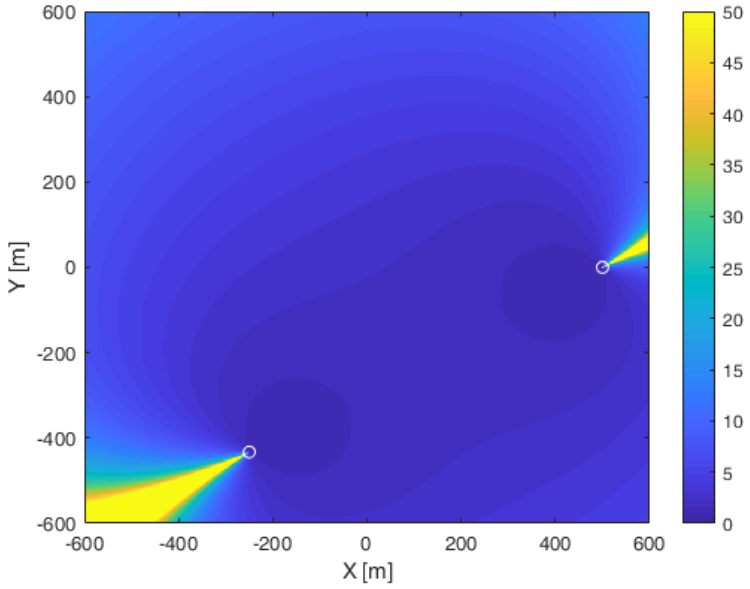

Figure 2.22. Standard deviation of the theoretical positioning errors for $\sigma_{\theta_1} = \sigma_{\theta_2} = 0.3°$ and $\sigma_{\theta} = 1.5$ m, for 2 AoA + 1 TDoA.

Comparing this figure with Figure 2.20, we can notice that the accuracies achieved with 2 AoA and the hybrid solution (2 AoA + 1 TDoA) are almost similar in the area of interest. The main advantage produced by the introduction of one measure of TDoA is the elimination of the ambiguity in the definition of the target position when it lies in the line which connects the two nodes.

Since in our tests we usually operate far from the receivers, the increase in complexity generated by the use of TDoA measurements when 2 measures of angles are already available is not useful for our purposes.

In conclusion, in the following analysis, we will use 1 AoA + 1 TDoA when only three antennas are available for the acquisition of the measures of interest, whereas we will use only 2 AoA when four surveillance antennas can be exploited.

2.3.3 Processing scheme

The processing scheme of the Passive Source Location system is presented in Figure 2.23.

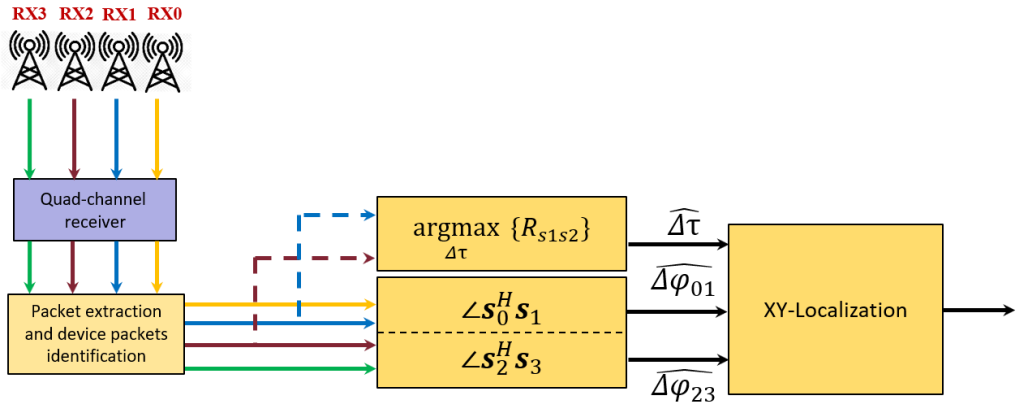

Figure 2.23. Processing scheme of the Passive Source Location.

This is the most general representation of the processing scheme for a PSL system. In fact, all the possible measurements that can be estimated with two receiving nodes are shown in this figure, namely two measures of AoA and one measure of TDoA. Since we use the same receiving channels for both the PBR and the PSL, if the reference signal for the passive radar is directly acquired from the AP, we can use only three surveillance antennas, and so the localization with the PSL can be performed only by combining one measure of AoA and one of TDoA, and the related processing scheme is obtained from Figure 2.23 by eliminating the additional measure of AoA. The other combination presented in Table 2 can be derived similarly.

In this scheme, as an example, we have explicitly written an expression for the TDoA estimation. Obviously, this can be changed according to the specific technique chosen in each particular case.

Comparing Figure 2.23 with the scheme of the PBR in Figure 2.4, it is evident that the device-based strategy is characterized by a lower complexity, and in turn the final localization is obtained with a lower computational cost. In fact, the higher SNR conditions of the direct signals transmitted by the device provide the possibility to avoid all the steps required for the PBR for the extraction of the target echoes, since the target position can be estimated directly on the received signals.

Therefore, after the acquisition of the signals present in the selected Wi-Fi channels, the packet extraction and the next classification of all the found packets based on their source address, the device transmissions are separately processed for the extraction of the measures of interest (TDoA/AoA). Finally, the localization in the XY-plane can be performed by using the desired positioning techniques.

Chapter 3
Comparative analysis of PBR and PSL

In Chapter 2, the PBR and PSL have been characterized in detail. At this point, it is interesting to analyze their capability to localize a target.

Therefore, in this Chapter, localization performance and characteristics of the two localization techniques are analyzed and compared, aiming at their joint exploitation inside sensor fusion systems. With two receiving nodes, the Passive Source Location can combine two measures of Angle of Arrival (AoA) or the AoA and the Time Difference of Arrival (TDoA) measures of the device transmissions to achieve the target position. The Passive Bistatic Radar, instead, exploits the AoA and the bistatic range measures of the target echoes. This means that for the PBR one node is sufficient to provide the target position estimates.

The results obtained on experimental data show that the Wi-Fi emission-based strategy is always effective for the positioning of human targets holding a Wi-Fi device, but it has a poor localization accuracy and the number of measured positions largely depends on the device activity. In contrast, the passive radar is only effective for moving targets and has limited spatial resolution, but it provides better accuracy performance, thanks to the possibility to integrate a higher number of received signals. These results also demonstrate a significant complementarity of these techniques, through a suitable experimental test, which opens the way to the development of appropriate sensor fusion techniques.

As mentioned above, the analysis is performed through the evaluation of the results obtained on experimental data. For this reason, the equipment and the experimental setup will be presented in Section 3.1, while the performance analysis will be discussed in the last two sections, where the relationship between data traffic conditions and performance is analyzed in Section 3.2.2 and the performance comparison of the proposed techniques is presented in Sections 3.2.3 and 3.3.2.

3.1 Experimental setup and equipment description

3.1.1 Acquisition site and geometry

The acquisition campaigns described in this thesis have been performed in an outdoor environment, specifically in a parking area located in the proximities of POMOS (Polo per la Mobilità Sostenibile) building in Cisterna di Latina, Italy.

During the acquisition measurements, we built on the ground a square grid of nine points, spaced 15 meters each other in both directions, as sketched in Figure 3.1.

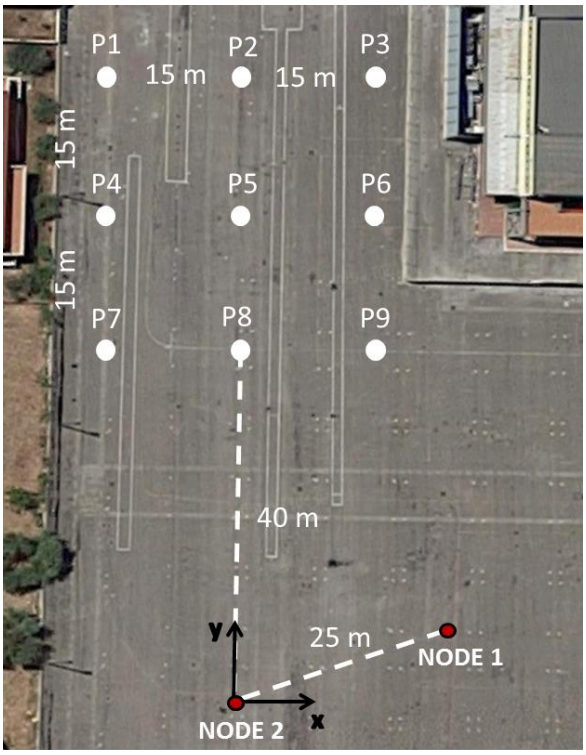

Figure 3.1. Acquisition grid and distances between the different elements.

These points have been used for the calibration stage and for comparing the estimated positions with the ground truth, as reported in Figure 3.15 and Figure 3.31.

As shown in Figure 3.1, two nodes, each one containing two antennas, have been dislocated to cover an area of interest. The antennas can be either receiving or transmitting, depending on the desired configuration of the antennas.

The node indicated with the label 'NODE 2' in Figure 3.1 has been placed at a distance of 40 meters with respect to the central element of the third row of the grid (P8). A second node, indicated as 'NODE 1' in Figure 3.1, has been located at a distance of 25 m from 'NODE 2'.

The position of the antenna pair which composes the second node has been also assumed as the origin of the local X-Y system of coordinates used to represent the obtained localization measures on the plane; specifically, Y-axis is oriented along the line connecting the two antennas which compose the 'NODE 2' with the central row (in vertical) of the grid. X-axis is oriented towards right in the represented scenario. As an example, the grid elements horizontally displaced in the closest row with respect to the 'NODE 2' are identified, from left point to right point, with the following coordinates in the described reference system: (-15,40) m, (0,40) m and (15,40) m. The coordinates of the remaining 6 points of the grid can be derived similarly.

With reference to the pointing of these two nodes, the antennas of the 'NODE 2' are oriented so as to point towards Y-axis, while those of 'NODE 1' have a misalignment of about -20° with respect to Y-axis pointing (so as to be pointed towards the grid, as easily perceivable by the geometry sketched in Figure 3.1).

The antennas of the two nodes are not aligned along X-axis.

For the calibration stage, we put an Access Point on each different point of the grid, and we recorded few seconds of transmission.

The AoA and the TDoA have been evaluated for each point and then they have been compared with the ground truth. The Minimum Mean Square Error (MMSE) approach has been used to estimate the errors to be compensated for. As it is apparent, the correction of the angle error can be applied to both the techniques, while the TDoA offset is related to the length of the used cables.

In the following sub-sections the main features of the used devices are described.

3.1.2 Access Point

A commercial Access Point (AP), DAP-1160 by D-LINK, has been used as cooperative source of Wi-Fi signals, Figure 3.2.

Figure 3.2. D-LINK DAP-1160 Access Point.

It is based on the IEEE 802.11 Standard, [28], it is compliant with IEEE 802.11g standard and can operate both as router and access point. The DAP-1160 is equipped with a 2dBi Gain detachable omnidirectional antenna with RP-SMA connector. Thanks to its easy-to-use web-based management interface, it is possible to configure the AP main parameters, according to the different tests to be performed. For example, it is possible to set the transmit output power, in percentage with respect to the maximum value (100%, 14dBm typical for 802.11g mode): allowed percentages are 50%, 25% and 12.5%. It is also possible to set the transmitting channel in the 2.4GHz band (from 1 to 13); this option is especially useful during experimental tests performed in different scenario, since it allows to select a transmission channel with no or reduced interference level from already existing Wi-Fi transmissions. Moreover, it is possible to configure the transmission modulation, for example DSSS, OFDM and so on, and other parameters such as beacon interval and beacon duration.

3.1.3 Receiving system

In this sub-section, the main elements of the used receiving system are described. Specifically,

- Wi-Fi antennas
- multi-channel receiver: NI USRP-2955

3.1.3.1 Wi-Fi antennas

Commercial Wi-Fi antennas have been used to acquire data transmitted by devices and AP during the performed tests. Specifically, two different antenna models have been tested:

- D-LINK ANT24-1200
- TP-LINK TL-ANT2409A

3.1.3.1.1 D-LINK ANT24-1200

The first considered antenna model is ANT24-1200, by D-LINK; it is a rectangular panel antenna, very light (190 g) and small sized (33 x 9.3 cm), see Figure 3.3.

Figure 3.3. Wi-Fi antennas: D-LINK ANT24-1200.

The main features of this antenna are summarized in the following, while Figure 3.4 shows the radiation diagrams provided by the manufacturer, horizontal and vertical, respectively in Figure 3.4(a) and Figure 3.4(b). Finally, Figure 3.5 shows the configuration of one couple of antennas, as previously described (specifically, the photo is referred to the couple identified as ‘NODE 1’, but the same configuration has been used for the ‘NODE 2’). The two antennas are horizontally displaced, with a distance of 12 cm between the respective phase centers, aiming at reducing angle ambiguities.

ANT24-1200 main features:

- frequency range: 2.4-2.5GHz
- impedance: 50 Ω
- gain: 12dB
- horizontal half power beamwidth: 80°
- vertical half power beamwidth: 23°
- front-to-back ratio: 15dB
- admitted power (max): 20 W
- connector: SMA (female)

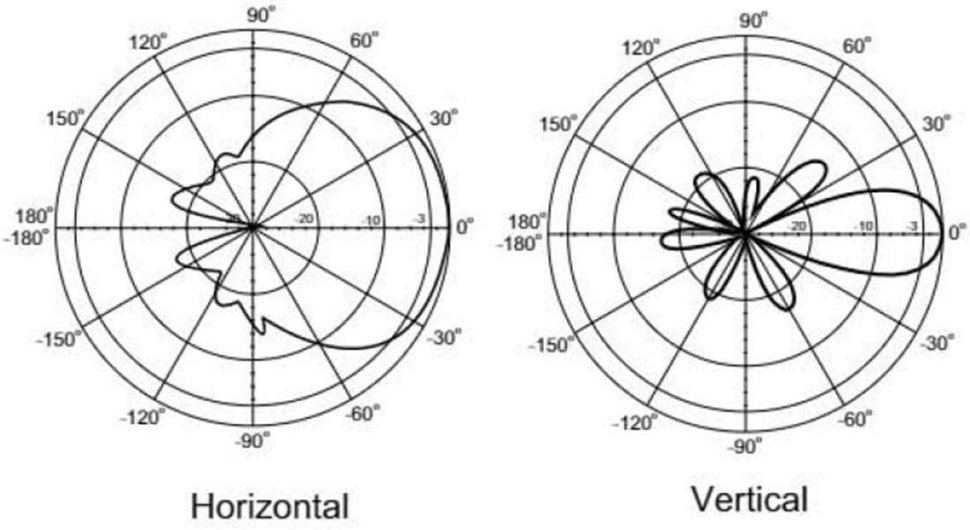

Figure 3.4. D-LINK ANT24-1200: radiation pattern, horizontal and vertical.

Figure 3.5. ANT24-1200: displaced configuration for a couple of antennas (‘NODE 1’).

3.1.3.1.2 TP-LINK TL-ANT2409A

The second considered antenna model is TL-ANT2409A, by TP-LINK; it is a square antenna, small sized (about 12 x 12 cm), see Figure 3.6.

Figure 3.6. Wi-Fi antennas: TP-LINK TL-ANT2409A.

The main features of this antenna are summarized in the following, while in Figure 3.7 the radiation diagrams are reported as provided by the manufacturer, horizontal and vertical, respectively in Figure 3.7(a) and Figure 3.7(b). Finally, Figure 3.8 shows the configuration of one couple of antennas, as previously described (specifically, the photo is referred to the couple identified as ‘NODE 1’, but the same configuration has been used for the ‘NODE 2’). The two antennas are horizontally displaced, with a distance of 14 cm between the respective phase centers, aiming at reducing angle ambiguities.

TL-ANT2409A main features:

- frequency range: 2.4-2.5GHz
- impedance: 50 Ω
- gain: 9dB
- horizontal half power beamwidth: 60°
- vertical half power beamwidth: 76°
- Return Loss: -10dB max
- admitted power (max): 1 W
- connector: RP-SMA (male)

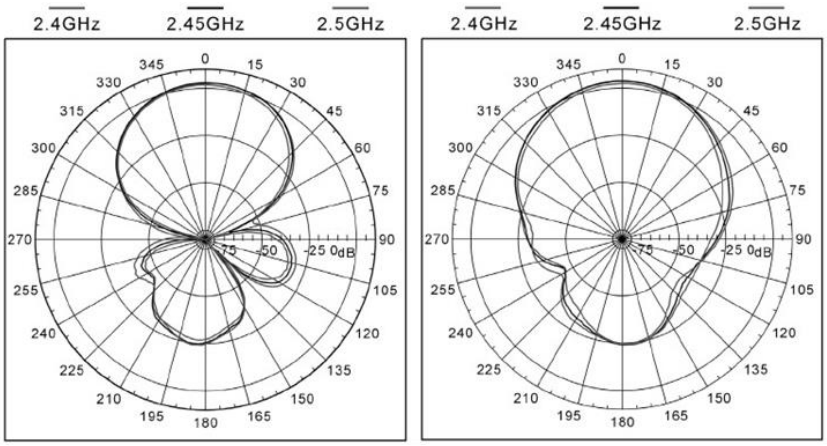

(a) (b)

Figure 3.7. TP-LINK TL-ANT2409A: radiation pattern, horizontal (a) and vertical (b).

Figure 3.8. TL-ANT2409A: displaced configuration for a couple of antennas (‘NODE 1’).

3.1.3.2 Multi-channel receiver: NI USRP-2955

The receiver used to collect and store data received with the four Wi-Fi antennas is a Software Defined Radio (SDR) platform providing an integrated hardware-software solution for demonstrators or prototypal systems. Specifically, the device is the NI USRP-2955, by National Instruments (Figure 3.9). It is a 4-channel tunable receiver, able to collect and simultaneously sample signals (up to a maximum rate of 100 MS/s) in the frequency range 10 MHz – 6 GHz.

Figure 3.9. NI USRP-2955.

The receiver is also equipped with a GPS-disciplined oscillator (GPSDO) that allows to lock the device internal clock to a GPS reference signal, so as to synchronize the receiving channels using the timing information provided by GPS. It is also possible to set via software the gain of each receiving channel, independently by other three channels, in the range 0-95dB, with 1dB step.

The main features of the receiver are summarized in the following:

- number of channels: 4
- frequency range: 10 MHz to 6 GHz
- frequency step: < 1 KHz
- gain range: 0 dB to 95 dB, in 1 dB steps
- maximum input power (P_{in}): +10 dBm
- frequency accuracy: 2.5 ppm
- maximum instantaneous real-time bandwidth: 80 MHz
- maximum I/Q sample rate: 100 MS/s
- analog-to-digital converter (ADC) resolution: 14 bit
- ADC spurious free dynamic range (SFDR): 88 dB
- Noise Figure (NF):
    - < 5 dB, 10 MHz to 3 GHz

- < 4 dB, 3 GHz to 5 GHz
- < 8 dB, 5 GHz to 6 GHz

Figure 3.10 shows a typical configuration for this kind of receiving systems, with the interface (MXIe adapter) between the USRP and the host PC.

Figure 3.10. NI USRP-2955: URSP RIO system components.

The USRP is programmed and controlled via LabVIEW (Laboratory Virtual Instrument Engineering Workbench) software, developed by National Instruments. LabVIEW is system-design platform and development environment for a visual programming language. It runs on the host PC, which also provides the storage environment for acquired data.

As an example, Figure 3.11 and Figure 3.12 show two user interfaces (front panels) of codes for the test of signal levels and for data acquisition, respectively.

In particular, during the acquisition campaign the first step is to use the interface presented in Figure 3.11 to check the signal levels, in order to understand the possible presence of errors in the receiving chain (if some signal is not shown in the relative plot window) and conveniently set the different gains of each receiving channel.

After this preliminary operation, the second interface is used to acquire the signals in the selected Wi-Fi band.

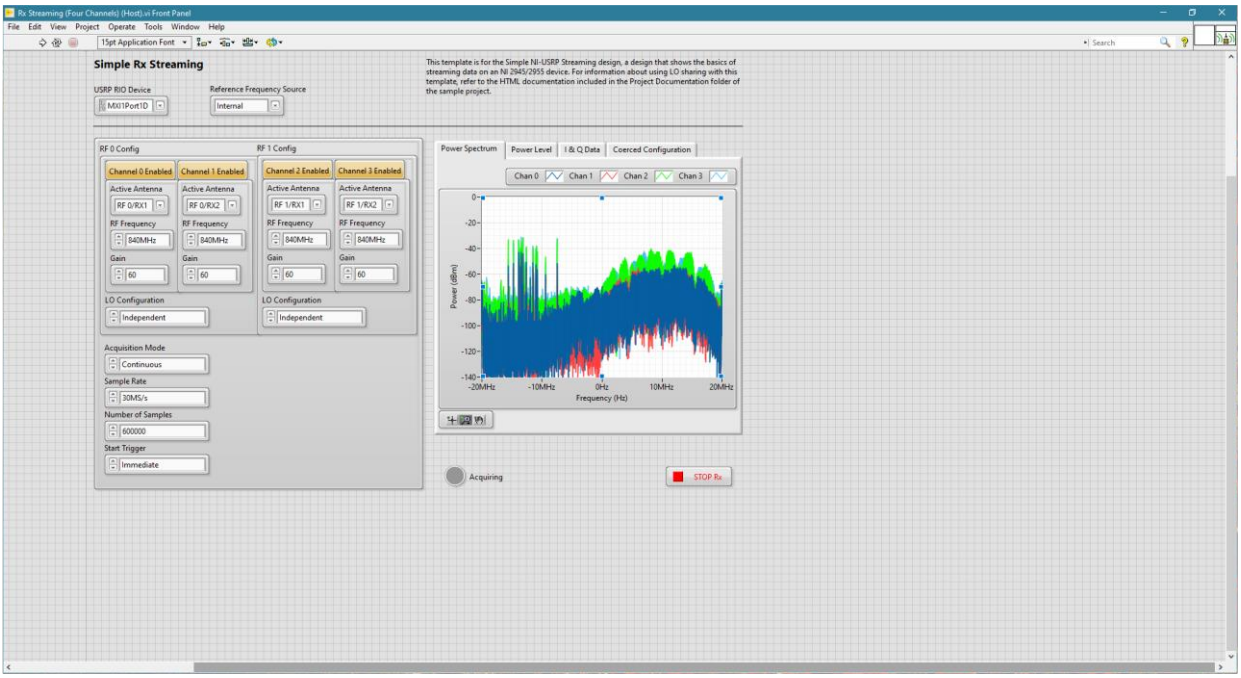

Figure 3.11. NI USRP-2955: LabVIEW interface for signal test.

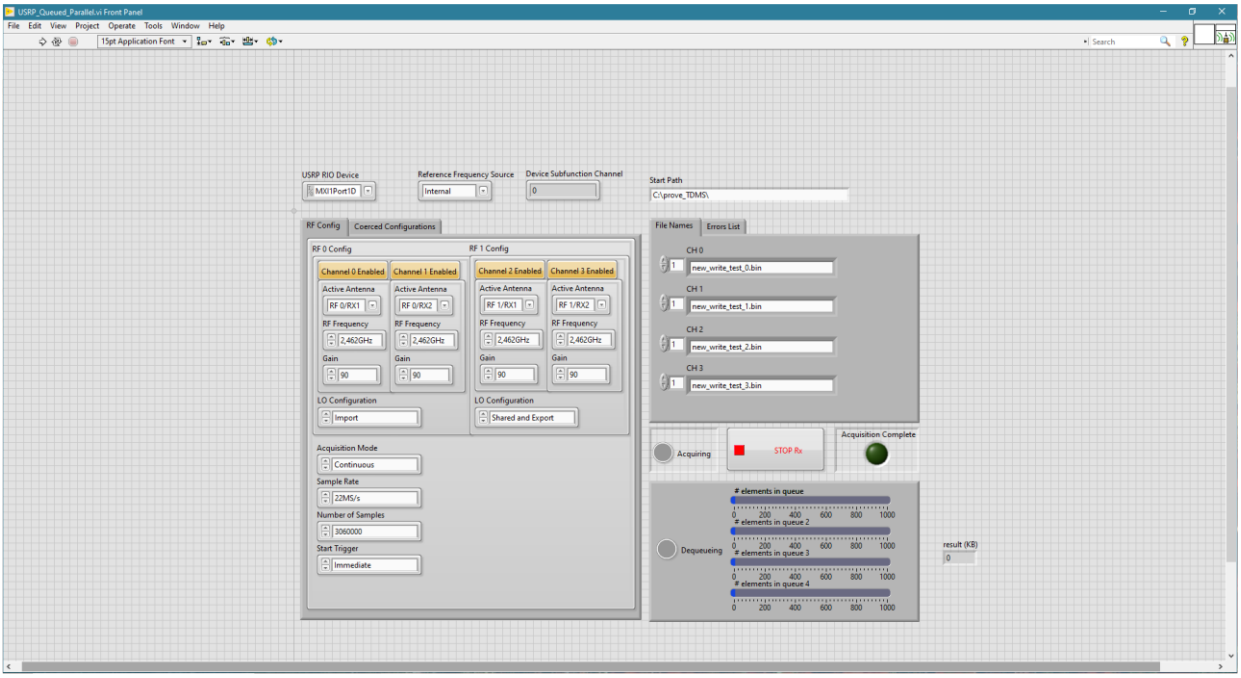

Figure 3.12. NI USRP-2955: LabVIEW interface for data acquisition.

As is apparent, during configuration stage the main acquisition parameters are specified via software, for example the number of receiving channels to be acquired, the center frequency of each channel, the desired sampling frequency, the gain for each channel. Data from the sampling of each channel are stored as binary files (*.bin* extension) on the memory of the host PC, and are ready for the post-processing, performed off-line with Matlab®.

3.1.4 Antenna configurations

With respect to the antennas, we have used two different configurations based on the number of antennas available for the specific purpose. In fact, as explained in the USRP description, we have the possibility to exploit four receiving channels, and so we can use up to four receiving antennas. This number is reduced if one of the four channels of the USRP is dedicated to the acquisition of the reference signal.

In particular, the first configuration used in our tests exploits three surveillance antennas and the reference signal is spilled directly from the Access Point used as transmitter of opportunity, as displayed in Figure 3.13.

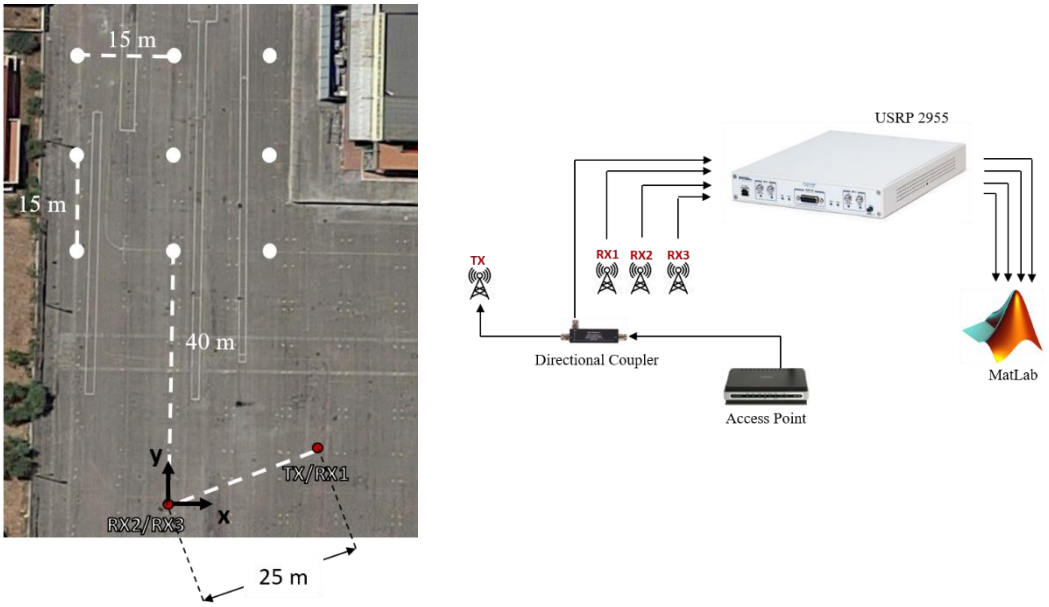

(a) (b)

Figure 3.13. Experimental setup (3 surveillance antennas): (a) scenario and antenna configurations, (b) receiving channel configuration.

In particular, as can be seen in Figure 3.13(a), two receiving antennas were located very close to each other, whereas the third one was positioned 25 m far from them, near a transmitting directive antenna connected to the AP through a directional coupler. The second output of the coupler was linked to the fourth channel of the USRP, as explained before and displayed in Figure 3.13(b). Therefore, the second antenna contained in 'NODE 1' in Figure 3.1 is a transmitter and not a receiving antenna.

With these three antennas, a human target (carrying an active mobile device) moving in the observed area can be located in 2D by exploiting the signals emitted by their devices (PSL sensor). Specifically, the two closely spaced antennas (RX2 and RX3) can be used in interferometric mode to estimate the signal AoA, whereas the TDoA between the signals collected at antenna RX1 and RX2 provide the hyperbola that contains the target location. As apparent, using together the two measurements, two equation can be written in the two spatial unknowns (target x and y coordinates) so that the 2D target position can be obtained.

However, this setup also allows exploiting the signals emitted by the Wi-Fi AP that are scattered by the human targets and reach the two closely spaced antennas (RX2 and RX3). In this case, the AP acts as the

illuminator of opportunity of a WiFi-based PBR; moreover, the human target localization does not depend on carrying a Wi-Fi device, since they are not required to emit their own signals to be localized.

In detail, the passive radar can estimate the target position through the measure of the Angle of Arrival (AoA) and the bistatic range, both estimated by the closest antennas (RX2 and RX3 in Figure 3.13). In this case, the fourth channel is used to collect a reference copy of the transmitted signal that allows measuring the bistatic range.

With both the device-based system and the passive radar system, three receiving channels are exploited to obtain two measurements (respectively AoA and TDoA, and AoA and bistatic range), which are finally used to solve the 2D localization system. The two types of received packets can be easily discriminated by decoding their bits, where we can find both source and destination addresses, so that they are exploited in the correct way.

In the second configuration, the four receiving channels of the USRP are completely occupied by the surveillance antennas. This means that a higher number of measures can be estimated, but at the same time, the possibility to acquire a copy of the reference signals is lost.

Therefore, four receiving antennas, divided in two couples, have been considered in the described acquisition campaigns, as can be seen in Figure 3.14.

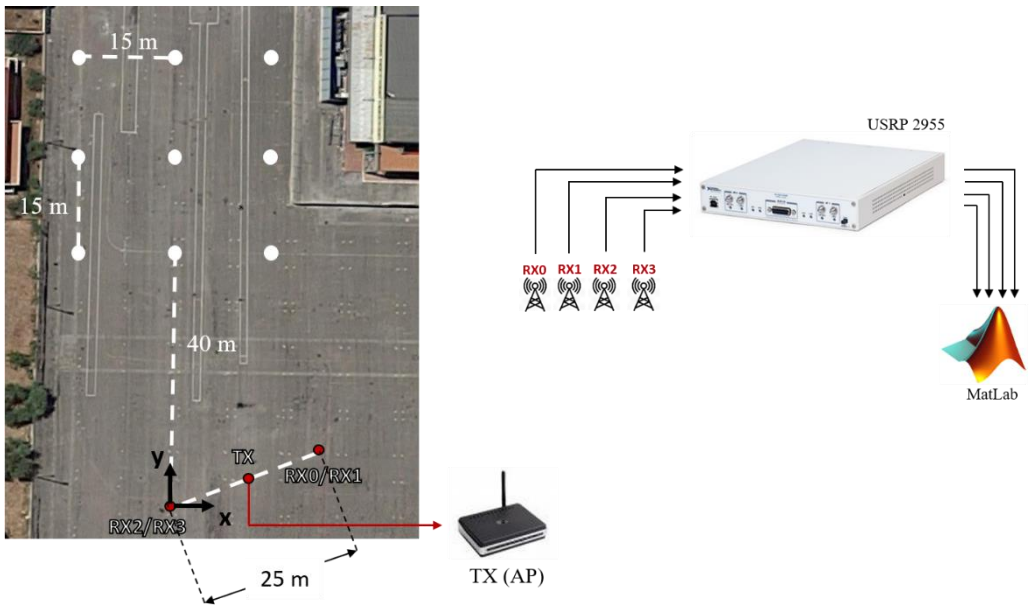

Figure 3.14. Experimental setup (4 surveillance antennas): (a) scenario and antenna configurations, (b) receiving channel configuration.

Two out of the four antennas, indicated in Figure 3.14 as ‘RX2/RX3’, have been placed very close one another, in the place occupied by the ‘NODE 2’ in Figure 3.1. As shown in the figure, a second couple of receiving antennas is present: these two antennas are identified as ‘RX0/RX1’, located at a distance of 25 m from antennas ‘RX2/RX3’ and not aligned along X-axis. ‘RX2/RX3’ are oriented so as to point towards Y-axis, while ‘RX0/RX1’ antennas have a misalignment of about -20° with respect to Y-axis pointing (so as to be pointed towards the grid, as easily perceivable by the geometry sketched in Figure 3.14).

In this configuration, the transmitter is the AP omnidirectional antenna (a directive antenna has not been used), and the reference signal has not been acquired. This means that the signals emitted by the AP must be reconstructed from a surveillance antenna in post-processing operations.

3.2 Low data traffic for PSL sensor

The results presented in this Section are discussed in [41]-[43].

3.2.1 Acquisition campaign description

The illuminator of opportunity of the passive radar system was the commercial wireless Access Point presented in Section 3.1.2, which was connected to a transmitting directive antenna. Its transmissions were also used to establish the communication between AP and mobile devices. The AP was configured to transmit in channel 4 of the Wi-Fi band (carrier frequency equal to 2.427 GHz). The beacon interval was set to 3 milliseconds, that defines the Pulse Repetition Time (PRT) of the passive radar. Under these conditions, the 3 ms beacon rate provides a very high number of packets that can be exploited to locate the target. Moreover, the AP was set with a transmission rate of 1 Mbps (namely modulation and coding schemes are respectively DBPSK and 11-chip Barker sequence).

For this experimental campaign, the acquisition system was characterized by three receiving channels, connected to three surveillance antennas (D-Link ANT24-1200) used to acquire the signals emitted by both AP and Wi-Fi devices carried by the human targets. In addition, we set an additional gain for each USRP receiving channel in order to have a comparable signal level. The gains are set to compensate the attenuations due to the employment of different length cables. In fact, as displayed in Figure 3.15, two receiving antennas were located very close one another (with spacing of 12 cm between them), near the receiving system, and 40 m from the side of the square grid, whereas the third one was positioned 25 m far from them, close to the transmitting antenna.

As shown in Figure 3.15, Cartesian reference system is considered with origin in the midpoint of RX2-RX3 and axes aligned with the sides of the grid.

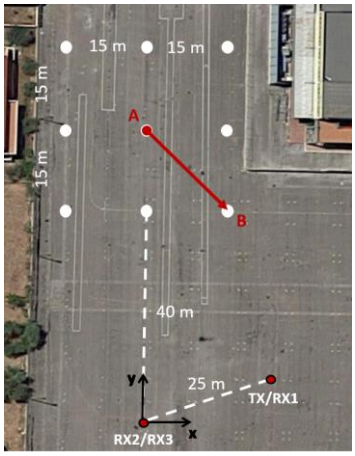

Figure 3.15. Target localization and tracking experiment (Test 1).

The acquired signal was sampled with a sampling frequency of 22 MHz, then it was stored and processed off-line. The first processing operation is the classification of the acquired packets, based on the possible transmitting source, to perform the association between packet and target (or AP).

We carried out a test that could be interesting for both the techniques described before and could show the analogies and the complementarity between them. In this test, as shown in Figure 3.15, a target with an active mobile device (Asus Zenfone 2) moves from the central point of the grid, namely the point A in the figure, and arrives to the point B. The acquisition duration is about 28s. The target takes 20s to reach point B, and then he stops there for about 8s. It is worth mentioning that the path sketched in Figure 3.15 along the grid is purely nominal.

During the whole 28 seconds, the user attempts connecting to the Wi-Fi router used as illuminator multiple times, but there is not an ongoing continuous data upload, therefore the device-emitted waveforms occupy the medium for a short time and only a few packets sent by the mobile device are collected by the three receive antennas.

While a continuous upload would increase the emissions from the device, this condition appears to be largely more representative of a typical practical case, where a specific device is not strongly loading the network and the router is able to accept many connections.

3.2.2 Relationship between data traffic conditions and performance

The aim of this section is to investigate the relationship between data traffic condition and performance of the proposed localization techniques based on Wi-Fi signals. In fact, the performance of both systems is closely linked to the signal-to-noise ratio (SNR) of the data used for the estimation, and accordingly, to the signal energy and the number of samples available. As it is apparent, the higher the signal energy and the number of signal samples, the better the performance. In detail, the number of samples depends on i) the Wi-Fi packet length, and ii) the number of packets occurred in a specific time interval, so that a time integration operation might be potentially performed. This means that the best possible situation is to have a big number of long packets for the estimation of the parameters of interest.

Nevertheless, these characteristics are related to the actual communication activity between AP and devices. In fact, as defined in the IEEE 802.11 Standard, [28], the packets length changes according to the packet type (beacon, probe request, authentication, etc.), therefore it is possible to have available even very short signals. In addition, in a normal communication system, multiple users, e.g. APs and devices, could share the same channel. Therefore, they cannot transmit simultaneously, and the number of Wi-Fi packets transmitted by each of them depends on the specific case. It is evident that when the device uploads data, the transmission rate of the AP decreases and the performance of the passive radar worsens, while the device-based technique performs better. In contrast, during download activities, the AP transmits more packets, thus the passive radar provides the best performance. These considerations provide a first proof of the complementarity between the described approaches, that makes them suitable for a possible fusion in an integrated system, which provides the position estimation of targets during the whole observation time, regardless the traffic conditions.

In this specific case, the two techniques are characterized by different transmission rates of the employed signals, as shown in Figure 3.16. In fact, while the passive radar can exploit the periodical beacon transmission of the AP (approximately each 3 milliseconds), the device-based approach has available only the signals sent during the device upload activities. In particular, in this work, we only analyzed connection activities between the AP and the mobile device, so that there is a very limited upload activity from the device, which affects the performance of device-based techniques.

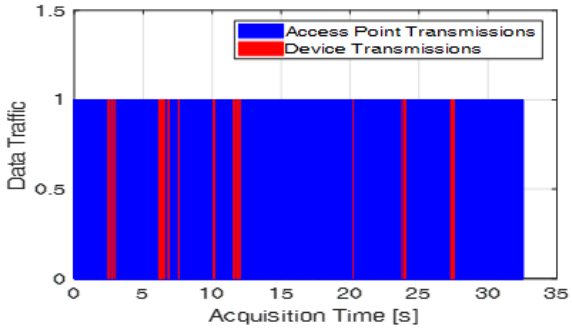

Figure 3.16. Data traffic conditions for the proposed test.

In order to understand the characteristics of these strategies, we investigate the relationship between AoA estimation accuracy and energy features of the exploited signals. The analysis has been carried out on experimental data, acquired during appropriate measurement campaigns.

In particular, for the device-based localization, the study has been performed through the estimation of the parameters of interest using different packet lengths. The basic idea is to emulate the decrease of the SNR, in order to observe its influence on the localization accuracy.

For the passive radar, in addition to the employment of less samples, as for the device-based localization, the effect of the reduction of the Pulse Repetition Frequency (PRF) has been investigated. In fact, it is typical that a big number of echo packets can be integrated, so that a reasonable power can be collected from the target, which in turn provides an accurate position measurement. The number of pulses available depends on the Beacon Interval (BI) that is defined as the time spacing from consecutive beacons, which are packets periodically sent by the Access Point (AP). However, when the BI decreases, the nice performance of the PBR

tends to degrade. This situation is typical of loaded networks, where the AP has to share the medium with other stations, which might also transmit with a high transmission rate. In this work, we show the result of controlled localization experiments that allow us to analyze this degradation. An analysis of some important effects of this type was already provided in [18]. In this work, we analyze the impact of the longer BI not only on the target detection, but also on the accuracy of the measurements and finally on the 2D localization. In this case, limit values are suggested for practical applications.

3.2.2.1 Accuracy of device-based AoA measurements

Both device-based and passive radar target positioning techniques exploit the AoA measurement, obtained by the phase difference between the closely spaced antennas RX2 and RX3 in Figure 3.15. The former extracts the AoA of the signals emitted by the Wi-Fi devices, the latter the AoA of the AP signal scattered by the human targets towards the two closely spaced antennas.

Therefore, it is of high interest to compare the accuracy obtained by the two techniques. Unlike in the FM-passive radar case, it is not useful to attempt using multiple frequencies to increase the performance, [44]. In contrast, it is quite interesting to investigate the relationship between received signal energy and the AoA measurement accuracy. While a direct monotonic relationship is expected under ideal conditions (disturbance consisting of only constant level white Gaussian thermal noise), the practical accuracy also depends on packet distortion due to channel conflicts, interferences, etc… If the performance only depends on signal energy, it is quite essential to understand the relative number of packets available for the Wi-Fi device-based technique and for the Wi-Fi passive radar. Similarly, also the number of samples present inside the single packet is quite essential to obtain a global energy measure.

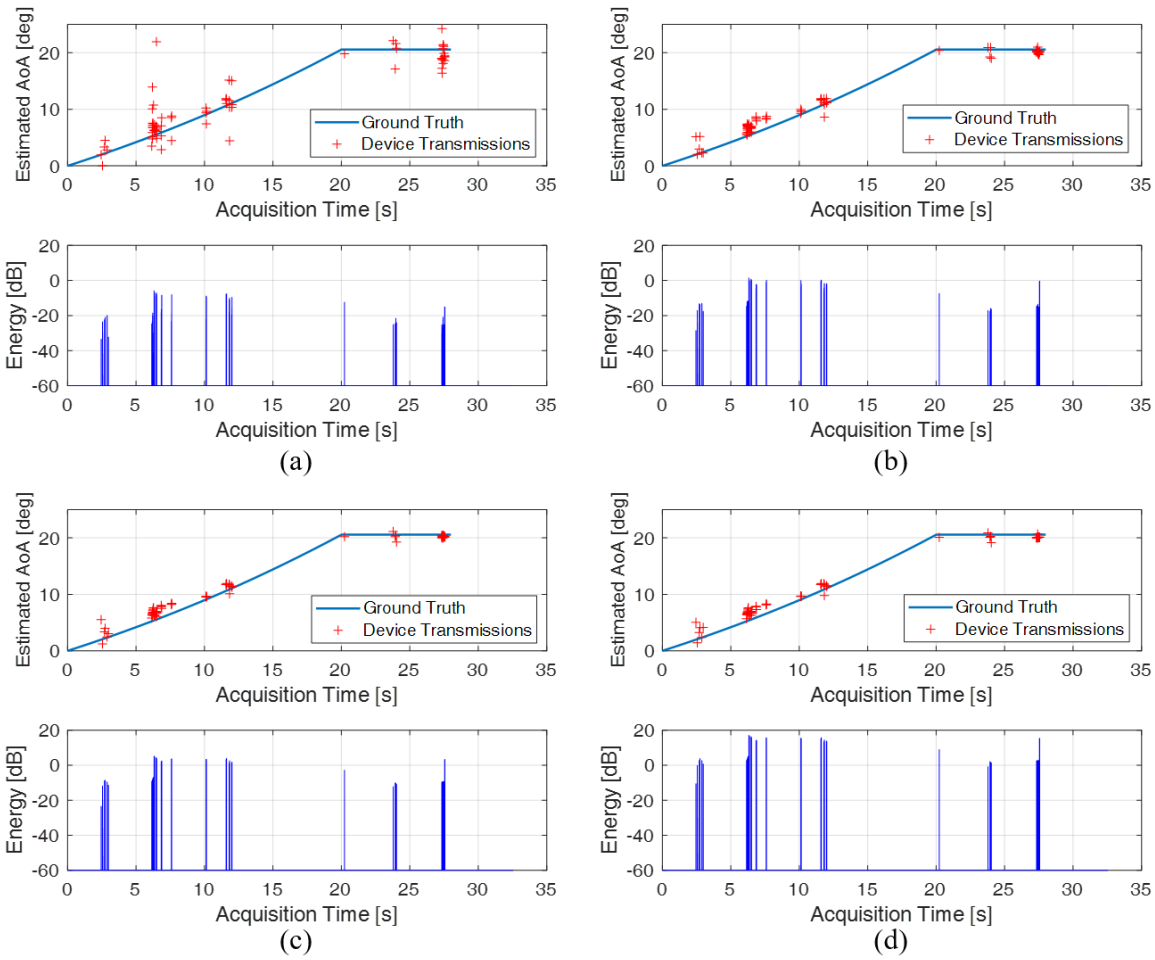

Figure 3.17. Comparison between estimated AoA and the ground truth for: (a) 1, (b) 8, (c) 23 and (d) 375 samples, for the device-based technique.

We first analyze the estimate of the AoA obtained by the device-based technique. The estimates obtained using the individual packets are reported in Figure 3.17 (red crosses), together with the ground truth (blue solid line). The latter is obtained by assuming that the target was moving with a uniform linear motion along the assigned path (see Figure 3.15). To assess the relationship between accuracy and signal energy, subplots (a), (b), (c) and (d) are obtained by using only the first L samples of each received packet, being respectively L = 1, 8, 23 and 375.

In the lower subplot, also the corresponding energy level $E = \sum_{l=1}^{L} |s_l|^2$ is reported, for comparison, being s_l the l-th sample.

For direct comparison, Figure 3.18 shows the AoA estimation error as a function of the time instant t_k, $e(t_k) = \hat{\theta}(t_k) - \theta(t_k)$, where $\hat{\theta}(t_k)$ is the estimated angle of arrival, whereas $\theta(t_k)$ represents the ground truth at the same time. As in Figure 3.17, we report below the corresponding energy level for the single estimation.

We can see that, as expected, the accuracy increases when the number of samples, and consequently the energy level of the employed signal, increases. In addition, since we are in high SNR condition, the estimation provides good performance with just L=8 samples.

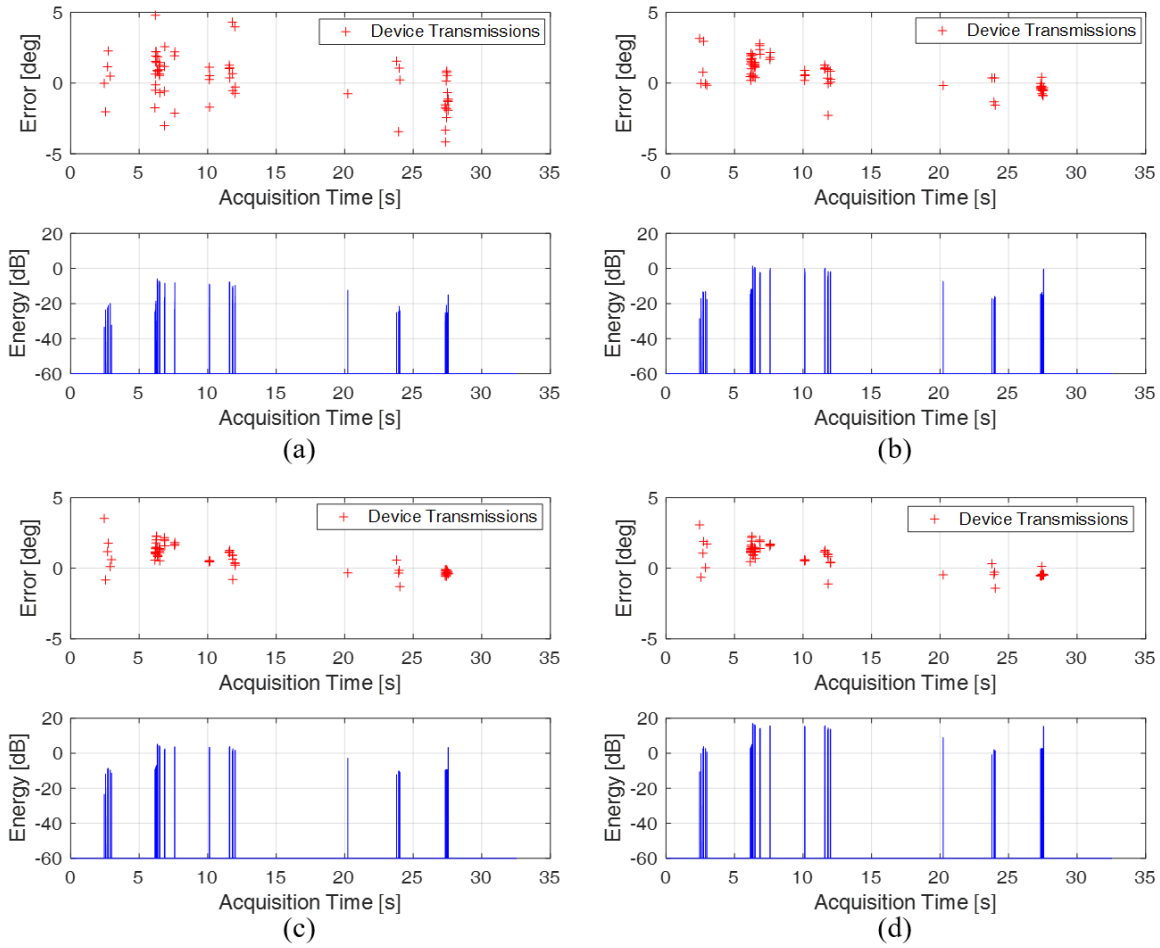

Figure 3.18. Difference between the estimated AoA and the ground truth for: (a) 1, (b) 8, (c) 23 and (d) 375 samples, for the device-based technique.

From the figures above, it is clear that the signal energy is high and the estimation errors are limited even using a few samples per packet. It is interesting to analyze the impact of the degradation of the Signal to Noise Ratio (SNR) on the performance. To this purpose, we deliberately inject white Gaussian noise to degrade the SNR by 10 dB and 20 dB. In order to perform a quantitative comparison of the performance obtained in different case studies we report in Table 3 the Root Mean Square Error (RMSE) evaluated along the whole target path, $rmse = \sqrt{\frac{1}{N}\sum_{k=1}^{N}|e(t_k)|^2}$, based on all the available packets N. In this case also longer packet fragments are considered, with L=1, 2, 8, 23, 94, 375, 1500, 6000 and 9000 samples.

Table 3. Root mean square errors achieved without additive noise, with 10dBs of additive noise and with 20dBs of additive noise, for the device-based technique.

Number of samples	No noise	+10 dB noise	+20 dB noise
1	8.5947	13.4757	21.1637
2	5.2420	8.9204	17.0615
8	1.3111	7.0607	10.3149
23	1.1745	1.6963	7.6186
94	1.1802	1.1947	4.8639
375	1.1764	1.1795	2.8863
1500	1.1784	1.1787	1.2412
6000	7.7847	7.7931	7.8306
9000	6.8102	6.8096	6.8132

Figure 3.19 shows the values of Table 3, making it evident that the RMSE decreases as the number of samples L increases up to the value of L=1500. After this value, a performance degradation is experienced, which has been verified to be caused by the possible presence of collisions between AP and device packets. In fact, notice that such RMSE increase start at the same value of L, independently of the SNR condition. This analysis suggests exploiting only the first short portion of each emitted packet in order to limit the probability of collision. However, we also observe that, when operating against a noisier environment, a larger number of samples L is required to achieve the lowest RMSE value, namely L=94 and L=1500 for SNR degraded respectively by 10 and 20 dB, instead of L=8 samples of the experiment conditions.

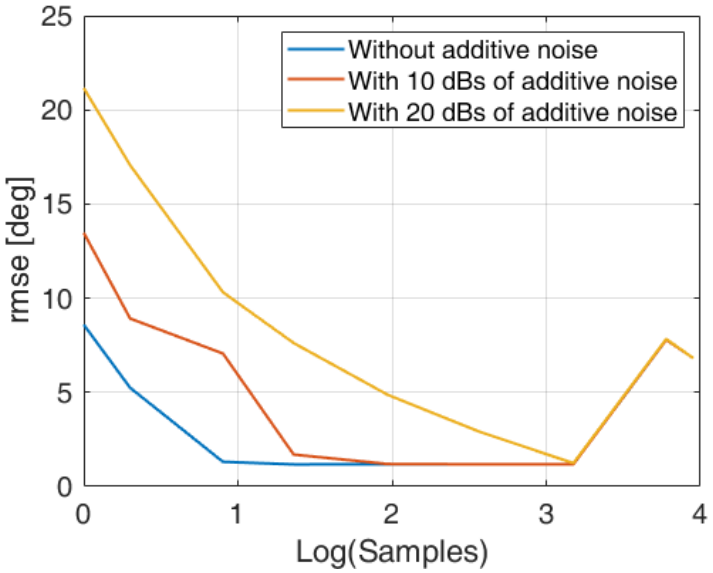

Figure 3.19. Comparison between the rmse values achieved without additive noise, with 10dBs of additive noise and with 20dBs of additive noise.

3.2.2.2 Accuracy of passive radar AoA measurements

A similar analysis is performed for the estimate of the AoA obtained by the passive radar technique. In this case, the AoA estimation is based on a train of coherently integrated packet echoes; therefore, the available signal energy depends both on the packet length and on the Packet Repetition Time (PRT).

The first study consists in the replication of the analysis presented for the PSL, namely the limitation of the number of samples exploited for each packet within the coherent integration time of 0.5 s. The results are reported in Figure 3.20 for 9000, 6000 and 375 samples. Table 4 compares the RMSE for the entire packet to the RMSE obtained using the first L= 9000, 6000, 1500 and 375 samples.

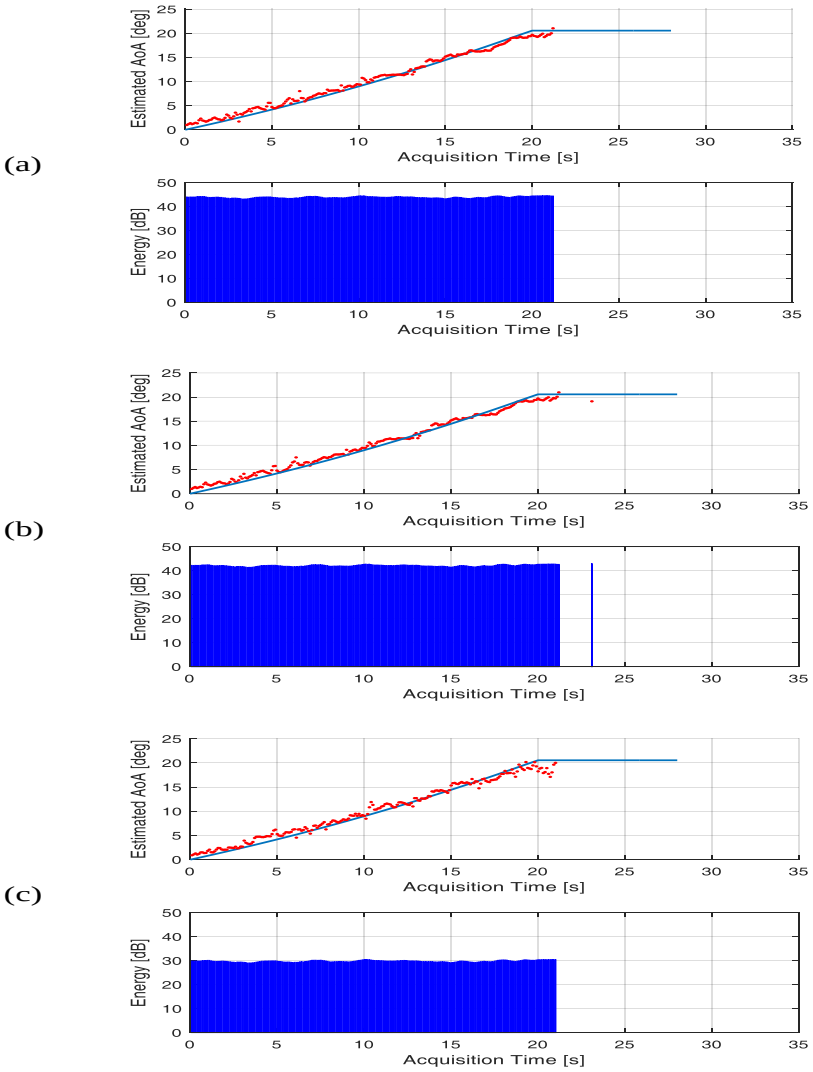

Figure 3.20. Comparison between estimated AoA and the ground truth for: (a) 9000, (b) 6000 and (c) 375 samples, for the passive radar technique.

It is evident that with 375 samples the AoA estimation is less accurate than for longer packet fragments due to the reduced SNR. However, Table 4 shows that the estimation accuracy is sufficiently robust to a reduction of the packet length until the number of samples L falls below 6000 and even in this case it outperforms the device-based technique, except for static targets.

Table 4. Root mean square errors obtained for the passive radar technique and different number of samples.

Number of samples	375	1500	6000	9000	Entire beacon
RMSE	0.9429	1.0011	0.7619	0.7591	0.7493

While this analysis has been performed using beacon transmissions by the AP, it shows that the passive radar technique can be effectively exploited against moving targets even in the presence of short data packets or using few collected samples to reduce processing hardware and costs.

An alternative way to degrade the available SNR is to increase the BI of the transmitted beacon. In this analysis, this behavior is emulated by discarding packets in the specific experimental dataset (where PRT was equal to 3 ms) in order to increase the average PRT to 12 ms, 24 ms and 48 ms.

The resulting AoA estimates (red dots), and their comparison with the ground truth (solid blue line), are shown in Figure 3.21. In addition, the overall processed energy of the received signal is presented in the lower plot.

In particular, when exploiting all the available packets within a 0.5 s coherent integration time, we obtain the results shown in Figure 3.21(a).

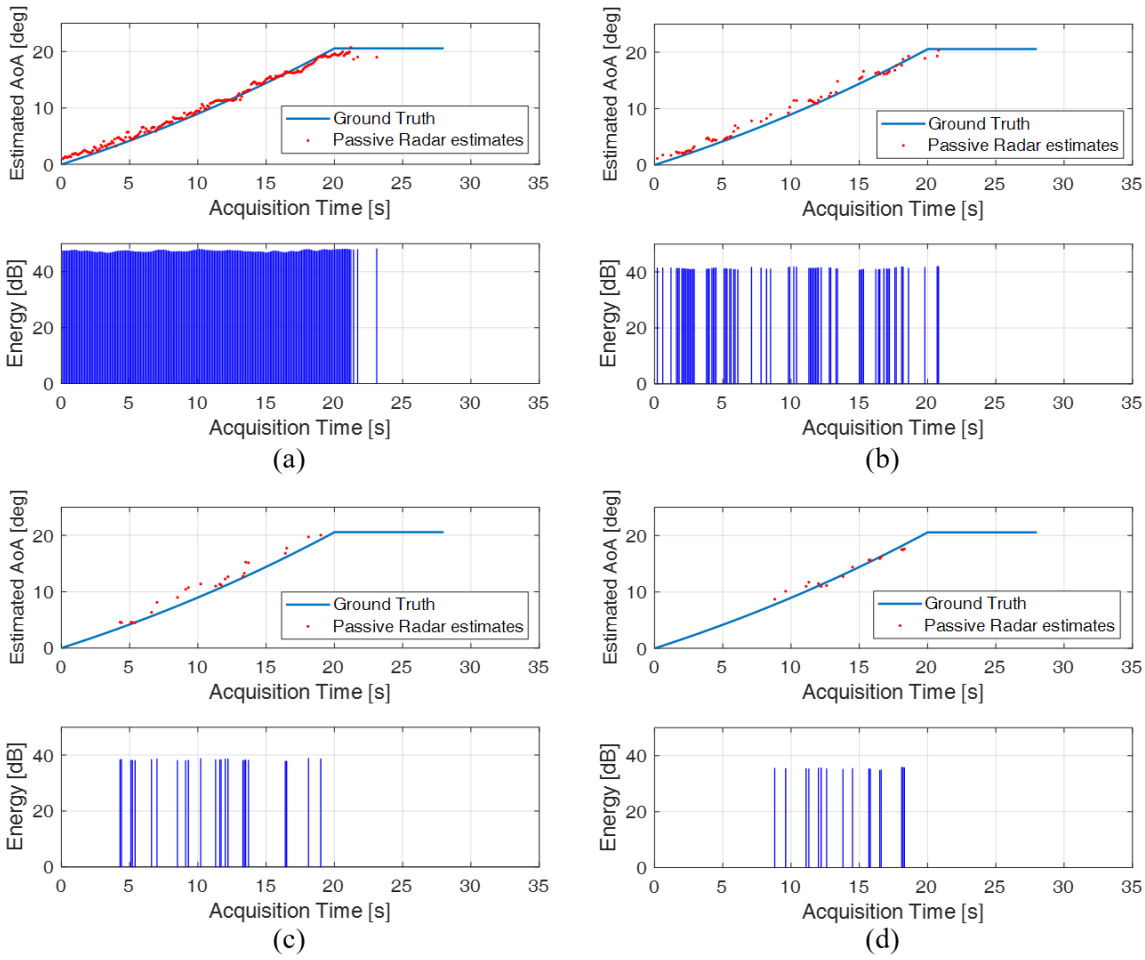

Figure 3.21. Comparison between estimated AoA and the ground truth for: (a) BI = 3ms, (b) BI = 12ms, (c) BI = 24ms and (d) BI = 48ms, for the passive radar technique.

Compared to the case of the device-based AoA approach, when BI = 3 ms, the measurements show a high continuity thanks to the high packet transmission rate of the Wi-Fi AP. It has to be noted that in the passive radar case a much stronger signal attenuation is present due to the two-way propagation loss. Moreover, since the AP-emitted signals are scattered by all fixed object in the scene, appropriate cancellation filters are employed to remove all echoes from stationary objects. This allows an effective extraction and detection of the moving targets, while makes it impossible to detect and localize static persons, thus the track is lost when the target stops.

The long (0.5 s) coherent integration time clearly allows to gather enough energy to provide a remarkable estimation accuracy, as well as to separate the moving target echoes from those scattered by the stationary scene.

In fact, the coherent integration time depends on the number of beacon transmissions occurred in that particular time interval. In detail, with a BI of 3 ms (Figure 3.20(a)) and an integration time equal to 0.5 s, it is possible to integrate about 167 packets, while when the BI reaches 48 ms (Figure 3.20(d)), this number decreases to about 10. In this figure, the results show that the main problem of increasing the BI is the loss of detections, and accordingly, of the AoA estimates, due to the corresponding SNR degradation. Moreover, it is possible to notice that also the accuracy is affected by the integration of less beacons, due to the degradation of the Signal-to-Noise Ratio (SNR) of the employed signals.

With respect to the loss of detections, Figure 3.22 highlights this behavior. In particular, it shows the target detections in the bistatic Range-Doppler plane, for our case study.

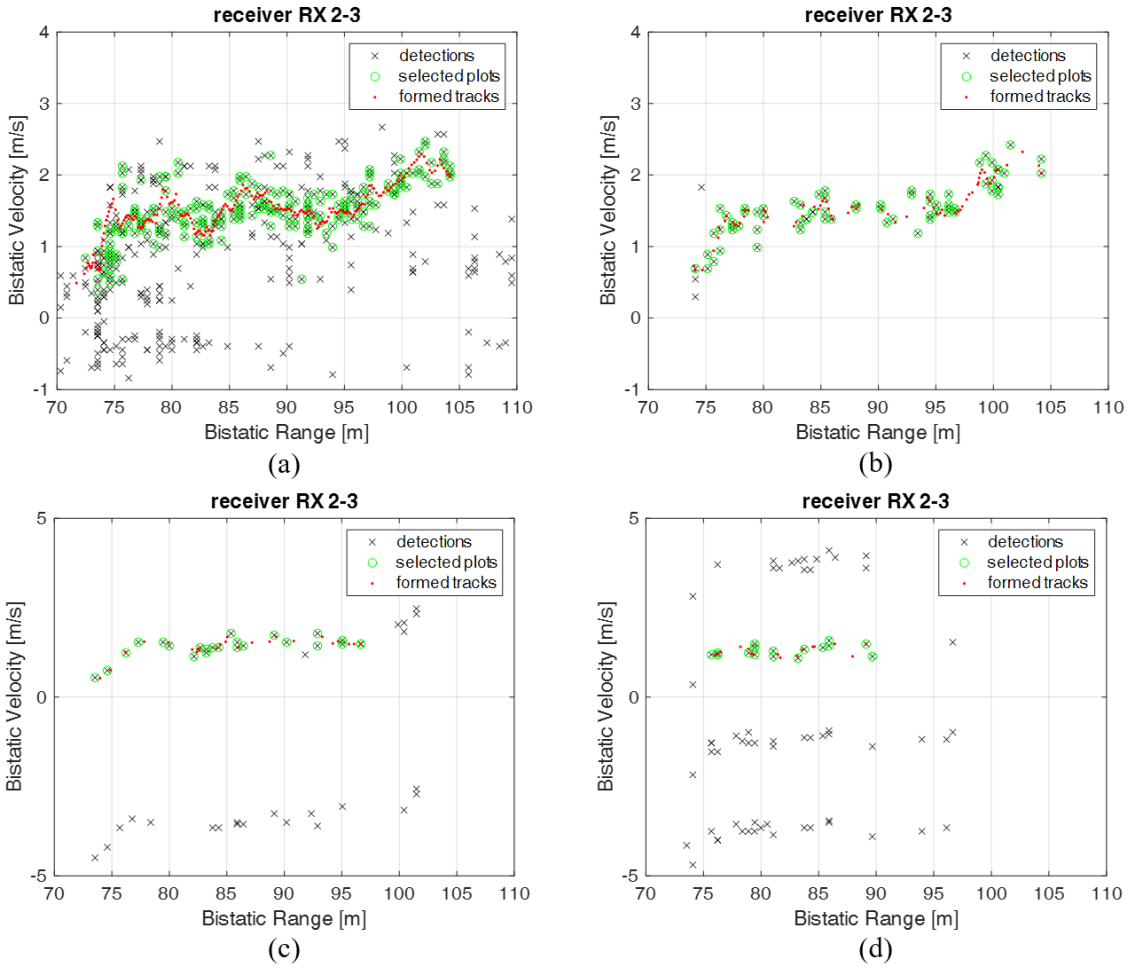

Figure 3.22. Target detection in the bistatic Doppler-Range plane for: (a) BI =3 ms, (b) BI = 12 ms, (c) BI = 24 ms, (d) BI = 48 ms.

It is apparent that when the BI increases (i.e. the PRT increases), the number of detections decreases and the non-ambiguous Doppler region is strongly reduced, being this parameter related to the inverse of the PRT. This causes a partial overlap of moving target echoes with the echoes from the stationary scene that are removed, as clearly displayed in Figure 3.22(c)-(d). In particular, while for BI=3, 12 ms Figure 3.22(a)-(b) shows many detections and a tracker is required to select the true target plots from false alarms and can be used to smooth their Doppler-range behavior, for BI=24, 48 ms many target plots are lost, so that the target tracking is required to fill the gaps and ensure continuity.

To understand better the accuracy, instead, in Figure 3.23 we show the AoA estimation error as a function of the time instant tk, $e(t_k) = \hat{\theta}(t_k) - \theta(t_k)$, where $\hat{\theta}(t_k)$ is the estimated angle of arrival, whereas $\theta(t_k)$ represents the ground truth.

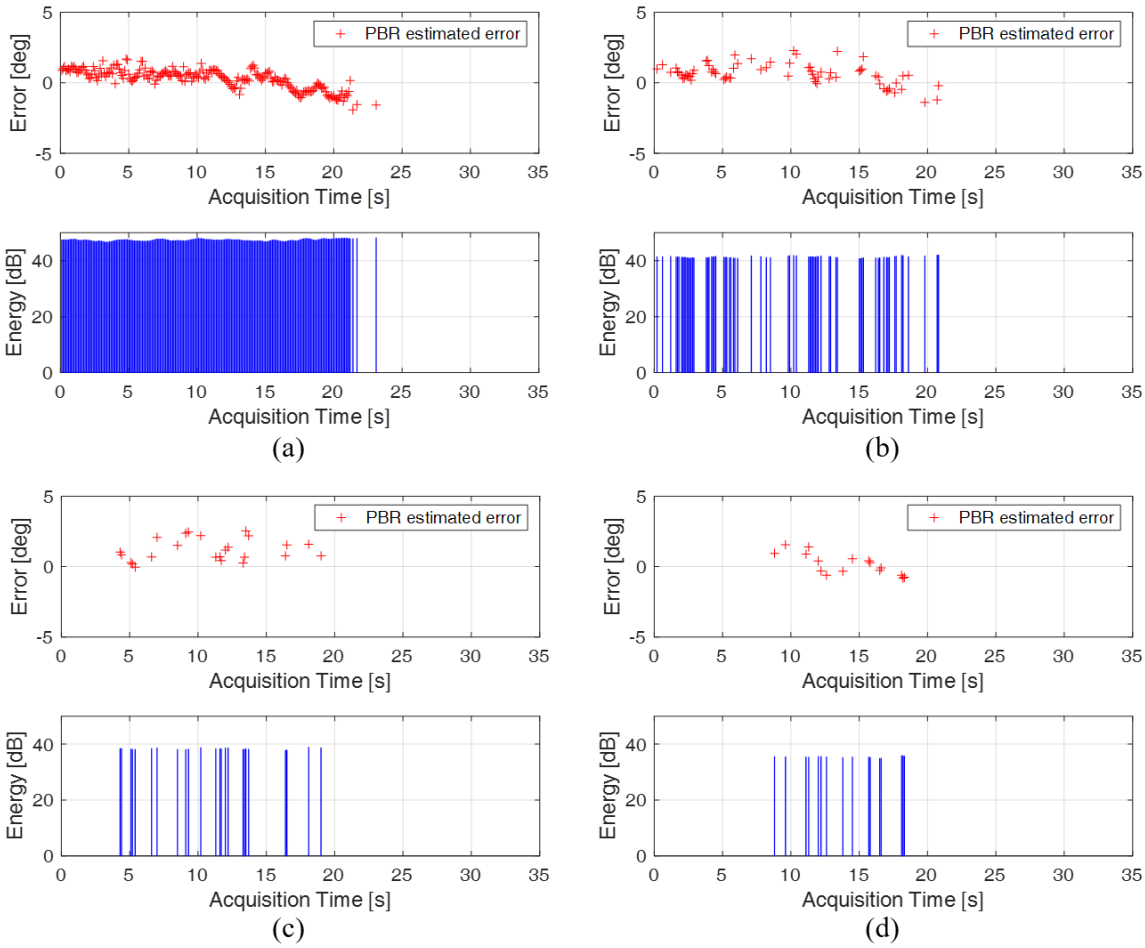

Figure 3.23. Target AoA error vs. time for: (a) BI =3 ms, (b) BI = 12 ms, (c) BI = 24 ms, (d) BI = 48 ms.

It is apparent that the time slot where estimates are available is reduced, continuity is lost and in some cases (Figure 3.23(c)) even some bias can appear.

By combining the two measures of AoA and bistatic range, the position estimation is easily obtained in the XY-plane, as shown in Figure 3.24, where the blue circles indicate the nine points of the grid created on the ground.

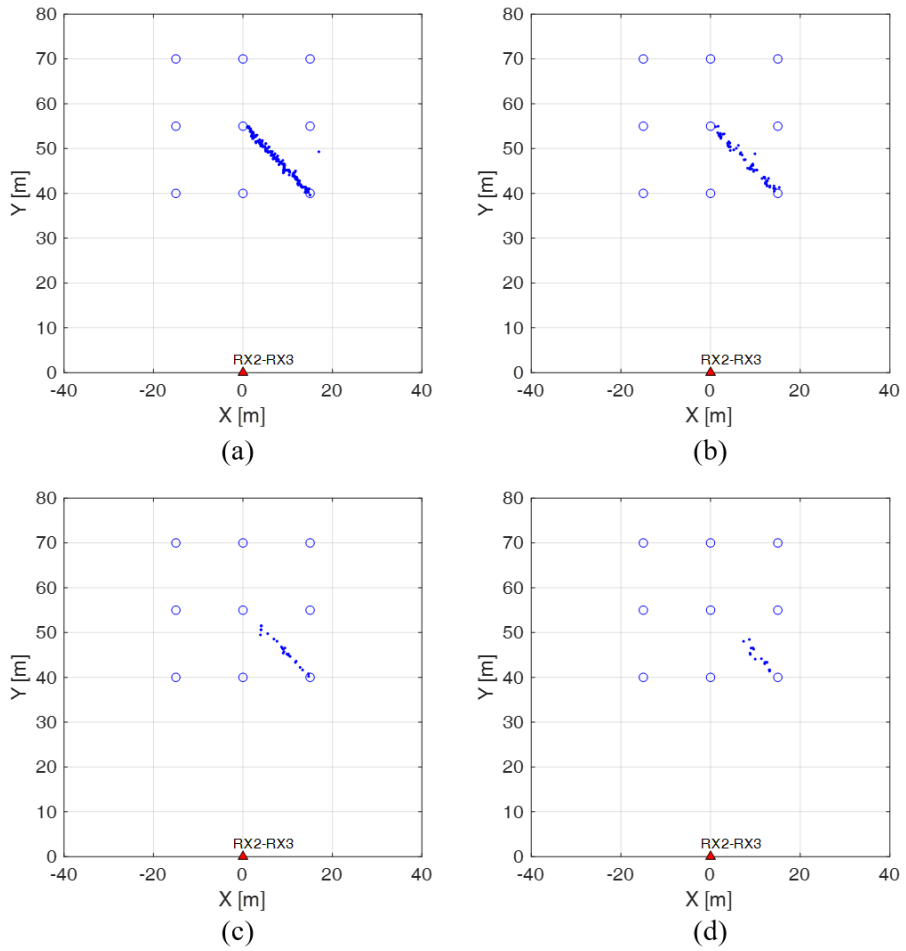

Figure 3.24. Target detection in the X-Y plane for: (a) BI =3 ms, (b) BI = 12 ms, (c) BI = 24 ms, (d) BI = 48 ms.

It can be noticed that the path of the target is correctly identified if compared to the theoretical behavior (see red line in Figure 3.15), especially when a small BI is used. According to the previous considerations, it is evident that increasing the BI, some position estimates are missing. This behavior is negligible when we pass from 3 ms to 12 ms, but becomes relevant for higher values of BI. In particular, for BI = 48ms, we lose the entire first part of the target motion, so we cannot find continuously the target position.

In order to have a quantitative idea of this results, we reported in Table 5 the values of RMSE and number of detections for each analyzed case.

Table 5. Root mean square errors obtained for the passive radar technique and different PRT.

Number of samples	**375**	**1500**	**6000**	**9000**	**Entire beacon**
RMSE	0.9429	1.0011	0.7619	0.7591	0.7493
Number of detections	215	171	71	24	16

The RMSE reported in Table 5 shows a progressive decrease of angular accuracy up to PRT=24 ms. For higher values of PRT, the number of target detections is extremely reduced so that it does not allow a statistically significant result.

3.2.3 Performance comparison of the two techniques

3.2.3.1 Passive Source Location performance

Based on the receiver configuration presented in Section 3.1, the device-based localization can be obtained by measuring the AoA and the TDoA of the Wi-Fi signals transmitted by the mobile device and received by the multiple receiving antennas. In practice, three receiving antennas are used to measure the device AoA and TDoA. In particular, the phase difference, $\widehat{\Delta\varphi}$, between the signals collected from each of the two closest antennas (RX2 and RX3 in Figure 3.15) is used to estimate the angle of arrival, $\hat{\theta}$, of the target, as

$$\hat{\theta} = arcsin\left(\frac{\lambda \cdot \widehat{\Delta\varphi}}{2\pi d}\right) \tag{3.1}$$

where λ is the wavelength related to the selected Wi-Fi channel, and d is the distance between RX2 and RX3. As explained in Section 2.3.1.2, to obtain a reliable estimate of the phase difference, $\widehat{\Delta\varphi}$, a Maximum Likelihood estimation technique is used, which leads to the following expression

$$\widehat{\Delta\varphi} = \angle \boldsymbol{s}_2^H \boldsymbol{s}_3 \tag{3.2}$$

where $\boldsymbol{s}_2$ and $\boldsymbol{s}_3$ are the vectors containing the samples of the packets received by antennas RX2 and RX3, respectively.

The displaced antenna (RX1), which is located close to the TX in our experiment, is necessary to measure the TDoA.

According to the analysis reported in Section 2.3.2.3, from these two measures, we can perform the XY-localization through the intersection of a line (AoA) and a hyperbola (TDoA). In particular, we found:

$$\begin{aligned} &\bullet \quad \widehat{x_t} = \begin{cases} \frac{(x_1^2+y_1^2)-(\widehat{\Delta\tau}\cdot c)^2}{2(x_1+\hat{m}y_1+\widehat{\Delta\tau}\cdot c\sqrt{\hat{m}^2+1})}, & if\ \hat{m} > 0 \\ \frac{(x_1^2+y_1^2)-(\widehat{\Delta\tau}\cdot c)^2}{2(x_1+\hat{m}y_1-\widehat{\Delta\tau}\cdot c\sqrt{\hat{m}^2+1})}, & if\ \hat{m} < 0 \end{cases} \\ &\bullet \quad \widehat{y_t} = \hat{m}\,\widehat{x_t} \end{aligned} \tag{3.3}$$

where $\widehat{x_t}$ and $\widehat{y_t}$ are the estimated coordinates of the target in the Cartesian reference system centred in RX2/RX3, x_1 and y_1 are the coordinates of RX1 in the same system, c is the speed of light, and $\hat{m} = \hat{m}(\hat{\theta})$ is the estimated slope of the line defined by the AoA.

The above device-based target localization technique has been applied to the experimental data collected during the acquisition campaign described in Section 3.2.1 and the resulting performance is presented in Figure 3.25. The resulting AoA and the TDoA estimates for the target-device transmissions are shown in Figure 3.25(a) and Figure 3.25(b), respectively (red crosses). Each point is the result of the coherent time integration

of packets, and it depends on the number of device transmissions occurred in that particular time interval. The integration time was set to 0.5s.

For comparison, also the ground truth is reported in the same plots (solid blue lines). It is obtained by assuming that the target was moving with a uniform linear motion along the assigned path (see Figure 3.15).

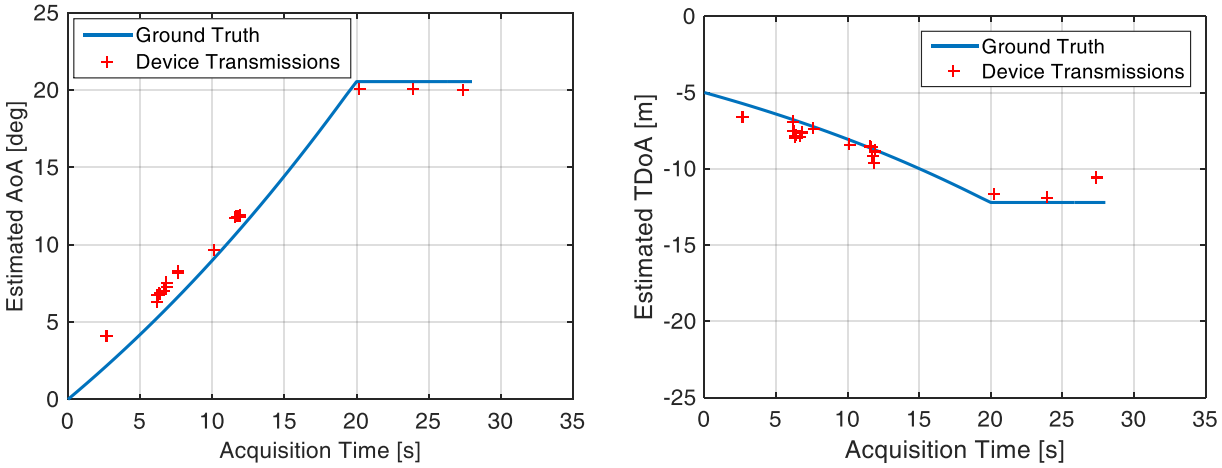

(a) (b)

Figure 3.25. Performance evaluation of device transmissions: (a) AoA estimation, (b) TDoA estimation.

The results show that the main problem of this technique is the limited number of device transmissions available for the estimation that allows us to reach a poor Signal-to-Noise Ratio (SNR) after the integration in the 0.5s. This is quite apparent by considering the interval between 13 and 20s in Figure 3.25, where there are no transmitted packets by the device under examination, so that both AoA and TDoA measurements are missing.

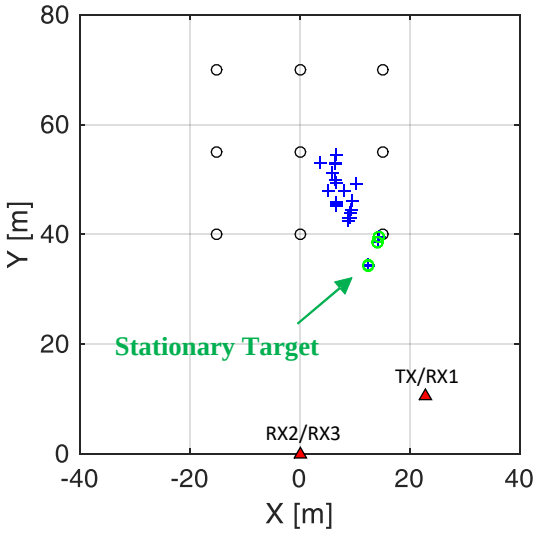

Figure 3.26. XY-localization of the human target with device transmissions-based technique.

Figure 3.26 shows the results obtained when the AoA and the TDoA values are combined to get the estimates in the XY-plane. In this figure, the black circles indicate the nine points of the grid created on the ground, whereas the red triangles represent the positions of the receiving antennas. The position estimates are shown

using blue crosses during the first 20s. The blue crosses are changed to green circles for the final 8s, to represent the estimates of the target position that is known to be stationary in this last part of the experiment. It can be noticed that the path of the target is correctly identified, but the estimates are quite variable when compared to the theoretical behavior (see red line in Figure 3.15). This makes this technique effective but not very accurate. As explained before, this depends principally on the small number of packets available for the device, during the common connection activity.

3.2.3.2 Passive Bistatic Radar performance

The passive radar localization experiment was carried out at the same time of the device-based one, so that the same configuration of the antennas and the same target motion are present. Therefore, it is possible to evaluate the position, for example, through the measure of the bistatic range and the AoA of the received target echoes, as explained in [17] and summarized in Section 2.2.2. This time, we have used the two closest antennas (RX2 and RX3) for the measure of both the bistatic range and the AoA, whereas the third receiving channel has been exploited to acquire a copy of the reference signal. To simplify the comparison of the results, as for the Wi-Fi emission-based localization technique, the coherent integration time is set to 0.5s.

The estimated measurements allow to obtain the position of the target on the XY-plane, by intersecting a bistatic ellipse (range) and a line (AoA), which provides the following solution:

$$\begin{aligned} &\bullet \quad \widehat{x_t} = \begin{cases} \frac{(x_{TX}^2+y_{TX}^2)-(\hat{R}_{bis})^2}{2(x_{TX}+\hat{m}y_{TX}-\hat{R}_{bis}\sqrt{\hat{m}^2+1})}, & if\ \hat{m} > 0 \\ \frac{(x_{TX}^2+y_{TX}^2)-(\hat{R}_{bis})^2}{2(x_{TX}+\hat{m}y_{TX}+\hat{R}_{bis}\sqrt{\hat{m}^2+1})}, & if\ \hat{m} < 0 \end{cases} \\ &\bullet \quad \widehat{y_t} = \hat{m}\,\widehat{x_t} \end{aligned} \tag{3.4}$$

where $\widehat{x_t}$, $\widehat{y_t}$ and $\hat{m} = \hat{m}(\hat{\theta})$ are defined as in (3.3)), whereas (x_{TX}, y_{TX}) are the coordinates of the transmitter and $\hat{R}_{bis}$ is the estimated bistatic range.

In detail, the AoA is obtained using the same approach of the Wi-Fi emission-based technique, namely through the estimation of the phase difference between the signals received at RX2 and RX3. In this case, the specific locations of the 2D-CCF, where the target has been detected, provide the estimate of the bistatic target range. Moreover, the phase difference is estimated as the phase difference of specific locations of the 2D-CCFs available for the two surveillance antennas, where the target has been detected.

As mentioned above, the calibration for the angle estimation is the same for the PBR and for the PSL technique. The results obtained for the AoA (red crosses) and the bistatic range (solid red line) estimation, and their comparison with the ground truth (solid blue line), are shown in Figure 3.27(a) and Figure 3.27(b), respectively. For the bistatic range, a conventional Kalman tracking algorithm has been applied, which provides filtered range values [17]. It is interesting to see that both the estimates of AoA and bistatic range follow the theoretical behavior for all the time that the target is moving, namely until it arrives at point B (from

seconds 0 to 20 of the acquisition). After that time, it is impossible to detect the target and in consequence measure angles and ranges. This is due to the cancellation stage employed by the passive radar processing chain that cancels all the echoes from static objects in the field of view, and therefore also the echoes of a static human target. In consequence, during the last 8 seconds the target disappears from the passive radar results.

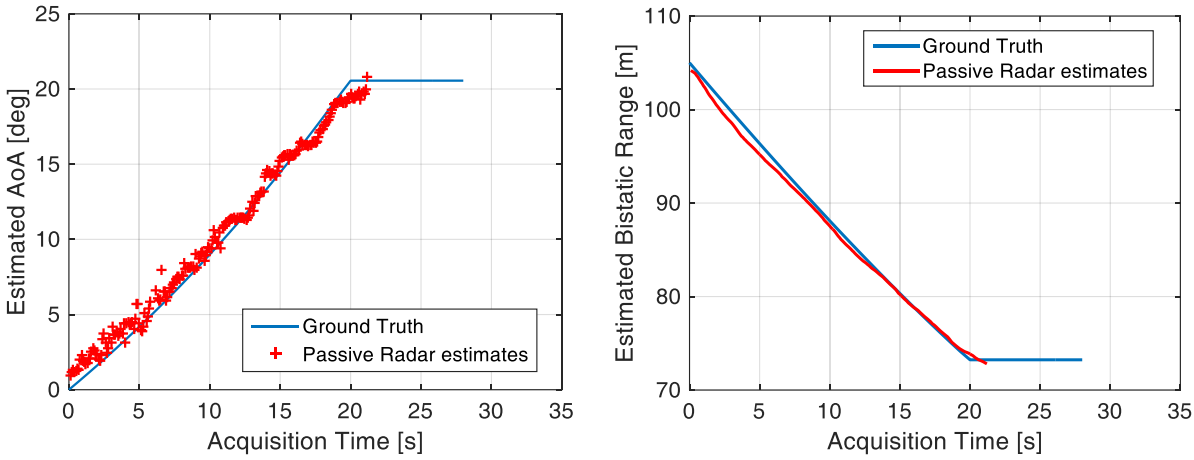

(a) (b)

Figure 3.27. Performance evaluation of passive radar technique: (a) AoA estimation, (b) bistatic range estimation.

By combining the two measures of AoA and bistatic range, during the first 20s, the position estimation is easily obtained in the XY-plane and displayed in Figure 3.28.

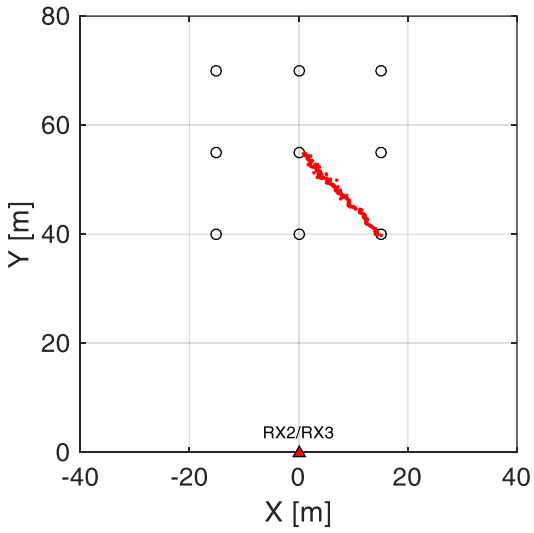

Figure 3.28. XY-localization of the human target with passive radar technique.

It is apparent that the passive radar technique provides a fairly accurate estimate of the human target's position.

3.2.3.3 Techniques comparison and complementarity

It is interesting to compare these two methodologies to understand relative merits and the relationship between them.

Firstly, we compare the AoA measurements, since they are available for both sensors.

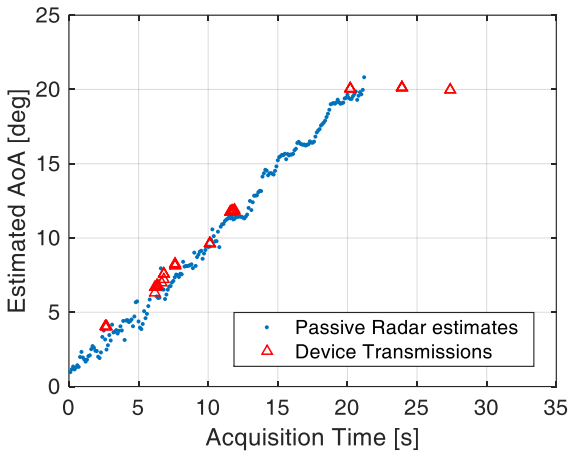

Figure 3.29. Comparison between the AoA estimation with the passive radar technique and the WiFi emission-based technique.

As shown in Figure 3.29, during the first 20 seconds of the acquisition, the two strategies lead to comparable results. However, it is apparent that the passive radar has a higher number of angle estimates, which provides an almost continuous set of measurements. In contrast, the device-based approach provides a reliable estimate only when bursts of packets are emitted. In our case, this provides a rather discontinuous set of measurements that is not quite desirable when the target is moving, since its AoA changes with time. As expected and discussed above, the PSL technique has a key role when the target is stationary (from 20 to 28 seconds) since the passive radar system cannot detect it.

In Figure 3.30, we present the comparison of the results obtained for the positions in the XY-plane.

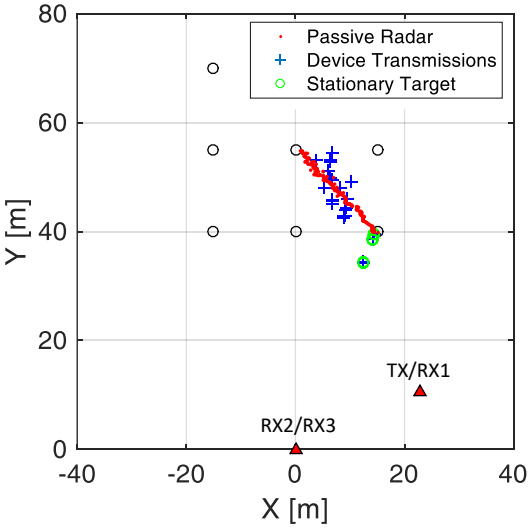

Figure 3.30. Comparison of the WiFi emission-based and the passive radar localization on the XY-plane.

As apparent from the dispersion of the measurements, we can assert that the WiFi-based PBR localization (red dots) provides better performance with respect to the device-based technique (blue crosses). This is due to the possibility to exploit a higher number of packets for the estimation of the measures of interest. In fact, we have to remind that the temporal distance between consecutive beacons is equal to 3 milliseconds, whereas the device transmits only when a communication with the AP occurs. In this particular experimental test, the device sends packets only to establish the connection with the AP.

The following additional considerations apply:

i. the range resolution of the passive radar is limited due to the limited frequency bandwidth of the Wi-Fi signals. This makes it difficult to discriminate closely positioned targets;

ii. the device-based technique can exploit the device code to discriminate between multiple closely spaced targets; in fact the acquired device signals can be associated to the related target, thanks to the classification stage, based on the reading of the MAC Address written in the packets, which is performed before the localization operations;

iii. the better performance of the passive radar is paid in terms of a higher computational cost with respect to the emission-based technique.

Summarizing the previous considerations, it is evident that these techniques present complementary aspects, which makes them suitable for a possible joint use. Firstly, the passive radar can help when the target has no active devices, so that the emission-based localization cannot be used. On the other hand, only the device-based technique can estimate the position when the target is stationary.

In addition, the passive radar can exploit a considerable number of data for the estimation of the parameters of interest, thanks to the high transmission rate of the AP, whereas the emission-based technique uses only the signals transmitted by the mobile device during the connection with the AP.

Under different conditions, the relative performance of the two can be somewhat different. In particular, if the target increases its device transmissions, for example in upload activities, the number of AP emissions (especially in terms of emitted beacons) decreases. In this case, the PSL would provide much more position estimates, whereas the signals available for the passive radar measurements would be reduced. Due to the impossibility to have simultaneous transmissions of AP and devices, it is clear that the joint use of both the techniques might compensate for the lack of data for one of them in a real scenario.

The considerations above provide a sound technical basis for a sensor fusion technique. This is expected to exploit at the best both the signals emitted by the AP and those emitted by the devices to provide a continuous tracking of the human targets carrying an active Wi-Fi device, while only resorting to the passive radar for human targets that do not carry any device.

3.3 High data traffic for PSL sensor

3.3.1 Acquisition campaign description

In order to test the behavior of the systems in different network conditions, we tried to analyze the effect of a real upload activity of the mobile device carried by the human target. Due to the environmental conditions, the AP did not provide the possibility to surf the Internet; therefore, it was necessary the exploitation of another device used as Hotspot. For this reason, the target connected its mobile device to that Hotspot and uploaded a video on a server. As apparent, this operation produced an increase of device transmissions with respect to the previous test.

Nevertheless, for the passive radar system, we used, as illuminator of opportunity, the same AP exploited in in the first test. This time, the omnidirectional antenna of the AP was used in transmission, instead of the directive antenna of the previous test. This choice provides an enhancement with respect to previous studies, because it allows the evaluation of the potential of this system in real scenarios.

The AP was configured to transmit in channel 5 of the Wi-Fi band (carrier frequency equal to 2.432 GHz). The beacon interval was set to 3 milliseconds, that defines the Pulse Repetition Time (PRT) of the passive radar.

The Hotspot, instead, occupied channel 1 of the Wi-Fi band (carrier frequency equal to 2.412 GHz). The use of different channels for the two systems has a double function: 1) it provides the possibility to avoid collisions between AP and device when both are characterized by high data rate, that is important in this first phase of system evaluation; 2) it provides the possibility to analyze a higher range of possible practical situations, as for instance the case where the device tries to connect to an AP different from that used for the PBR. As it is clear, this event needs a more complex processing, due to the necessity to manage a larger band in both data acquisition and post-processing (packet extraction) stages.

For this reason, the acquired signal was sampled with a sampling frequency of 40 MHz, then it was stored and processed off-line. In particular, the first processing operation is the filtering of the two specific frequency bands around the carrier frequencies of the exploited channels, the packet extraction from the two filtered signals and the classification of the acquired packets, based on the transmitting source, to perform the association between packet and target (or AP).

For this second test, the acquisition system was made of four receiving channels, connected to four surveillance antennas (TP-LINK TL-ANT2409A). Even in this case, we set an additional gain for each USRP receiving channel in order to have a comparable signal level. The four antennas were combined in two nodes: two receiving antennas (RX2-RX3) were located one beside the other, with spacing of 14 cm between them, near the receiving system, whereas the other two antennas (RX0-RX1) were placed one beside the other, with spacing of 14 cm, 25 m far from RX2-RX3, as displayed in Figure 3.31. The AP was placed in the midpoint of the line that links the two receiving nodes, namely the point (11.4 m, 5.25 m) in our Cartesian reference system.

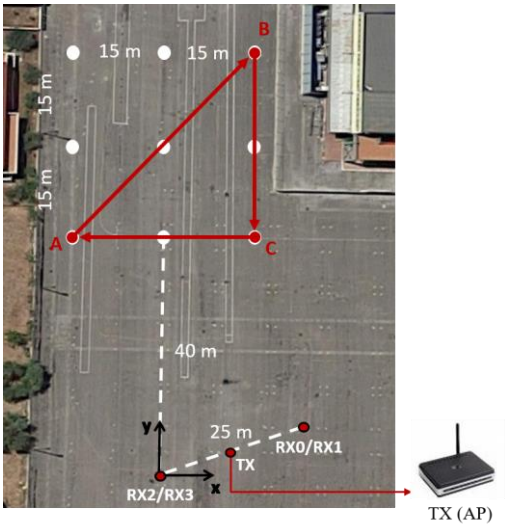

Figure 3.31. Target localization and tracking experiment (Test 2).

The employment of four surveillance antennas on one hand enables the exploitation of different combination of measurements (for example, two AoA measures for the PSL), but on the other hand it does not allow to acquire the reference signal from the AP, therefore a further operation of reference reconstruction is necessary.

In order to understand the potential of the proposed techniques, we decided to stress them through the definition of a more complicated trajectory. The test we carried out is sketched in Figure 3.31. In this test, a target with an active mobile device moves from point A (-15 m, 40 m) in the figure, and arrives to point B (15 m, 70 m). The target takes 19s to reach point B, and then it stops there for about 8s. Then it moves again and after 14s arrives in point C (15 m, 40 m). It is stationary for about 10s, then it starts again its motion to come back to point A. The target takes additional 14 s to cover this last segment. It is worth mentioning that the path sketched in Figure 3.31 along the grid is purely nominal.

During the whole acquisition time, the user uploads a video on a server through the exploitation of another device as Hotspot. However, the period of more intense traffic occurs in stop intervals, since it is reasonable that a person uses a mobile device especially when it is stationary, therefore the transmission of the video will occur principally in these intervals.

3.3.2 Performance comparison of the two techniques

3.3.2.1 Passive Source Location performance

In this second test, we analyzed the case where a real upload activity is carried out by the mobile device. In fact, the human target uploads a video on a server during its walk in the area of interest. In this section, we refer to the trajectory described in Section 3.3.1, and in particular in Figure 3.31.

This time, with the proposed receiver configuration (four surveillance antennas), we have the possibility to exploit two measurements of AoA and one of TDoA.

Since the results reported in Chapter 2 have shown that the use of TDoA measurements does not provide an increase in performance, especially in short range applications, in this test we decided to avoid the use of TDoA measurements and exploit only the measures of AoA provided by the two employed receiving nodes.

The approach followed for the AoA estimation is the same used in the previous test. Therefore, we reported in Figure 3.32 the results obtained for the AoA estimates (red crosses), compared with the ground truth (blue solid line). The latter is obtained by assuming that the target was moving with a uniform linear motion along the assigned path (see Figure 3.31) and considering the position of the target in each specific instant of the acquisition, as explained when the test has been described.

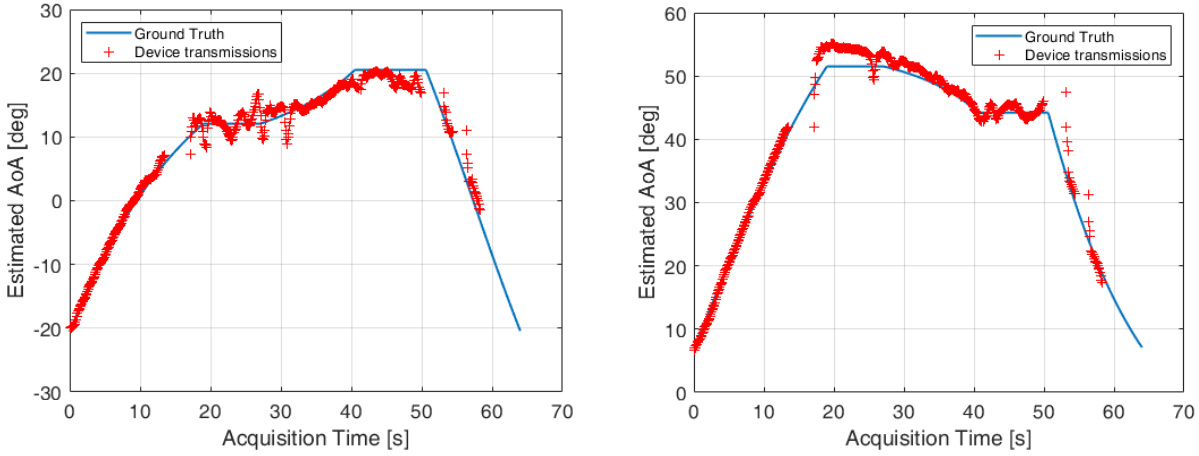

(a) (b)

Figure 3.32. Performance evaluation of PSL for Test 2: (a) AoA estimation with RX2-RX3, (b) AoA estimation with RX0-RX1.

The above results are obtained after a coherent integration of device packets, within an interval of 0.5 s. The shift between consecutive integration interval was set to 0.1 s. This means that, when at least one device transmission is available in the examined interval, the PSL produces a measurement every 0.1 s.

In this figure, it is evident that the AoA estimation with RX0-RX1 presents some problems of accuracy in the time interval between about 18 s and 40 s, which corresponds to the first stop and the subsequent segment of path. This behavior could be probably caused by the proximity of a building (as can be seen in Figure 3.31) and in particular of a metallic fence present on the right hand side of the reference square grid, and by the higher distance between target and receiver. This consideration matches with the results shown in [17] and [31]. Moreover, as expected, there are some instants where the PSL does not provide the angle estimates, especially when the target is moving.

For sake of completeness, we also reported the results for the TDoA estimates, obtained by RX1 and RX2 in Figure 3.33.

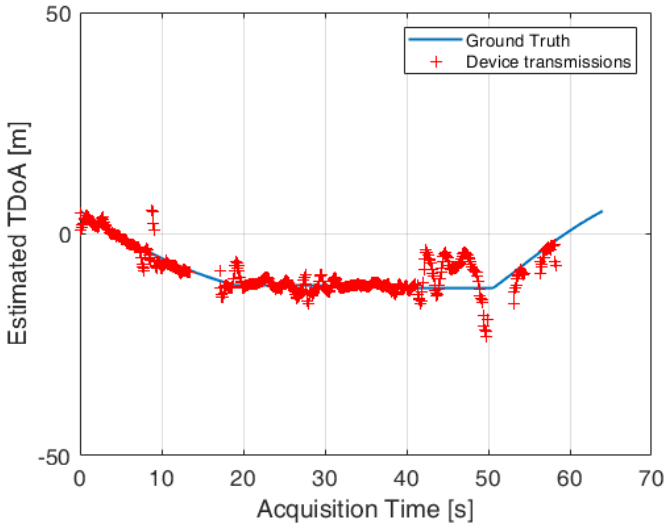

Figure 3.33. Performance evaluation of PSL for Test 2 in terms of TDoA estimation accuracy.

As mentioned above, the target position in the XY-plane is obtained through the combination of the two measurements of angle. The related results are presented in Figure 3.34.

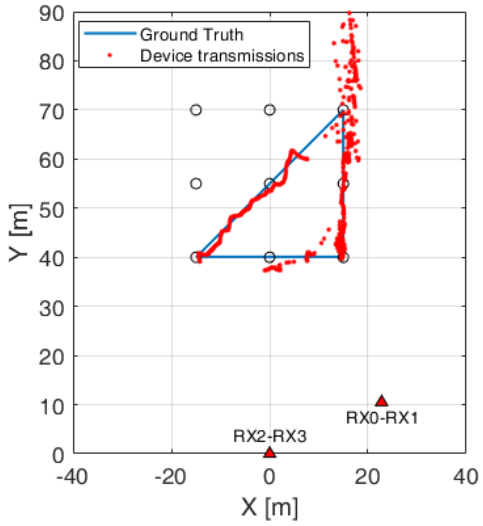

Figure 3.34. XY-localization of the human target with PSL technique for Test 2.

The position estimates shown in this figure highlight the problems of the PSL, in particular when the human target passes through the point (15 m, 70 m) of the grid.

3.3.2.2 Passive Bistatic Radar performance

In this second case, we used two receiving nodes, each composed by two antennas. This means that we have the possibility to exploit two measurements of angle and two measurements of bistatic Range (we have applied the two-out-of-two criterion)

In order to compare the results with the previous test, we consider the case when one measurement of angle and one measurement of bistatic Range are used to estimate the target position. In particular, we used the couple of antennas RX2-RX3.

We reported in Figure 3.35 the results obtained for the AoA estimates (red crosses) and the bistatic Range estimated by the same antennas (red crosses), in Figure 3.35(a) and Figure 3.35(b), respectively. In both cases, we also reported the comparison with the ground truth (blue solid line).

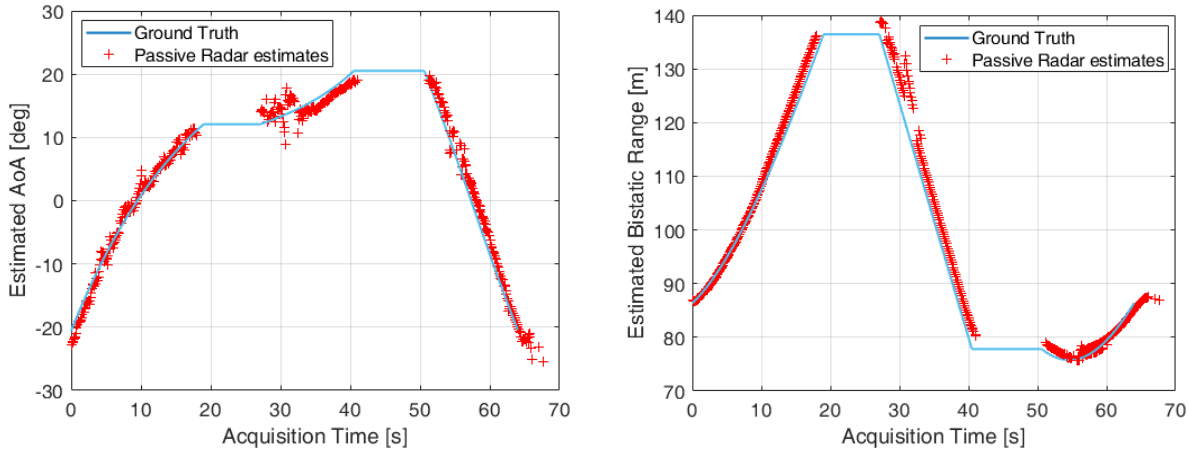

(a) (b)

Figure 3.35. Performance evaluation of passive radar technique for Test 2: (a) AoA estimation, (b) bistatic range estimation.

As for the PSL system and according to the results presented in Section 3.2.3.2, each point representing the PBR estimates is the results of a coherent integration of the AP packets received within intervals of 0.5 s, shifted in time of 0.1 s.

The results in Figure 3.35 confirm the behavior seen in Figure 3.27. Therefore, the introduction of the reference reconstruction, the employment of the AP omnidirectional antenna, the increase of device transmissions and the filtering of a larger frequency bandwidth, do not cause a degradation of PBR performance. We can notice that, even this time, the PBR estimates disappear when the target is stationary. It is also evident that we have selected different tracks to fill the entire trajectory.

The combination of the AoA and Range measures provides the target position estimates in the XY-plane. In Figure 3.36, we reported the passive radar position estimates of the human target (red dots) compared with the expected trajectory (blue solid line).

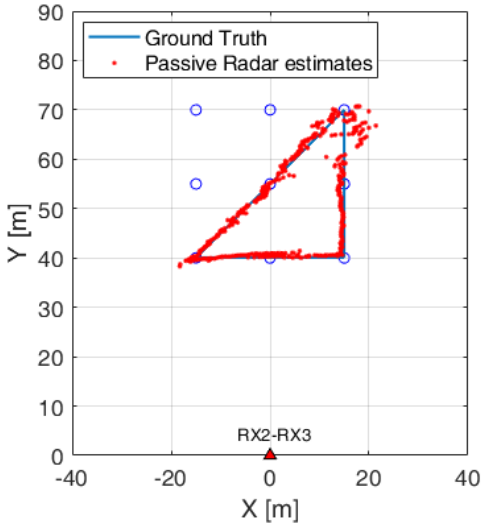

Figure 3.36. XY-localization of the human target with passive radar technique for Test 2.

The PBR provides very accurate position estimates when compared with the ground truth, also over this complicated trajectory. Therefore, these results confirmed that the Passive Radar is effective for human target localization in short-range applications. In this figure, we can also notice that there are some points (between y = 60 m and y = 70 m) where the PBR estimates are less accurate with respect to the general behavior of our Passive Radar. The increase of the error in these estimates could be probably due to the proximity of a building (as can be seen in Figure 3.31) and in particular of a metallic fence present on the right side of the reference square grid, as mentioned for the PSL system.

3.3.2.3 Techniques comparison and complementarity

As for Test 1, the first comparison can be made between the AoA measures provided by the couple RX2-RX3, since this is available for both the strategies. Therefore, in Figure 3.37 we displayed together the results shown in Figure 3.32(a) and Figure 3.35(a), with the purpose of making the visualization easier.

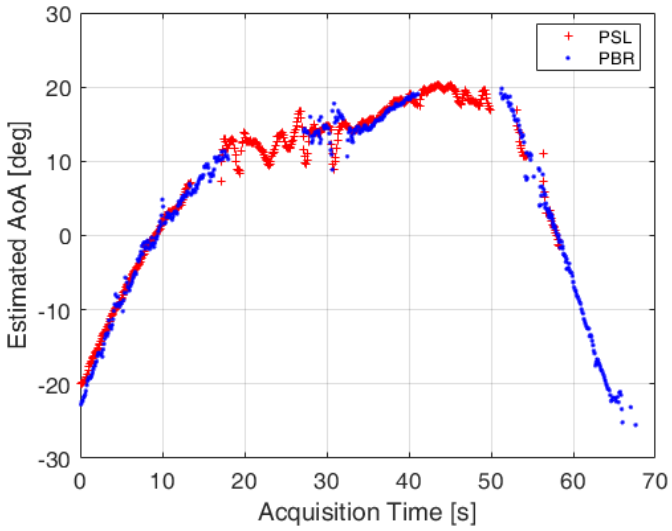

Figure 3.37. Comparison between the AoA estimation with the PBR technique and PSL technique.

The previous considerations are apparent in this figure. In fact, the AoA estimates of the PSL sensor (red crosses) compensate for the lack of measurements of the PBR sensor (blue dots) when the target is stationary (from 18 s to 27 s, and between 40 s and 50 s). On the other hand, the PBR compensates for the lack of PSL estimates when the target is moving but the person interrupts the transmission of the video or the communication is finished.

In contrast with the results shown in Figure 3.29 for the first test, this time the PSL provides a number of estimates comparable with that produced by the PBR. Moreover, it is interesting to notice that also the angles estimated by both the sensors are comparable when the measurements are available for both.

The comparison of the localization results on the XY-plane for the presented strategies is reported in Figure 3.38, where the blue dots represent the PBR estimates, while the red crosses are the position estimates of the PSL sensor.

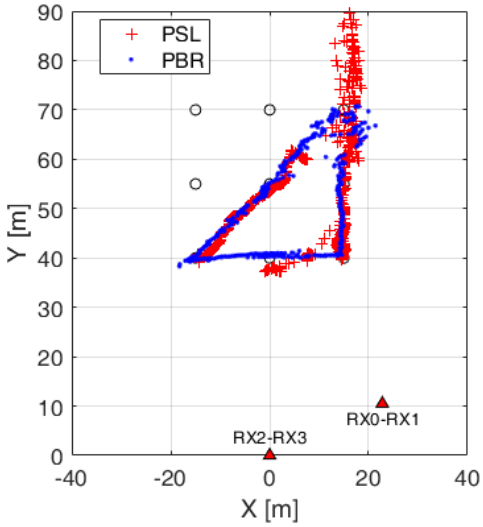

Figure 3.38. Comparison of the PSL and the PBR localization on the XY-plane.

These results confirm that the passive radar provides more accurate position estimates, whereas the Passive Source Location has basically a key role when the target is stationary and the PBR does not provide the target position.

3.4 Summary

In this first study, the relative merits of device-based and device-free techniques have been investigated, together with their complementarity. The former is the Passive Source Location (PSL), which exploits the signals emitted by the devices, so that provides measurements only when packets are transmitted by the mobile device, but have the capability to identify and discriminate even very closely spaced targets and measure their position also when they are stationary. The latter (device-free) is the Passive Bistatic Radar (PBR), that exploits the signals emitted by the AP, which tends to be more continuous due to the periodic environment scanning provided by the transmission of the beacon signals and provides quite accurate measurements. In addition, it has poor spatial target resolution capability and cannot detect or track stationary targets.

The evaluation was performed on experimental data for the two proposed techniques. In particular, we focused on two different analyses: *i)* the study of the relationship between data traffic condition and performance, and *ii)* the performance comparison of the two techniques in terms of localization accuracy.

Specifically, for the first point, the accuracy of the AoA measurements necessary for the 2D localization has been investigated.

As expected, the results show that for both techniques the AoA accuracy depends on the signal-to-noise ratio also in terms of the number of exploited received signal samples.

As expected, the results for the AoA have shown that a lower number of samples leads to a poor SNR, which provides poor performance in terms of accuracy. In contrast, the probability that a collision occurs increases with the number of samples. However, the PSL system provides the possibility of using a very small number of samples thanks to the high SNR of the direct signal transmitted by the device.

For the passive radar, in addition to the employment of less samples, as for the device-based localization, the effect of the reduction of the PRF has been investigated. We have shown that the PBR provides quite accurate measurements when the beacons emission is more continuous, namely when the BI is smaller. Its quality tends to degrade when the number of emitted beacon signals is strongly reduced, which might represent the situation where a significant activity is performed by other users of the medium. We have shown that both the detection capability and the localization accuracy progressively degrade as the BI increases due to both the reduction of the received beacons and to the intrinsic undersampling of the target motion. In particular, we have seen that the main problem when we use higher BIs is the loss of detections, which causes the impossibility to define the target position for the entire observation time and affects estimation accuracy. The results are largely in agreement with the study presented in [18], where the detection performance was addressed especially for vehicular targets. The better performance provided by the passive radar with higher values of BI is paid in terms of a higher computational cost with respect to the other investigated cases.

In addition, even for the PBR, the results of this study suggest the possibility of using less samples with respect to the entire packet, without compromising the performance. This allows to reduce the computational cost of the whole processing, that is essential for localization applications.

For the performance comparison in terms of localization accuracy, we have seen that both the strategies are effective for the positioning of human targets. It is interesting to notice that their estimates are comparable when the measurements are available for both sensors. Moreover, we have also shown that one sensor compensates for the lack of measurements of the other one.

As it is clear from the comparison between the presented techniques, it is not useful to keep these strategies separated, but it is necessary to add further processing stages, devised with the purpose of exploiting the benefits of the PBR and PSL and reducing the relative limitations.

The considerations above provide a sound technical basis for a sensor fusion technique, which allows to benefit of the good spatial discrimination and identification capability of the device-based technique, together with its capability to position static targets, as well as of the capability of passive radar to detect and position human targets that do not carry an active device. Such technique exploits at the best all both the signals emitted by the

AP and those emitted by the devices to provide a continuous tracking of the human targets carrying an active Wi-Fi device.

Chapter 4
Tracking techniques

We have already studied the possible techniques for the estimation of both the Time Difference of Arrival (TDoA) and the Angle of Arrival (AoA) and the positioning techniques based on TDoA and AoA for the PSL sensor, and on bistatic Range and AoA for the PBR. We have also studied the effectiveness of the proposed techniques in localization of small targets in local area environments.

Taking into account these studies, it is now necessary to define some tracking strategies, in order to improve the performance of our localization system.

In fact, the tracking is useful for:

- The improvement of the positioning accuracy with respect to the single measurement;
- The prediction of the future position of the target;
- The combination of heterogeneous measures, for instance when they derive from different sensors.

To reach this purpose, a considerable number of works have been devised through the years. Firstly, we can distinguish between strategies that perform the tracking directly on the estimated measures (TDoA and/or AoA and/or Range, etc.), and strategies that define the track over the XY-plane, namely after the application of the positioning techniques previously described.

We decided to face this second approach.

4.1 Kalman Filter (KF)

As explained before, the tracking can be obtained in different ways.

The most used is the filtering of the position measures through the employment of the Kalman Filter, [45]. With this method, the filtered measurement is obtained by conveniently weighting two contributions:

1) The new ‘raw’ measurement of the target position, obtained as described in Chapter 2;
2) The past history of the target, providing a prediction of the possible future position, calculated from an appropriate motion model assumed for the target, defined before the application of the filter.

As apparent, the potential causes of errors in target tracking are principally linked to these two contributions. In fact, inaccurate results can be due to both the excessive noisiness of the available position measurements, and the mismatching between the motion model of the filter and the actual behavior of the target.

The prediction is obviously based on the motion model assumed for the target. For example, each type of target is characterized by typical values of velocity or acceleration, which have to be considered during the setting of the filter.

The Kalman Filter can improve the performance of a localization system, but there are some situations where it is not sufficient to reach good accuracies. In fact, when the Kalman Filter is applied, it is necessary to define the motion model to be employed for the prediction stage. Good performance is obtained if that model matches the actual target motion during the entire observation time. This is not possible in real applications where the target, especially the smallest and fastest ones (humans or drones), can rapidly change their motion state more times in a few seconds. In these situations, the Kalman filter produces too high errors, making necessary the employment of different approaches. One of the possible solutions could be the relaxing of the constraints on the filter model, namely increasing the value of the standard deviation of the model errors σ_{ax} and σ_{ay}. In this way, the filter manages to follow even higher variations in the target motion state. On the other hand, this strategy generates the reduction of the benefits produced by the exploitation of a good prediction when the target motion coincides with the filter motion model.

Alternatively, to face this situation without sacrificing the benefits of a good filtering, different strategies have been devised. In particular, the Interacting Multiple Model (IMM) is a possible solution for this type of problems.

4.2 Interacting Multiple Model (IMM)

The IMM method allows the tracker to follow the changing of the target motion state.

The basic principles are almost the same of the Kalman Filter. The main difference is that the IMM can exploit more filters with different motion models. In this way, it is possible to reduce the errors due to the change of the target motion (when this motion is defined among the models of the designed IMM), without losing in accuracy of the single filter (as happens with the increase of σ_a in the Kalman Filter). Even this time, the more the motion models of the employed filters match the actual behavior of the target, the more the tracking is accurate.

It is possible to implement the IMM in different ways. The main differences between the possible implementations are: 1) the number of filters that are used, 2) the typology of the employed filters. With respect to the first aspect, in [46], it is demonstrated that a too low number of models does not allow to follow all the possible motion variations of the target; on the other hand, also a too high number of models could degrade the performance, and it is also evident that this second case is also characterized by a higher computational cost. In reference to the second point, namely the typology of the employed models, the choice strongly depends on the type of target that we need to localize and to its expected behavior in the specific application of interest.

The basic blocks which compose this method are the *Interaction*, the *Filtering*, the *Probability Update* and the *Combination* of the results obtained using the different filters, as explained in [47] and [48], and summarized in the scheme reported in Figure 4.1, where the generic version of the IMM with N_f filters is presented.

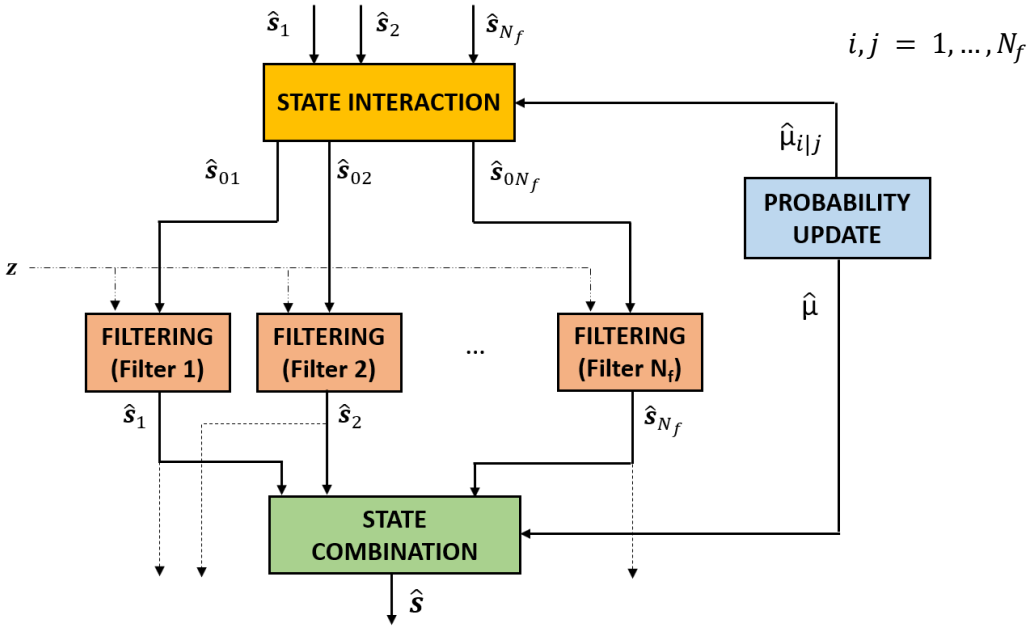

Figure 4.1. IMM processing scheme.

In this scheme, the inputs of the *Interaction* block are the filtered state vectors $\hat{\boldsymbol{s}}_j$ obtained at the previous iteration, namely $\hat{\boldsymbol{s}}_j(k-1|k-1)$; the outputs of the same block are the mixed states $\hat{\boldsymbol{s}}_{0j}(k-1|k-1)$, obtained by a linear combination of the contributions of each filter, where the weights are the mixing probabilities $\hat{\mu}_{i|j}$ calculated in the *Probability Update* stage. The *Filtering* block uses: i) the mixed states for the prediction stage, and ii) the measurement $\boldsymbol{z}$ that contains the coordinates (x and y) related to the target position estimated by the sensor. The filtered states are then used by the *Combination* block to obtain the output of the IMM method, namely the combined state estimate at time k, $\hat{\boldsymbol{s}}(k|k)$. Even this time, the weights for the combination are derived into the *Probability Update* block, and they are the mode probabilities, $\mu_j(k)$. The vector states produced by the N_f filters represent also the inputs for the *Interaction* of the next iteration.

As mentioned before, this method compensates for the limitation of the single Kalman Filter, when it operates over a target with changing dynamics.

A particular case is represented by a target, that alternates motion and stationary intervals during its path, the so called "Stop&Go" motion. This situation is particularly interesting since it is very common for small targets, as for example a drone that flies for a certain time with a nearly constant velocity and then it stops (in hovering) to examine an area, make panoramic videos, or deliver/leave objects, or a person who walks and stops to send a message or an email, and then walks again, and so on.

Although the motion is simple enough, the management of this situation is rather complicated. In fact, even if the static behavior can be seen as a uniform linear motion with velocity equal to zero, a single Kalman Filter could have some problems to track this type of target, due to the errors during the transition from a motion state to another (necessity to correctly estimate the new velocity). Therefore, due to the complexity of the target tracking in this type of situation, several works aimed to find a solution to this problem. In fact, as explained in [49]-[50], the classical IMM approach could not be appropriated to address the localization of move-stop-

move targets. In particular, in [49] a Variable Structure IMM (VS-IMM, [46]) has been used, while the authors of [50] employed the Multiple-hypothesis IMM (MH-IMM).

In this work we introduce a different strategy to perform the tracking in this kind of situation.

Chapter 5
Interacting Multiple Model - Modified Innovation (IMM-MI)

In this Chapter, we present a new methodology for target tracking, which is very useful specially to solve the problem of tracking move-stop-move targets.

The basic idea is to exploit the inherent differences between the device-based and the Passive Radar sensors, in order to develop a consistent and effective method for small target localization and tracking. To introduce the motivation that leads to the definition of our new approach, we can refer to the initial consideration of this work: we are using two sensors, whose performance are directly connected to the target motion status. In particular, the main differences are highlighted when the target alternates motion and stationary intervals during its path, as explained in detail in Chapter 3.

With the purpose of facing this specific situation, we propose a new strategy that uses a modified version of the IMM approach together with Data Fusion techniques, that take into account the differences between the measurement's accuracies of the employed sensors. In the modified version of the IMM method, the information related to the presence or the absence of the PBR estimates is used to help the choice between the employed filters, through the modification of the Innovation. Since the aim is just to help the choice of the best filter among that available, this modification is not performed during the Filtering stage, but only before the Probability Update (the detailed description is reported later in this Chapter). For this reason, we call this methodology **Interacting Multiple Model – Modified Innovation (IMM-MI)**. The processing scheme of the proposed strategy is reported in Figure 5.1.

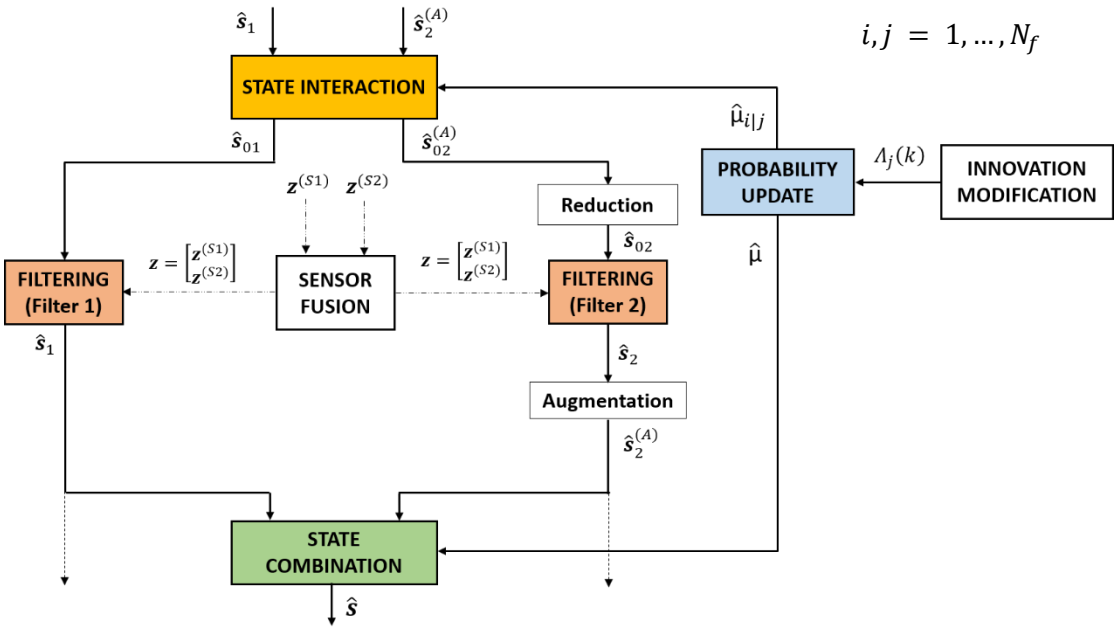

Figure 5.1. IMM-MI processing scheme.

As shown in this scheme, the basic structure is that of an IMM with two filters. Therefore, we can see the presence of the related blocks (*Interaction*, *Filtering*, *Probability Update* and *Combination*). With respect to the scheme shown in Figure 4.1, it is evident that this strategy is characterized by a higher complexity, due to the addition of more blocks, as for example the *Sensor Fusion* and the *Innovation Modification*. The *Augmentation* and *Reduction* blocks, instead, are necessary when the filters used in the IMM have different state dimensions.

5.1 Motion and Observation Models

As reported in Figure 5.1, we use $N_f = 2$ filters with two different models: the well-known **Nearly Constant Velocity (NCV) Motion Model**, that is one of the most adopted in various applications, especially when the target does not change its velocity and direction, and the **Stationary Model**, which represents the moments where the target is not moving and so its velocity is equal to zero; for this reason, in the following sections we will refer to this model with the acronym **V0**. In this specific case, the first filter is the NCV, while the second one is the V0.

The NCV Motion Model establishes that the velocity is almost constant (uniform linear motion), while the accelerations are seen as disturbance of this motion.

In the 2D case, namely when the tracking is performed on the XY-plane, the motion equations to be considered are the following:

$$\begin{cases} x_k = x_k + \dot{x}_{k-1} T + a_{x,k-1} T^2/2 \\ \dot{x}_k = \dot{x}_{k-1} + a_{x,k-1} T \\ y_k = y_{k-1} + \dot{y}_{k-1} T + a_{y,k-1} T^2/2 \\ \dot{y}_k = \dot{y}_{k-1} + a_{y,k-1} T \end{cases} \tag{5.1}$$

where (x_k, y_k) are the coordinates of the target at time k, $(\dot{x}_k, \dot{y}_k)$ are the related velocities along the *x* and *y* component, respectively, (x_{k-1}, y_{k-1}) are the coordinates at time $k-1$, $(\dot{x}_{k-1}, \dot{y}_{k-1})$ are the related velocities, T is the elapsed time between consecutive measurements, and $(a_{x,k-1}, a_{y,k-1})$ are the accelerations/disturbance along the two components.

In matrix form, we obtain:

$$\begin{bmatrix} x_k \\ \dot{x}_k \\ y_k \\ \dot{y}_k \end{bmatrix} = \begin{bmatrix} 1 & T & 0 & 0 \\ 0 & 1 & 0 & 0 \\ 0 & 0 & 1 & T \\ 0 & 0 & 0 & 1 \end{bmatrix} \begin{bmatrix} x_{k-1} \\ \dot{x}_{k-1} \\ y_{k-1} \\ \dot{y}_{k-1} \end{bmatrix} + \begin{bmatrix} T^2/2 & 0 \\ T & 0 \\ 0 & T^2/2 \\ 0 & T \end{bmatrix} \begin{bmatrix} a_{x,k-1} \\ a_{y,k-1} \end{bmatrix} \tag{5.2}$$

where the two vectors containing the target position and velocity components at time $k-1$ and k, are defined '**state vectors**'

$$\boldsymbol{s}_{k-1} = \begin{bmatrix} x_{k-1} \\ \dot{x}_{k-1} \\ y_{k-1} \\ \dot{y}_{k-1} \end{bmatrix}, \quad \boldsymbol{s}_k = \begin{bmatrix} x_k \\ \dot{x}_k \\ y_k \\ \dot{y}_k \end{bmatrix} \tag{5.3}$$

while we define

$$\boldsymbol{\Phi_1} = \begin{bmatrix} 1 & T & 0 & 0 \\ 0 & 1 & 0 & 0 \\ 0 & 0 & 1 & T \\ 0 & 0 & 0 & 1 \end{bmatrix}, \qquad \boldsymbol{G_1} = \begin{bmatrix} T^2/2 & 0 \\ T & 0 \\ 0 & T^2/2 \\ 0 & T \end{bmatrix} \tag{5.4}$$

where $\boldsymbol{\Phi_1}$ is the state transition matrix for the NCV model.

In compact form we can write equation (5.2) as

$$\boldsymbol{s}_k = \boldsymbol{\Phi_1} \cdot \boldsymbol{s}_{k-1} + \boldsymbol{v}_{k-1} \tag{5.5}$$

with

$$\boldsymbol{v}_{k-1} = \boldsymbol{G_1} \cdot \boldsymbol{a}_{k-1} \quad \text{and} \quad \boldsymbol{a}_{k-1} = \left[a_{x,k-1}, a_{y,k-1}\right]^T \tag{5.6}$$

Moreover, we indicate with Σ_a the covariance matrix of the model errors (assumed Gaussians) defined by the acceleration $\boldsymbol{a}_{k-1}$

$$\boldsymbol{\Sigma}_a = \begin{bmatrix} \sigma_{ax}^2 & 0 \\ 0 & \sigma_{ay}^2 \end{bmatrix} \tag{5.7}$$

and with $\boldsymbol{Q_1}$ the covariance matrix of $\boldsymbol{v}_{k-1}$.

It is appropriate to highlight that $\boldsymbol{\Sigma}_a$ represents one of the filter parameters to be set in the design phase. The choice of this parameter, and so of the standard deviations σ_{ax} and σ_{ay}, have to be pondered thinking to the behavior that we want to attribute to the filter: for the NCV case, small values of σ_{ax} and σ_{ay} indicate a high degree of confidence that the target is moving with a constant velocity, providing the possibility to follow accurately targets moving with a uniform linear motion. On the other hand, this choice generates great errors

when the actual motion of the target differs from the preset model. In contrast, when $\boldsymbol{\Sigma}_a$ is set with higher values, it is assumed to have a higher uncertainty on the actual target motion and so a lower weight is attributed to the prediction. As apparent, this strategy generates the reduction of the benefits produced by the exploitation of a good prediction when the target motion coincides with the filter motion model.

The observation model associated to this motion model is now presented. It relates the measurements provided by the sensor (angle, distance, etc.) and the target coordinates. In this case, we suppose that the sensor provides the position estimates to which it is added a measure error, namely

$$\boldsymbol{z}_k = \boldsymbol{H_1} \cdot \boldsymbol{s}_k + \boldsymbol{w}_k \tag{5.8}$$

where

$$\boldsymbol{z}_k = \begin{bmatrix} \boldsymbol{z}_x \\ \boldsymbol{z}_y \end{bmatrix} \tag{5.9}$$

is the vector containing the measurements, whereas $\boldsymbol{H_1}$ represents the incidence matrix defined as

$$\boldsymbol{H_1} = \begin{bmatrix} 1 & 0 & 0 & 0 \\ 0 & 0 & 1 & 0 \end{bmatrix} \tag{5.10}$$

This means that only the position components of the state vector are considered.

Finally, the observation noise $\boldsymbol{w}_{k+1}$ is a Gaussian random variable with zero mean and covariance matrix

$$\boldsymbol{R_1} = \begin{bmatrix} \sigma_x^2 & 0 \\ 0 & \sigma_y^2 \end{bmatrix} \tag{5.11}$$

where σ_x^2 and σ_y^2 are the variances of the measurement errors, along the x and y axes, respectively.

With the same approach, we also define the equations for the V0 Model. This model is characterized by the following relations

$$\begin{cases} x_k = x_{k-1} + v_{x,k-1} T \\ y_k = y_{k-1} + v_{y,k-1} T \end{cases} \tag{5.12}$$

where (x_k, y_k) are the coordinates of the target at time k, (x_{k-1}, y_{k-1}) are the coordinates at time $k-1$, T is the elapsed time between consecutive measurements, and $(v_{x,k-1}, v_{y,k-1})$ are the velocities/disturbance along the two components. In fact, in contrast with the NCV model, in this case the velocities are considered as errors.

In matrix form:

$$\begin{bmatrix} x_k \\ y_k \end{bmatrix} = \begin{bmatrix} 1 & 0 \\ 0 & 1 \end{bmatrix} \begin{bmatrix} x_{k-1} \\ y_{k-1} \end{bmatrix} + \begin{bmatrix} T & 0 \\ 0 & T \end{bmatrix} \begin{bmatrix} v_{x,k-1} \\ v_{y,k-1} \end{bmatrix} \tag{5.13}$$

where we define '**state vectors**' the two vectors containing the position components at time $k-1$ and k

$$\boldsymbol{s}_{k-1} = \begin{bmatrix} x_{k-1} \\ y_{k-1} \end{bmatrix}, \quad \boldsymbol{s}_k = \begin{bmatrix} x_k \\ y_k \end{bmatrix} \tag{5.14}$$

while we define

$$\boldsymbol{\Phi_2} = \begin{bmatrix} 1 & 0 \\ 0 & 1 \end{bmatrix}, \qquad \boldsymbol{G_2} = \begin{bmatrix} T & 0 \\ 0 & T \end{bmatrix} \tag{5.15}$$

where $\boldsymbol{\Phi_2}$ is the state transition matrix for the V0 model.

In compact form we can write the equation (5.13) as

$$\boldsymbol{s}_k = \boldsymbol{\Phi_2} \cdot \boldsymbol{s}_{k-1} + \boldsymbol{d}_{k-1} \tag{5.16}$$

with

$$\boldsymbol{d}_{k-1} = \boldsymbol{G_2} \cdot \boldsymbol{v}_{k-1} \quad \text{and} \quad \boldsymbol{v}_{k-1} = \left[v_{x,k-1}, v_{y,k-1}\right]^T \tag{5.17}$$

Moreover, we indicate with $\boldsymbol{\Sigma}_v$ the covariance matrix of the model errors (assumed Gaussians) defined by the velocity $\boldsymbol{v}_{k-1}$

$$\boldsymbol{\Sigma}_v = \begin{bmatrix} \sigma_{vx}^2 & 0 \\ 0 & \sigma_{vy}^2 \end{bmatrix} \tag{5.18}$$

and with $\boldsymbol{Q_2}$ the covariance matrix of $\boldsymbol{d}_{k-1}$. Even this time, as for the NCV model, $\boldsymbol{\Sigma}_v$ represents one of the filter parameters. Therefore, we can apply the same considerations reported above.

With respect to the observation model, the relations (5.8), (5.9) and (5.11) are valid. Only the incidence matrix will change, and it is represented by the identity matrix

$$\boldsymbol{H_2} = \begin{bmatrix} 1 & 0 \\ 0 & 1 \end{bmatrix} \tag{5.19}$$

As explained before, these two models have been used in the IMM that composes the proposed strategy.

After the presentation of the employed models, we can describe in detail the blocks in Figure 5.1.

5.2 Augmentation and Reduction

As apparent from the previous descriptions, the two models have different state dimensions, since the V0 filter does not have the velocity component. This is a problem when we combine the filtered estimates of both filters, during the *Interaction* and *Combination* stages. To solve this problem, we introduce a further operation in the scheme in Figure 5.1, namely the *Augmentation* block, where we increase the dimensions of the filtered state vectors with less elements (V0 model). Obviously, the same operation has been performed also in the initialization phase, at the first two iterations.

The possible solutions to obtain the augmentation have been extensively discussed in [51], where three different strategies have been compared: 1) the **simple augmentation**, which replaces the missed components of both the state vector and its covariance matrix with zeros, 2) the **unbiased augmentation**, which uses for the missed components the same values of the model that has the higher number of elements, and 3) the **uniform distribution augmentation**, which uses the mean and the variance of a random variable uniformly distributed between two values that have to be properly chosen according to the motion characteristics of the target. Our analyses, performed through Monte Carlo simulations, have confirmed the results reported in [51]

also for our scopes, therefore we decided to use the third strategy, which yields better performance in terms of position and velocity estimation accuracy and capability to recognize the actual motion of the target (model switching capability). As shown in Figure 5.1, the augmented version of the filtered state vector for the model V0 is indicated as $\hat{\boldsymbol{s}}_2^{(A)}$.

In contrast, the *Reduction* block in Figure 5.1 implements the opposite operation. In fact, before the *Filtering* stage, it is necessary to reduce again the dimensions of the augmented vectors, as we want to perform the filtering with the minimum dimensions for each model, in order to reduce the computational load and avoid any processing errors linked to the selected augmentation technique. To achieve the decrease of dimensions for V0 model, from four ($\hat{\boldsymbol{s}}_{02}^{(A)}(k-1|k-1)$) to two elements ($\hat{\boldsymbol{s}}_{02}(k-1|k-1)$), the velocity components of its state vector are deleted.

5.3 Sensor Fusion

Before starting with the detailed description of this methodology, it is necessary to define how to perform the fusion of the measurements available from different sensors.

There are different approaches to face this problem. First of all, in [45], the sensors are divided into two categories: synchronous and asynchronous. The first case is used if at a given sampling time there is one measurement from each sensor. The second one is applied if the measurements are obtained asynchronously. For the synchronized sensors, it is possible to define a second kind of classification with respect to the way of updating the measurement: the Sequential Updating, where this operation is carried out with the measurement of a sensor at a time, and the Parallel Updating, where the measurements from each sensor are used at the same time.

In our case, we assume to perform the coherent integration of packets for both the techniques, as described in [41]. This produces two important advantages: 1) the increase of the SNR, and 2) the possibility to synchronize the measurements of the employed sensors. In fact, with respect to this second point, we can assert that if we use, for both the approaches, the same receiving system (unique acquisition time), the same integration interval and the same time shift between consecutive intervals, we can suppose to deal with synchronized sensors, that give measurements at the same time instant. In this condition, it is possible to apply the Parallel Updating presented in [45], where the measurements of the employed sensors can be collected in a single vector as follows:

$$\boldsymbol{z}(k) = \begin{bmatrix} \boldsymbol{z}(k,1) \\ \vdots \\ \boldsymbol{z}(k,N_S) \end{bmatrix} = \boldsymbol{H}(k)\boldsymbol{s}(k) + \boldsymbol{w}(k) \tag{5.20}$$

where k represents the step of the filtering and N_S is the number of sensors available.

$$\boldsymbol{H}(k) = \begin{bmatrix} \boldsymbol{H}(k,1) \\ \vdots \\ \boldsymbol{H}(k,N_S) \end{bmatrix} \tag{5.21}$$

is the incident matrix that contains the contributions for each sensor,

$$\boldsymbol{w}(k) = \begin{bmatrix} \boldsymbol{w}(k,1) \\ \vdots \\ \boldsymbol{w}(k,N_S) \end{bmatrix}, \qquad \boldsymbol{R}(k) = E[\boldsymbol{w}(k)\boldsymbol{w}^T(k)] = diag[\boldsymbol{R}(k,l)] \tag{5.22}$$

are the observation noise and its covariance matrix. Moreover, l represents the index of the relative sensor.

At this point, it is possible to explain how we use this information in this work, through the description of the methodology reported in the next sections.

5.4 State interaction

After the initialization of the state vectors and their covariance matrices, the first step of the IMM is the interaction of the filtered states obtained at the previous iteration by the two employed filters, $\hat{\boldsymbol{s}}_1(k-1|k-1)$ and $\hat{\boldsymbol{s}}_2^{(A)}(k-1|k-1)$, respectively (at the first iterations, the filtered states are replaced with the results of the initialization). It is evident that the state of the V0 model has been modified with the augmentation operation (indicated with the superscript '*(A)*'), as described in Section 5.2.

This interaction produces two mixed states, $\hat{\boldsymbol{s}}_{01}(k-1|k-1)$ and $\hat{\boldsymbol{s}}_{02}^{(A)}(k-1|k-1)$, obtained by a linear combination of the contributions of each filter, where the multiplicative coefficients, which properly weigh them, are the mixing probabilities $\widehat{\mu}_{i|j}$ calculated in the *Probability Update* stage, namely

$$\mu_{i|j}(k-1|k-1) = \frac{1}{\bar{c}_j} p_{ij}\mu_i(k-1), \qquad i,j = 1,\dots,N_f \tag{5.23}$$

where p_{ij} are the Markov transition probabilities (from model i to model j), $\bar{c}_j$ is a normalization factor defined as

$$\bar{c}_j = \sum_{i=1}^{N_f} p_{ij}\mu_i(k-1)\,, \qquad j = 1,\dots,N_f \tag{5.24}$$

while $\mu_i(k-1)$ are the mode probabilities, namely the probability that the target moves according to the model i, at time $k-1$. Even these probabilities are calculated during the phase of *Probability Update*, while during the first two iterations they are initialized according to the designer considerations about the possible target motion. One of the most common choices is to consider the models identically distributed, and so $\mu_i(2) = 1/N_f = 1/2$, for two filters ($k-1=2$, because the filtering starts after the arrival of at least three measures).

After defining these quantities, it is possible to describe the real *Interaction* phase.

$$\hat{\boldsymbol{s}}_{0j}(k-1|k-1) = \sum_{i=1}^{N_f} \hat{\boldsymbol{s}}_i(k-1|k-1)\mu_{i|j}(k-1|k-1)\,, \quad j = 1,\dots,N_f \qquad \text{State Interaction} \tag{5.25}$$

$$\boldsymbol{P}_{0j}(k-1|k-1) = \sum_i \{\hat{\boldsymbol{P}}_i(k-1|k-1) + [\hat{\boldsymbol{s}}_i(k-1|k-1) - \hat{\boldsymbol{s}}_{0j}(k-1|k-1)] \cdot \left[\hat{\boldsymbol{s}}_i(k-1|k-1) - \hat{\boldsymbol{s}}_{0j}(k-1|k-1)\right]^T\} \cdot \mu_{i|j}(k-1|k-1)$$

State Interaction Covariance (5.26)

It is clear that the equations (5.25) and (5.26) have to be modified by replacing, where necessary, the "augmented" versions of the state vectors and covariance matrices.

The mixed states are then used as input at the two filters that compose the IMM. Before starting with the *Filtering* block, it is necessary to reduce again the dimensions of the augmented vectors, as explained in Section 5.2. This operation is performed by the *Reduction* block in Figure 5.1, where the velocity components are deleted, providing a decrease of dimensions for $\hat{\boldsymbol{s}}_{02}(k-1|k-1)$, from four to two elements.

5.5 Filtering

The Filtering block is made of several operations. Their description has been summarized in Figure 5.2.

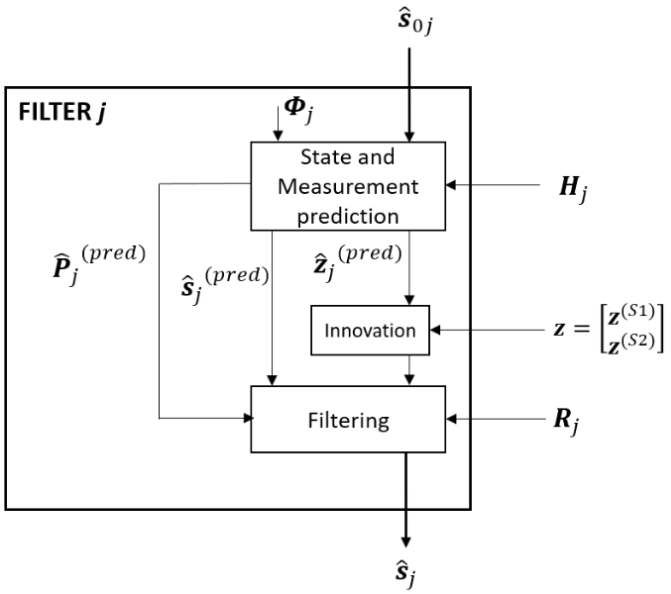

Figure 5.2. Filtering scheme.

The operations for a single filter are basically the same of a Kalman Filter, since the different filters operate separately, without any type of interaction in this phase.

1) <u>*State Prediction*</u>:

   The prediction exploits the mixed states previously calculated and obviously the information about the model, in particular the state transition matrix $\boldsymbol{\Phi}_j$.

$$\hat{\boldsymbol{s}}_j(k|k-1) = \boldsymbol{\Phi}_j(k-1)\hat{\boldsymbol{s}}_{0j}(k-1|k-1)$$

State Prediction (5.27)

$$\boldsymbol{P}_j(k|k-1) = \boldsymbol{\Phi}_j(k-1)\boldsymbol{P}_{0j}(k-1|k-1)\boldsymbol{\Phi}_j^T(k-1) + \boldsymbol{Q}_j(k-1)$$

State Prediction Covariance (5.28)

2) *Measurement Prediction:*

The observation model is then applied in order to determinate the predicted measurements (in our case, due to the use of the measurements defined directly over the XY-plane, the predicted measurements will be exactly the position components of the predicted state, see the incidence matrices defined in (5.10) and (5.19)). It is important to highlight that $\boldsymbol{H}_j(k)$ is the result of the application of Data Fusion techniques, whose description has been presented in Section 5.3.

$$\hat{\boldsymbol{z}}_j(k|k-1) = \boldsymbol{H}_j(k)\hat{\boldsymbol{s}}_j(k|k-1) \qquad \text{Measurement Prediction} \qquad (5.29)$$

3) *Innovation and Kalman Gain*:

Then, the innovation and the Kalman gain are calculated. The innovation represents the quantity of new information that is carried by the new measurement $\boldsymbol{z}(k)$, with respect to the past knowledge, namely the predicted measurement $\hat{\boldsymbol{z}}(k|k-1)$. Even this time $\boldsymbol{z}(k)$, $\boldsymbol{H}_j(k)$ and $\boldsymbol{R}_j(k)$ have been obtained into the Sensor Fusion block, described in detail in Section 5.3.

$$\boldsymbol{r}_j(k) = \boldsymbol{z}(k) - \hat{\boldsymbol{z}}_j(k|k-1) \qquad \text{Innovation} \qquad (5.30)$$

$$\boldsymbol{S}_j(k) = \boldsymbol{H}_j(k)\boldsymbol{P}_j(k|k-1)\boldsymbol{H}_j^T(k) + \boldsymbol{R}_j(k) \qquad \text{Innovation Covariance} \qquad (5.31)$$

$$\boldsymbol{K}_j(k) = \boldsymbol{P}_j(k|k-1)\boldsymbol{H}_j^T(k)\boldsymbol{S}_j^{-1}(k) \qquad \text{Gain of the Kalman Filter} \qquad (5.32)$$

4) *Filtering*:

From the obtained estimated values, the filtering operation is performed and the target state at the next iteration is obtained.

$$\hat{\boldsymbol{s}}_j(k|k) = \hat{\boldsymbol{s}}_j(k|k-1) + \boldsymbol{K}_j(k)\boldsymbol{r}_j(k) \qquad \text{Filtered State} \qquad (5.33)$$

$$\boldsymbol{P}_j(k|k) = \boldsymbol{P}_j(k|k-1) - \boldsymbol{K}_j(k)\boldsymbol{S}_j(k)\boldsymbol{K}_j^T(k) \qquad \text{Filtered State Covariance} \qquad (5.34)$$

At this point, each filter has produced its output, according to the specific motion model. These outputs have to be combined, in order to achieve a unique target position. To reach this purpose, it is necessary to update the model probabilities, that represent the multiplicative coefficients of the linear combination.

5.6 Innovation Modification and Probability Update

For the final *Combination* stage, the mode probabilities at time k depend on three factors: the mode probability at time $k-1$, the Markov transition probabilities p_{ij} and the likelihood, that represents the capability of the specific model to predict the target behavior.

$$\Lambda_j(k) = \frac{1}{\sqrt{|2\pi \boldsymbol{S}_j(k)|}} \cdot exp\{-\frac{1}{2}\boldsymbol{r}_j^T(k)\boldsymbol{S}_j^{-1}(k)\boldsymbol{r}_j(k)\} \quad \text{Likelihood} \quad (5.35)$$

$$c = \sum_{i=1}^{N_f} \Lambda_i(k) \cdot \bar{c}_i \quad \text{Normalization Factor} \quad (5.36)$$

$$\mu_j(k) = \frac{1}{c}\Lambda_j(k) \cdot \bar{c}_j \quad \text{Mode Probability} \quad (5.37)$$

where $\bar{c}_i$ is defined as in (5.24).

It is clear that we can modify the behavior of the IMM through the modification of the likelihood, and in particular of the innovation used to calculate it.

When both sensors provide the measurement at a given sampling time, the innovation is

$$\boldsymbol{r}_j = [r_j^{(S1)}(x),\ r_j^{(S1)}(y),\ r_j^{(S2)}(x), r_j^{(S2)}(y)]^T \quad \text{Innovation vector after Sensor Fusion} \quad (5.38)$$

where $j = 1$ for NCV model and $j = 2$ for V0 model, whereas the superscripts $(S1)$ and $(S2)$ stand for Sensor 1 and Sensor 2, respectively. In particular, we assume that Sensor 1 is the PSL, while Sensor 2 is the PBR. Therefore, $r_j^{(S1)}(x)$ is the x-component of the innovation for the model j and the PSL sensor. The other three components are defined similarly.

As explained above, the two sensors have a different behavior with respect to the motion status of the target. In fact, when it is stationary, the Passive Radar cannot detect it. This is a problem if only the PBR is available, because it yields the target missing. When another sensor (PSL) can be exploited together with the radar, two benefits can be reached: 1) the device-based strategy compensate for the lack of detections of the Passive Radar, because it could provide information about the target position, 2) the lack of detections may be used as an additional knowledge of the target behavior, since it is possible to be confident that the specific target is stationary when the PBR does not provide any detection.

As a consequence, the possibility to exploit this information to modify the IMM method to obtain a suitable methodology is an attractive solution.

The basic idea of the proposed approach is to unbalance the classical IMM made of two models, namely the NCV and the V0 models described before, with the objective of reaching a better matching between motion models and actual target motion.

A way to obtain this goal is to modify the innovation of the specific sensor for both the models depending on the presence or absence of PBR detections.

5.6.1 Absence of PBR detections

There are two basic reasons for which the PBR does not provide measurements at a given time: 1) the target is stationary, and so it is difficult to detect it, due to the cancellation stage performed during the processing, 2) the target is moving but the detection is missing ($P_d \neq 1$, where P_d is the Detection Probability).

In this situation, even the components $r_j^{(S2)}(x)$ and $r_j^{(S2)}(y)$ that are contained in the vector $\boldsymbol{r}_j$ defined in (5.38) are missing. This situation produces a reduction of the innovation dimensions. During the Filtering stage, we use this vector as it is; this only means that we operate with a single sensor instead of two. In contrast, during the Probability Update, since we want to exploit this information, we decided to operate as we had both the sensors available. In other words, the innovation is employed with all the four components. In order to unbalance the likelihood, we fill the components related to the innovation of Sensor 2 in (5.38), with artificial values. Since the absence of PBR measurements usually occurs when the target is stationary, we attribute lower values to the innovation of the V0 model, aiming at increasing the probability to choose this model, while we attribute higher values to the innovation of the NCV model.

The lowest value that can be attributed to $r_2^{(S2)}$ is zero, therefore it is possible to write

$$r_2^{(S2)} = [0, 0]^T \tag{5.39}$$

The artificial innovation for the first model (NCV) needs further considerations. As explained in the initial part of this Section, the absence of PBR detections can also occur when the target is moving, but the probability of detection is not equal to 1. This consideration leads to the introduction of a sort of '*Memory*' when we have to change $r_1^{(S2)}$: at the first missed measurement, the components of the artificial innovation for the NCV model are set with the standard deviations associated to the PBR measurements; from the second consecutive missed detection, those values are increased to twice the standard deviations, in order to further reduce the probability to select the NCV model. Therefore, the equations for the artificial innovation for the NCV model are defined as follows

$$r_1^{(S2)} = [\sigma_x^{(S2)}, \sigma_y^{(S2)}]^T, \quad if\ m = 1 \tag{5.40}$$

$$r_1^{(S2)} = [2 \cdot \sigma_x^{(S2)}, 2 \cdot \sigma_y^{(S2)}]^T, \quad if\ m > 1 \tag{5.41}$$

where m represents the counter of the consecutive missed detections. Obviously, this counter is reset when a new detection occurs.

For the sake of clarity, the entire vector, whose general form has been written in (5.38), is reported below:

$$\begin{cases} \boldsymbol{r}_1 = \left[r_1^{(S1)}(x),\ r_1^{(S1)}(y), \sigma_x^{(S2)}, \sigma_y^{(S2)}\right]^T, & if\ m = 1 \\ \boldsymbol{r}_1 = \left[r_1^{(S1)}(x),\ r_1^{(S1)}(y), 2 \cdot \sigma_x^{(S2)}, 2 \cdot \sigma_y^{(S2)}\right]^T, & if\ m > 1 \end{cases} \tag{5.42}$$

Innovation vector after Sensor Fusion for NCV model

$$\boldsymbol{r}_2 = [r_2^{(S1)}(x),\ r_2^{(S1)}(y), 0, 0]^T$$ Innovation vector after Sensor Fusion for V0 model (5.43)

5.6.2 Presence of PBR detections

A similar discussion can be made when the PBR sensor provides measurements.

This time, two situations can be found:

1) the PSL does not estimate any target position;
2) even the PSL sensor provides its measurement at the same time.

For the first point, we can use the same approach described in Section 5.6.1, but in this case the components related to the PSL sensor are missing. Therefore, the artificial innovations will fill the places occupied by the sensor indicated with $(S1)$ in (5.38).

$$\boldsymbol{r}_1 = [0, 0, r_1^{(S2)}(x),\ r_1^{(S2)}(y)]^T$$ Innovation vector after Sensor Fusion for NCV model (5.44)

$$\begin{cases} \boldsymbol{r}_2 = \left[\sigma_x^{(S1)}, \sigma_y^{(S1)}, r_2^{(S2)}(x),\ r_2^{(S2)}(y)\right]^T & ,\quad if\ m = 1 \\ \boldsymbol{r}_2 = \left[2 \cdot \sigma_x^{(S1)}, 2 \cdot \sigma_y^{(S1)}, r_2^{(S2)}(x),\ r_2^{(S2)}(y)\right]^T & ,\quad if\ m > 1 \end{cases}$$ Innovation vector after Sensor Fusion for V0 model (5.45)

where the case $m = 1$ is used to avoid errors due to false alarms for PBR when the target is stationary.

As mentioned above, this time we have also another case to face: both sensors provide the measurement at the same sampling time. In this case, it is important to exploit the innovations calculated in (5.30), for both measurements/sensors. However, it is also interesting to use our modification. To integrate these two considerations, we decided to use another strategy: the innovations obtained in the *Filtering* stage are used, but they are weighted through a multiplicative factor $F > 1$ that increases the innovation of the V0 model and decreases the innovation of the NCV model. In this way, the NCV model has a higher probability to be chosen.

$$\boldsymbol{r}_1 = \frac{1}{F} \cdot [r_1^{(S1)}(x),\ r_1^{(S1)}(y),\ r_1^{(S2)}(x), r_1^{(S2)}(y)]^T$$ Innovation vector after Sensor Fusion for NCV model (5.46)

$$\boldsymbol{r}_2 = F \cdot [r_2^{(S1)}(x),\ r_2^{(S1)}(y),\ r_2^{(S2)}(x), r_2^{(S2)}(y)]^T$$ Innovation vector after Sensor Fusion for V0 model (5.47)

A possible choice can be $F = 10$.

5.7 Combination

As for the Interaction, the Combination is calculated through the weighted sum of the filtered states estimated by the two filters. This time, the multiplicative coefficients are the mode probabilities $\mu_j(k)$ at time k.

$$\hat{\boldsymbol{s}}(k|k) = \sum_{j=1}^{N_f} \hat{\boldsymbol{s}}_j(k|k)\mu_j(k) \qquad \text{Final state} \qquad (5.48)$$

$$\boldsymbol{P}(k|k) = \sum_{j=1}^{N_f} \mu_j(k) \cdot \{\widehat{\boldsymbol{P}}_j(k|k) + [\hat{\boldsymbol{s}}_j(k|k) - \hat{\boldsymbol{s}}(k|k)] \cdot \left[\hat{\boldsymbol{s}}_j(k|k) - \hat{\boldsymbol{s}}(k|k)\right]^T\} \qquad \text{Final State Covariance} \qquad (5.49)$$

In the next sections the proposed approach will be evaluated over simulated target and experimental data. As mentioned above, the employed sensors, which provide the raw measurements to be filtered, are the PSL and the PBR.

Chapter 6
Tests on simulated target

The proposed methodology has been evaluated over simulated data. In order to show the potential of our strategy with respect to existing approaches, we will show the comparison with the classical Kalman Filter and IMM. In particular, the methodologies that we have tested are:

- The single Kalman Filter with the NCV Model that exploits the measurements of a single sensor (KF-NCV (Single Sensor)).
- The single Kalman Filter with the NCV Model that exploits the measurements of 2 sensors (KF-NCV (Sensor Fusion)).
- The IMM with 2 models (NCV and V0) that exploits the measurements of a single sensor (IMM (Single Sensor)).
- The IMM with 2 models (NCV and V0) that exploits the measurements of 2 sensors (IMM (Sensor Fusion)).
- The IMM-MI with 2 models (NCV and V0) that exploits the measurements of 2 sensors (IMM-MI (Sensor Fusion)).

An appropriate number of Monte Carlo simulations have been performed, each time with different noisy measurements related to the path we want to analyze.

6.1 Measurements generation

Before starting with the description of the simulations, it is necessary to define how to choose the position accuracies. We have defined the positioning standard deviations (σ_x and σ_y) based on the accuracies of the measurements obtained from each sensor (σ_θ (AoA), σ_r (Range), σ_τ (TDoA), etc.), through a theoretical evaluation of the position error maps for specific receiver locations, as described in Chapter 2.

For the sake of clarity, we reported here the related expressions

$$\sigma^2_{u_{LS}} = \mathrm{Tr}\{\left(\mathbf{H}^T\mathbf{H}\right)^{-1}\mathbf{H}^T\mathbf{\Sigma_R}\mathrm{H}\left(\mathrm{H}^T\mathrm{H}\right)^{-1}\} \tag{6.1}$$

$$\sigma^2_{u_{ML}} = \mathrm{Tr}\{\left(\mathrm{H}^T\Sigma_R^{-1}\mathrm{H}\right)^{-1}\} \tag{6.2}$$

When we work on simulated data, the accuracies impact in two different points of the processing:

1) In the definition of the Gaussian additive noise that we add to the real measurement of the expected path, for the definition of the simulated measurements, which we suppose to be those provided by the sensors;
2) In the determination of the matrices $\boldsymbol{R}_j(k)$, defined in (5.11), which represent one of the parameters used in the filtering stage, to be set during the initialization of the filter.

At this point, the positioning errors shown in the related accuracy maps, for the specific area of interest, will be the values that we can attribute to σ_x and σ_y.

Therefore, for the receiver geometry used in the preliminary tests presented in Chapter 3, the area of interest is defined by the grid depicted in Figure 3.1. The positioning error can be identically distributed between the x and y components of the target position. Therefore, for the selected region, it is possible to assume

$$\sigma_x = 2\ m,\ \ \sigma_y = 2\ m \tag{6.3}$$

As explained above, these values will be attributed to the standard deviations of the measurements used in (5.11). In addition, they will be used also to generate the noisy position of the simulated target.

The measurements generation has been performed two times, one for each sensor separately. Without loss of generality, both sensors have been considered with the same accuracies.

With reference to the available measurements, we assumed that the sensors provide the position estimates each $T = 0.1$ seconds. This choice is interesting because this is the same value used in our sensors for the time shift used to perform the coherent integration of both the AP (PBR) and device (PSL) packets.

According to the characteristics of the employed sensors, described in detail in the previous sections, the PSL could potentially provide a position estimate each T seconds, regardless the target motion status. Obviously, in real applications, it depends on the device activity and the data traffic conditions of the wireless network used to communicate, as explained in Chapter 3. Note that the PBR provides its estimates only when the target is moving, therefore we generate the radar measurements only for the 'MOVE' intervals.

Nevertheless, for the Passive Radar, it is necessary to consider even different cases that could be found in real applications. Firstly, there is the possibility to miss PBR measurements when the target is moving. This situation can be emulated through the definition of a Detection Probability, P_d, which is used only for the generation of the radar measurements during the 'MOVE' intervals. Secondly, there is also the possibility to have some '*False Plots*' associated to the target track during the tracking stage in the Range-Velocity plane reported in Figure 2.4. Therefore, we will define a False Target Probability, P_{ft}, which will be set (when necessary) with a low value, since this event has a very small probability to occur in our case.

With the purpose of facing all these situations, we have carried out different analyses, which have been reported in Section 6.4.

First of all, in order to study the behavior of all the employed filters with respect to the motion status of the target, we compare the methodologies in terms of errors produced during the path, through the evaluation of the Root Mean Square Error (RMSE) as a function of simulation time. Secondly, we also evaluate the RMSE

as a function of the Detection Probability for the PBR sensor, with the aim of analyzing the impact of the events mentioned above, especially on our technique.

6.2 Setting of the employed methodologies

We have already defined how to choose the measurement accuracy. It is now necessary to establish the value that we attribute to the principal parameters of the employed filters, namely the standard deviations of the model errors and the Markov transition matrix P.

6.2.1 KF-NCV (Single Sensor)

As explained in Section 5.1, one of the filter parameters to be set in the design phase is the covariance matrix $\boldsymbol{\Sigma}_a$ of the NCV model errors, defined in (5.7). In particular, it is important to choose representative standard deviations σ_{ax} and σ_{ay}. In the same Section, we also made some considerations on the effect of this choice on the performance of the Kalman Filter. In detail, we have to remind that with lower values of the standard deviations for the NCV model, the filter provides the possibility to follow accurately targets moving with a uniform linear motion.

In fact, considering a target that moves with a constant velocity during the whole simulation time, we obtain the results shown in Figure 6.1 for the RMSE normalized to the measurement error, with the aim to obtain the value 1 if the filtering is not performed. In the considered path, the target trajectory is characterized by a slope of $\alpha = 45^0$ with respect to the x-axis, therefore we present only the results for this component, since the curves for the y-component will be similar. In this figure, the Kalman Filter has been tested with four different values of standard deviation, namely $\sigma_{ax} = \sigma_{ay} = 1\ m/s^2$, $\sigma_{ax} = \sigma_{ay} = 0.5\ m/s^2$, $\sigma_{ax} = \sigma_{ay} = 0.1\ m/s^2$ and $\sigma_{ax} = \sigma_{ay} = 0.01\ m/s^2$, where we assumed that the filter behavior is the same on the two axes.

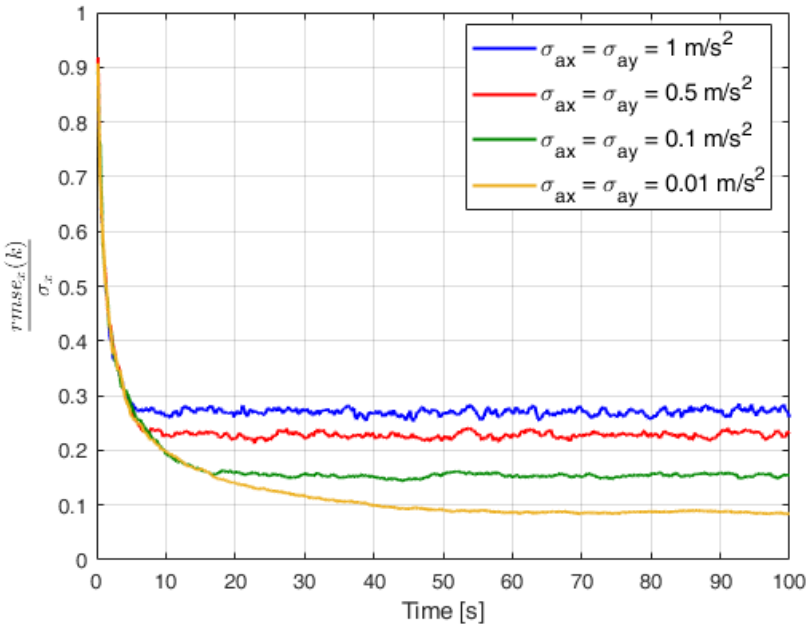

Figure 6.1. Comparison of the normalized positioning RMSE with respect to the x-axis, over a simulated target that moves with a uniform linear motion, for the Kalman Filters with four different values of σ_a.

The four curves confirm the previous considerations. In particular, the steady-state values are the same of the steady-state covariance obtained by solving the Riccati equation, as explained in [52].

Another confirmation can be found in the results of the tracking in the XY-plane, reported in Figure 6.2, only for three cases. In these plots, only the zoom around the point (0m, 55m) has been presented.

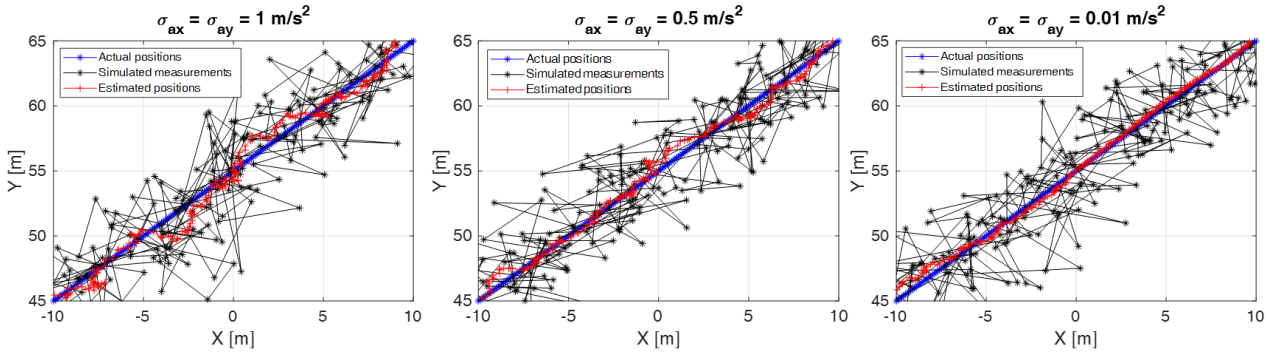

Figure 6.2. Tracking over the XY-plane of a target that moves with a constant velocity, for the Kalman Filter.

It is evident that when the target motion matches the motion model, the performance increases if the standard deviation of the model errors is chosen smaller.

On the other hand, this choice generates great errors when the actual motion of the target differs from the preset model. The errors can be reduced by increasing the values of σ_{ax} and σ_{ay}, but in contrast the filter behavior is less accurate when the target actually moves with a constant velocity.

Therefore, in order to highlight this aspect, we tried to apply these Kalman Filters over a simple Move-Stop-Move target.

The path is similar to the previous one, but this time the target will be stationary in a few points during the simulation time. The results have been shown in Figure 6.3.

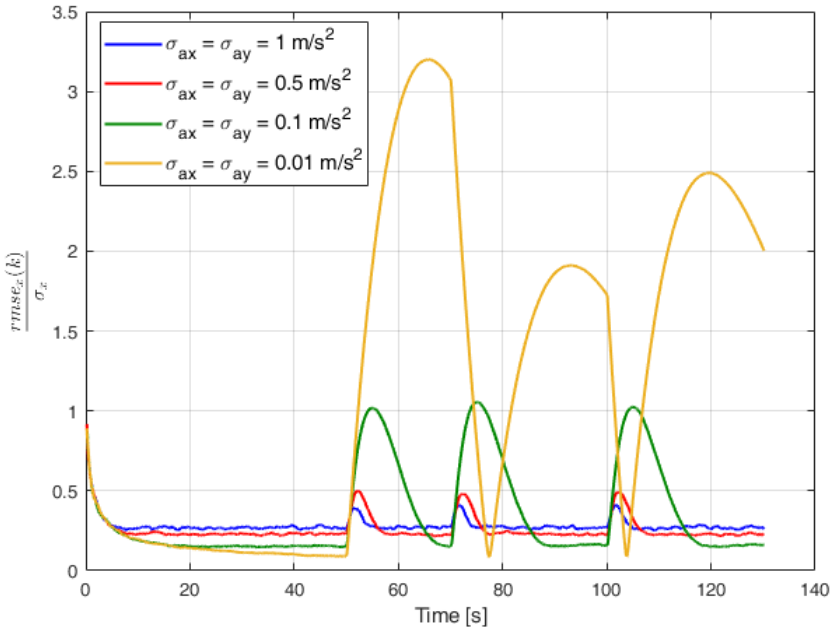

Figure 6.3. Comparison of the normalized positioning RMSE with respect to the x-axis, over a simulated Move-Stop-Move target, for the Kalman Filters with four different values of σ_a.

This figure confirms our considerations. Although with $\sigma_{ax} = \sigma_{ay} = 0.01\ m/s^2$ we achieve the best results when the target moves with a constant velocity, it produces too high errors in the transition phase between different motion status. This is due to the higher weight that is attributed to the prediction based on the employed model. The described event is less evident as the standard deviations decrease.

These considerations can be also noticed in Figure 6.4, where a small slot of a simulation is reported.

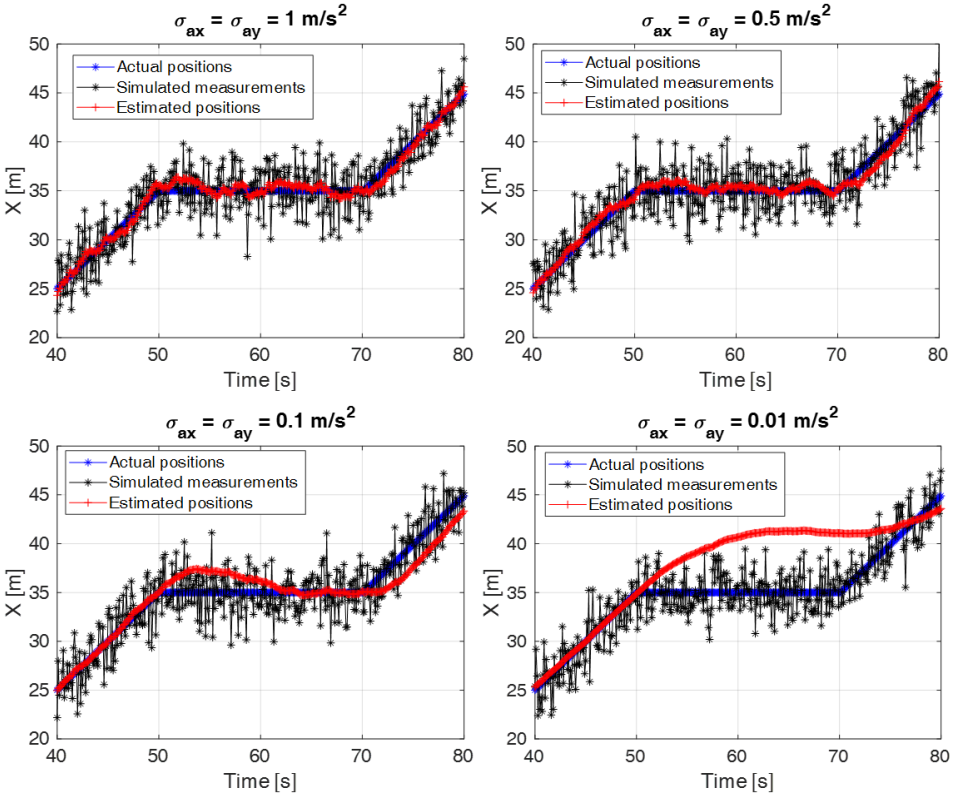

Figure 6.4. Tracking over the XY-plane of a Move-Stop-Move target, for the Kalman Filter.

In this figure, it is evident that lower values of σ_{ax} provide better performance in the intervals where the target is moving (before 50 s and after 70 s) but the main problem is the difficulty of the Kalman Filter to estimate the correct velocity when this changes rapidly. However, after a certain transient, the Kalman Filter starts again to follow the correct path of the target. This is due to the fact that when the target is stationary, its behavior is the same of a uniform linear motion where the constant velocity is equal to zero. The described phenomenon is particularly evident by observing the case with $\sigma_{ax} = \sigma_{ay} = 0.1\ m/s^2$ in Figure 6.4.

In conclusion, we have to find a tradeoff between the advantages and the drawback of each choice. Therefore, we decided to use $\sigma_{ax} = \sigma_{ay} = 0.5\ m/s^2$ because, for our purposes, it provides the best compromise between accuracies in both the transient and steady-state.

6.2.2 KF-NCV (Sensor Fusion)

The same considerations can be made for the Kalman Filter that uses the measurements of two sensors. Therefore, also in this case we used the values $\sigma_{ax} = \sigma_{ay} = 0.5\ m/s^2$.

6.2.3 IMM (Single Sensor)

For the IMM approach, we have to set two types of standard deviations: 1) σ_{ax} and σ_{ay} for the NCV model, and 2) σ_{vx} and σ_{vy} for the V0 model.

As explained in Section 4.2, the IMM is not characterized by the problem described for the Kalman Filter, since the change of motion is managed with the multiple models structure.

Therefore, for the NCV model, we can choose a lower value for the standard deviations of the model errors. A good choice could be the lowest value examined for the Kalman Filter, that is $\sigma_{ax} = \sigma_{ay} = 0.01\ m/s^2$. The proof of this statement can be seen in Figure 6.5, where we fixed the standard deviations of the V0 model, in this case we use $\sigma_{vx} = \sigma_{vy} = 0.1\ m/s$, and we use four different values for the standard deviations of the NCV model errors. The examined cases are the same analyzed for the KF-NCV method, namely $\sigma_{ax} = \sigma_{ay} = 1\ m/s^2$, $\sigma_{ax} = \sigma_{ay} = 0.5\ m/s^2$, $\sigma_{ax} = \sigma_{ay} = 0.1\ m/s^2$ and $\sigma_{ax} = \sigma_{ay} = 0.01\ m/s^2$.

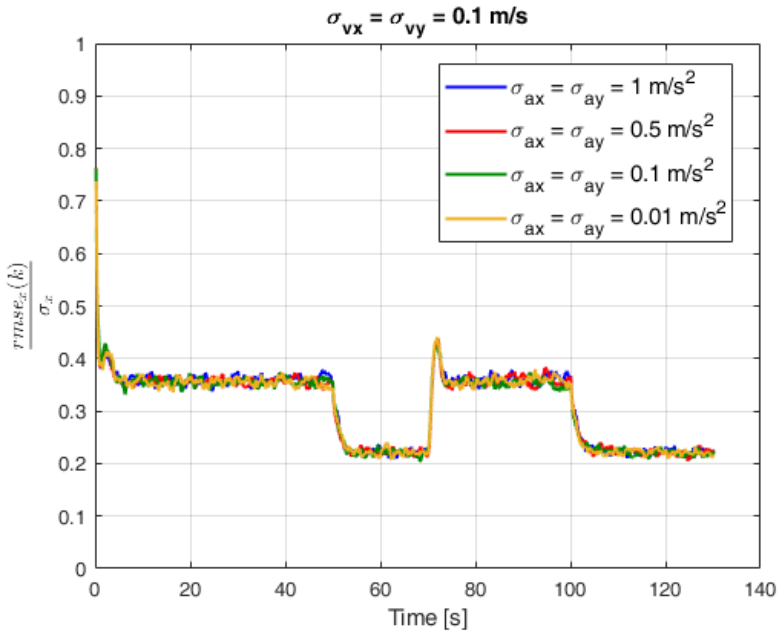

Figure 6.5. Comparison of the normalized positioning RMSE with respect to the x-axis, over a simulated Move-Stop-Move target, for the IMM method with four different values of σ_a.

We can notice that this time the errors in the instants between different motion status have been avoided, thanks to the exploitation of two models. In addition, the performance is quite similar for all cases, therefore we can choose indifferently one of the proposed values for σ_{ax}.

However, if we analyze the results for a higher time interval between consecutive measurements, for example $T = 1$ second, the decision can be addressed towards the choice of $\sigma_{ax} = \sigma_{ay} = 0.01\ m/s^2$, as mentioned previously and shown in Figure 6.6.

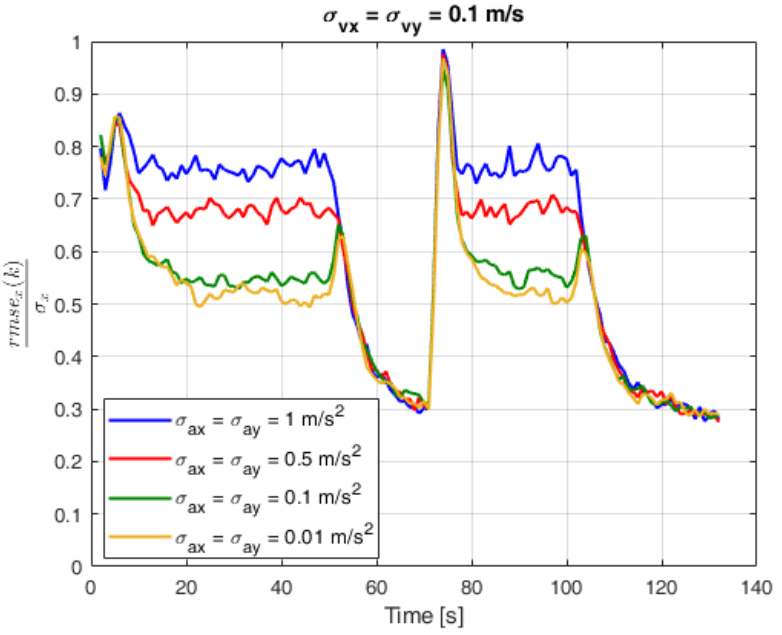

Figure 6.6. Comparison of the normalized positioning RMSE with respect to the x-axis, over a simulated Move-Stop-Move target, for the IMM method with four different values of σ_a, when T = 1 s.

The explanation of the reasons for which there are differences between the behavior of the IMM when $T = 1$ and $T = 0.1$, will be discussed in Section 6.4.

For the selected value $\sigma_{ax} = \sigma_{ay} = 0.01\ m/s^2$, we also evaluated the possible solution for σ_{vx}. The same four values have been evaluated, namely $\sigma_{vx} = \sigma_{vy} = 1\ m/s$, $\sigma_{vx} = \sigma_{vy} = 0.5\ m/s$, $\sigma_{vx} = \sigma_{vy} = 0.1\ m/s$ and $\sigma_{vx} = \sigma_{vy} = 0.01\ m/s$. The results can be observed in Figure 6.7.

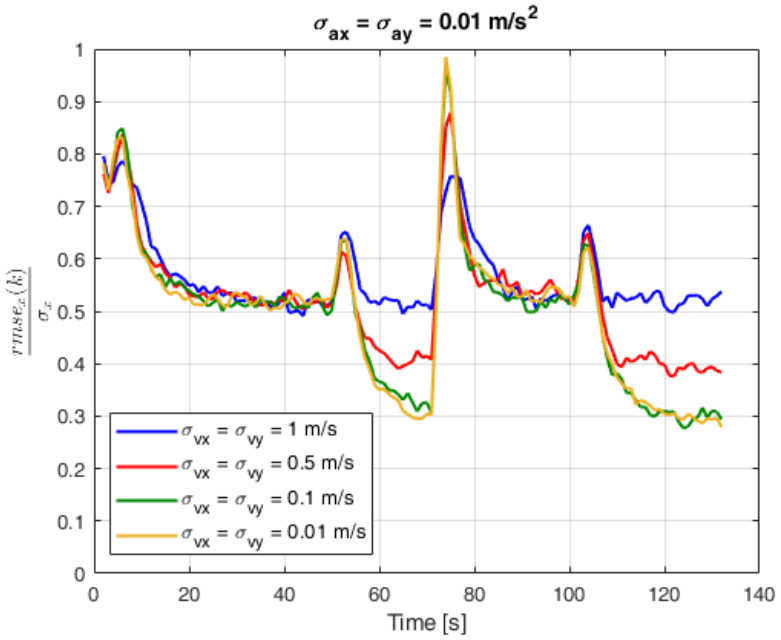

Figure 6.7. Comparison of the normalized positioning RMSE with respect to the x-axis, over a simulated Move-Stop-Move target, for the IMM method with four different values of σ_v, when T = 1 s.

In this figure, we can notice that the curves for $\sigma_{vx} = \sigma_{vy} = 0.1\ m/s$ and $\sigma_{vx} = \sigma_{vy} = 0.01\ m/s$ are very close one to the other, therefore we can chose for example the first solution.

For the IMM, even another parameter has to be set, that is the Markov transition matrix P, which contains the probabilities to pass from a state to another, p_{ij}.

We decided to choose the following values, with the purpose of avoiding the preference of a model with respect to the other.

$$P = \begin{bmatrix} 0.95 & 0.05 \\ 0.05 & 0.95 \end{bmatrix} \tag{6.4}$$

6.2.4 IMM (Sensor Fusion)

The same considerations can be applied to the Interacting Multiple Model that uses the measurements of two sensors. Therefore, also in this case we have the same choices for σ_{vx}, σ_{ax} and P.

6.2.5 IMM-MI (Sensor Fusion)

Since the IMM and the IMM-MI have the same basic structure, even for the IMM-MI we use the same values of σ_{vx}, σ_{ax} and P of the IMM.

In this case, we implement also the Innovation Modification as described in Section 5.6. In particular, in equations (5.46)-(5.47) we consider $F = 10$.

In Table 6, we summarize the setting of the parameters for the employed methodologies.

Table 6. Setting of the employed methodologies.

Approach	$\sigma_{ax} = \sigma_{ay}\ [m/s^2]$	$\sigma_{vx} = \sigma_{vy}\ [m/s]$	P
KF-NCV (Single Sensor)	0.5	-	-
KF-NCV (Sensor Fusion)	0.5	-	-
IMM (Single Sensor)	0.01	0.1	$\begin{bmatrix} 0.95 & 0.05 \\ 0.05 & 0.95 \end{bmatrix}$
IMM (Sensor Fusion)	0.01	0.1	$\begin{bmatrix} 0.95 & 0.05 \\ 0.05 & 0.95 \end{bmatrix}$
IMM-MI (Sensor Fusion)	0.01	0.1	$\begin{bmatrix} 0.95 & 0.05 \\ 0.05 & 0.95 \end{bmatrix}$

6.3 Case study: Simulated Move-Stop-Move Target with changes of direction

As the parameters of the filters have been already defined, in this Section we present a specific trajectory, characterized by a complexity that is higher than the previously exploited paths, designed to highlight the main differences between the analyzed methodologies. In particular, we want to demonstrate the advantages of our strategies with respect to the others in a typical situation. The simulated trajectory is the following

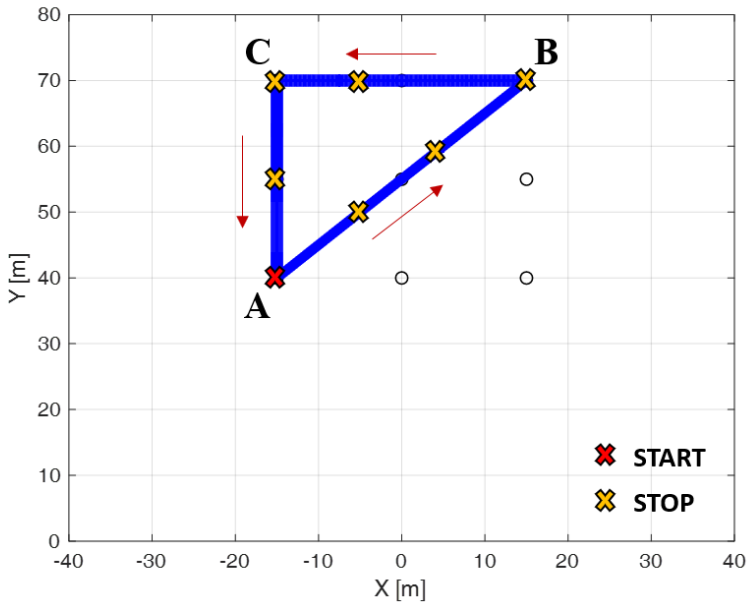

Figure 6.8. Simulated trajectory.

In Figure 6.8, the black circles are the nine points of a grid used as reference, in analogy with that used in the acquisition campaigns described in Chapter 3, the blue points are the true measurements (without noise) of the ideal path, the red cross is the starting point of the trajectory, and the yellow crosses are the points where the simulated target is assumed to be stationary.

The target starts from point A, indicated with the red cross in Figure 6.8, namely the point (-15m, 40m) of the grid. It moves with an angle $\alpha = 45^0$ with respect to the x-axis, with a constant velocity along both the axis ($v_x = v_y = 1\frac{m}{s} \Rightarrow v = 1.4\frac{m}{s}$). It stops two times before reaching point B (15m, 40m). After a few seconds where the target is stationary, it moves again towards point C, and finally comes back to the starting point A. In both cases the absolute velocity is $v = 1.5\frac{m}{s}$. For the considered trajectory, the duration of each interval is reported in Figure 6.9.

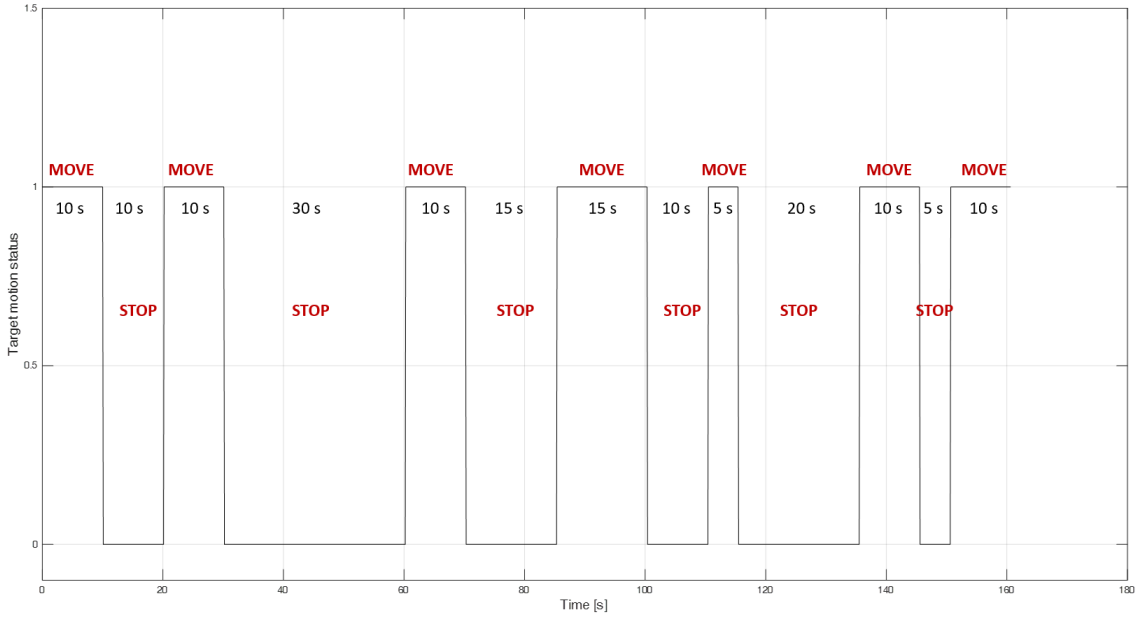

Figure 6.9. Target motion description: value = 1, the target is moving; value = 0, the target is stationary.

In this figure, the value 1 represents the intervals where the target is moving with a uniform linear motion, whereas the value 0 indicates the intervals where the target is stationary. In addition, also the duration in seconds of each interval has been reported. It is clear that the 6 intervals labeled with the word 'STOP' correspond to the 6 yellow crosses in Figure 6.8.

The measurements defined with this procedure represent the ground truth, that is the real path of the target. In order to simulate the measurements provided by the sensors, we have injected Gaussian additive noise, generated through the exploitation of the values reported in (6.3).

Over this trajectory, we perform the following tests:

1) The comparison of the methodologies in terms of errors produced during the path, through the evaluation of the Root Mean Square Error (RMSE) as a function of simulation time.
2) The evaluation of the RMSE as a function of the Detection Probability for the PBR sensor.

6.4 Evaluation of the RMSE as a function of simulation time

The first analysis that we present is the evaluation of the Root Mean Square Error (RMSE) with respect to the simulation time, as reported also for the setting of the filters in Section 6.2. This study is important to observe the behavior of all the employed filters with respect to the motion status of the target. To achieve this purpose, $N = 1000$ trials of Monte Carlo simulations have been run.

The five approaches mentioned in the initial part of the Chapter 6 have been analyzed and compared.

The standard deviation of the model errors, σ_a and σ_v, have been chosen in Section 6.2, and the generation of the measurements has been carried out as described in Section 6.1, therefore $T = 0.1$ seconds.

This first test has been performed in ideal conditions. In fact, the Detection Probability, P_d, and the False Target Probability, P_{ft}, are set with the following values

$$P_d = 1, \quad P_{ft} = 0 \tag{6.5}$$

In this way, the PBR sensor does not provide any measurements when the target is stationary ($P_{ft} = 0$), while it always estimates the target position when this is moving ($P_d = 1$). The results in these conditions are reported in Figure 6.10.

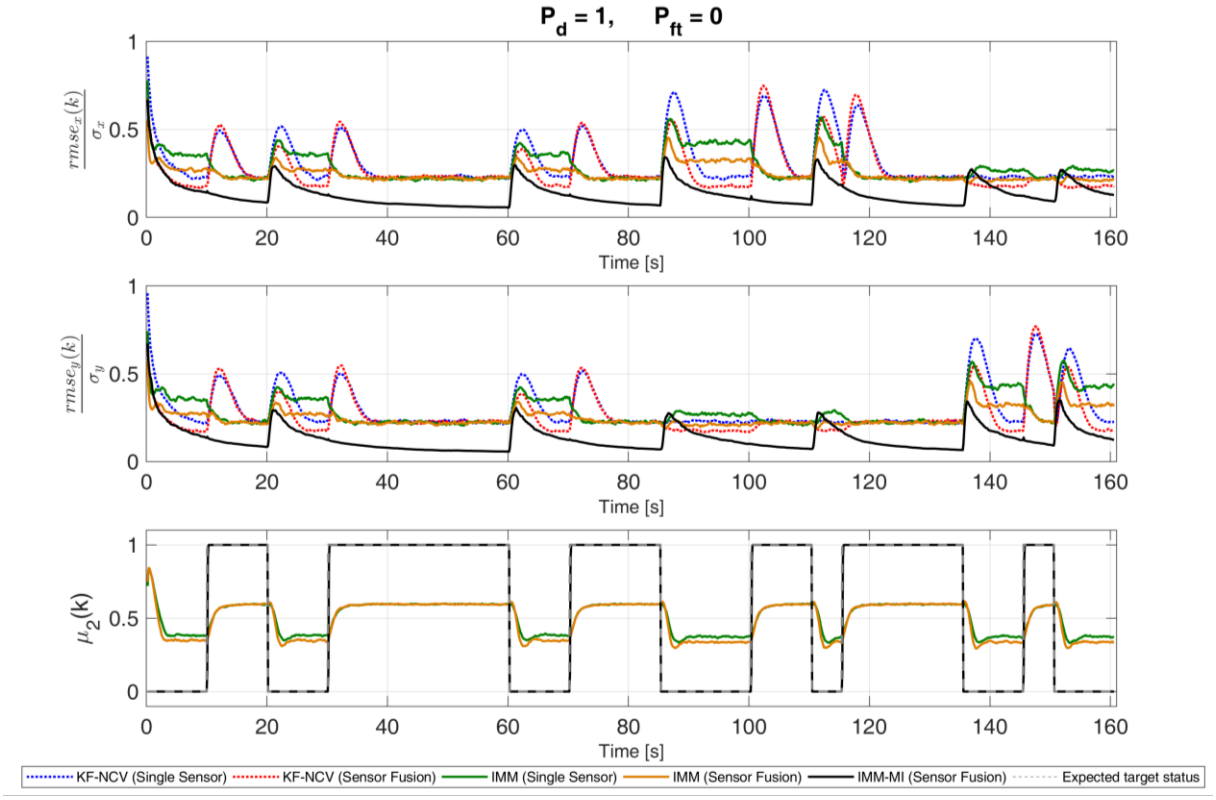

Figure 6.10. Comparison of the normalized positioning RMSE with respect to the x-axis (top), and the y-axis (center), over a simulated Move-Stop-Move target for $P_d = 1$ and $P_{ft} = 0$. In the subplot at the bottom, there is the relative V0 model probability.

Figure 6.10 is composed by three subplots. The first two graphics show the normalized RMSE with respect to the x-axis and the y-axis, respectively, whereas the third one presents the V0 model probabilities of the filters with the IMM structure, compared with the expected target status (value = 1 for STOP, value = 0 for MOVE) that is drawn with the grey dashed line. As apparent, the model probability of the Kalman Filters is not reported, since the model is just one.

The curves show that the IMM-MI (black solid line) outperforms the other strategies for almost the entire simulation. In particular, very good performance can be achieved when the target is stationary and the proposed approach allows the reduction of the error of about 90-95% with respect to the use of the raw measurements, for which the normalized RMSE would be equal to 1. In the same intervals, the other strategies provide an improvement of accuracy of about 75-80% with respect to the use of the raw measurements.

As expected, by observing the transient states, when the target changes its motion status, the KF-NCV is the approach that yields the worst performance, since it is not devised to manage change of dynamics. In contrast, the IMM-MI is still the best approach, even in this situation, especially in the transition between MOVE and

STOP status, where the IMM-MI is not characterized by an increase of error. This is due to the fast capability of our strategy to change motion model and attribute the correct velocity ($v = 0$) to the target when the PBR measurements are not received by the tracker. On the other hand, the tracking in the transition between STOP and MOVE intervals is less accurate, since a longer time is necessary to estimate the correct velocity when the target starts to move again.

The exception can be found in few points, and in the specific case in the part of the trajectory where the target moves orthogonally to the axes. In fact, we can observe what happens after the third (about 85 s) and the fourth (about 110 s) stops, when the target starts again to move orthogonally to the y-axis. In these cases, the IMM-MI does not provide the lowest error for the RMSE calculated over the y-axis (second subplot in Figure 6.10). The reason of this result is clear if we think that, in this portion of path, the target is stationary with respect to the y-axis, while is moving along the x-axis, but the model probability is the same for the two directions and the model selection for the IMM-MI strongly depends on the presence or the absence of PBR detections. Therefore, the selected model does not match the real motion of the target in that direction. The same considerations can be made for the last segment of the path, this time for the x-component of the RMSE (subplot on the top in Figure 6.10). Nevertheless, the increase of the error is negligible, since the achieved values are not too high, and they occur for a very short time.

Another point that has to be highlighted is the behavior of the IMM in the steady-state intervals and in particular when the target is moving. In these situations, the RMSE of the IMM is higher than the RMSE of both the KF-NCV and the IMM-MI. This is probably due to the small time interval between consecutive measurements ($T = 0.1$ s) when the target is not very fast, as in this case. Therefore, the change of position of the target is so small that it is hard for the IMM to understand if the target is stationary or moving. In fact, by observing the V0 model probability reported in Figure 6.10, it is evident that the decision of the motion model is characterized by a high uncertainty for the two classical IMM methods (close to 50% of choosing V0 or NCV). This confirm that the classical IMM is not appropriate to face the problem of Move-Stop-Move target tracking.

It is evident that the exploitation of two complementary sensors (PBR and PSL) and the information about the presence of PBR measurements for the innovation modification is a good solution for this problem, as this strategy helps the choice of the correct model, when operates in ideal conditions.

The second test aims to analyze the case of non-ideal conditions. In real applications, reasonable values for the Detection Probability and False Target Probability are

$$P_d = 0.9, \quad P_{ft} = 10^{-2} \tag{6.6}$$

This means that there is the possibility that the PBR provides measurements when the target is stationary ($P_{ft} = 10^{-2}$), and it misses some target position estimates when this is moving ($P_d = 0.9$). The results in these conditions are reported in Figure 6.11.

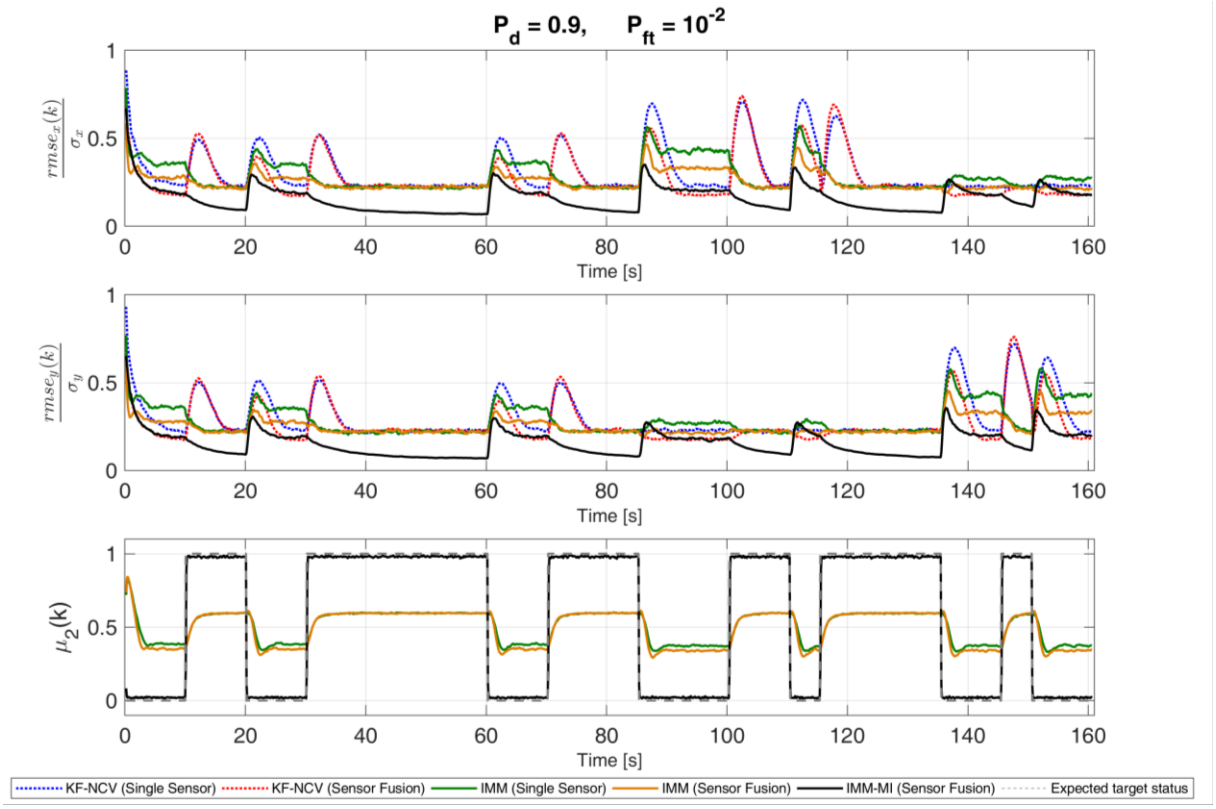

Figure 6.11. Comparison of the normalized positioning RMSE with respect to the x-axis (top), and the y-axis (center), over a simulated Move-Stop-Move target for $P_d = 0.9$ and $P_{ft} = 10^{-2}$. In the subplot at the bottom, there is the relative V0 model probability.

The results are similar to the ideal case shown in Figure 6.10, but as expected the performance of the IMM-MI decreases, especially in the moving intervals, where it is evident that the black solid line assumes higher values for the RMSE, according to the reduction of the matching between the V0 model probability and the expected target status (grey dashed line). However, the proposed strategy generally outperforms the other approaches during the whole simulation time.

6.5 Evaluation of the RMSE as a function of the Detection Probability for the PBR sensor

As shown in Section 6.4, the possible limitation of our methodology could be represented by the irregularity of PBR behavior, based on the presence of the detections when the target is stationary and their missing when the target is moving.

In this Section, we stress this situation through the evaluation of the performance with respect to the P_d, for fixed values of P_{ft}.

For the first test, we consider having ideal conditions for the False Target Probability, therefore we set $P_{ft} = 0$. In contrast, we consider 10 different values for the Detection Probability, namely

$$\boldsymbol{P_d} = [1, 0.99, 0.97, 0.95, 0.90, 0.85, 0.80, 0.70, 0.60, 0.50] \tag{6.7}$$

The vector containing the possible Detection Probabilities is denser for higher values of P_d, since they represent typical situation in real applications.

The results achieved with these configurations for the normalized RMSE, averaged over the entire simulation, are reported in Figure 6.12.

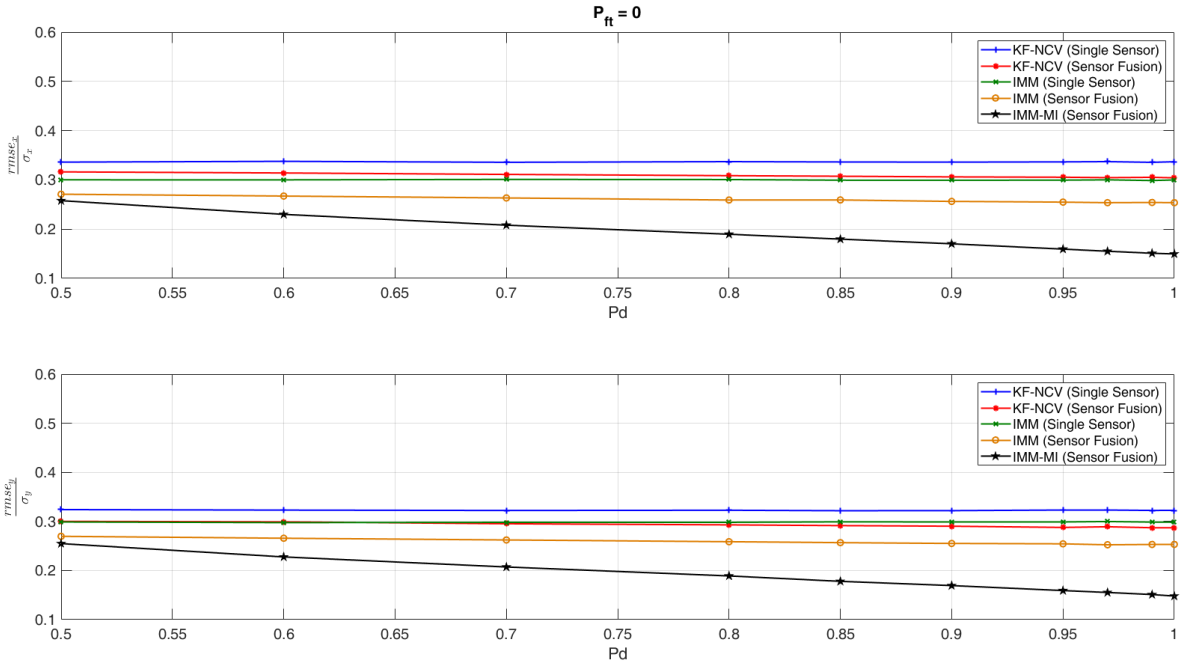

Figure 6.12. Comparison of the normalized positioning RMSE averaged over the entire simulation vs P_d, with respect to the x-axis (top), and the y-axis (bottom), over a simulated Move-Stop-Move target for $P_{ft} = 0$.

The curves show that the IMM-MI (black line) provides the best performance in terms of positioning accuracies. This behavior is more evident when the sensors work in better conditions, namely for higher values of P_d. It is interesting to notice that also for very low values of P_d the IMM-MI approach is yet the best one. However, in contrast with the other methodologies, we can also notice that our strategy is strongly influenced by the behavior of the PBR sensor, and in particular by the presence of its measurements.

In order to have a higher knowledge of the behavior of the compared strategies, the performance is also evaluated in specific points of the simulation. In particular, it is interesting to analyze the results for the transient state and the steady state, separately.

In detail, the transient is evaluated few seconds after the transition between different motion status, while the steady state is calculated in the subsequent interval.

These evaluations have been presented in Figure 6.13 for the transient and Figure 6.14 for the steady state.

Due to graphical needs, we use just one legend for both the subplot in Figure 6.13.

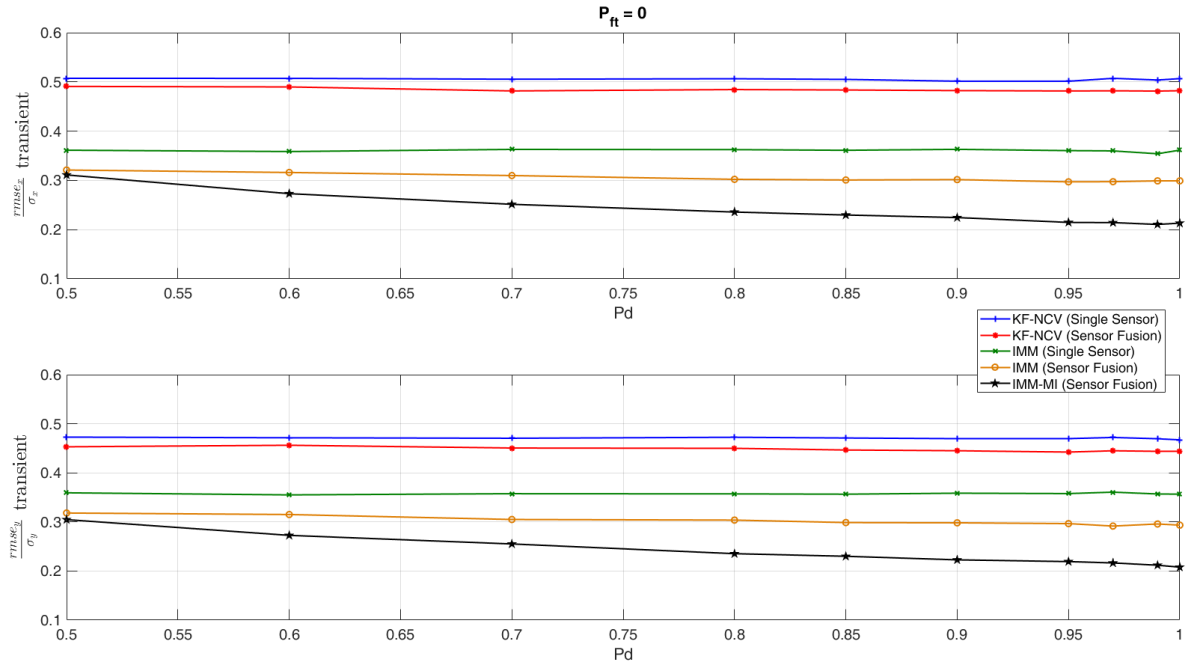

Figure 6.13. Comparison of the normalized positioning RMSE in transient state vs P_d, with respect to the x-axis (top), and the y-axis (bottom), over a simulated Move-Stop-Move target for $P_{ft} = 0$.

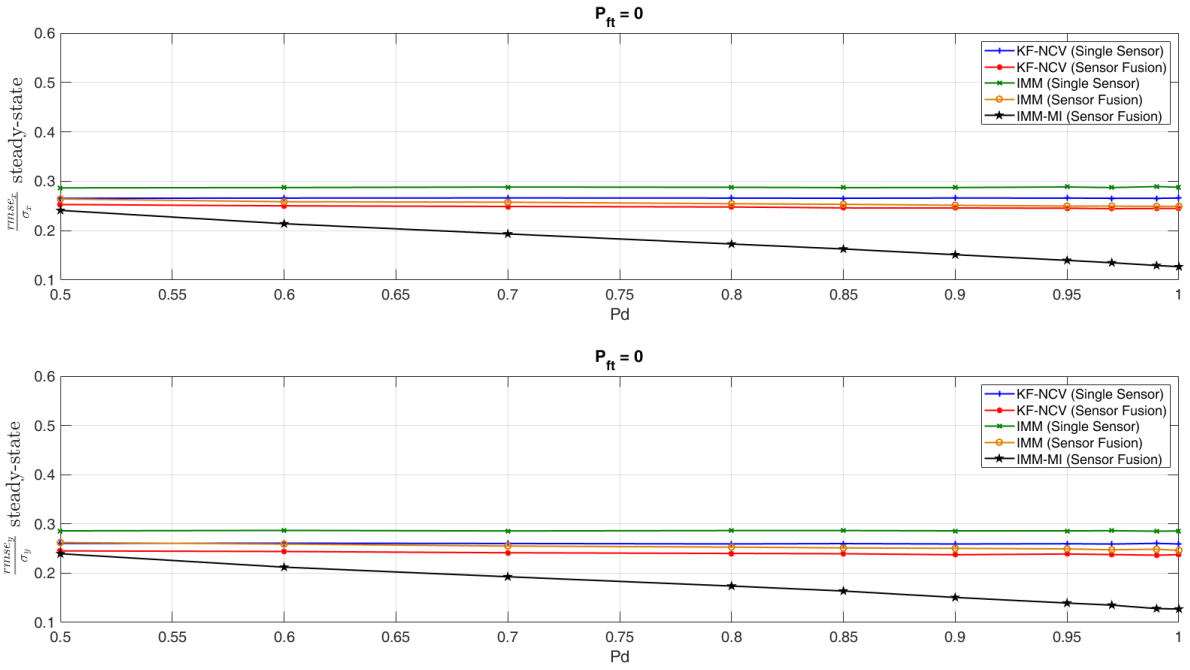

Figure 6.14. Comparison of the normalized positioning RMSE in steady state vs P_d, with respect to the x-axis (top), and the y-axis (bottom), over a simulated Move-Stop-Move target for $P_{ft} = 0$.

For the second test, we make the conditions worse even for the False Target Probability, therefore we set $P_{ft} = 10^{-2}$. In this way, the IMM-MI is further stressed, with the purpose of quantifying its limitations when the operating conditions are unfavorable.

The results for this case are reported in Figure 6.15, Figure 6.16 and Figure 6.17, for the entire simulation, the transient and the steady state, respectively.

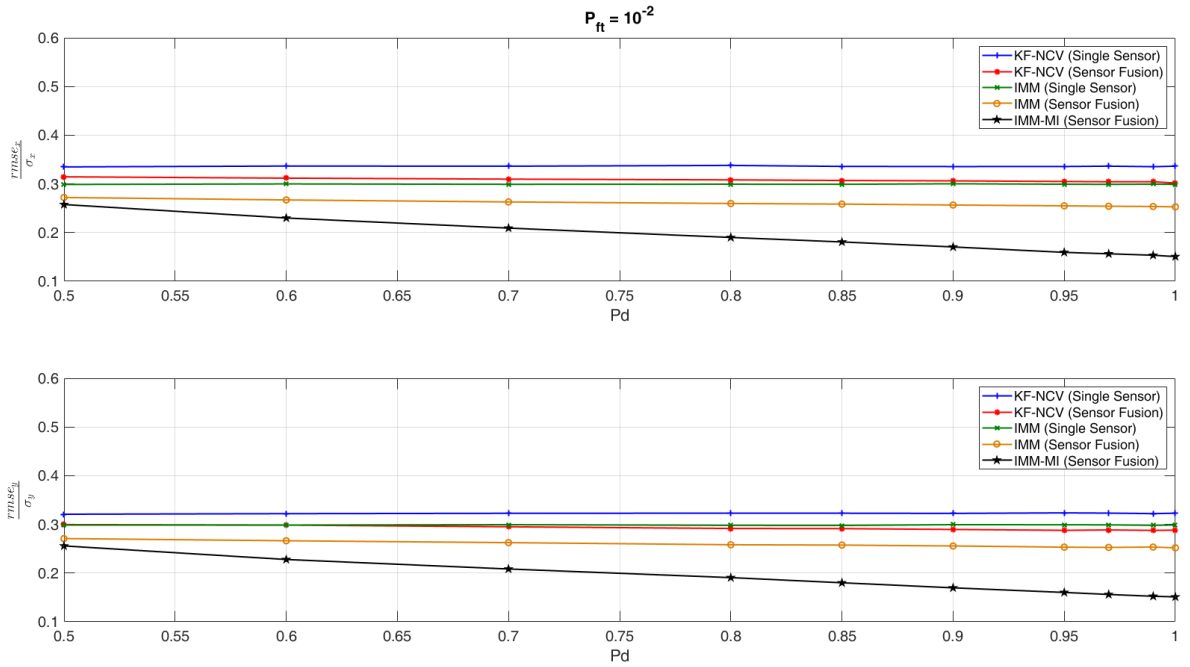

Figure 6.15. Comparison of the normalized positioning RMSE averaged over the entire simulation vs P_d, with respect to the x-axis (top), and the y-axis (bottom), over a simulated Move-Stop-Move target for $P_{ft} = 10^{-2}$.

Even this time, the performance of the proposed approach (black line) is better than the other ones. This is encouraging because it means that our strategy can be applied also in real applications.

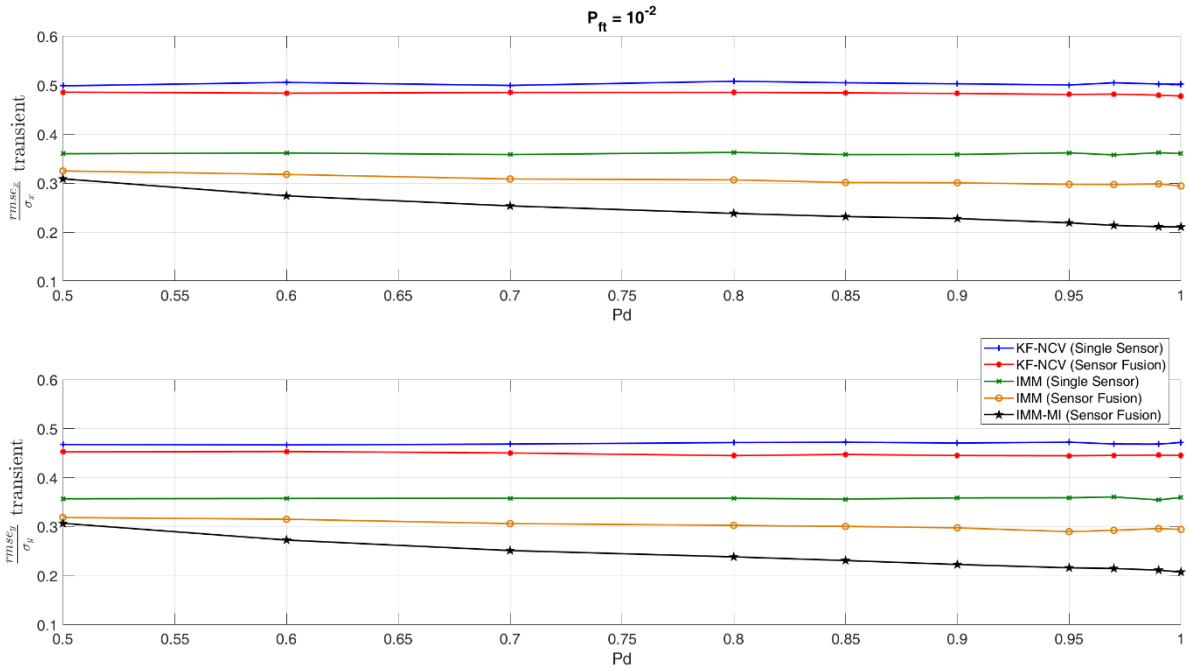

Figure 6.16. Comparison of the normalized positioning RMSE in transient state vs P_d, with respect to the x-axis (top), and the y-axis (bottom), over a simulated Move-Stop-Move target for $P_{ft} = 10^{-2}$.

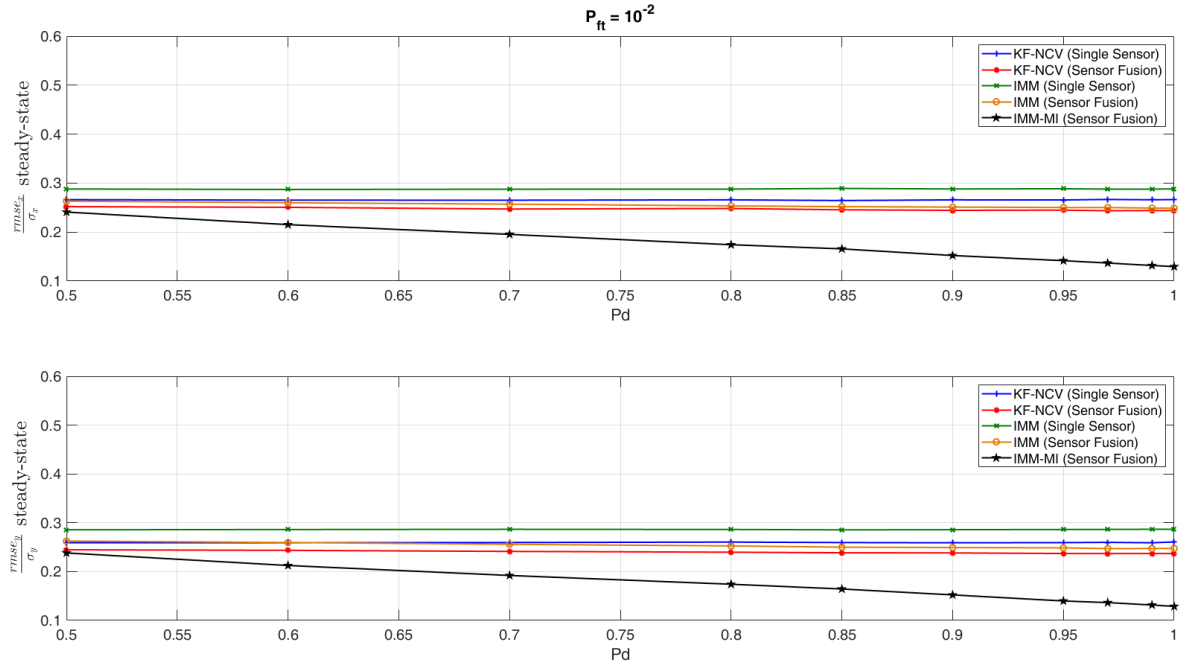

Figure 6.17. Comparison of the normalized positioning RMSE in steady state vs P_d, with respect to the x-axis (top), and the y-axis (bottom), over a simulated Move-Stop-Move target for $P_{ft} = 10^{-2}$.

An analysis with worse condition can be useful. This time we reported just the results for the average over the entire simulation time, that provides the idea of the general performance of the tested methodologies. We can set, for example, the False Target Probability with the value $P_{ft} = 0.1$. The related results are reported in Figure 6.18.

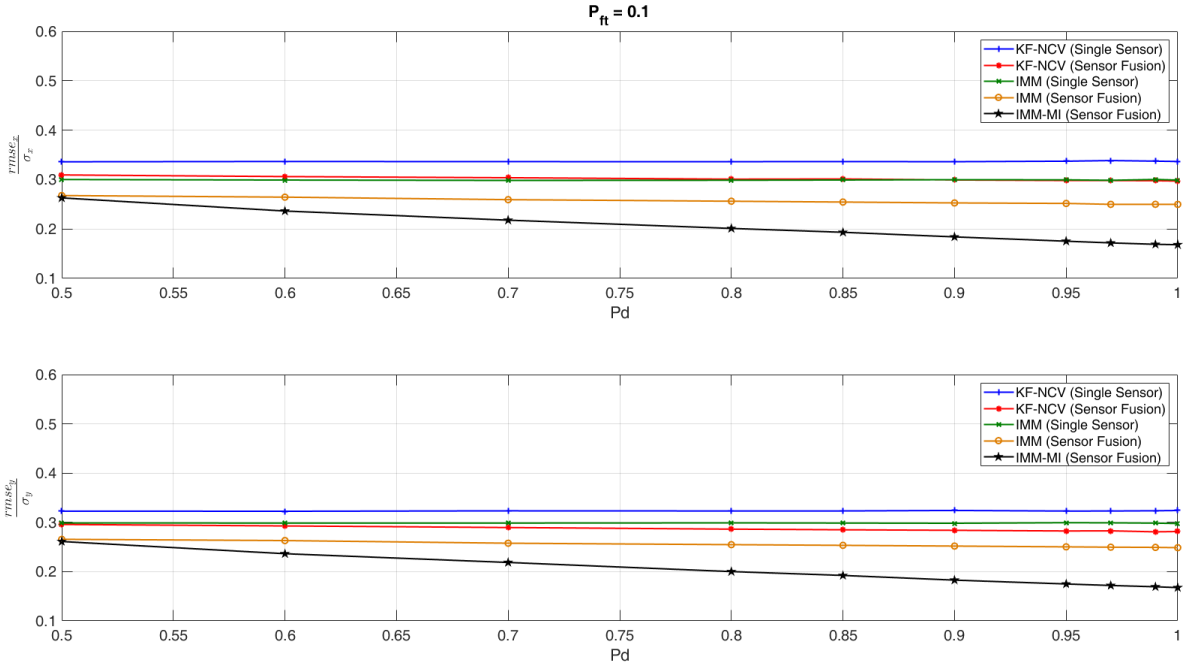

Figure 6.18. Comparison of the normalized positioning RMSE averaged over the entire simulation vs P_d, with respect to the x-axis (top), and the y-axis (bottom), over a simulated Move-Stop-Move target for $P_{ft} = 0.1$.

We can see that the IMM-MI matches the results of the classical IMM, which uses the same number of sensors, for $P_d = 0.5$, while it is better for all the other cases.

We have to highlight that the mentioned situation ($P_d = 0.5, P_{ft} = 0.1$) is not typical in localization and tracking application, because it means that the sensors are working in very poor operating conditions.

Chapter 7
Tests on experimental data

In Chapter 3, two different tests on human targets have been presented. The first one was characterized by a very small number of position estimates for the PSL sensor (Section 3.2). In contrast, in Section 3.3 the device transmissions are increased thanks to the possibility for the active mobile device to perform a real upload activity. For this reason, in this Section we refer to this second test for the experimental validation of our strategy, since we have enough measurements from both sensors to perform the tracking and data fusion and evaluate the performance of all the methodologies presented in Chapter 4 and Chapter 5. Moreover, the experimental setup exploited in this second test for the Passive Radar is enhanced with respect to the previous one, since it is more representative of a real scenario, therefore its analysis is much more interesting for the proposed evaluation.

In order to simplify the subsequent comparison between the localization of the human target before and after the application of the analyzed filters, we report here (Figure 7.1) the results shown in Figure 3.38.

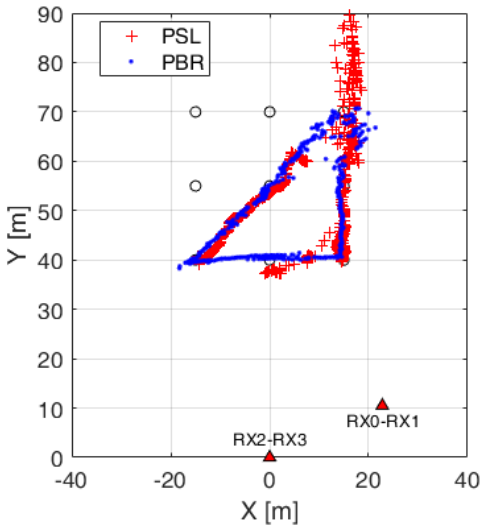

Figure 7.1. Comparison of the PSL and the PBR localization on the XY-plane.

The target positions displayed in Figure 7.1 represent the measurements provided by the two employed sensors. Specifically, the Sensor 1 is the PSL (red crosses), while the Sensor 2 is the PBR (blue dots).

As it is clear, the two sensors are characterized by different measurement accuracies. Exploiting both the theoretical evaluation of the positioning accuracies in the area of interest for the proposed techniques, based on the measures estimated to perform the localization (AoA, TDoA, etc.), and the empirical evaluation, based

on the results obtained in a real scenario, we have established the standard deviations to be used for our analysis.

For the PBR sensor, the standard deviations of the measurement errors have been set to

$$\sigma_x = 0.6\ m,\ \ \sigma_y = 1\ m \tag{7.1}$$

For the PSL sensor, instead, we have followed a different approach. We have seen, from the results reported in Figure 7.1, that the position estimates for the PSL are strongly influenced by the geometry and the scenario used in the specific acquisition campaign. In particular, it is evident the problems that occur in point (15 m, 70 m), where the errors drastically increase, especially for the y-component. Therefore, it is reasonable to use a dynamic change of the standard deviation of the PSL measurement errors.

For the x component, the positioning accuracy is proportional to the distance from the receiving system, that is

$$\sigma_x = \sigma_\varphi \cdot R \tag{7.2}$$

where σ_x is the standard deviation of the measurement errors for the x-component, σ_φ represents the angular errors, and R is the distance from the surveillance antennas.

The accuracy is also linked to the SNR. For a generic estimator, the following relation can be written

$$\sigma_\varphi = \frac{c_0}{\sqrt{SNR}} \tag{7.3}$$

Therefore

$$\sigma_x = \frac{c_0}{\sqrt{SNR}} \cdot R \tag{7.4}$$

In particular, we can distinguish between *Near* and *Far* accuracy

$$\sigma_{xN} = \frac{c_0}{\sqrt{SNR_N}} \cdot R_N \tag{7.5}$$

$$\sigma_{xF} = \frac{c_0}{\sqrt{SNR_F}} \cdot R_F \tag{7.6}$$

We are interested in finding a relationship between these two quantities. Through some mathematical operations, we can write

$$\sigma_{xF} = \frac{c_0}{\sqrt{SNR_N} \cdot \sqrt{\frac{SNR_F}{SNR_N}}} \cdot R_N \cdot \frac{R_F}{R_N} = \sigma_{xN} \cdot \frac{R_F}{R_N} \cdot \sqrt{\frac{SNR_N}{SNR_F}} \tag{7.7}$$

For the SNR we have

$$SNR = \frac{SNR_0}{R^4} \tag{7.8}$$

Therefore

$$\sigma_{xF} = \sigma_{xN} \cdot \frac{R_F}{R_N} \cdot \sqrt{\frac{R_F^4}{R_N^4}} \tag{7.9}$$

Finally, we can find

$$\sigma_{xF} = \sigma_{xN} \cdot \left(\frac{R_F}{R_N}\right)^3 \tag{7.10}$$

For a generic distance Y, considered along the y axis, the equation (7.10) becomes

$$\sigma_x(Y) = \sigma_{xN} \cdot \left(\frac{Y}{R_N}\right)^3 \tag{7.11}$$

where σ_{xN} is the standard deviation calculated at a distance equal to R_N.

In this case, σ_{xN} has been set to

$$\sigma_{xN} = 1\ m \tag{7.12}$$

which represents a reasonable value for the specific case of interest.

For the y component, instead, the following relation applies

$$\sigma_y = \frac{c_1}{\sqrt{SNR}} \tag{7.13}$$

As for the x component, it is possible to distinguish between *Near* and *Far* accuracy

$$\sigma_{yN} = \frac{c_1}{\sqrt{SNR_N}} \tag{7.14}$$

$$\sigma_{yF} = \frac{c_1}{\sqrt{SNR_F}} \tag{7.15}$$

We can write

$$\sigma_{yF} = \frac{c_1}{\sqrt{SNR_N}} \cdot \sqrt{\frac{SNR_N}{SNR_F}} = \sigma_{yN} \cdot \sqrt{\frac{SNR_N}{SNR_F}} \tag{7.16}$$

For the SNR, the (7.8) applies, therefore

$$\sigma_{yF} = \sigma_{yN} \cdot \sqrt{\frac{R_F^4}{R_N^4}} \tag{7.17}$$

Finally, we can find

$$\sigma_{yF} = \sigma_{yN} \cdot \left(\frac{R_F}{R_N}\right)^2 \tag{7.18}$$

Even this time, for a generic distance Y, considered along the y axis, the equation (7.18) becomes

$$\sigma_y(Y) = \sigma_{yN} \cdot \left(\frac{Y}{R_N}\right)^2 \tag{7.19}$$

where σ_{yN} is the standard deviation calculated at a distance equal to R_N.

In this case, σ_{yN} has been set to

$$\sigma_{yN} = 2.85\ m \tag{7.20}$$

which represents a reasonable value for the specific case of interest.

The value of Y in (7.11) and (7.19) changes at each iteration, and it is set with the filtered position of the current iteration.

According to the results shown in Figure 7.1, considering the specific area of interest, the previous choices allow to attribute more importance to the PBR measurements, since they are more accurate than the position estimates of the PSL.

The five methodologies for target tracking have been set with the same values used in Section 6.2 (Table 6), for the standard deviations of the model errors and the Markov transition matrix P. We remind in Table 7 the choice for each methodology.

Table 7. Setting of the employed methodologies.

Approach	$\sigma_{ax} = \sigma_{ay}\ [m/s^2]$	$\sigma_{vx} = \sigma_{vy}\ [m/s]$	P
KF-NCV (Single Sensor)	0.5	-	-
KF-NCV (Sensor Fusion)	0.5	-	-
IMM (Single Sensor)	0.01	0.1	$\begin{bmatrix} 0.95 & 0.05 \\ 0.05 & 0.95 \end{bmatrix}$
IMM (Sensor Fusion)	0.01	0.1	$\begin{bmatrix} 0.95 & 0.05 \\ 0.05 & 0.95 \end{bmatrix}$
IMM-MI (Sensor Fusion)	0.01	0.1	$\begin{bmatrix} 0.95 & 0.05 \\ 0.05 & 0.95 \end{bmatrix}$

In the next sub-sections, the results for these methodologies have been presented, focusing the attention on the advantages and the drawbacks of each one.

7.1.1 KF-NCV (Single Sensor)

In this case, it is necessary to choose one of the two sensors for the test of the "Single Sensor" versions of the proposed strategies. We decided to analyze the PSL sensor, because

1) a previous filtering has not been used over its measurements, while for the PBR we applied a first step of tracking over the Range-Doppler plane, that provides fairly accurate position estimates;
2) it is important to observe the behavior of the filters when the target changes its motion status (move-stop-move). In fact, for this analysis, the PBR is not interesting, since in stop intervals it does not provide target detection, therefore the filtering in these instants stops to work and the track is closed until a new one is opened again, after the arrival of a new measurement.

The effect of the Kalman Filter, implemented with a single NCV model, over the PSL position measurements is shown in Figure 7.2. In particular, the results in the XY-plane are reported in Figure 7.2(a), while Figure 7.2(b) and Figure 7.2(c) present the trend in time of the x and y components, respectively.

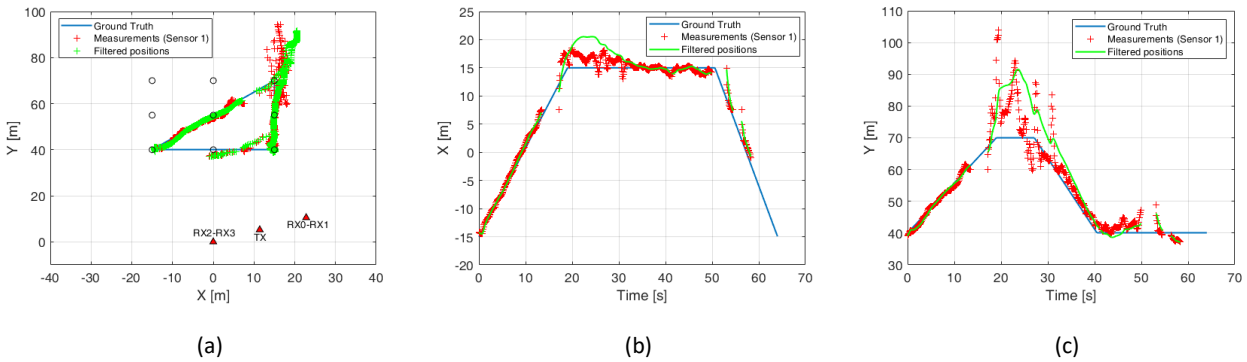

Figure 7.2. Effect of the KF-NCV (Single Sensor), over the PSL position measurements: (a) in the XY-plane, (b) for the x-component vs Time, and (c) for the y-component vs Time.

The results show that the selected value for the standard deviation of the model error, namely $\sigma_{ax} = \sigma_{ay} = 0.5\ m/s^2$ (see Table 7), on one hand, reduces the filtering power of the Kalman Filter, due to the small weight attributed to the prediction based on the considered motion model; on the other hand, it allows to avoid excessive errors during the transition between different motion status, as apparent in Figure 7.2(c) after 40 s. In fact, this is true especially when the target walks near the receiver and the measurement accuracies defined in (7.11) and (7.19) are smaller. In this way, the tracker relies mainly on the position estimates provided by the sensor, reducing the impact of an incorrect motion model.

This produces a very small difference between the raw measurements provided by the PSL sensors (red crosses in Figure 7.2) and the filtered positions (green crosses in Figure 7.2(a) and green solid line in Figure 7.2(b)-(c)). As a consequence, there is a good correspondence between the results obtained after the application of the filter (in green) and the ground truth (blue solid line in the same figure) in the first part of the proposed test (up to about 15 seconds), where the filter model matches the target motion and the PSL measurements are more stable. The problems occur when the target walks close to the metallic fence of the building on the right in Figure 3.31. This effect is evident in Figure 7.2(c), in the interval between 18 s and 26 s: when the target

reaches the point (15 m, 70 m), the position estimates are too inaccurate. This yields bad performance in terms of accuracy in the examined area. After that moment, the Kalman Filter needs long time to reach again the actual path of the target.

In addition, since in this point the distance between target and receiver increases, the measurement accuracies defined in (7.11) and (7.19) assume a higher value, and the tracker attributes more importance to the prediction. This effect is clear in Figure 7.2(a) and Figure 7.2(b) during the first change of motion, when the filtered positions follow the previous trajectory even after the target stops.

Therefore, it is clear that the measurement accuracy has a key role especially in these conditions.

This situation confirms our proposal of using an additional sensor (PBR), which may increase the performance in terms of accuracy.

7.1.2 KF-NCV (Sensor Fusion)

In this second case, we exploit both the available sensors. The approach analyzed in this section uses the same parameters of the single sensor version.

The effect of the Kalman Filter, implemented with a single NCV model, and the additional employment of Data Fusion techniques, over the PSL and PBR position measurements, is shown in Figure 7.3. As for the previous approach, we reported the results in the XY-plane and the trend in time of the x and y components in Figure 7.3(a), Figure 7.3(b) and Figure 7.3(c), respectively.

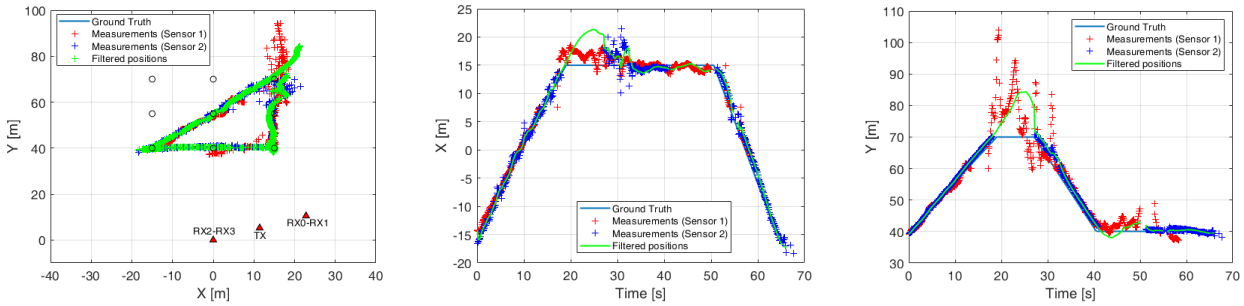

Figure 7.3. Effect of the KF-NCV (Sensor Fusion), over the PSL and PBR position measurements: (a) in the XY-plane, (b) for the x-component vs Time, and (c) for the y-component vs Time.

The results show that the exploitation of the PBR sensor, whose measurements have been displayed with blue crosses in Figure 7.3, helps the tracker to follow the actual target motion, thanks to the possibility to i) rely on more accurate position estimates, and ii) compensate for the lack of measurements of the PSL sensor when the target is moving but it is not involved in upload activities. On the other hand, the PSL is necessary to know the target position when the target is stationary. This is quite apparent during the second stop (from about 40 s to 50 s), where the position is estimated only through the information given by the mobile device, but it is not very useful in the first stop, when the scenario and the operating conditions affect the quality of the PSL estimates, making impossible an accurate localization. Nevertheless, even this time, the setting of the

parameter of interest, defined with the purpose of reducing the errors when the target changes its motion status, does not allow to exploit the potentialities of a filtering operation.

As explained before, the possible solution is represented by the IMM method.

7.1.3 IMM (Single Sensor)

The results for the IMM method, when only the PSL sensor is employed, have been displayed in Figure 7.4.

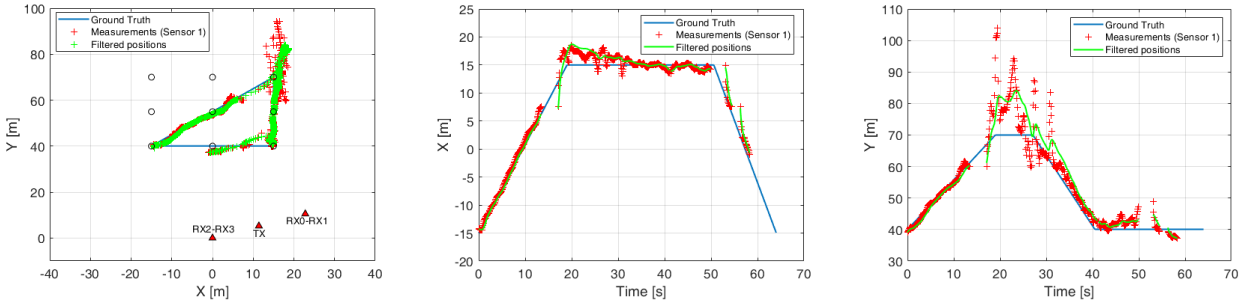

Figure 7.4. Effect of the IMM (Single Sensor), over the PSL position measurements: (a) in the XY-plane, (b) for the x-component vs Time, and (c) for the y-component vs Time.

The images above meet the considerations presented for the KF-NCV (Single Sensor), presented in Section 7.1.1, with reference to the employment of only one sensor, specifically the PSL system. In contrast with the KF-NCV, the IMM allows to limit the errors that occur when the target changes its motion status, as it is clear comparing Figure 7.2(b) and Figure 7.4(b), during the first stop.

Moreover, this figures also show the agreement with the results achieved on simulated target, where we have noticed that the availability of measurements each 0.1 s, when the target is quite slow, produces a worsening in performance, due to the difficulties to understand the target motion status (move or stop), and consequently, to select the correct motion model.

This can be easily seen in Figure 7.5, where the model probabilities for the NCV model (top) and the V0 model (below) have been presented.

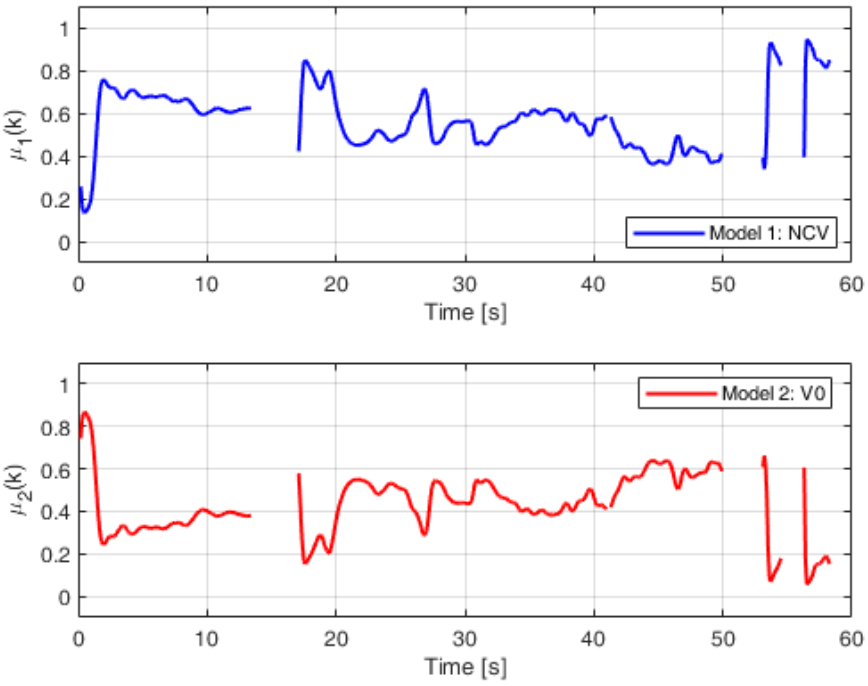

Figure 7.5. Model probabilities for the IMM (Single Sensor) approach.

In this figure, apart from some moments, we can see the incapability of this methodology to choose the correct motion model. In fact, the model probabilities are quite stable around the 50% of choosing one model or the other one, for almost the entire acquisition.

7.1.4 IMM (Sensor Fusion)

Even in this case, the implementation of Data Fusion techniques which combine the measurements of PSL and PBR, produces an improvement in performance thanks to the exploitation of the information carried by an additional sensor.

The results are reported in Figure 7.6.

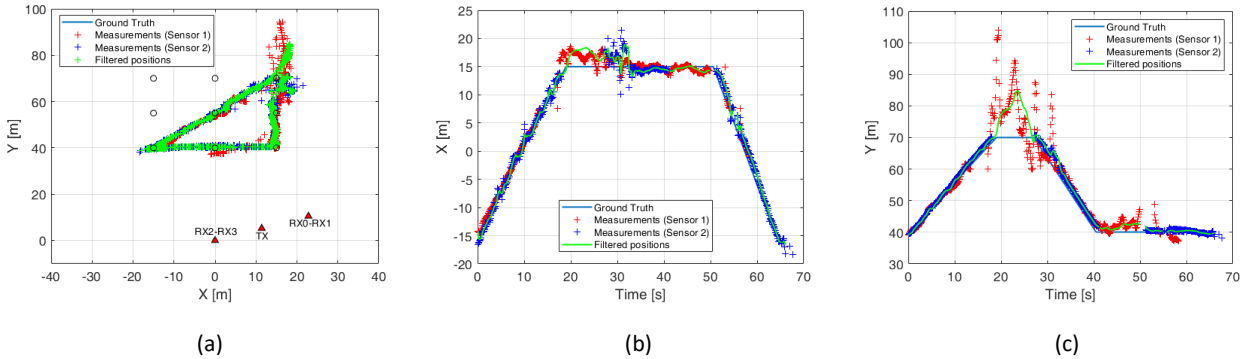

Figure 7.6. Effect of the IMM (Sensor Fusion), over the PSL and PBR position measurements: (a) in the XY-plane, (b) for the x-component vs Time, and (c) for the y-component vs Time.

These images confirm the previous considerations about the advantages produced by the joint exploitation of two different sensors.

The model probabilities for the IMM (Sensor Fusion) are shown in Figure 7.7.

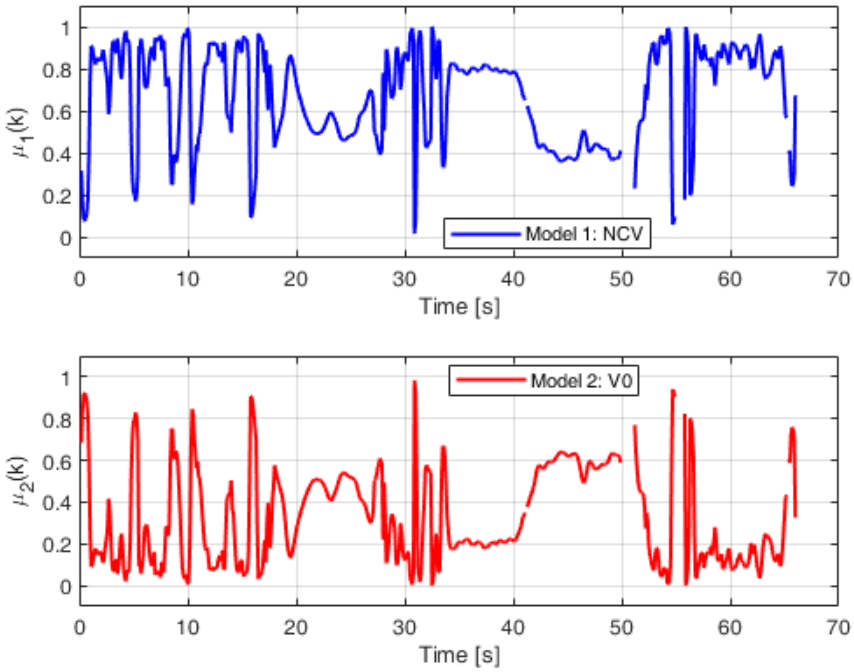

Figure 7.7. Model probabilities for the IMM (Sensor Fusion) approach.

We can notice that the behavior of the two versions of IMM (Single Sensor and Sensor Fusion) are similar when the PBR does not provide the target positions, namely when the target is stationary (from 18 s to 26 s, and from 40 s to 50 s). See Figure 7.5 for comparison.

This time, when the target is moving, the probability to choose the NCV model is higher (μ_1 close to 1) with respect to the single sensor results ($\mu_1 \cong 0.6 \div 0.8$), although the estimates fluctuate more, especially in the first part of the acquisition.

7.1.5 IMM-MI (Sensor Fusion)

In line with the four methods presented above, the IMM-MI has been implemented with the parameter shown in Table 7.

The localization and tracking in the XY-plane and the trend in time of the x and y components are reported in Figure 7.8(a), Figure 7.8(b) and Figure 7.8(c), respectively.

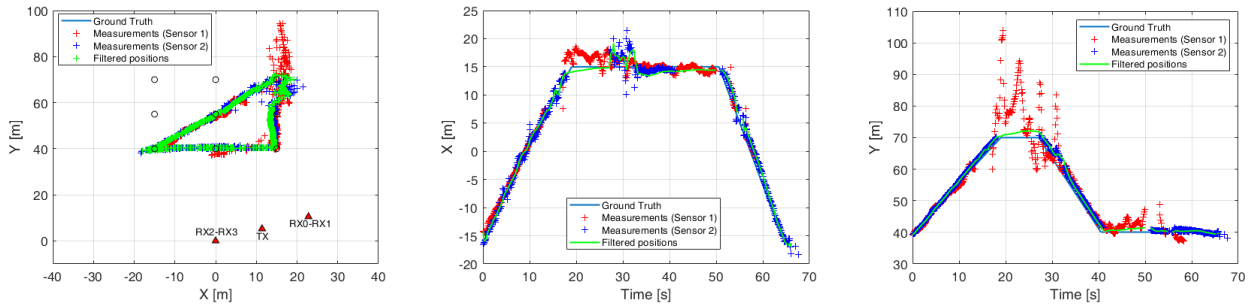

(a) (b) (c)

Figure 7.8. Effect of the IMM-MI (Sensor Fusion), over the PSL and PBR position measurements: (a) in the XY-plane, (b) for the x-component vs Time, and (c) for the y-component vs Time.

The proposed strategy provides a further performance improvement. In fact, its effect is evident i) in the interval where the target is moving, where we can see that the IMM-MI produces more smoothed filtered positions, which are very close to the line of the ground truth, and ii) in the second stop, where the variation around the point (15 m, 40 m) in Figure 7.8(a) are smaller with respect to that shown for the previous methodologies, and in particular in Figure 7.8(b) and Figure 7.8(c), where the green line is much more stable and close to the ground truth, when compared with the other four cases.

A positive effect is also obtained for the first stop, namely between 18 s and 26 s in Figure 7.8(b)-(c). In this part, the increase of the quality is apparent not only in Figure 7.8(a), but also in Figure 7.8(b)-(c) where the trend of the green line is very similar to the ground truth. Moreover, an interesting behavior can be also seen, in the same interval, by observing only Figure 7.8(c), where the PSL measurement errors are limited by the innovation modification, which produces a reduction of the relative errors with respect to the curves shown in Figure 7.2(c), Figure 7.3(c), Figure 7.4(c) and Figure 7.6(c). This result highlights the advantages of the use of a modified version of the IMM, since it improves the performance even in noisy environments.

On the other hand, we can also notice that, despite we have unbalanced the IMM, with the purpose of helping the model selection, the PSL measurements still have a considerable influence on the final results. This means that with better operating conditions, the PSL sensor can refine the filtered position estimates, through the introduction of its measurements into the system.

The previous considerations show that the combination of Data Fusion techniques and the proposed modification of the IMM represents a good solution for target localization and tracking in short range applications.

This is confirmed in Figure 7.9, where the model probabilities for the IMM-MI (Sensor Fusion) are displayed.

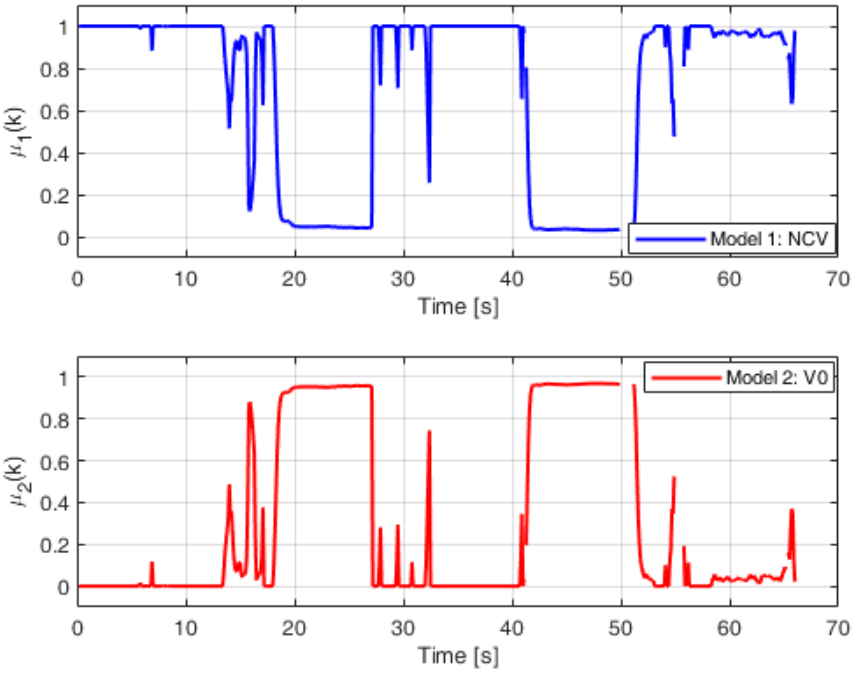

Figure 7.9. Model probabilities for the IMM-MI (Sensor Fusion) approach.

In this figure, the capability of our system to follow the target motion and select the correct model is sufficiently evident. In fact, the model probabilities reach values very close to 1 or 0 in the correct time instants.

In particular, when both the sensors provide their measurements, the NCV model manages to achieve the value $\mu_1 = 1$. When the device interrupts its transmission, and so the PSL does not provide the target position estimates, the model probability for the NCV model reaches a value lower than 1, as apparent between about 58 s and the end of the acquisition.

Moreover, in contrast with the other strategies, this time, during the first stop, the effect on motion recognition of poor accuracy in PSL measurements is strongly reduced, since this operation is performed thanks to the knowledge of the presence or the absence of PBR detections.

7.1.6 Comparison of the analyzed methodologies in terms of positioning error

According to the analysis carried out for the tests on simulated target, we report in Figure 7.10 the results for the instantaneous positioning errors of the five examined approaches, over the presented experimental test. In particular, when the combination of the two coordinates is considered we refer to Figure 7.10(a), while the analysis of the single components are reported in Figure 7.10(b) and Figure 7.10(c), for the x-component and the y-component, respectively.

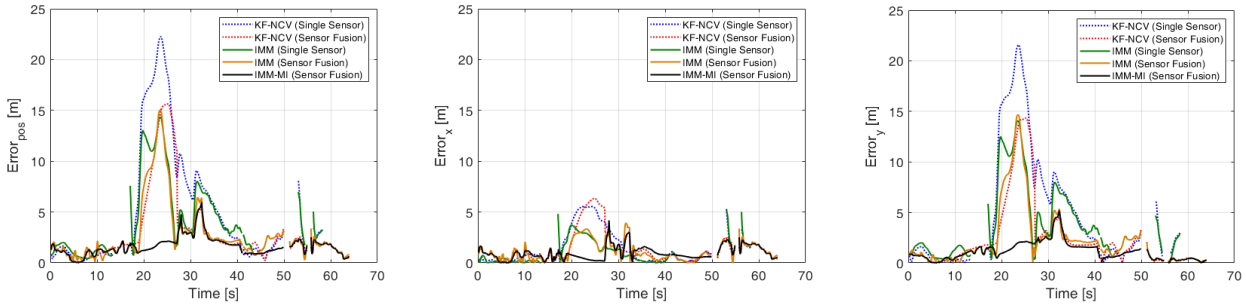

(a) (b) (c)

Figure 7.10. Positioning errors (a) considering both the coordinates, (b) for the x-component, and (c) for the y-component.

As expected, the higher errors occur during the first stop, where the distance from the receiving antennas and the proximity to the metallic fence and the building affect the quality of the available measurements, especially when the target is stationary and only the PSL provides information about the target location. In this case, the IMM-MI is the strategy that limits the negative effect of these situation, containing the errors even with inaccurate measurements.

On average, the strategy proposed in this thesis, namely the IMM-MI that combines the measurements of PBR and PSL sensors, outperforms the other strategies, and it allows to localize and track moving and stationary targets, regardless the Wi-Fi network traffic conditions.

The benefits of this methodology are also shown in Table 8.

Table 8. Mean errors and percentage of acquisition covered by the tracking.

	Mean Error x [m]	**Std Error x [m]**	**Mean Error y [m]**	**Std Error y [m]**	**Mean Error pos [m]**	**Std Error pos [m]**	**% Acquisition covered**
PSL Measures	0.9072	0.9028	3.6605	5.2823	3.9294	5.2439	77%
PBR Measures	1.1202	0.8661	1.1229	0.9152	1.7477	1.0236	71%
KF-NCV (Single Sensor)	1.4850	1.7182	4.9247	5.8583	5.2545	6.0098	77%
KF-NCV (Sensor Fusion)	1.4288	1.5498	2.4048	3.3880	2.9605	3.5971	97%
IMM (Single Sensor)	0.9716	1.0915	3.8201	3.5282	4.0352	3.5906	77%
IMM (Sensor Fusion)	1.1305	0.8977	2.2490	2.9444	2.7105	2.9091	97%
IMM-MI (Sensor Fusion)	0.9589	0.6479	1.1397	0.9056	1.6152	0.9213	97%

It is evident the decrease of the total error when the IMM-MI is used (last row of Table 8). In fact, with this strategy we can obtain very accurate position estimates. In particular, the errors are comparable with those

achieved by the passive radar, after the application of a first step of tracking in the Range-Doppler plane (see the second row of Table 8), but the percentage of acquisition covered by the IMM-MI approach (97%), thanks to the Sensor Fusion strategy, is higher with respect to the passive radar capability (71%).

This aspect is in line with the expected results of this thesis.

Chapter 8
Conclusion

In this section we draw the final conclusions of this work, focusing mainly the attention on the main contributions of this Thesis.

The aim of this thesis is the definition of innovative methodologies able to solve the problem of the localization of human targets and small objects in local area environments in any operating conditions. To achieve this result, in this work we proposed the fusion of two different positioning techniques based on Wi-Fi signals: Passive Bistatic Radar (PBR) and Passive Source Location (PSL).

Therefore, we started with the description of the employed sensors, through the evaluation of measurement estimation and positioning techniques. Then, the two localization strategies have been analyzed and compared, and their complementarity has been demonstrated also on experimental data.

After that, existing tracking techniques have been briefly described. In particular, the advantages and limitations of the Kalman Filter and the Interacting Multiple Model (IMM) are explained, especially when they operate on a typical move-stop-move target.

A new Sensor Fusion tracking filter is proposed, which exploits both the advantages provided using Data Fusion techniques and a modified version of the IMM, based on the knowledge of the sensor characteristics.

The main contributions of this thesis are the following:

1. The estimation techniques for the measurements used in PBR and PSL sensors are reviewed and innovative techniques are proposed for the TDoA estimation of PSL sensors. In particular, starting from the CCF, a slope-based method and its iterative version are proposed and shown to outperform the other available techniques.
2. According to previous studies on the PBR system, the positioning techniques based on different combinations of measurements (only AoA measurements, only TDoA measurements and the hybrid solution with both AoA and TDoA) for the PSL sensor are extensively analyzed. Specifically, it is shown that the higher realization simplicity in practical applications and the better accuracies achieved, especially in very short applications, by using only AoA measurements, suggest avoiding the employment of TDoA measurements when possible.
3. The characteristics of PBR and PSL measurements and positioning capabilities have been analyzed and compared to assess the relative performance. In particular:
    a. The PBR provides a good accuracy for moving targets when the network traffic load is limited and a short beacon interval (BI) can be used. In contrast, measurements are absent for static targets. Moreover, using long BI the performance shows a neat degradation.

b. The PSL provides good accuracy localization for both moving and static targets, when the device is active and transmits packets with a high rate. In contrast, PSL measurements can be not enough to track a target if its device does not transmit with regularity.
c. PBR and PSL show a high complementarity, since the one of the two is able to operate effectively in all conditions where the other shows sensible degradations.

4. The limitations of the use of PBR and PSL sensors based on the signals emitted on a specific Wi-Fi channel are characterized. Specifically, it is shown that the performance of the PBR largely depends on the network load, which in turns depend on the level of activity of the devices. Therefore, good PBR performance are not available when the activity of the devices allows a good performance of the PSL sensor and vice-versa.
5. The fusion of PBR and PSL measurements is shown to be able to provide significant improvement with respect to the single sensor. This is clearly demonstrated by applying an IMM Sensor Fusion filter to PBR and PSL using both simulated data and the data collected by an experimental setup that aims at tracking moving people carrying Wi-Fi devices.
6. A new Sensor Fusion tracking filter is proposed based on the IMM scheme, but with a modified innovation (MI) evaluation, to improve the localization performance in the typical *stop & go* motion scenario of human targets. Specifically, the new IMM-MI tracking filter exploits the characteristics of the two sensors to identify soon the transition from a “move” phase to a “stop” phase and vice-versa, so that can always base its filtering on the most appropriate sensor in each phase.
7. The new IMM-MI tracking filter is applied against the experimental data from an experimental setup with people following a stop and go motion pattern. The improved performance is clearly demonstrated by comparing the results of the IMM-MI against the standard IMM.

BIBLIOGRAPHY

[1] Giuliano R., Mazzenga F., Petracca M., Vari M., “Indoor localization system for first responders in emergency scenario”, *9th International Wireless Communications and Mobile Computing Conference (IWCMC 2013)*, Cagliari Italy, pp. 1821-1826, Jul. 2013.

[2] T. Gallagher, E. Wise, H. C. Yam, B. Li, E. Ramsey-Stewart, A. G. Dempster & C. Rizos, “Indoor navigation for people who are blind or vision impaired: where are we and where are we going?”, *Journal of Location Based Services*, Vol. 8, No. 1, pp. 54-73, Mar. 2014.

[3] S. A. Shah and F. Fioranelli, "RF Sensing Technologies for Assisted Daily Living in Healthcare: A Comprehensive Review", *IEEE Aerospace and Electronic Systems Magazine*, vol. 34, no. 11, pp. 26-44, 1 Nov. 2019.

[4] A. Popleteev, V. Osmani, O. Mayora, “Investigation of indoor localization with ambient FM radio stations”, *IEEE International Conference on Pervasive Computing and Communications (PerCom’12)*, pp.171-179, Mar. 2012.

[5] C. Bongioanni, F. Colone, P. Lombardo, “Performance Analysis of a Multi-Frequency FM Based Passive Bistatic Radar”, *IEEE Radar Conference 2008*, Rome, Italy, 26-30 May 2008.

[6] M. Malanowski, G. Mazurek, K. Kulpa, J. Misiurewicz, “FM based PCL radar demonstrator*”, Proc. International Radar Symposium 2007*, 431-435.

[7] M. Malanowski, K. Kulpa, K.E. Olsen, “Extending the integration time in DVB-T-based passive radar”, *2011 European Radar Conference (EuRAD)*, 2011, pp. 190-193.

[8] F. Colone, D. Langellotti, P. Lombardo, “DVB-T Signal Ambiguity Function Control for Passive Radars”, *IEEE Trans. on Aerospace and Electronic Systems* N. 1, 2014, pp 329-347.

[9] J. Huang, L. Lo Presti, "DVB-T positioning with a one shot receiver", *International Conference on Localization and GNSS (ICL-GNSS)*, pp. 1-5, June 2013.

[10] F. Filippini, T. Martelli, F. Colone and R. Cardinali, "Exploiting long coherent integration times in DVB-T based passive radar systems", *2019 IEEE Radar Conference (RadarConf)*, Boston, MA, USA, 2019, pp. 1-6.

[11] N. del-Rey-Maestre, M. Jarabo-Amores, J. Bárcena-Humanes, D. Mata-Moya and P. Gómez-del-Hoyo, "ECA Filter Effects on Ground Clutter Statistics in DVB- T Based Passive Radar", *2018 26th European Signal Processing Conference (EUSIPCO)*, Rome, 2018, pp. 1217-1221.

[12] P. Wojaczek, A. Summers, D. Cristallini, I. Walterscheid, P. Lombardo and F. Colone, "Results of Airborne PCL Under CCI Conditions Using DVB-T Illuminators of Opportunity", *2018 International Conference on Radar (RADAR)*, Brisbane, QLD, 2018, pp. 1-6.

[13] B. Tan, K. Woodbridge, K. Chetty, “A real-time high resolution passive WiFi Doppler-radar and its applications”, *2014 International Radar Conference (Radar)*, 13-17 Oct. 2014, Lille (France).

[14] P. Falcone, F. Colone, C. Bongioanni, P. Lombardo, "Experimental Results for OFDM WiFi-based Passive Bistatic Radar", *IEEE Radar Conference 2010*, pp. 10-14, May 2010.

[15] P. Falcone, F. Colone, P. Lombardo, "Potentialities and challenges of WiFi-based passive radar", *IEEE Aerosp. Electron. Syst. Mag.*, vol. 27, no. 11, pp. 15-26, Nov. 2012.

[16] P. Falcone, F. Colone, A. Macera, P. Lombardo, "Localization and tracking of moving targets with WiFi-based passive radar", *Proc. IEEE Radar Conf.*, pp. 0705-0709, May 2012.

[17] P. Falcone, F. Colone, A. Macera, and P. Lombardo, "Two-dimensional location of moving targets within local areas using WiFi-based multistatic passive radar," *IET Radar Sonar Navig.*, vol. 8, no. 2, pp. 123–131, Feb. 2014.

[18] S. Rzewuski, K. Kulpa, P. Samczyński, "Duty factor impact on WIFIRAD radar image quality", *2015 IEEE Radar Conference*, 2015, pp. 400-405.

[19] F. Shi, K. Chetty and S. Julier, "Passive Activity Classification Using Just WiFi Probe Response Signals", *2019 IEEE Radar Conference (RadarConf)*, Boston, MA, USA, 2019, pp. 1-6.

[20] C. R. Karanam, B. Korany and Y. Mostofi, "Tracking from One Side - Multi-Person Passive Tracking with WiFi Magnitude Measurements", *2019 18th ACM/IEEE International Conference on Information Processing in Sensor Networks (IPSN)*, Montreal, QC, Canada, 2019, pp. 181-192.

[21] H. Liu, H. Darabi, P. Banerjee, J. Liu, "Survey of wireless indoor positioning techniques and systems", *IEEE Trans. Syst. Man Cybern. Syst. Part C: Applications and Reviews*, vol. 37, no. 6, pp. 1067-1080, 2007.

[22] S. Shukri, L. Munirah Kamarudin, M. Hafiz Fazalul Rahiman, "Device-Free Localization for Human Activity Monitoring", *Intell. Video Surveill.*, 2019.

[23] F. Colone, D. Pastina, P. Falcone, P. Lombardo, "WiFi-based passive ISAR for high resolution cross-range profiling of moving targets", *IEEE Transactions on Geoscience and Remote Sensing (GRS)*, Vol 52, N. 6, 2014, pp. 3486-3501.

[24] Y. Jin, W. Soh, and W. Wong, "Indoor Localization with Channel Impulse Response Based Fingerprint and Nonparametric Regression", *IEEE Transactions on Wireless Communications*, Vol. 9, No. 3, pp. 1120-1127, March 2010.

[25] M. Kotaru, K. Joshi, D. Bharadia, S. Katti, "SpotFi: Decimeter Level Localization Using WiFi", *SIGCOMM '15*, London, United Kingdom, Aug. 2015.

[26] J. Wilson and N. Patwari, "Radio Tomographic Imaging with Wireless Networks", *IEEE Transaction on Mobile Computing*, Vol. 9, No. 5, pp. 621-632, Jan. 2010.

[27] D. Pastina, F. Colone, T. Martelli, and P. Falcone. "Parasitic exploitation of Wi-Fi signals for indoor radar surveillance", *IEEE Transactions on Vehicular Technology*, vol. 64, no. 4, pp. 1401-1415, Jan. 2015.

[28] Wireless LAN Medium Access Control (MAC) and physical Layer (PHY) Specifications, IEEE Std. 802.11, 2016.

[29] F. Colone, K. Woodbridge, H. Guo, D. Mason and C. J. Baker, "Ambiguity Function Analysis of Wireless LAN transmissions for passive radar", *IEEE Trans. on Aerospace and Electronic Systems*, Vol. 47 , Issue 1, January 2011, pp. 240-264.

[30] P. Falcone, F. Colone, P. Lombardo, T. Bucciarelli, "Range Sidelobes Reduction Filters for WiFi-Based Passive Bistatic Radar", *EURAD 2009*, Rome, Italy, 30 September-2 October 2009.

[31] P. Falcone, F. Colone, P. Lombardo, "Doppler frequency sidelobes level control for WiFi-based passive bistatic radar", *Proc. 2011 IEEE Radar Conf.*, Kansas City, MO, USA, May 2011, pp. 435–440.

[32] F. Colone, C. Palmarini, T. Martelli, E. Tilli, "Sliding extensive cancellation algorithm for disturbance removal in passive radar," *IEEE Transactions on Aerospace and Electronic Systems*, vol. 52, no. 3, pp. 1309-1326, June 2016.

[33] G. Jacovitti, G. Scarano, "Discrete time techniques for time delay estimation", *IEEE Trans. Signal Proc.*, vol 41, pp.525-533, Feb 1993.

[34] F. Babich, M. Noschese, C. Marshall, M. Driusso, "A simple method for ToA estimation in OFDM systems", *European Navigation Conference (ENC)*, pp. 305-310, May 2017.

[35] M. Noschese, F. Babich, M. Comisso, C. Marshall, M. Driusso, "A low-complexity approach for time of arrival estimation in OFDM systems", *Wireless Communication Systems (ISWCS) 2017 International Symposium on*, pp. 128-133, Aug. 2017.

[36] K. Keunecke, G. Scholl, "IEEE 802.11 n-based TDOA performance evaluation in an indoor multipath environment", *The 8th European Conference on Antennas and Propagation (EuCAP 2014)*, The Hague, 2014, pp. 2131-2135.

[37] F. Benedetto, G. Giunta, E. Guzzon, "Enhanced TOA-based indoor-positioning algorithm for mobile LTE cellular systems", *2011 8th Workshop on Positioning, Navigation and Communication*, Dresden, 2011, pp. 137-142.

[38] A. Giorgetti, M. Chiani, "Time-of-Arrival Estimation Based on Information Theoretic Criteria", *IEEE Transactions on Signal Processing*, vol. 61, no. 8, pp. 1869-1879, April15, 2013.

[39] C. C. Chong, D. I. Laurenson, C. M. Tan, S. McLaughlin, M. A. Beach, A. R. Nix, "Joint detection-estimation of directional channel parameters using the 2-D frequency domain SAGE algorithm with serial interference cancellation", *2002 IEEE International Conference on Communications. Conference Proceedings. ICC 2002*, New York, NY, USA, 2002, pp. 906-910 vol.2.

[40] B. H. Fleury, M. Tschudin, R. Heddergott, D. Dahlhaus and K. Ingeman Pedersen, "Channel parameter estimation in mobile radio environments using the SAGE algorithm", *IEEE Journal on Selected Areas in Communications*, vol. 17, no. 3, pp. 434-450, March 1999.

[41] I. Milani, F. Colone, C. Bongioanni, P. Lombardo, "WiFi emission-based vs passive radar localization of human targets", *2018 IEEE Radar Conference*, Oklahoma City, OK, USA, 23-27 April 2018.

[42] I. Milani, F. Colone, P. Lombardo, "2D Localization with WiFi Passive Radar and Device-Based Techniques: An Analysis of Target Measurements Accuracy", *2018 19th International Radar Symposium (IRS)*, Bonn, Germany, 20-22 June 2018.

[43] I. Milani, F. Colone, C. Bongioanni, P. Lombardo, "Impact of Beacon Interval on the performance of WiFi-based passive radar against human targets", *2018 22nd International Microwave and Radar Conference (MIKON)*, Poznan, Poland, 14-17 May 2018.

[44] F. Colone, C. Bongioanni, P. Lombardo, "Multifrequency integration in FM radio-based passive bistatic radar. Part II: Direction of arrival estimation", *IEEE Aerospace and Electronic Systems Magazine*, Vol. 28, N. 4 April 2013, pp. 40-47.

[45] Y. Bar-Shalom, X. R. Li, ″Multitarget-Multisensor Tracking: Principles and Techniques ″, 1995.

[46] X. R. Li, Y. Bar-Shalom, "Multiple-model estimation with variable structure", *IEEE Transactions on Automatic Control*, vol. 41, pp. 478-493, Apr. 1996.

[47] E. Mazor, A. Averbuch, Y. Bar-Shalom, J. Dayan, "Interacting multiple model methods in target tracking: A survey", *IEEE Transactions on Aerospace and Electronic Systems*, vol. 34, no. 1, pp. 103-123, Jan. 1998.

[48] A. F. Genovese, "The interacting multiple model algorithm for accurate state estimation of maneuvering targets", *Johns Hopkins APL Technical Digest*, vol. 22, no. 4, pp. 614-623, 2001.

[49] T. Kirubarajan, Y. Bar-Shalom, "Tracking Evasive Move-Stop-Move Target with a GMTI Radar Using a VSIMM Estimator", *IEEE Transactions on Aerospace and Electronic Systems*, vol. 39, no. 3, July 2003.

[50] S. Coraluppi, C. Carthel, "Multiple-hypothesis IMM (MH-IMM) filter for moving and stationary targets", *Proceedings of 2001 International Conference on Information Fusion*, Montreal, Canada, Aug. 2001.

[51] K. Granström, P. Willett, Y. Bar-Shalom, "Systematic approach to IMM mixing for unequal dimension states", *IEEE Transactions on Aerospace and Electronic Systems*, vol. 51, no. 4, pp. 2975-2986, Oct. 2015.

[52] N. Assimakis, M. Adam, "Kalman Filter Riccati Equation for the Prediction Estimation and Smoothing Error Covariance Matrices", *ISRN Computational Mathematics*, vol. 2013, pp. 1-7, 2013.

LIST OF PUBLICATIONS

Conference Proceedings

[C1] I. Milani, F. Colone, P. Lombardo, "2D Localization with WiFi Passive Radar and Device-Based Techniques: An Analysis of Target Measurements Accuracy", *2018 19th International Radar Symposium (IRS)*, Bonn, Germany, 20-22 June 2018.

[C2] I. Milani, F. Colone, C. Bongioanni, P. Lombardo, "Impact of Beacon Interval on the performance of WiFi-based passive radar against human targets", *2018 22nd International Microwave and Radar Conference (MIKON)*, Poznan, Poland, 14-17 May 2018.

[C3] I. Milani, F. Colone, C. Bongioanni, P. Lombardo, "WiFi emission-based vs passive radar localization of human targets", *2018 IEEE Radar Conference*, Oklahoma City, OK, USA, 23-27 April 2018.

Speeches at National and International Workshops

[W1] I. Milani, C. Bongioanni, F. Colone, P. Lombardo, "2D Localization of UAVs and human targets with WiFi-based PBR and PSL", *2019 3rd Italian Workshop on Radar and Remote Sensing*, Rome, Italy, 30-31 May 2019.

[W2] I. Milani, F. Colone, C. Bongioanni, P. Lombardo, "Localization of Human Targets: WiFi Emission-Based vs Passive Radar Techniques", *2018 2nd Italian Workshop on Radar and Remote Sensing*, Pavia, Italy, 28-29 May 2018.